
Nonequilibrium phenomena in many-body quantum systems: dynamics, thermodynamics, and dynamical phase transitions

Markus Philip Ludwig Heyl



München 2012

Nonequilibrium phenomena in many-body quantum systems: dynamics, thermodynamics, and dynamical phase transitions

Markus Philip Ludwig Heyl

Dissertation
an der Fakultät für Physik
der Ludwig-Maximilians-Universität
München

vorgelegt von
Markus Philip Ludwig Heyl
aus Starnberg

München, den 16.05.2012

Erstgutachter: Prof. Dr. Stefan Kehrein

Zweitgutachter: Prof. Dr. Wilhelm Zwerger

Tag der mündlichen Prüfung: 13. Juli 2012

Contents

Zusammenfassung	ix
1 Introduction	1
2 Local quantum quenches	9
2.1 Publication: Interaction quench dynamics in the Kondo model	12
2.2 Publication: Electron-plasmon scattering in chiral Luttinger liquids	24
2.3 Publication: Real-time energy dynamics in spin-1/2 Heisenberg chains	31
3 Work distribution functions and x-ray edge absorption spectra	47
3.1 Work distribution functions	49
3.2 Work fluctuation theorems	51
3.2.1 Jarzynski equality	52
3.2.2 The Crooks relation	53
3.3 Publication: The Crooks relation in optical spectra	55
3.4 Absorption spectra of quantum dots	65
3.4.1 Minimal model for the description of quantum dots	65
3.4.2 Description of x-ray absorption in quantum dots	67
3.5 Publication: The X-ray edge singularity in optical spectra of Quantum Dots	70
4 Dynamical phase transitions	77
4.1 The concept of a dynamical quantum phase transition	78
4.1.1 Loschmidt amplitude	78
4.1.2 Fisher zeros	79
4.1.3 Observables	82
4.2 Dynamical quantum phase transitions in the Ising model	83
4.2.1 Quenches in the transverse magnetic field	87
4.2.2 Loschmidt amplitude	88
4.2.3 Work distribution function	89
4.2.4 Fisher zeros and real-time nonanalyticities	96
4.2.5 Topological quantization: Chern number	98
4.2.6 Equilibrium order parameter	104

5 Periodically driven many-body quantum systems	109
5.1 Publication: Periodically driven Kondo model	110
5.2 Publication: Nonlinear ac transport through a resonant level model	125
5.3 Parametric instability in periodically driven Luttinger Liquids	137
5.3.1 Nonequilibrium time evolution	140
5.3.2 Internal energy density	141
5.3.3 Fermionic density	143
5.3.4 Momentum distribution	145
5.3.5 Conclusions	147
6 Conclusion and outlook	149
List of publications	160
Acknowledgements	162

List of Figures

1.1	Collapse and revival	2
1.2	Typical nonequilibrium protocol	3
2.1	Central questions associated with quantum quenches	10
2.2	Linearization of the fermionic dispersion relation	25
3.1	X-ray edge absorption process	48
3.2	Nonequilibrium protocol	49
3.3	Work distribution function $P(W)$	52
3.4	Forward and backward processes	53
3.5	Implementation of x-ray edge spectra in quantum dots	67
4.1	Partition function zeros	81
4.2	Equilibrium phase diagram of the one-dimensional Ising model	84
4.3	Illustration for the magnetic field quench in the Ising model	87
4.4	Cumulant generating functions of the work distribution in the Ising model	91
4.5	Work rate function for extreme quenches	93
4.6	Work rate functions for quenches in the transverse magnetic field	94
4.7	Fisher zeros for magnetic field quenches in the Ising model	96
4.8	Nonanalytic behavior of the Loschmidt rate function	98
4.9	Closed manifolds and Chern numbers	99
4.10	Topological equivalence of the effective Brioullin zone and the S^2 -sphere . .	101
4.11	Dynamics of the longitudinal magnetization	105
5.1	Protocol of the ac transport through a resonant level model	126
5.2	Internal energy density for the periodically driven Luttinger liquid	142
5.3	Fermionic particle density under the influence of a periodic driving.	144
5.4	Momentum distribution for the periodically driven Luttinger liquid	146

Zusammenfassung

Diese Arbeit beschäftigt sich mit Nichtgleichgewichtsphänomenen in quantenmechanischen Vielteilchensystemen. Die Bedeutung des Gebiets der Nichtgleichgewichtsphysik wurde in den letzten Jahren maßgeblich durch die jüngsten Fortschritte in Experimenten geprägt. Die Realisierung von kalten Atomgasen in optischen Gittern ermöglicht die experimentelle Simulation der Dynamik von isolierten quantenmechanischen Vielteilchensystemen jenseits des Gleichgewichts mit einer hohen Präzision. Der Fokus der vorliegenden theoretischen Arbeit liegt dabei auf zwei generischen Vorgehensweisen eine Nichtgleichgewichtsdynamik zu erzeugen. Einerseits werden Systeme untersucht, deren Dynamik durch eine instantane Änderung eines Systemparameters entsteht, andererseits Systeme, die einer periodischen Störung unterworfen sind.

Die Eigenschaften von Systemen, deren Nichtgleichgewichtsdynamik durch instantane Störungen verursacht ist, werden dabei unter drei unterschiedlichen Gesichtspunkten betrachtet - Dynamik, Thermodynamik und dynamische Phasenübergänge. Die Arbeit beginnt mit der Untersuchung der zeitabhängigen Dynamik anhand von expliziten Beispielen stark korrelierter Systeme wie dem Kondo Modell, einer Luttinger Flüssigkeit und der anisotropen Heisenbergkette. Von einem thermodynamischen Gesichtspunkt ist die an dem System geleistete Arbeit eine zentrale Größe. Dessen quantenmechanische Bedeutung als Zufallsvariable ist erst jüngst genau untersucht worden. Die dazugehörige Wahrscheinlichkeitsdichte, work distribution genannt, ist die zentrale Größe der Nichtgleichgewichtsfluktuationstheoreme wie der Jarzynski-Gleichung oder der Crooks Relation, die man als Nichtgleichgewichtserweiterungen der Fluktuations-Dissipations-Theoreme interpretieren kann. Eine wesentliche Beobachtung der vorliegenden Arbeit ist die Erkenntnis, dass quantenmechanische work distributions in optischen Spektren des x-ray edge Typs gemessen werden können und damit erstmals eine experimentelle Verifizierung und Untersuchung der Nichtgleichgewichtsfluktuationstheoreme möglich wird.

Der zentrale Aspekt der vorliegenden Arbeit ist die Definition eines dynamischen Phasenübergangs für abgeschlossene quantenmechanische Vielteilchensysteme. Im Falle eines Gleichgewichtsphasenübergangs ändern sich die Eigenschaften des untersuchten Systems schlagartig. Dies äußert sich in Nichtanalytizitäten der thermodynamischen Potentiale an kritischen Punkten. Wie in dieser Arbeit untersucht wird, kann ein solches Verhalten auch in der Zeitentwicklung quantenmechanischer Vielteilchensysteme auftreten mit Nichtanalytizitäten zu gewissen kritischen Zeiten. Dieses Verhalten wird anhand des eindimensionalen Ising Modells mit transversalem Magnetfeld als konkretem Beispiel im Detail analysiert.

Zum Abschluss werden die Eigenschaften periodisch getriebener quantenmechanischer Vielteilchenmodelle behandelt für drei exemplarische Systeme. Dazu zählen das Kondo Modell mit periodisch ein- und ausgeschalteter Wechselwirkung, Wechselstromtransport durch einen Quantenpunkt jenseits des Regimes linearer Antwort und eine periodisch getriebene Luttinger Flüssigkeit.

x

Zusammenfassung

Chapter 1

Introduction

Nonequilibrium processes are omnipresent in every-day life. Among all the countless phenomena nonequilibrium processes can manifest in the emergence and buildup of macroscopically large structures. A liquid in a gravitational field and subject to a sufficiently large temperature difference between its top and bottom develops collective rotating matter currents in macroscopically large cells. This is Rayleigh-Bénard convection. Convection can also manifest in the formation of monstrous hurricanes that are driven by the ascent of warm moist air from the sea. These are examples of nonequilibrium phenomena of macroscopic classical systems. Recently, the study of nonequilibrium processes in quantum many-body systems has regained particular interest.

Some nonequilibrium processes are induced by slow external forces such that the system under study can be considered to be in equilibrium at every instant of time. Those processes are termed quasistatic. In the opposite limit the system is perturbed massively inducing dynamics that is beyond an equilibrium description. Provided the force only acts for a finite time interval equilibrium thermodynamics, remarkably, is still capable to predict the properties of the steady state the system asymptotically evolves into as long as the system equilibrates which is a commonly accepted feature of nearly all realistic physical systems. Contrary to this common expectation there exists, however, a specific class of isolated systems termed integrable that have been realized in experiments only recently for which equilibration is hindered by the presence of particular conservation laws [93]. The microscopic conditions necessary or sufficient for closed quantum systems to equilibrate, however, are still under debate [137]. Continuously driven systems such as in case of Rayleigh-Bénard convection develop steady states that are beyond an equilibrium description.

The recent interest in nonequilibrium phenomena in quantum many-body systems has been initiated by developments in experimental technology to simulate the nonequilibrium dynamics of interacting quantum many-body systems with a high degree of controllability on the system parameters. Cold atomic gases confined in optical lattices constitute nearly ideal implementations of minimal models in quantum many-body theory such as the Bose-Hubbard and Fermi-Hubbard model [17]. Due to the control on the system parameters it is possible to address the system's nonequilibrium dynamics. Different kinds of nonequilib-

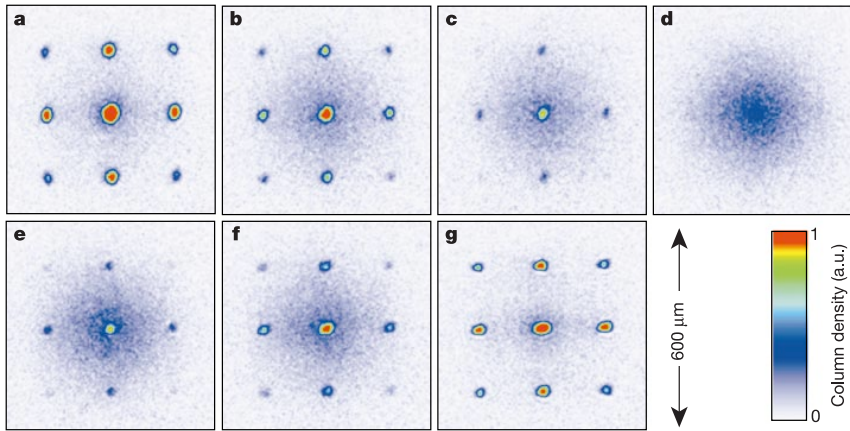


Figure 1.1: Collapse and revival oscillations in a Bose-Einstein condensate. This picture shows the matter wave interference pattern for different times after the increase in the depth of the optical lattice potential. The initial superfluid state at time $t = 0$ is characterized by the upper left part *a* of this figure. For increasing time the interference pattern vanishes signaling a collapse of the superfluid order that, however, revives for later times as is shown in part *g* of this picture.

Adapted by permission from Macmillan Publishers Ltd: Nature **419**, 52 copyright (2012)

<http://www.nature.com/nature/journal/v419/n6902/full/nature00968.html>

rium scenarios have been realized such as sudden quenches [63] or periodic perturbations as used for spectroscopy [165, 178]. The seminal contribution in this field dates back to the work on collapse and revival oscillations in a system of interacting lattice bosons [63]. Due to a sudden increase of the depth of the confining optical lattice corresponding to an increase of the particle interaction the initial superfluid state does not equilibrate to the Mott insulator directly. Rather, signatures of the initial superfluid reappear periodically leading to the notion of collapse and revival. For an illustration see Fig. 1.1. The revivals of the superfluid can be traced back to the proximity to an integrable point of the system where approximate local conservation laws cause a memory of the initial state. The restrictions in the dynamics of integrable systems has been also demonstrated by the implementation of Newton's cradle in a many-body quantum system [93]. Two one-dimensional clouds of Bose particles in the Tonks-Girardeau limit collide with each other periodically in a confining harmonic potential. Due to the integrability of the model the system does not evolve to a thermal distribution even for long times.

While cold atomic gases allow for the experimental simulation of interacting many-body systems quantum dots embedded in semiconductor heterostructures provide the framework for the study of the nonequilibrium properties of quantum impurity models. Connecting quantum dots to leads it is possible to study nonequilibrium transport at large bias voltages [183]. For impurities in metals, for example, this is a nearly impossible task as the presence of long-ranged electric fields within the bulk is prevented through screening via the mobile charge carriers. Another route that has been pursued for the study of nonequi-

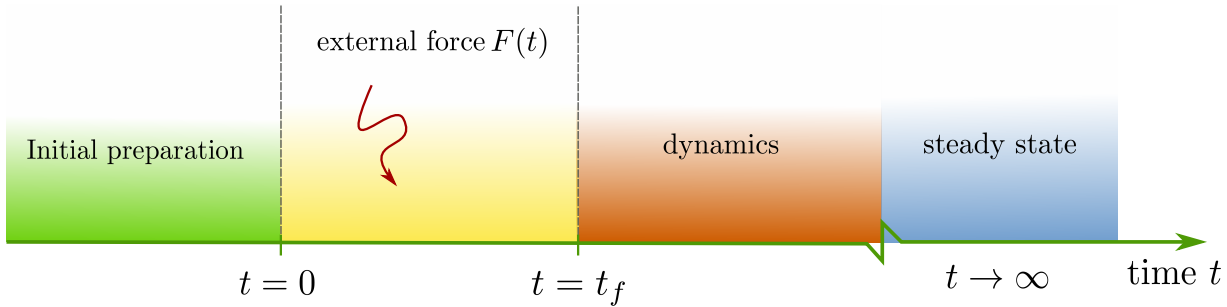


Figure 1.2: Typical stages of a nonequilibrium process.

librium properties of strongly correlated quantum impurity systems is the coupling to light fields. Microwave fields applied to a quantum dot allow for the study of periodic time-dependent perturbations as has been demonstrated for a Kondo impurity [44]. Appropriate experimental setups implement nearly ideal prerequisites for x-ray edge spectra with which one can associate the sudden switch on of local perturbations embedded in fermionic reservoirs [104].

Among all imaginable nonequilibrium protocols two generic will be considered in this thesis, namely sudden perturbations also called quantum quenches and periodically driven systems. Consider first the case where the external force acts within a finite time interval as illustrated in Fig. 1.2. Within this field of nonequilibrium processes different important aspects will be addressed among which are thermalization, thermodynamics, real-time dynamics, and dynamical phase transitions.

By acting with an external force on an otherwise isolated system its internal energy changes and at the end of the protocol the system ends up in an excited state. It is commonly accepted that realistic physical systems thermalize in the long-time limit. This means that the properties of the asymptotic state of the system are captured by a single parameter, the temperature T , irrespective of the details of the initial configuration and the details of the driving protocol. The temperature itself only depends on the total energy the system has when the external force stops its action onto the system. Along with the loss in memory about the details of the past comes another fundamental aspect, namely that of reversibility. The Schrödinger equation as the fundamental quantum mechanical time evolution equation is in principle time reversible invariant. So how can the system nevertheless forget about initial conditions?

From a physical point of view, the notion of an equilibrium state itself may be viewed to be deeply connected to such a nonequilibrium protocol as schematically illustrated in Fig. (1.2). Most physical definitions of equilibrium require the notion of being not in equilibrium at some instant of time in the sense that equilibrium states are special because they are those particular states that any physical system in the laboratory evolves into after a sufficiently long time. Note that this scenario implies the subtle imposition of initial conditions and thus the coupling to an environment that establishes this initial preparation. Thus, such a system can be considered as closed at most only in a pertur-

bative sense. Even though the coupling is necessary to establish the initial condition it is assumed to be sufficiently weak in order to not affect the time evolution and thus the build up of the equilibrium state. The conceptual importance of equilibrium states in statistical mechanics originates in the possibility to describe their properties in terms of the appropriate ensembles- the microcanonical, canonical, and grand-canonical. For nonequilibrium systems a comparable theory of ensembles is out of reach.

The fundamental question, however, which microscopic conditions are actually necessary for closed quantum many-body systems to equilibrate is still not fully answered [137]. Central to this question is the notion of integrability for which, however, no precise and generally accepted definition exists [28]. Integrable systems are supposed to be “simple” and in most cases - at least in principle - exactly solvable. In contrast to integrable systems nonintegrable ones are expected to thermalize. The microscopic origin of thermalization for nonintegrable systems is attributed to the conjecture that each eigenstate of a nonintegrable model system itself is thermal [164, 35, 144]. This conjecture is termed Eigenstate Thermalization Hypothesis. In contrast, the asymptotic steady state for integrable system is believed to be captured by generalized Gibbs ensembles [144] that bear a formal similarity to canonical states but require the maximization of entropy constrained by much more constants of motion than just energy. The mechanism and the conditions, however, that allow for this drastic reduction of the number of constants of motion from a generalized Gibbs ensembles to a canonical ensemble is yet unknown.

The external force changes the internal energy of the system and thus work is performed that is a central quantity for a thermodynamic description of any nonequilibrium process. Thermodynamics not only captures the equilibrium properties of the system of interest but also the transitions between different equilibrium states even though the system might not be in equilibrium in the meantime. Sometimes, however, physical systems cannot be considered to be equilibrated in experiments as a matter of time scales [110, 30]. In this context nonequilibrium work fluctuation theorems such as the Jarzynski equality [80] and the Crooks relation [32] constitute an important recent development as they allow for predictions of thermodynamic equilibrium quantities even though the system of interest might be far beyond equilibrium.

For weak external perturbations there exists a general theory for the description of the system’s properties called linear response theory. If the external force acting on the system can be treated perturbatively, the response of the system is captured completely by the system’s equilibrium fluctuations. This relation manifests itself in the famous Fluctuation-Dissipation theorem [24] connecting susceptibilities with the system’s fluctuations. This is particularly important for the description of experiments where the measurement apparatus is supposed to couple to the system in order to extract information - typically in terms of susceptibilities. At the same time, however, the measurement is supposed to be weak enough not to alter the system’s properties that one is actually interested in.

In nonequilibrium scenarios beyond linear response the fluctuation-dissipation theorems are in general violated. Starting with a seminal contribution by Jarzynski [80] it was realized that there exists a more general class of fluctuation theorems that are also valid arbitrarily far away from equilibrium. Contrary to its classical analogue the defi-

nition of work performed on quantum systems has been clarified only recently [167]. As a consequence of the inherent randomness in mixed states due to quantum fluctuations work is a random variable with an associated probability distribution function termed work distribution [167]. Despite of the average work performed the work distributions also contain information about the corresponding fluctuations. The work fluctuation theorems, most prominently the Jarzynski equality [80] and the Crooks relation [32], relate work distribution functions - that are associated with nonequilibrium processes - to *equilibrium* free energies that are inherently independent of the specific nonequilibrium protocol under study. These remarkable identities have been used in experiments to extract free energy differences of equilibrium states for classical systems [110, 30]. Concerning quantum systems it has not been possible to experimentally study the work fluctuation theorems in particular due to the difficulty of measuring the elementary ingredient, the work distribution. An experimental realization for ions in Paul traps has been proposed [73] but not realized yet.

In Sec. 3.3 it will be shown that there exists a class of optical absorption and emission spectra that can be identified with work distribution functions for sudden quenches in quantum impurity systems. These spectra are associated with the large class of x-ray edge problems [115, 128, 129] that constitute one of the first nonequilibrium phenomena beyond linear response discussed in the context of quantum many-body systems. In particular, the experimental realization of x-ray edge spectra of simple quantum impurity model systems in quantum dots will be discussed in Sec. 3.4 and the respective spectra are determined analytically near the threshold in Sec. 3.5. The analysis in Ch. 3 provides the framework to measure quantum work distributions for the first time and to experimentally verify the Jarzynski equality or the Crooks relation in quantum systems.

The real-time dynamics on intermediate time scales before relaxation occurs offers a different perspective onto nonequilibrium processes. The time scales involved in the relaxational dynamics of observables contain important information about the system's elementary excitations and the redistribution of excitations among the internal degrees of freedom during time evolution. Systems can be trapped in meta-stable states, for example, such as prethermalization plateaus [13]. In case of the Hubbard model they can be traced back to the fermionic nature of the elementary excitations in the metallic phase and to the restrictions for scattering processes in consequence of energy and momentum conservation in combination with the Pauli principle [120].

In recent work it has been realized that the dynamical properties of quantum many-body systems undergoing nonequilibrium time evolution can change sharply as a function of a control parameter [11, 40, 153, 159, 117] suggesting a dynamical equivalent to equilibrium phase transitions. In equilibrium a phase transition is associated with a sudden change of properties in macroscopically large systems. For temperature driven phase transitions, for example, the free energy becomes nonanalytic at the critical temperature. Whether similar behavior can be found in nonequilibrium dynamics where the parameter is not temperature but rather time itself is a recent subject of research. For classical systems a definition for a dynamical phase transition has been introduced in the context of glasses [67]. These ideas have later been extended to also capture *open* quantum systems [57, 10].

Concerning closed quantum systems, however, no conceptual framework for a dynamical phase transition exists in the literature. In Ch. 4 a framework of a dynamical phase transition in closed quantum systems will be introduced. It is based on the observation that real-time nonanalyticities can occur in nonequilibrium time evolution at a critical time generically. In this context the notion of generically is supposed to mean as generic as there are equilibrium phase transitions. This property is based on an extension of the concept of Fisher or Lee-Yang zeros to nonequilibrium quantities. In Sec. 4.2 this concept of a dynamical phase transition will then be illustrated for a particular and paradigmatic example of equilibrium phase transitions, the one-dimensional transverse field Ising model.

Systems under the influence of external forces that act continuously approach steady states that are almost exclusively nonthermal and thus allow to generate states with new properties not accessible in equilibrium. One such class of continuous driving is provided by perturbations that act periodically. Periodic forces can induce effectively renormalized parameters allowing to design model Hamiltonians dynamically [38, 134, 175]. For suitable values of the driving frequency this can even yield a dynamical localization of particles on a chain [37]. The mapping onto dynamically generated effective equilibrium Hamiltonians happens typically in the fast driving limit where the existence of the mapping can be traced back to applying the Trotter formula on the time evolution operator. In Sec. 5.1 it is shown that for a particular periodic driving in a Kondo model the Trotter formula is inapplicable yielding a time-translational invariant state that, however, is not of equilibrium type as Fluctuation-Dissipation theorems are violated. A periodic driving can also significantly influence tunneling processes through barriers. In particular, hopping processes can be enhanced because of a phenomenon known as photon-assisted tunneling [170] that can be associated with tunneling processes under the absorption or emission of multiple quanta of the driving frequency. In Sec. 5.1 and Sec. 5.2 it is demonstrated that this effect influences the dynamics particularly for the case of a periodically driven Kondo model and ac transport through a quantum dot beyond linear response, respectively.

Interacting quantum many-particle systems under the influence of periodic external forces pose new challenges especially in terms of methodology and have thus be discussed in the literature only for a restricted class of systems among which are the Falicov-Kimball [50, 49, 173, 174], Bose- [38, 134] as well as the Fermi-Hubbard model [82, 42, 41, 175, 9]. In contrast, the one-dimensional paradigmatic model of strongly correlated systems - the Luttinger liquid - has not been studied in detail yet. Certain aspects, however, have been analyzed recently [84, 133, 62]. In Sec. 5.3 the dynamics of a periodically driven system of interacting fermions in one dimension will be investigated on the basis of the exact bosonization solution.

From a technical point of view the nonequilibrium dynamics of quantum many-particle systems is still a great challenge. There are exactly solvable models, of course, their dynamics, however, in the long-time limit are not necessarily generic. In particular, such integrable models do not thermalize yielding instead an asymptotic steady state that is rather described by a generalized Gibbs ensemble as already discussed before. Apart from free fermionic or bosonic systems that can be solved directly, there are techniques that allow for exact analytical solutions for complicated models. Among these are Bethe

Ansatz [45, 119], bosonization [29, 111], and conformal field theory techniques [21]. In this thesis the bosonization technique will be used extensively for the study of nonperturbative model systems such as the Kondo model in Secs. 2.1 and 5.1, Luttinger liquids in Secs. 2.2 5.3, and the anisotropic Heisenberg chain in Sec. 2.3. For perturbative calculations of the dynamics of nonequilibrium systems the Keldysh technique [85] provides a general framework. Due to its perturbative nature, however, it is only capable of weak perturbations and its validity is only guaranteed for not too large times. Analytical access to the dynamics beyond straightforward perturbation theory is provided by the flow equation technique [91, 120, 65] that can be interpreted as a renormalization group method respecting all energy scales on equal footing. It thereby allows to address nonequilibrium problems within a renormalization group scheme where not just low energy degrees of freedom contain important contributions. The flow equation technique is used in Sec. 3.3 to calculate x-ray edge spectra of a Kondo model that is the paradigmatic system for strongly correlated impurities. A different renormalization group approach for the analysis of nonequilibrium dynamics is the real-time renormalization group in frequency space [154].

For the exact study of complicated models one typically has to resort to numerical simulations. For one-dimensional systems the time-dependent density matrix renormalization group (t-DMRG) [155] has proven a highly flexible and valuable method for the simulation of nonequilibrium dynamics. In Sec. 2.3 t-DMRG is used for the simulation of the local energy dynamics in anisotropic Heisenberg chains. So far this technique is limited to one-dimensional systems, extensions to also address higher dimensions are currently under extensive research. Concerning low-dimensional systems another method of general applicability is exact diagonalization [144]. The corresponding feasible system sizes, however, are limited such that it is sometimes difficult to predict the system's properties extrapolated to the thermodynamic limit that one is mostly interested in. In the opposite limit of large spacial dimensions or large lattice coordination number nonequilibrium extensions of the dynamical mean-field theory (DMFT) provide the framework for exact numerical solutions of correlated quantum systems in the thermodynamic limit [177, 50]. Within DMFT the local dynamics of a complicated many-body lattice system such as the Hubbard model is mapped onto a self-consistent impurity problem. This reduction in turn, however, can cause problems for the study of systems without translational invariance or with magnetic order although there is progress also in this direction. Within DMFT the local nonequilibrium impurity problem has still to be solved. For that purpose other reliable methods for the solution of impurity problems are required. One is provided by real-time Quantum Monte Carlo techniques [122, 180] that are in principle exact. However, they suffer from a dynamical sign problem for fermionic systems such that the maximal times that can be reached are limited. The noncrossing approximation (NCA) and its extensions can be used for the simulation of strong coupling impurity problems [125, 42]. In the low-temperature limit, however, this method can fail. For equilibrium problems the Wilson NRG technique has proven extremely useful for the numerical simulation of impurity problems. A nonequilibrium extension has been introduced in terms of the so-called time-dependent NRG [4]. Due to the logarithmic discretization in some cases, however, the weak resolution at high frequencies can lead to problems in nonequilibrium scenarios. The functional renormaliza-

tion group (fRG) [150] provides a generic procedure for the analysis of strongly correlated systems. It is especially suitable for static quantities, frequency-dependent quantities, however, are not easily accessible. Additionally, there exist semiclassical methods such as the truncated Wigner approximation [135, 2]. This technique, however, can underestimate the influence of quantum effects as quantum fluctuations are only incorporated via the initial preparation of the system and the dynamics is simulated classically.

The outline of this thesis is as follows. In the beginning of Ch. 2 a generic nonequilibrium protocol will be introduced - the quantum quench. Its implications will be studied taking into account different aspects in terms of real-time dynamics, properties of steady states, and thermodynamics. The real-time dynamics caused by sudden local perturbations is studied for particular and paradigmatic examples of strongly correlated systems in Ch. 2. This includes the switch on of the exchange interaction in the Kondo model in Sec. 2.1, the properties of an injected mobile impurity propagating in a chiral Luttinger liquid 2.2, and the local energy dynamics in anisotropic one-dimensional Heisenberg chains 2.3. The thermodynamic perspective of quantum quenches will be studied in Ch. 3. The concept of work distribution functions is introduced in Sec. 3.1 and the related nonequilibrium work fluctuation theorems such as the Jarzynski equality and the Crooks relation in Sec. 3.2. Particular attention will be paid to the difficulty to measure quantum work distribution functions which has not been achieved yet experimentally. In this context it will be shown in Sec. 3.3 that work distribution functions for quantum impurity models have been measured for decades in terms of optical x-ray edge spectra. A specific experimental implementation of x-ray edge spectra in quantum dots will be discussed in Sec. 3.4.2 and 3.5 allowing to study the nonequilibrium work fluctuation theorems in experiments. In Ch. 4 the possibility of the existence of dynamical phase transitions will be discussed and a new framework will be proposed for its definition. This concept will then be applied to a particularly important example in terms of the one-dimensional transverse field Ising model in Sec. 4.2. The influence of a periodic driving onto the properties of quantum many-body systems will be addressed in Ch. 5. As particular examples a periodic switch on and off of the exchange interaction in the Kondo model in Sec. 5.1, ac transport through a resonant level model in Sec. 5.2, and a periodic modulation of the interaction strength in a Luttinger liquid 5.3 will be investigated.

Chapter 2

Local quantum quenches

The prime and paradigmatic example for the study of nonequilibrium dynamics consists in preparing the system in a prescribed nonequilibrium state whose evolution according to the system's Hamiltonian is then monitored in time. Practically, such a scenario can be implemented in terms of a so-called quantum quench. Note that we will consider only quantum systems in the following. Let the system Hamiltonian $\mathcal{H} = \mathcal{H}(\lambda)$ depend on some external parameter λ that can for example be an electric or magnetic field, the hopping amplitude of particles on a lattice, the interaction strength between particles etc. In a quantum quench the system is prepared in the equilibrium state ρ_0 of the Hamiltonian $H_0 = \mathcal{H}(\lambda_0)$ at some given initial value λ_0 of the external parameter. At a certain moment in time, $t = 0$ say, this parameter is suddenly changed to a new value λ_f corresponding to a new Hamiltonian $H_f = \mathcal{H}(\lambda_f)$. For the general case where the initial state density matrix ρ_0 does not commute with the final Hamiltonian H_f the system will acquire a time-dependence and its nonequilibrium dynamics are governed by the von Neumann equation:

$$i \frac{d}{dt} \rho_0(t) = [H_f, \rho_0(t)]. \quad (2.1)$$

Quantum quenches can be classified into two different categories termed *global* and *local*. For global quenches the perturbation acts on the whole system yielding an extensive average work performed. Local quenches only affect small nonextensive parts of the system implying a nonextensive average work. Here, pathological cases with sub- or superextensive scaling of the work performed as they appear in nonextensive thermodynamics are ignored.

For a quantum quench one may address different aspects as schematically depicted in Figure 2.1. Due to the change in the Hamiltonian work is performed on the system - an essential element of thermodynamics. Thermodynamics is not only capable of characterizing the equilibrium properties of macroscopic systems. It can also describe transitions between equilibrium states even though the system may be out of equilibrium in the meantime as in the quantum quench scenario. The question whether the asymptotic final state of the quenched system can be identified with an equilibrium state, i.e., whether the system thermalizes, is an important question from a fundamental point of view. For intermediate

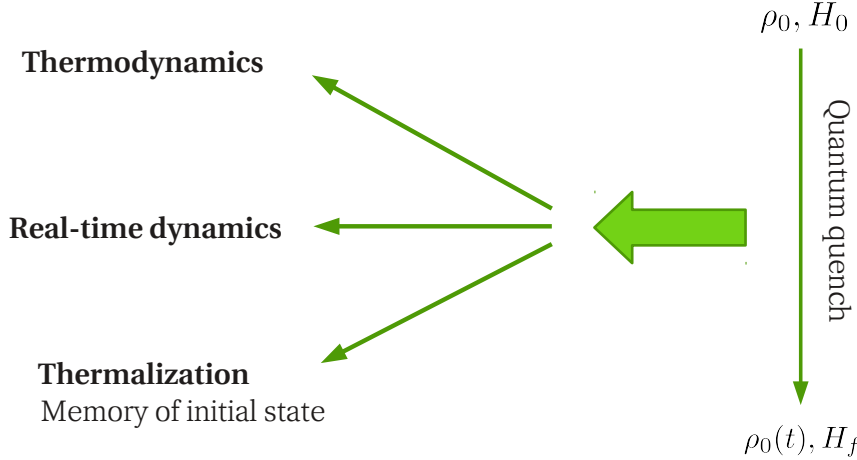


Figure 2.1: Illustration of the central questions associated with quantum quenches.

times the system undergoes a real-time evolution that can be characterized on the basis of the dynamical behavior of the system's observables.

Thermodynamics. From a thermodynamic point of view the sudden switching of an external parameter λ of an otherwise isolated and closed physical system induces an abrupt change in its internal energy. Due to the first law of thermodynamics this is equivalent of having performed the work

$$W_{av} = \text{Tr}[\rho_0 H_f] - \text{Tr}[\rho_0 H_0] \geq \Delta F. \quad (2.2)$$

According to the second law of thermodynamics W_{av} is bounded from below by the free energy difference $\Delta F = F(\lambda_f, T) - F(\lambda_0, T)$ of the equilibrium states corresponding to the parameters λ_0 and λ_f at the same temperature T provided the system is initially prepared in a state at temperature T . As already emphasized in the Introduction, see Ch. 1, quantum work is a random variable [167]. The associated probability distribution function termed work distribution is the central object for the study of work fluctuation theorems such as the Jarzynski equality [80, 123] and the Crooks relation [32, 168, 166, 26]. These constitute a far from equilibrium analogue to the well-known fluctuation-dissipation theorem [24]. The Jarzynski equality replaces the lower bound for the average work in the second law by a strict equality relating work with free energy differences ΔF . A more detailed account on this subject can be found in Ch. 3.

Thermalization. In statistical physics it is commonly accepted that realistic macroscopic systems once taken out of equilibrium evolve into their equilibrium configuration describable by microcanonical, canonical or grand-canonical ensembles after a sufficiently long time. One fundamental question associated with this expected behavior is whether and under which conditions a specific *closed* system prepared in a non-equilibrium state is actually able to reach equilibrium without coupling to an environment. For classical systems there exists a comprehensive understanding of this thermalization process in terms of ergodicity, mixing and chaos. Concerning quantum systems, however, the understanding is far from being complete.

For local quenches it is generally expected that local observables thermalize for thermodynamically large systems despite of special cases where symmetry constraints can cause a memory of the initial state [65]. The argument for the expected thermalization is as follows. A local quench generates localized excitations. During time evolution the initial perturbation will delocalize. For a thermodynamically large system this will yield a spread of the localized perturbation over the whole space to infinity in the asymptotic long-time limit. In this way the influence of the local perturbation on local observables will at most be of the order $\mathcal{O}(1/V)$ with V the system size and thus negligible in the thermodynamic limit. For a finite system the situation differs, of course, due to finite recurrence times. Concerning global observables the influence of the local perturbation can survive. The total energy, for example, still contains the information about the initial perturbation. Analogously, the average work performed after the local quench contains non vanishing contributions in the thermodynamic limit. In Secs. 2.1, 2.2, and 2.3 below local quenches are analyzed in detail in different model systems.

In case of global quenches the question of thermalization is much more subtle and still under debate [137]. Elementary to the discussion of thermalization is the notion of integrability. Note, however, that there is no precise generally accepted definition of integrability in the quantum case [28]. Typically, integrable systems are supposed to be simple and in most cases exactly solvable.

Concerning the relaxation behavior one generically expects that nonintegrable systems, such as the Hubbard model [40] and the Bose-Hubbard model [96, 16] thermalize. Within the Eigenstate Thermalization Hypothesis (ETH), put forward independently by Deutsch [35] and Srednicki [164], the thermalization of nonintegrable systems is attributed to the conjecture that operator expectation values are smooth functions of energy or equivalently that the individual eigenstates themselves are thermal. The ETH has been confirmed for systems whose eigenstates obey Berrys conjecture [164], integrable systems perturbed by a single matrix of a Random matrix ensemble [35], and in numerical simulations of hard-core bosons on a lattice [144, 143].

For the description of the steady state of integrable systems Rigol et al. [144] proposed a Generalized Gibbs Ensemble (GGE) that is constructed by maximizing the entropy constrained by constants of motion. The validity of the GGE when considering a maximal set of constants of motion has been shown by Ref. [144]. The question whether there exists a reduced set [145], confirmed for several exactly solvable systems [29, 39], is still not fully answered. For initial states with broken translational invariance, for example, the reduced set is not capable of describing correlations [52]. When restricting to a local subsystem the validity of the reduced set has been proven for a large class of quadratic Fermi and Bose systems [12] as well as for special limits in the Bose-Hubbard model [31].

Real-time dynamics. Another important aspect related to quantum quenches concerns the system's real-time and relaxational dynamics. Due to the quench the system has to adapt to the externally prescribed perturbation and to redistribute the corresponding excitations among its internal degrees of freedom. Depending on the details of the respective system and the quench parameters the time scales for relaxation contain important information about the elementary excitations and processes for the system under study.

Even though nonintegrable systems such as the Fermi-Hubbard model are expected to thermalize there can exist extended regimes where the corresponding system is trapped in an approximate nonthermal steady state before complete thermalization occurs [13, 120, 40]. For a restricted class of systems these so-called prethermalization plateaus [13, 120] can be traced back to the proximity of integrable points [95]. In case of the Hubbard model this reflects the fermionic nature of elementary excitations in the metallic phase whose dynamics is strongly restricted by energy and momentum conservation in combination with the Pauli principle [120].

Depending on the quench parameters it has been shown for a number of model systems that the relaxational dynamics can change its qualitative behavior abruptly [11, 40, 159, 153, 117]. In analogy to equilibrium phase transitions this suggests the existence of a dynamical equivalent in nonequilibrium dynamics. For classical systems a framework for dynamical phase transitions has been invented initially for the study of glasses [67, 55, 56]. This phase transition happens in the space of trajectories where according to a measure of activity the dominant trajectories can be classified either as active or inactive. Recently, this concept has been transferred first to small [57, 54] and later to macroscopically large *open* quantum systems [10]. In Ch. 4 a different concept for a dynamical phase transition is introduced for *closed* quantum systems that is defined on the basis of real-time nonanalyticities. This corresponds to a breakdown of short time expansions in analogy to the breakdown of, e.g., high-temperature, expansions at equilibrium critical points.

An important question in the study of real-time dynamics concerns the asymptotic relaxational scaling laws of observables and their dependence on the parameters of the model. The relaxational dynamics can show new emergent nonequilibrium time scales not present in equilibrium such as the doublon decay rate in the Fermi-Hubbard model [161]. In Ch. 4 another example of emergent time scales will be shown for transverse magnetic field quenches in the one-dimensional Ising model and as well as the connection to the above mentioned dynamical quantum phase transition.

Below, the real-time dynamics in consequence of local quenches will be studied for an interaction quench in the Kondo model (Sec. 2.1), for the sudden switch on of a mobile impurity in a chiral Luttinger liquid (Sec. 2.2), and for the local energy dynamics in spin-1/2 Heisenberg chains (Sec. 2.3).

2.1 Publication: Interaction quench dynamics in the Kondo model

The Kondo model constitutes the paradigm for the field of strongly correlated impurity systems. Historically, the Kondo effect is connected to resistivity measurements of metals showing an increase of the resistivity for decreasing temperature below a certain threshold. For details see the book by Hewson [70]. This anomalous behavior is not consistent with the picture emerging from electron-electron interactions and the scattering between electrons and phonons which predicts a decline in resistivity onto a finite value due to static

impurities. The essential mechanism has been identified by Jun Kondo who showed that magnetic impurities - which support internal dynamical degrees of freedom in contrast to static impurities - yield the desired behavior [97]. Magnetic impurities interact with the itinerant electrons via a spin exchange interaction [70]

$$H = \sum_{k,\eta=\uparrow\downarrow} \varepsilon_k c_{k\eta}^\dagger c_{k\eta} + \frac{J}{2} \sum_{kk'} \left[c_{k\uparrow}^\dagger c_{k'\uparrow} - c_{k\downarrow}^\dagger c_{k'\downarrow} \right] S^z + \frac{J}{2} \sum_{kk'} \left[c_{k\uparrow}^\dagger c_{k\downarrow} S^- + c_{k\downarrow}^\dagger c_{k\uparrow} S^+ \right]. \quad (2.3)$$

The operator $c_{k\eta}^\dagger$ creates an electron of spin $\eta = \uparrow, \downarrow$ and momentum k with energy ε_k in the conduction band of the metal. The electrons can scatter off the magnetic impurity either by retaining both the impurity as well as the electron spin or by flipping both of them. The internal spin-1/2 degree of freedom is implemented in terms of the spin raising S^+ and lowering S^- operators. The spin state of the impurity is measured by the operator S^z . The strength of the exchange interaction is determined by the dimensionless coupling $g = \rho J$ with ρ the noninteracting density of states of the conduction band at the Fermi level.

Even though $g \ll 1$ for nearly all realistic systems the properties of the Hamiltonian H in Eq. 2.3 are not accessible perturbatively in g except at very high temperatures. The energy and temperature scale associated with the breakdown of perturbation expansions is the Kondo temperature

$$k_B T_K = D \sqrt{g} e^{-1/g} \quad (2.4)$$

with k_B Boltzmann's constant and D an energy scale of the order of the bandwidth of the conduction band. The nonperturbative relation between T_K and the interaction strength g is a signature of the strong correlations in the system.

For temperatures $T \gg T_K$ the local spin essentially behaves as if it were free up to small logarithmic corrections residual of the strong correlations. As the temperature is lowered the itinerant electrons develop a localized spin polarization in the vicinity of the local magnetic moment that is termed the Kondo cloud. For temperatures $T \ll T_K$ the Kondo cloud establishes a mechanism to screen the local spin by successively binding the local spin at lower temperatures into a singlet at zero temperature. This so-called Kondo singlet now acts as a strong static potential scatter with an associated phase shift $\delta/\pi = 1/2$ [127]. The most prominent feature of the Kondo effect at temperatures $T \lesssim T_K$ is the buildup of the Kondo resonance that is a sharp peak in the local density of states pinned to the Fermi level.

The nonperturbative nature of the Kondo effect stimulated many important developments in condensed matter theory such as poor man's scaling [7] and the numerical renormalization group (NRG) [184]. The Kondo model is exactly solvable via Bethe ansatz [8, 182] allowing for the calculation of thermodynamic quantities. Additionally, the Kondo model has been analyzed using a variety of different approaches such as flow equations [91], functional renormalization group [90], and many more [70].

Before the invention of quantum dots experiments on the Kondo effect were limited to bulk samples of metals with a finite concentration of magnetic impurities where it is practically impossible to address individual magnetic moments. Moreover, screening effects

due to the itinerant electrons in the bulk prevent the presence of large electric or magnetic fields such that only the linear response regime has been experimentally accessible. For systems based on quantum dots, however, it is possible to apply large fields to single quantum impurities. For more details on quantum dots see Ch. 3. In the appropriate regimes they can act as single Kondo impurities [59]. Thus, it is possible to study the nonequilibrium properties of Kondo systems beyond linear response. In transport measurements the conductance of Kondo impurities has been measured also for large bias voltages across the quantum dot [183]. Additionally, the influence of microwave radiation on the Kondo effect and its suppression for increasing light intensity has been investigated [44]. Recently, optical spectra have been recorded that correspond in the spirit of the x-ray edge problem - for more details see Ch. 3 - to the sudden switch on of a Kondo impurity [104].

Local quench dynamics of Kondo and related models have been investigated in a number of works using different methods [107, 111, 112, 125, 5, 6, 108, 140]. The noncrossing approximation (NCA) has been used to demonstrate that the time scale $t_k = T_K^{-1}$ for the buildup of the Kondo effect is set by the inverse of the Kondo temperature T_K [125]. The exponential relaxation of the local spin magnetization has been analyzed on the basis of the time-dependent numerical renormalization group approach (TD-NRG) [5, 6], flow equations [111], form-factor approach [108], and bosonization in the Toulouse limit [107, 111, 140]. The nonequilibrium local spin-spin correlation function has been studied both using flow equations and bosonization in the Toulouse limit [111, 112].

In the above mentioned Toulouse limit [172] the anisotropic Kondo model becomes exactly solvable by bosonization and refermionization [107, 186] even under nonequilibrium conditions [111, 112]. Below, the local magnetization dynamics and the local spin-spin correlation function are investigated on the basis of the exact solution on the Toulouse line for a sudden switch on of the Kondo exchange interaction in the presence of a magnetic field. As for the case without magnetic field the local observables such as the magnetization and the spin-spin correlation function thermalize in the long-time limit. It is found that the time scale for relaxation is solely set by the Kondo temperature. Even though the magnetic field does not enter the value of the decay rate of the local magnetization it changes its asymptotic long-time scaling law. For both the spin-spin correlation function as well as the magnetization the magnetic field leads to oscillations in real-time evolution.

Interaction quench dynamics in the Kondo model in the presence of a local magnetic field

This article has been downloaded from IOPscience. Please scroll down to see the full text article.

2010 J. Phys.: Condens. Matter 22 345604

(<http://iopscience.iop.org/0953-8984/22/34/345604>)

View [the table of contents for this issue](#), or go to the [journal homepage](#) for more

Download details:

IP Address: 129.187.254.47

The article was downloaded on 27/11/2011 at 08:33

Please note that [terms and conditions apply](#).

Interaction quench dynamics in the Kondo model in the presence of a local magnetic field

M Heyl and S Kehrein

Department of Physics, Arnold Sommerfeld Center for Theoretical Physics and Center for NanoScience, Ludwig Maximilians Universität München, Theresienstraße 37, 80333 Munich, Germany

E-mail: Markus.Heyl@physik.lmu.de

Received 2 February 2010, in final form 9 June 2010

Published 10 August 2010

Online at stacks.iop.org/JPhysCM/22/345604

Abstract

In this work we investigate the quench dynamics in the Kondo model on the Toulouse line in the presence of a local magnetic field. It is shown that this setup can be realized by either applying the local magnetic field directly or by preparing the system in a macroscopically spin-polarized initial state. In the latter case, the magnetic field results from a subtlety in applying the bosonization technique where terms that are usually referred to as finite-size corrections become important in the present non-equilibrium setting. The transient dynamics are studied by analyzing exact analytical results for the local spin dynamics. The timescale for the relaxation of the local dynamical quantities turns out to be exclusively determined by the Kondo scale. In the transient regime, one observes damped oscillations in the local correlation functions with a frequency set by the magnetic field.

(Some figures in this article are in colour only in the electronic version)

1. Introduction

In recent years the possibility to experimentally study non-equilibrium dynamics in quantum many-body systems stimulated theoretical investigations of various model systems out of equilibrium. Of particular interest for this work is the observation that quantum dots can act as magnetic impurities displaying Kondo physics [1]. Due to the flexibility to vary system parameters in time by applying unscreened electrical or magnetic fields, quantum dots offer the framework for the experimental investigation of non-equilibrium dynamics in quantum impurity systems.

The Kondo model describes the physics of a localized spin 1/2 coupled to a fermionic bath via an exchange interaction. At low temperatures, the sea of conduction band electrons develops a spin polarization cloud, the so-called Kondo cloud, providing a mechanism to screen the local magnetic moment. In the zero temperature limit, the screening becomes dominant leading to the emergence of the Kondo singlet such that the spin polarization cloud is bound to the local spin with an associated binding energy T_K , the Kondo temperature. The Kondo effect manifests itself most prominently in the Kondo

resonance, a sharp peak in the local density of states that is pinned at the Fermi energy.

As the Kondo model is the paradigm model for strongly correlated impurity systems, it is of particular interest that for a certain line in parameter space, the Toulouse limit, the Kondo model becomes exactly solvable by a mapping onto a quadratic resonant level model [2, 3]. In equilibrium as well as for an interaction quench, the Toulouse limit describes correctly many generic and universal properties of the Kondo model [3–5] such as the local spin dynamics that are also investigated in this work. Due to the complexity of time evolution for systems out of equilibrium it is instructive to investigate those particular examples where exact and nonperturbative solutions are accessible.

Most of the work on time-dependent non-equilibrium systems has been concentrating on interaction quenches [4–12]. Due to its paradigmatic importance, the non-equilibrium quench dynamics in the Kondo model or the related Anderson impurity model in the local moment regime have been analyzed in a number of works [4–10]. Here, the transient dynamics in the Kondo model will be investigated for an interaction quench in presence of a local magnetic field. It will be shown that this

scenario may be realized by either applying a local magnetic field directly or by preparing the system in a state in which the conduction band carries a macroscopic spin polarization. As the Kondo effect is sensitive to spin degeneracy, the local magnetic field is expected to influence the properties in the Kondo model considerably. The analysis of the transient dynamics and the emergence of the steady state will focus on the local spin dynamics as they are directly affected by the local magnetic field.

In the non-equilibrium setting where the lead carries a macroscopic initial spin polarization a subtlety in the application of the bosonization technique arises. Under certain circumstances as in this setting, terms that are usually referred to as finite-size corrections may turn out to be relevant in the non-equilibrium case. As a consequence of the ‘finite-size contributions’ the spin-polarized initial state effectively acts as a local magnetic field applied to the local spin.

This paper is organized as follows. In section 2, the effective Hamiltonian for the dynamics in the presence of a local magnetic field is derived. Afterward, the magnetization of the impurity spin is investigated in section 3. Section 4 is devoted to an analysis of the spin–spin correlation function and the results for the dynamical spin susceptibility are presented in section 5.

2. Effective Hamiltonian

The dynamics of a spin-1/2 coupled to a sea of electrons via an exchange interaction is described by the Kondo model:

$$H = \sum_{k\eta} k :c_{k\eta}^\dagger c_{k\eta}: + \sum_i \frac{J_i}{2} \sum_{\eta, \eta'} : \Psi_\eta^\dagger(0) \sigma_i^{\eta, \eta'} S_i \Psi_{\eta'}(0) :. \quad (1)$$

The operator $c_{k\eta}^\dagger$ creates an electron with wavevector k and spin $\eta = \uparrow, \downarrow$ in the reservoir. Here, we allow for an anisotropy in the exchange interaction resulting in different couplings in the z -direction, $J_z = J_{\parallel}$, and in the xy plane, $J_x = J_y = J_{\perp}$. In the following, the couplings are all given in units of the noninteracting density of states. The colons $: \dots :$ denote normal ordering with respect to the Fermi sea. The local spin operator \vec{S} with components $S_i, i = x, y, z$, is coupled to the local spin density of the conduction band electrons whose components are determined by the Pauli matrices σ_i . The electron’s dispersion relation has been linearized around the Fermi level and energies are measured in units of v_F relative to the Fermi energy, i.e. $v_F = 1$ and $\varepsilon_F = 0$. As the local scatterer is assumed to be pointlike, only s-wave scattering occurs reducing the problem to a one-dimensional one [3]. For an additional magnetic field h_* applied to the local spin, the Hamiltonian in equation (1) acquires an extra contribution $-h_* S_z$.

In the following, we will work in the Toulouse limit of the Kondo model where the parallel coupling takes a special value $J_{\parallel} = 2 - \sqrt{2}$. The relevance of the Toulouse point in the single channel Kondo model is twofold. First, it allows for exact analytical results in a strongly correlated system. Secondly, the Toulouse point governs many generic and universal properties for the whole parameter regime including the experimentally

relevant isotropic case. Especially, it has been shown that the local spin dynamics, also investigated in this work, show generic behavior in equilibrium as well as out of equilibrium. Other universal quantities, however, such as the Wilson ratio explicitly depend on the anisotropy.

In the following, two non-equilibrium scenarios will be investigated that turn out to induce the same dynamics. The first is an interaction quench in the Kondo model in the presence of a magnetic field, i.e. the coupling J in the Kondo Hamiltonian is suddenly switched on while a local magnetic field is acting on the local spin. The second scenario investigates the dynamics in the Kondo model if the system is initially prepared in a state with a macroscopic spin polarization.

In equilibrium, the anisotropic Kondo Hamiltonian in the Toulouse limit can be mapped onto an exactly solvable resonant level model using bosonization and refermionization [3]. As has been shown by Lobaskin and Kehrein, such a mapping also exists in the case of an interaction quench where an additional local potential scattering term emerges [4]. Below, the implementation of the bosonization technique for the Kondo Hamiltonian with an applied local magnetic field will be presented. The bosonization technique is based on the bosonization identity

$$\psi_\eta(x) = \frac{1}{\sqrt{a}} F_\eta e^{-i\frac{2\pi}{L} N_\eta x} e^{-i\phi_\eta(x)}, \quad \eta = \uparrow, \downarrow, \quad (2)$$

that establishes a connection between fermionic fields $\psi_\eta(x)$ and bosonic fields $\phi_\eta(x)$ as an elementary operator identity in Fock space, see [13] for a recent review. Here, $\phi_\eta(x) = -\sum_{q>0} [e^{-iqx} b_{q\eta} + e^{iqx} b_{q\eta}^\dagger] e^{-aq/2}/\sqrt{n_q}$, $b_{q\eta} = -i/\sqrt{n_q} \sum_k c_{k-q\eta}^\dagger c_{k\eta}$, $q = 2\pi n_q/L$ with $n_q \in \mathbb{N}$, L is the system size and $a^{-1} > 0$ is an ultraviolet cutoff. The Klein factor F_η accounts for the annihilation of one electron as this cannot be accomplished by the bosonic field $\phi_\eta(x)$.

As usual, the bosonized Hamiltonian in the Toulouse limit can be simplified tremendously by applying a sequence of unitary transformations. First, the charge and spin (c, s) degrees of freedom are separated by introducing $\phi_{c/s}(x) = \frac{1}{\sqrt{2}} [\phi_\uparrow(x) \pm \phi_\downarrow(x)]$, $\hat{N}_{c/s} = \frac{1}{2} [\hat{N}_\uparrow \pm \hat{N}_\downarrow]$. The charge sector decouples from the impurity problem and will be neglected in the following.

In the Toulouse limit where $J_{\parallel} = 2 - \sqrt{2}$, the Emery–Kivelson transformation $U = e^{i[(\sqrt{2}-1)\phi_s(0)[S_z-1/2]}}$ eliminates the many-body interaction term in the Kondo Hamiltonian that couples to the S_z operator. Refermionization of the transformed Hamiltonian reduces the problem to a quadratic and therefore exactly solvable one. For that purpose, another unitary transformation $U_2 = e^{i\pi \hat{N}_s S_z}$ has to be imposed [14]. This allows us to define the fermionized spin operator $d = e^{-i\pi[\hat{N}_s - S_z]} S_-$ and its Hermitian conjugate d^\dagger as well as new spinless fermionic fields

$$\psi(x) = \frac{1}{\sqrt{a}} F_s e^{-i\frac{2\pi}{L} \hat{N}_s x} e^{-i\phi_s(x)}, \quad F_s = F_\downarrow^\dagger F_\uparrow, \quad (3)$$

with modes $c_k = (2\pi L)^{-1/2} \int dx e^{ikx} \psi(x)$. In the case of an applied local magnetic field h_* , an additional contribution

$-h_*S_z$ appears in the Hamiltonian. The S_z operator commutes with the unitary transformations U and U_2 and can be related to the fermionic d operators in the following way:

$$S_z = d^\dagger d - \frac{1}{2}. \quad (4)$$

Thus, a local magnetic field induces a shift of the energy of the d fermion. After the mapping, the effective Hamiltonian reduces to a noninteracting resonant level model with an additional local scatterer:

$$\begin{aligned} H_{\text{eff}} = & \sum_k k :c_k^\dagger c_k: - \varepsilon_0 d^\dagger d + g \sum_{kk'} :c_k^\dagger c_{k'}: \\ & + V \sum_k [c_k^\dagger d + d^\dagger c_k] + \Delta E \end{aligned} \quad (5)$$

where $V = J_\perp \sqrt{\pi/(2aL)}$, $g = [\sqrt{2} - 1]\pi/L$, $\varepsilon_0 = h_*$ and ΔE denotes a constant energy shift. The magnetic field solely enters the Hamiltonian by shifting the local d level ε_0 away from the Fermi level.

The Kondo scale can be related to parameters of the resonant level model Hamiltonian by the impurity contribution to the Sommerfeld coefficient in the specific heat [4]: $C_{\text{imp}} = \gamma_{\text{imp}} T$ with $\gamma_{\text{imp}} = w\pi^2/3T_K$. Here, $w = 0.4128$ is the Wilson number. In this way the Kondo temperature is determined by $T_K = \pi w \Delta$ where $\Delta = V^2 L/2$.

As will be shown in the following, a Hamiltonian of the same structure as in equation (5) is induced by preparing the system in a state with a macroscopic spin polarization:

$$|\psi_0\rangle = \prod_{0 < k < k_*} c_{k\uparrow}^\dagger |0\rangle \otimes |\chi\rangle. \quad (6)$$

Here, $|0\rangle$ is the filled Fermi sea and $|\chi\rangle$ a wavefunction for the local spin. For simplicity, we set the initial spin wavefunction $|\chi\rangle = |\uparrow\rangle$ in the following. The wavevector k_* denotes the electronic state up to which the spin-up electrons are filled. Indeed, the state $|\psi_0\rangle$ carries a macroscopic spin polarization:

$$\hat{N}_s |\psi_0\rangle = \frac{L}{4\pi} k_* |\psi_0\rangle. \quad (7)$$

The operator $\hat{N}_s = [\hat{N}_\uparrow - \hat{N}_\downarrow]/2$ measures the total spin of the conduction band electrons.

Note, that Kondo impurities attached to ferromagnetic leads [15] describe a different setup, as there the chemical potentials for the up and down spin electron species are identical, whereas the corresponding densities of states are different. Here, the chemical potentials differ in the initial state and it is assumed that the densities of states are identical by choosing the same Fermi velocities for the up and down spin electrons. This is reasonable as long as the wavevector k_* is small enough in order to neglect the influence of curvature on the dispersion relation.

Using the bosonization technique for the mapping onto a quadratic effective Hamiltonian, it is important to recognize that expressions like

$$\lim_{L \rightarrow \infty} \frac{2\pi}{L} \hat{N}_s \neq 0 \quad (8)$$

do not vanish in the thermodynamic limit due to the macroscopic initial spin polarization. Those terms usually

appear as finite-size corrections when expressing the fermionic density in terms of the bosonic fields and the number operators and cannot be neglected in the present study. As has been shown recently, the application of the bosonization technique requires additional effort in non-equilibrium scenarios [16, 17]. The implications of equation (8) will be studied in the following for the kinetic energy of the spin sector H_{0s} that equals in terms of the bosonic field ϕ_s and the number operator \hat{N}_s :

$$H_{0s} = \int dx \frac{1}{2} :(\phi_s(x))^2: + \frac{2\pi}{L} \hat{N}_s^2. \quad (9)$$

Due to the spin conservation condition [14]

$$S_T = \hat{N}_s + S_z = \text{const.} = \frac{L}{4\pi} k_* + \frac{1}{2} \xrightarrow{L \rightarrow \infty} \frac{L}{4\pi} k_* \quad (10)$$

one can express the latter term of the right-hand side in equation (9) in terms of the total spin S_T and the S_z operator such that:

$$\frac{2\pi}{L} \hat{N}_s^2 = \frac{2\pi}{L} S_T^2 - k_* S_z + \frac{\pi}{2L} = -k_* S_z + \text{const.} \quad (11)$$

Here, the identity $S_z^2 = 1/4$ has been used. Only in the case of a macroscopic spin-polarized initial state, one therefore obtains an additional non-vanishing contribution that is equivalent to a magnetic field of strength k_* applied to the local spin. As in this example, the operator \hat{N}_s can always be converted into a constant and the local spin operator S_z generating new terms in the Hamiltonian compared to the equilibrium or interaction quench case without a magnetic field. In the end one arrives at an effective Hamiltonian that is equal to equation (5) with $\varepsilon_0 = \frac{2\pi}{L}[1 - J_\parallel]S_T = [\sqrt{2} - 1]k_*/2$.

As shown in appendix, the occupation distribution $f_k = \langle \psi_0 | c_k^\dagger c_k | \psi_0 \rangle$ of the spinless fermionic operators in the initial state equals:

$$f_k = \theta\left(\frac{k_*}{2} - k\right). \quad (12)$$

The chemical potential $k_*/2$ in the initial state can be compensated by defining new operators $a_k = c_{k-k_*/2}$ in terms of which the structure of the effective Hamiltonian does not change. All c_k operators are replaced by a_k s, only the energy of the local level gets modified to $\tilde{\varepsilon}_0 = k_*/\sqrt{2}$. Therefore, the initial state effectively acts as a magnetic field of strength:

$$h_* = \frac{k_*}{\sqrt{2}}. \quad (13)$$

Notice that the magnetic field seen by the impurity spin depends on J_\parallel , that characterizes the strength of the coupling between the z component of the local spin and the z component of the spin polarization cloud generated by the itinerant electrons. In the Toulouse limit, the parallel coupling is fixed to a comparatively large value $J_\parallel = 2 - \sqrt{2}$. We expect, however, that independent of the actual coupling strength and away from the Toulouse limit the spin-polarized initial state always acts as a local magnetic field. Moreover, even in the limit $J_\parallel \rightarrow 0$, there is an effective magnetic field stemming from the kinetic energy of the spin sector, see equation (11).

The only relevant quantity is the total effective magnetic field h_* seen by the impurity spin.

Concluding, it has been shown that the dynamics in the Kondo model for an initially spin-polarized state of the type in equation (6) is equivalent to an interaction quench in presence of a magnetic field, see equation (5).

3. Magnetization

The local spin dynamics for an interaction quench in the Kondo model without magnetic field are well studied in the literature. In such a scenario, the magnetization $P_{h_*=0}(t) = \langle S_z(t) \rangle_{h_*=0}$ of the impurity spin [4, 3, 10, 18]

$$P_{h_*=0}(t) = P(0)e^{-2\Delta t} \quad (14)$$

decays to zero exponentially fast on a timescale $1/2\Delta$ that is set by the Kondo timescale $t_K = 1/T_K = 1/(\pi w\Delta)$.

As the local spin is sensitive to a local magnetic field, one expects that the magnetization dynamics differ considerably compared to the interaction quench case. Due to equation (4), the magnetization $P(t)$ is equivalent to the local d level occupation $\hat{n}_d = d^\dagger d$ up to a constant:

$$P(t) = \langle \hat{n}_d(t) \rangle - \frac{1}{2}. \quad (15)$$

As the effective Hamiltonian in equation (5) is quadratic, the time evolution of the single-particle operators c_k and d is entirely determined by Green's functions $G_{ll'}(t) = \theta(t)\langle\{c_l(t), c_{l'}\}\rangle$:

$$c_l(t) = \sum_{l'} G_{ll'}(t) c_{l'}, \quad l, l' = k, d \quad (16)$$

where G is a unitary matrix. Green's functions $G_{ll'}(t)$ can be obtained by using the equations of motion approach, for example. As a result, one obtains for the magnetization of the impurity spin:

$$P(t) = \frac{1}{2}[1 + \Lambda(0)]e^{-2\Delta t} - e^{-\Delta t}\Lambda(t) + \frac{1}{2}\Lambda(0) \quad (17)$$

where $\Lambda(t) = (2/\pi) \int_0^{h_*/\Delta} d\omega \cos(\omega\Delta t)/(1 + \omega^2)$ and $\Lambda(0) = (2/\pi) \operatorname{atan}(h_*/\Delta)$. Notice that this agrees with the result in equation (14) in the limit $h_* \rightarrow 0$ as expected. Plots of the magnetization for different values of the magnetic field h_* are shown in figure 1. As one can see, the timescale for relaxation of the magnetization is exclusively set by the Kondo scale t_K independent of the magnetic field. For the local level occupation in an interaction quench in a Majorana resonant level model, the equivalent relaxation behavior has been observed in a recent work by Komnik [12]. The timescale $t_* = 1/h_*$ associated with the magnetic field dominates the transient dynamics as long as $t_* < t_K$, i.e. the magnetic field $h_* > T_K$ is sufficiently large.

As the curves in figure 1 indicate, the initial decay of the magnetization is universal in the sense that it is independent of the magnetic field or equivalently the initial spin polarization and exactly equals the interaction quench case:

$$\langle S_z(t) \rangle \stackrel{t \ll t_*, t_K}{\approx} \frac{1}{2} - \Delta t + \mathcal{O}(t^2). \quad (18)$$

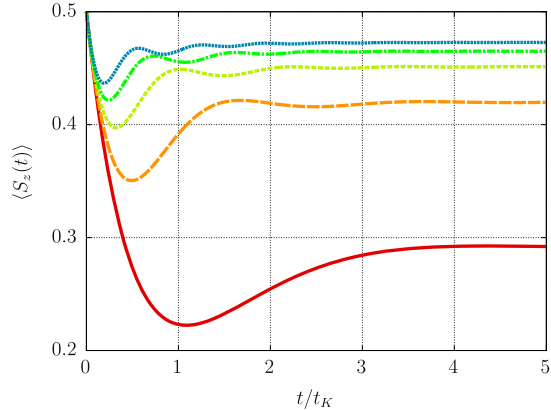


Figure 1. Magnetization $P(t) = \langle S_z(t) \rangle$ for different values of the local magnetic field $h_*/T_K = 9, 7, 5, 3, 1$ from top to bottom.

The impurity spin is flipped without recognizing the presence of the magnetic field or the spin-polarized lead at short times. Approaching the timescale t_* , one observes a deviation from this universal initial decay and $P(t)$ reaches its minimum leading to overshooting. For sufficiently large magnetic fields $h_* > T_K$ and for times $t > t_*$, damped oscillations appear and the magnetization finally saturates at a value $P(t = \infty) = \pi^{-1} \operatorname{atan}(h_*/\Delta)$, that is the equilibrium value of the magnetization in the Kondo model with an applied magnetic field h_* .

In terms of the initial spin polarization, the finite asymptotic value of the magnetization indicates that the impurity is not able to depolarize the system although it can flip spins. Due to spin conservation, compare equation (10), the subspace of the total Hilbert space \mathcal{H}_{dyn} that is accessible by the dynamics can be restricted to [14]:

$$\mathcal{H}_{\text{dyn}} = \mathcal{H}_+ \oplus \mathcal{H}_- \quad (19)$$

where the subspaces \mathcal{H}_\pm

$$\mathcal{H}_+ = \text{span}[|S_T + \frac{1}{2}, \downarrow\rangle], \quad \mathcal{H}_- = \text{span}[|S_T - \frac{1}{2}, \uparrow\rangle] \quad (20)$$

contain those states that have a sea of conduction band electrons with spin $S_T \pm \frac{1}{2}$ and a local spin on the impurity with spin \downarrow, \uparrow . The impurity is therefore able to flip spins, the spin conservation condition, however, limits the maximally possible induced change of spin in the conduction band to one spin flip process from spin-up to spin-down such that the impurity is not able to compensate for the macroscopic initial spin polarization.

For large magnetic fields, $h_* \gg T_K$, the magnetization for times $t \gg t_* = 1/h_*$

$$\delta P(t) \xrightarrow{h_* \gg T_K} \left[\Lambda(0) - \frac{1}{2} \right] e^{-2\Delta t} - \frac{2\Delta}{\pi h_*} \frac{\sin(h_* t)}{h_* t} e^{-\Delta t} \quad (21)$$

reveals the frequency $\Omega_* = h_*$ of the oscillations in the magnetization that can be clearly seen in figure 1. Here

$\delta P(t) = P(t) - P(t = \infty)$ denotes the deviation from the asymptotic equilibrium value $P(t = \infty)$.

For arbitrary fields $h_* \neq 0$, the asymptotic long-time behavior of the magnetization

$$\delta P(t) \xrightarrow{t \gg t_s, t_K} -\frac{2}{\pi} \frac{\Delta^2}{\Delta^2 + h_*^2} \frac{\sin(h_* t)}{\Delta t} e^{-\Delta t} \quad (22)$$

changes significantly compared to the interaction quench case without magnetic field, see equation (14), where it is exponential with rate 2Δ . Even a small magnetic field slows down the decay. It becomes exponential at a rate Δ times an algebraic contribution proportional to $(\Delta t)^{-1}$. Recently, a similar slow asymptotic decay for the magnetization in presence of a magnetic field was found in the work by Ratiani and Mitra [9] where the transient dynamics in a quench from a single to a two-channel Kondo model has been studied. In the work of [19], the relaxation dynamics of the local level occupation in an interacting resonant level model has been investigated. Comparing their analytical long-time asymptotics with the result in equation (22), one finds perfect agreement. Regarding equation (22), in the limit $h_* \rightarrow 0$ the asymptotic long-time behavior of the magnetization crosses over into the interaction quench dynamics without magnetic field, compare equation (14), since the prefactor vanishes. The decay becomes proportional to $e^{-2\Delta t}$ as one can see from equation (17) with $\Lambda(t) = 0$ for $h_* = 0$.

In equilibrium as well as for an interaction quench, it has been shown that the Toulouse limit of the Kondo model describes qualitatively correct the dynamics of the local spin observables [3–5]. One may raise the question whether this extends to the present case with an additional magnetic field. In a recent work, Anders and Schiller [7] determined the magnetization for the same setup in the experimentally relevant case of an isotropic Kondo model at small couplings using the time-dependent numerical renormalization group technique. Comparing their numerically exact results with the analytical treatment shown here one finds very good qualitative agreement. As in the present Toulouse limit analysis, they observe an initial universal decay. Approaching $t \sim t_*$, the magnetization develops a minimum and damped oscillations appear for $t > t_*$ as long as the magnetic field is sufficiently large. The magnetization relaxes on the timescale t_K to a finite asymptotic value. Those main features all appear in the present analysis such that one can expect that the behavior of the other local dynamical quantities such as the spin–spin correlation function and the dynamical spin susceptibility obtained on the Toulouse line are describing qualitatively the correct behavior for the isotropic Kondo model at small couplings.

4. Spin–spin correlation function

Additional information about the local dynamical properties of the system is contained in the spin–spin correlation function

$$\langle S_z(t) S_z(t_w) \rangle = C(t, t_w) - \frac{i}{2} \chi(t, t_w) \quad (23)$$

that probes the correlation between two spin measurements at different times. Its real part $C(t, t_w) = \frac{1}{2} \langle \{S_z(t), S_z(t_w)\} \rangle$

is connected to the strength of the spin fluctuations and its imaginary part determines the response function $\chi(t, t_w) = i\theta(t - t_w) \langle [S_z(t), S_z(t_w)] \rangle$ for times t bigger than the waiting time t_w .

Due to equation (4), the spin–spin correlation function can be related directly to operators of the effective Hamiltonian:

$$\langle S_z(t) S_z(t_w) \rangle = \langle \hat{n}_d(t) \hat{n}_d(t_w) \rangle - \frac{1}{2} [P(t) + P(t_w)] - \frac{1}{4}. \quad (24)$$

From the evaluation of $\langle \hat{n}_d(t) \hat{n}_d(t_w) \rangle$ one obtains for the cumulant $\langle S_z(t) S_z(t_w) \rangle_C = \langle S_z(t) S_z(t_w) \rangle - \langle S_z(t) \rangle \langle S_z(t_w) \rangle$ of the spin–spin correlation function:

$$\langle S_z(t) S_z(t_w) \rangle_C = \Omega(t, t_w) [\Lambda(t - t_w) - e^{-\Delta t} \Lambda(t_w) - e^{-\Delta t_w} \Lambda(t) + e^{-\Delta(t+t_w)} (1 + \Lambda(0)) + \Omega(t, t_w)] \quad (25)$$

where the function Ω is given by:

$$\Omega(t, t_w) = \frac{1}{\pi} \int_{h_*/\Delta}^{\infty} d\omega \frac{[e^{-i\omega\Delta t} - e^{-\Delta t}] [e^{i\omega\Delta t_w} - e^{-\Delta t_w}]}{1 + \omega^2}. \quad (26)$$

One fundamental question connected to non-equilibrium quench dynamics concerns the thermalization behavior of observables [4, 5, 11, 6–9]. As for the magnetization, the relaxation of the spin–spin correlation function happens exponentially fast on a timescale $1/\Delta \propto t_K$ set by the Kondo scale with a further suppression by an additional algebraic contribution $(\Delta t_w)^{-1}$:

$$\delta \langle S_z(t + t_w) S_z(t_w) \rangle \xrightarrow{t_w \gg t_s, t_K} F(t, t_w) \frac{e^{-\Delta t_w}}{\Delta t_w}. \quad (27)$$

Here, $\delta \langle S_z(t + t_w) S_z(t_w) \rangle = \langle S_z(t + t_w) S_z(t_w) \rangle - \langle S_z(t) S_z \rangle_{eq}^{h_*}$ denotes the deviation of the spin–spin correlation function from its asymptotic relaxed form which is just the equilibrium spin–spin correlation function $\langle S_z(t) S_z \rangle_{eq}^{h_*}$ with applied magnetic field h_* . The function $F(t, t_w)$ is an oscillating function of t_w with period $2\pi/h_*$ and does not contribute to the relaxation dynamics. Comparing equation (27) with the result for an interaction quench obtained by Lobaskin and Kehrein [4], one observes that the relaxation behavior of the spin–spin correlation function does not change considerably. The magnetic field only leads to a modification of the function $F(t, t_w)$. As already observed for the magnetization, the timescale for thermalization of the spin–spin correlation function is exclusively set by the Kondo scale t_K .

In equilibrium at zero temperature without magnetic field, the spin–spin correlation function shows a universal algebraic long-time behavior [3]

$$\langle S_z(t) S_z \rangle_{eq} \xrightarrow{t \gg t_K} -\frac{1}{[\pi \Delta t]^2}. \quad (28)$$

In the present non-equilibrium setting, the universal long-time behavior remains unchanged:

$$\begin{aligned} \langle S_z(t) S_z(t_w) \rangle_C &\xrightarrow{t \gg t_K, t_s, t_w} -\left[\frac{\Delta^2}{h_*^2 + \Delta^2} \right]^2 \\ &\times \frac{1 - 2 \cos(h_* t_w) e^{-\Delta t_w} + e^{-2\Delta t_w}}{[\pi \Delta(t - t_w)]^2} \end{aligned} \quad (29)$$

with only a different prefactor. This universality originates from the property of the spin–spin correlation function that its asymptotic long-time behavior is solely dependent on the low-energy excitations in the vicinity of the Fermi level as one can show by a simple Fermi liquid argument. In equilibrium, one can expand the d operator in the energy representation of operators a_ε that diagonalize the Hamiltonian in equation (5), such that one obtains:

$$d = \rho_0^{-1/2} \sum_\varepsilon f_\varepsilon a_\varepsilon. \quad (30)$$

Here, $|f_\varepsilon|^2$ is the local single-particle density of states $\rho_d(\varepsilon)$ of the effective Hamiltonian at energy ε and $\rho_0 = L/(2\pi)$ is the noninteracting density of states of the lead. In the energy representation, the spin–spin correlation function then reduces to:

$$\langle S_z(t)S_z \rangle_{eq} = \left[\rho_0^{-1} \sum_{\varepsilon > 0} |f_\varepsilon|^2 e^{-i\varepsilon t} \right]^2. \quad (31)$$

Performing a Wick rotation $t \rightarrow -i\tau$, one observes that for large τ only the low-energy states contribute. Assuming that $|f_\varepsilon|^2$ is well behaved near the Fermi level $\varepsilon = 0$ such that it may be expanded around $\varepsilon = 0$ and replacing τ by it , the long-time behavior of the spin–spin correlation function is given by:

$$\langle S_z(t)S_z \rangle_{eq} \xrightarrow{t \rightarrow \infty} \left[\frac{\rho_d}{it} \right]^2. \quad (32)$$

In equilibrium at zero magnetic field, the local level $\varepsilon_0 = 0$ exactly lies at the Fermi energy such that the local density of states ρ_d at the Fermi level equals $\rho_d = 1/(\pi\Delta)$ and the exact result of equation (28) is reproduced. In case of an applied magnetic field h_* , the local d level is shifted away from the Fermi energy leading to a reduction of the local density of states $\rho_d = (\Delta^2/\pi)/(\Delta^2 + h_*^2)$. Comparing with the result in equation (29), one observes that the prefactor in the long-time behavior of the relaxed spin–spin correlation function for $t_w \rightarrow \infty$ exactly equals the square of the local density of states as expected from the Fermi liquid argument above.

For intermediate waiting times $0 < t_w < \infty$, the long-time behavior acquires a modification by damped oscillations with period $2\pi/h_*$ as a function of the waiting time t_w . This is a consequence of the transient non-equilibrium state where the Fermi liquid argument is not valid. At zero waiting time $t_w = 0$, the decay becomes exponential as the initial state is an eigenstate of the S_z operator and the spin–spin correlation function reduces to the magnetization of section 3 as has been observed for the case of an interaction quench without magnetic field [4].

5. Dynamical spin susceptibility

The imaginary part of the spin–spin correlation function determines the response of the system to a small external magnetic field $h(t)$ applied to the local spin. In the linear response regime, the magnetization in presence of $h(t)$ equals:

$$\langle S_z(t) \rangle_h = \langle S_z(t) \rangle + \int_{-\infty}^{\infty} dt' \chi(t, t') h(t'). \quad (33)$$

Expectation values without an index h are to be evaluated with the unperturbed Hamiltonian. In equilibrium, the response function depends only on the time difference thereby establishing a spectral representation in terms of one frequency. Its imaginary part $\chi''(\omega)$, the dynamical spin susceptibility, shows a peak near the Kondo temperature representing the Kondo singlet. In the non-equilibrium setting considered in this work, the suitable generalization of the spectral representation of the response function is the following [4]:

$$\chi(t_w, \omega) = 2 \int_0^\infty \frac{dt}{2\pi} e^{i\omega t} \chi(t + t_w, t_w). \quad (34)$$

The integration is only taken over the positive real axis as a consequence of causality such that an additional prefactor of 2 is required in order to reproduce the equilibrium case. The function $\chi(t_w, \omega)$ may be interpreted as the spectral decomposition of the response function at a given point t_w in time. Accordingly, $\chi''(t_w, \omega) = \text{Im } \chi(t_w, \omega)$ determines the dynamical spin susceptibility at a given point t_w in this non-equilibrium setup. False color plots of $\chi''(t_w, \omega)$ are shown in figure 2 for different degrees of initial spin polarization.

As one can see from figure 2, the timescale for relaxation of the dynamical spin susceptibility is solely determined by the Kondo scale t_K as already found for the magnetization and the spin–spin correlation function.

For small magnetic fields $h_* < T_K$, the behavior of the dynamical spin susceptibility resembles the interaction quench case without magnetic field. In the transient regime up to times $t \sim t_K$, the dynamical spin susceptibility approaches its equilibrium shape exponentially fast with a peak located at $\omega \approx T_K$ associated with the Kondo singlet as one observes in the case without magnetic field [6, 4].

For magnetic fields $h_* \gtrsim T_K$, as can be seen in the plots of figure 2, a maximum builds up on a timescale t_* whose position roughly scales proportional to the magnetic field. Importantly, the peak associated with the Kondo singlet near T_K is not visible any more indicating that the large magnetic field avoids the buildup of Kondo correlations. The spin fluctuations that are the basis for the emergence of the Kondo effect are suppressed as the impurity spin is pinned by the strong magnetic field. After a fast initial buildup on a timescale t_* associated with the initial spin polarization, damped oscillations appear in the dynamical spin susceptibility with frequency h_* decaying on a scale t_K .

6. Conclusions

In this work, the quench dynamics of the Kondo model in the Toulouse limit have been analyzed in the presence of a local magnetic field. It has been shown that this setup can be realized either by applying the magnetic field directly or by preparing the system in a macroscopically spin-polarized state. The effective magnetic field caused by the initial state results from a subtlety in applying the bosonization technique. Terms that are usually referred to as finite-size corrections become important in this non-equilibrium setting. The transient dynamics have been investigated by analyzing exact analytical results for the local spin dynamics such as the magnetization, the spin–spin correlation function and the dynamical spin susceptibility.

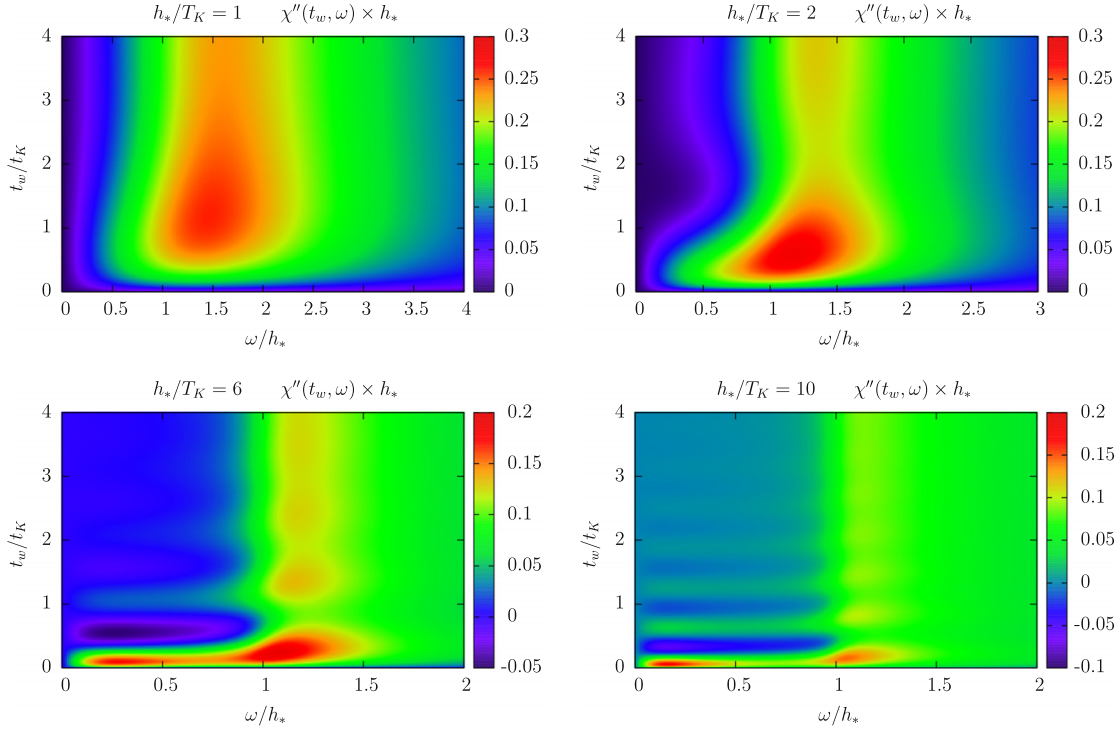


Figure 2. False color plots of the dynamical spin susceptibility $\chi''(t_w, \omega)$ for different values of the magnetic field h_* .

The analysis revealed that the timescale for relaxation of all the investigated local dynamical quantities is exclusively set by the Kondo scale t_K and is independent of the magnetic field h_* , compare equations (14), (27) and figures 1 and 2.

The magnetization shows damped oscillations with a frequency h_* set by the magnetic field for $h_* > T_K$. Compared to the interaction quench case without magnetic field, the asymptotic long-time decay of the magnetization becomes slower in the present setup with a different scaling behavior, compare equation (22). Overall, the analysis of the magnetization on the Toulouse line shows very good qualitative agreement with a recent numerically exact analysis for the isotropic Kondo model obtained from a time-dependent numerical renormalization group study [7]. Therefore, one can expect that the other local dynamical quantities analyzed in this work such as the spin–spin correlation function and the dynamical spin susceptibility also display the main features and that the results presented in this work are qualitatively valid also away from the Toulouse limit.

The relaxation behavior of the spin–spin correlation function, see equation (27), is not altered considerably compared to the interaction quench case without a magnetic field. Remarkably, the asymptotic long-time behavior of the spin–spin correlation function is universal and its scaling behavior equals the equilibrium case. This universality originates in the property that the asymptotic long-time behavior of the spin–spin correlation function is solely dependent on the low-energy excitations in the vicinity of the

Fermi level. By using a simple Fermi liquid argument, it was shown that the only relevant quantity for the prefactor is the local density of states of the quadratic effective Hamiltonian at the Fermi level.

The dynamical spin susceptibility is not influenced substantially for magnetic fields $h_* < T_K$ smaller than the Kondo temperature and behaves as in an interaction quench scenario without magnetic field. For $h_* > T_K$, one observes a rapid buildup of correlations on a timescale $t_* = 1/h_*$ and damped oscillations appear for times $t > t_*$ that decay on a timescale t_K . The dynamical spin susceptibility shows a maximum whose position roughly scales proportional to the applied magnetic field. Most importantly, the Kondo peak near T_K disappears for sufficiently large h_* indicating that the magnetic field seen by the impurity spin avoids the buildup of Kondo correlations by pinning the local spin thereby suppressing the local spin fluctuations.

In summary we have obtained exact results for the interaction quench dynamics of the Kondo model on the Toulouse line and studied its thermalization behavior. This is a rare case where rigorous results can be found even in non-equilibrium and provides another benchmark in the growing field of non-equilibrium quantum impurity physics [4–10, 12].

Acknowledgments

This work was supported through SFB TR12 of the Deutsche Forschungsgemeinschaft (DFG), the Center for Nanoscience

(CeNS) Munich, and the German Excellence Initiative via the Nanosystems Initiative Munich (NIM).

Appendix

For the evaluation of correlation functions in the macroscopically spin-polarized initial state, it is essential to determine the initial occupation distribution of the spinless fermions

$$f_{kk'} = \langle \psi'_0 | c_k^\dagger c_{k'} | \psi'_0 \rangle \quad (\text{A.1})$$

where the state $|\psi'_0\rangle$ is given by:

$$|\psi'_0\rangle = e^{i\pi \hat{N}_s S_z} e^{i(\sqrt{2}-1)\phi_s(0)(S_z - \frac{1}{2})} |\psi_0\rangle = e^{iLk*/8} |\psi_0\rangle \quad (\text{A.2})$$

as the initial state $|\psi_0\rangle$ is an eigenstate of both S_z and N_s . Expressing the modes c_k in terms of the fields $\psi(x)$ and by using the bosonization identity for $\psi(x)$ one obtains:

$$\begin{aligned} f_{kk'} &= \frac{1}{2\pi aL} \int \frac{dx}{2\pi} \int \frac{dx'}{2\pi} e^{-ikx} e^{ik'x'} \\ &\times \langle \psi'_0 | e^{i\phi_s(x)} e^{i\frac{2\pi}{L}\hat{N}_s x} e^{-i\frac{2\pi}{L}\hat{N}_s x'} e^{-i\phi_s(x')} | \psi'_0 \rangle. \end{aligned} \quad (\text{A.3})$$

Due to equation (7), $e^{-i\frac{2\pi}{L}\hat{N}_s x} |\psi_0\rangle = e^{-ik_*x/2} |\psi_0\rangle$ such that:

$$f_{kk'} = \delta_{kk'} \theta\left(\frac{k_*}{2} - k\right). \quad (\text{A.4})$$

Therefore, the initial spin-polarized state induces a shift of the chemical potential of the spinless fermionic operators.

References

- [1] Goldhaber-Gordon D, Shtrikman H, Mahalu D, Abusch-Magder D, Meirav U and Kastner M A 1998 *Nature* **391** 156
- Cronenwett S M, Oosterkamp T H and Kouwenhoven L P 1998 *Science* **281** 540
- Schmid J, Weis J, Eberl K and von Klitzing K 1998 *Physica B* **258** 182
- van der Wiel W G, De Franceschi S, Fujisawa T, Elzerman J M, Tarucha S and Kouwenhoven L P 2000 *Science* **289** 2105
- [2] Toulouse G 1969 *C.R. Acad. Sci. Paris* **268** 1200
- [3] Leggett A J, Chakravarty S, Dorsey A T, Fisher M P A, Garg A and Zwerger W 1987 *Rev. Mod. Phys.* **59** 1
- [4] Lobaskin D and Kehrein S 2005 *Phys. Rev. B* **71** 193303
- [5] Lobaskin D and Kehrein S 2006 *J. Stat. Phys.* **123** 301
- [6] Nordlander P, Pustilnik M, Meir Y, Wingreen N S and Langreth D C 1999 *Phys. Rev. Lett.* **83** 808
- [7] Anders F and Schiller A 2006 *Phys. Rev. B* **74** 245113
- [8] Costi T A 1997 *Phys. Rev. B* **55** 3003
- Plihal M, Langreth D C and Nordlander P 2000 *Phys. Rev. B* **61** R13341
- Schiller A and Hershfield S 2000 *Phys. Rev. B* **62** R16271
- Anders F B and Schiller A 2005 *Phys. Rev. Lett.* **95** 196801
- Tureci H E, Hanl M, Claassen M, Weichselbaum A, Hecht T, Braunecker B, Govorov A, Glazman L I, von Delft J and Imamoglu A 2009 arXiv:0907.3854
- Affleck I and Ludwig A W W 1994 *J. Phys. A: Math. Gen.* **27** 5375
- [9] Ratiani Z and Mitra A 2010 *Phys. Rev. B* **81** 125110
- [10] Lesage F and Saleur H 1998 *Phys. Rev. Lett.* **80** 4370
- [11] Möckel M and Kehrein S 2008 *Phys. Rev. Lett.* **100** 175702
- Eckstein M, Kollar M and Werner P 2009 *Phys. Rev. Lett.* **103** 056403
- Calabrese P and Cardy J 2006 *Phys. Rev. Lett.* **96** 136801
- Kollath C, Läuchli A M and Altman E 2007 *Phys. Rev. Lett.* **98** 180601
- Faribault A, Calabrese P and Caux J-S 2009 *J. Stat. Mech.* P03018
- Eckstein M and Kollar M 2008 *Phys. Rev. Lett.* **100** 120404
- Rigol M 2009 *Phys. Rev. Lett.* **103** 100403
- Manmana S R, Wessel S, Noack R M and Muramatsu A 2007 *Phys. Rev. Lett.* **98** 210405
- Cazalilla M A 2006 *Phys. Rev. Lett.* **97** 156403
- [12] Komnik A 2009 *Phys. Rev. B* **79** 245102
- [13] von Delft J and Schoeller H 1998 *Ann. Phys., Lpz.* **7** 225
- [14] Zarand G and von Delft J 2000 *Phys. Rev. B* **61** 6918
- [15] Martinek J, Utsumi Y, Imamura H, Barnas J, Maekawa S, Koenig J and Schoen G 2003 *Phys. Rev. Lett.* **91** 127203
- Martinek J, Sindel M, Borda L, Barnas J, Koenig J, Schoen G and von Delft J 2003 *Phys. Rev. Lett.* **91** 247202
- [16] Gutman D B, Gefen Y and Mirlin A D 2010 *Phys. Rev. B* **81** 085436
- [17] Segal D, Reichman D R and Millis A J 2007 *Phys. Rev. B* **76** 195316
- [18] Guinea F, Hakim V and Muramatsu A 1985 *Phys. Rev. B* **32** 4410
- [19] Karrasch C, Andergassen S, Pletyukov M, Schuricht D, Borda L and Schoeller H 2010 *Eur. Phys. Lett.* **90** 30003

2.2 Publication: Electron-plasmon scattering in chiral Luttinger liquids

In dimensions $d > 1$ the properties of fermions with repulsive interactions are determined by Fermi liquid theory as long as the elementary excitations in the system can be considered as a dilute gas. Most importantly, in presence of interactions the elementary excitations - the quasiparticles - are still fermionic. Their occupation distribution shows a jump at the Fermi surface at zero temperature reminiscent of a finite quasiparticle weight.

In one dimension the picture changes completely [58]. Within the Luttinger liquid limit paradigm the fermionic occupation distribution becomes a continuous function of energy. There is no jump at the Fermi surface but still it is nonanalytic at this point with an algebraic dependence. The spectral function shows a power-law divergence with a nonuniversal exponent that depends on the interaction strength. The elementary excitations become bosonic and of collective nature.

Within the Luttinger liquid limit, a system of interacting spinless fermions in one dimension is modeled by the following Hamiltonian

$$H_{\text{LL}} = H_0 + H_{\text{int}} \quad (2.5)$$

containing the kinetic energy contribution with a linearized spectrum

$$H_0 = v_F \sum_{k,\eta=L/R} k : c_{k\eta}^\dagger c_{k\eta} : \quad (2.6)$$

and the interactions between the particles

$$\begin{aligned} H_{\text{int}} = & \sum_{\eta=L/R} \int_{-L/2}^{L/2} dx \int_{-L/2}^{L/2} dx' \rho_\eta(x) \frac{1}{2} U(x - x') \rho_\eta(x') + \\ & + \int_{-L/2}^{L/2} dx \int_{-L/2}^{L/2} dx' \rho_L(x) U(x - x') \rho_R(x'). \end{aligned} \quad (2.7)$$

For a schematic picture about the linearization procedure and the introduction of two independent species of electrons, left- and right-movers associated with the label $\eta = L/R$, see Fig. 2.2. The state $(k\eta)$ corresponds to a fermion near the left or right Fermi point - depending on whether $\eta = L$ or $\eta = R$ - with a momentum k measured relative to the Fermi momentum p_F . Thus, $(k = 0, R)$ is the fermionic state located exactly at the right Fermi point. The operator $c_{k\eta}^\dagger$ creates a fermion near the Fermi point $\eta = L/R$ with a momentum k . The colons $: \dots :$ denote normal ordering relative to the noninteracting Fermi sea at zero temperature. The Fermi velocity is denoted by v_F . In the above choice the interaction potential $U(x - x')$ takes a general form which has not to be of contact type as in most treatments. Below the finite range of U will become important. The electrons interact with each other via a repulsive density-density interaction where $\rho_\eta(x) =: \psi_\eta^\dagger(x) \psi_\eta(x) :$, $\psi_\eta(x) = 1/\sqrt{L} \sum_k e^{ikx} c_{k\eta}$, and L the system size.

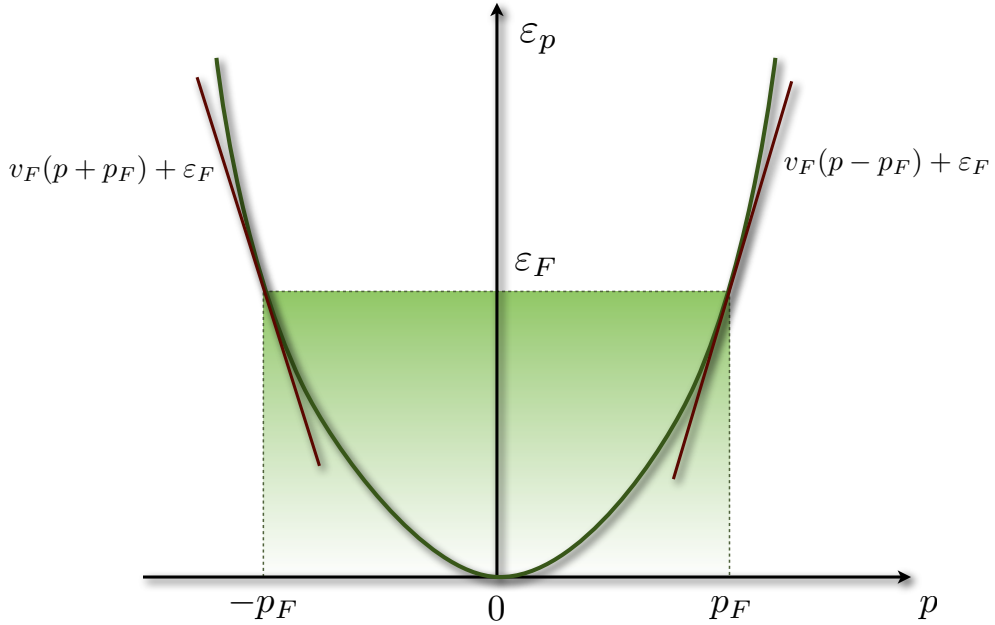


Figure 2.2: Schematic visualization of the linearization of the initial dispersion relation ε_p and the introduction of left- and right-moving fermions. As a particular example, a quadratic dispersion $\varepsilon_p = p^2/(2m)$ is shown where m is the mass of the particle. For a noninteracting system all states below the Fermi energy $\varepsilon_F = p_F^2/(2m)$ with p_F the Fermi momentum are occupied at zero temperature. In the low-energy limit the dispersion relation ε_p can be linearized around the two Fermi points p_F and $-p_F$ to a good approximation. As a consequence it is suitable to introduce two new fermionic species associated with the left- and right Fermi point called right- and left-movers. For the right-movers, for example, one introduces the corresponding dispersion relation $\varepsilon_{kR} = v_F k$ with $k = p - p_F$ and v_F the Fermi velocity.

The Luttinger liquid paradigm requires a linearized dispersion relation for the initial fermionic particles. In this case the problem can be reformulated in a bosonic language where the Hamiltonian becomes exactly solvable. Including also quadratic corrections to the fermionic dispersion spoils the exact solvability and introduces a three-body interaction between the bosonic particles that cannot be treated in simple perturbation theory [139]. But recently there has been considerable progress in the description of interacting fermions in one dimension beyond the Luttinger liquid paradigm [77].

At first sight there seems to be no connection to nonequilibrium dynamics and local quantum quenches in the problem of Luttinger liquids with nonlinear dispersion. As it turns out, however, the calculation of the Green's function and spectral function at high energies where the nonlinearity becomes important can be mapped onto a simple nonequilibrium problem [139, 130, 76]. The effective model is equivalent to a Luttinger liquid where suddenly a mobile propagating impurity is switched on. In this way it shows a remarkable similarity to the x-ray edge problem as has been realized in the work by Pustilnik *et al.* [139].

For more details on the x-ray edge problem see Ch. 3. The Green's function is interpreted in terms of a nonequilibrium process where suddenly a fermion is injected into the Luttinger liquid. Provided its energy is sufficiently large it can be treated as a mobile impurity constituting a local potential scatterer onto which the Luttinger liquid has to adapt. This separation of high-energy fermion and low-energy degrees of freedom is deeply connected to the surprising observation that the high-energy fermion becomes distinguishable from the remaining ones forming the Luttinger liquid. This is a consequence of the finite range of the interaction which suppresses exchange processes between low- and high-energy sectors of the theory, see below. Note that not every correlation function should be associated with a nonequilibrium process. It is rather a consequence of the specific details of the present system that really allows to map the evaluation of the fermionic Green's function onto a nonequilibrium x-ray edge problem.

In the following a reduced system of just one of the two left- or right-moving species will be studied. This is the chiral Luttinger liquid with a Hamiltonian

$$H_{cLL} = v_F \sum_k \varepsilon_k : c_k^\dagger c_k : + \int_{-L/2}^{L/2} dx \int_{-L/2}^{L/2} dx' \rho(x) \frac{1}{2} U(x - x') \rho(x'). \quad (2.8)$$

Note that in comparison to Eq. (2.6) the kinetic energy of the fermions in the Hamiltonian H_{cLL} contains a general dispersion relation allowing to include also nonlinear corrections of the spectrum. Chiral Luttinger liquids have been realized, for example, in integer quantum Hall edge channels. Among other things they are used as interferometer arms for the electronic version of Mach-Zehnder interferometers [81]. This example becomes particularly important for the study below.

In the following the dynamics of a mobile impurity injected into a chiral Luttinger liquid is investigated. In contrast to prior work the finite range of the interaction potential between the fermions is taken fully into account. This opens the window for a regime where the Green's function represented in real-space acquires an exponential decay as a function of distance. The associated spectral function of the fermions then exhibits a form without any power-law singularities. This in turn contrasts the low-energy Luttinger paradigm which is characterized by power-law singularities or at least regions of finite support [156]. Before, finite decay rates have only been found as a consequence of backscattering [92]. The discussion presented below shows that finite decay rates can also be present in chiral Luttinger liquids without backscattering provided a finite range of the interaction is taken into account. The injected fermion is scattered off a resonant plasmonic mode of the underlying Luttinger liquid. This yields an emanating monochromatic density pattern in the wake of the mobile impurity.

The following article has been published in *Physical Review B*.

M. Heyl, S. Kehrein, F. Marquardt, and C. Neuenhahn, *Phys. Rev. B* **82**, 033409 (2010).
Copyright 2010 by the American Physical Society.
<http://prb.aps.org/abstract/PRB/v82/i3/e033409>

Electron-plasmon scattering in chiral one-dimensional systems with nonlinear dispersion

M. Heyl,¹ S. Kehrein,¹ F. Marquardt,^{1,2} and C. Neuenhahn^{1,2}

¹Department of Physics, Arnold Sommerfeld Center for Theoretical Physics, and Center for NanoScience, Ludwig-Maximilians-Universität München, Theresienstr. 37, 80333 Munich, Germany

²Institut für Theoretische Physik, Universität Erlangen-Nürnberg, Staudtstr. 7, 91058 Erlangen, Germany
(Received 16 June 2010; published 20 July 2010)

We investigate systems of spinless one-dimensional chiral fermions realized, e.g., in the arms of electronic Mach-Zehnder interferometers, at high energies. Taking into account the curvature of the fermionic spectrum and a finite interaction range, we find a new scattering mechanism where high-energy electrons scatter off plasmons (density excitations). This leads to an exponential decay of the single-particle Green's function even at zero temperature with an energy-dependent rate. As a consequence of this electron-plasmon scattering channel, we observe the coherent excitation of a plasmon wave in the wake of a high-energy electron resulting in the buildup of a monochromatic sinusoidal density pattern.

DOI: 10.1103/PhysRevB.82.033409

PACS number(s): 72.15.Nj, 71.10.Pm

I. INTRODUCTION

Many-particle physics in one dimension (1D) drastically differs from that in higher dimensions. In higher dimensions within the scope of Fermi-liquid theory, the presence of interactions between fermions does not change the character of the elementary low-energy excitations that are still fermionic. In one dimension this is completely different. Even weak interactions alter the character of the low-energy excitations. They become bosonic and of collective nature. Recently, however, it has been shown that 1D fermionic systems show Fermi liquid behavior at higher energies if one accounts for the curvature in the spectrum.¹

In this work we consider the properties of a system of spinless 1D chiral fermions under the injection of a high-energy fermion with well-defined energy ε beyond the low-energy paradigm. We take into account the influence of the curvature of the fermionic dispersion and a finite-range interaction. In experiments, electrons with well-defined energy may be injected via a quantum dot filter into an integer quantum hall edge state.^{2,3} Employing these edge channels as the arms of electronic Mach-Zehnder interferometers (MZI), for example, one may investigate the decoherence of the injected electrons as a function of injection energy ε . In this regard, we analyze the Green's function (GF) $G^>(x, \varepsilon) = -i\int dt e^{i\varepsilon t} \langle \hat{\psi}(x, t) \hat{\psi}^\dagger(0, 0) \rangle$ (which, in the context of MZIs, is directly related to the interference contrast⁹), the spectral function $A(k, \varepsilon)$ and the density $\varrho(x, t)$ of the fermionic background in presence of the high-energy fermion.

Our main observation is the existence of a new scattering mechanism in chiral 1D systems at high energies due to an interplay of both curvature and finite interaction range. A fermion injected with a high energy such that it experiences the curvature of the spectrum scatters off low-energy density excitations, so-called plasmons. This gives rise to an exponential decay of the GF in the large distance limit with a nonzero decay rate Γ_ε even at zero temperature in stark contrast to the low-energy case where the asymptotic behavior is algebraic. The excitation of plasmons happens coherently leading to the buildup of a sinusoidal density pattern in the fermionic density in the wake of the injected high-energy electron.

At low energies, interacting 1D fermions are described perfectly well by a linearized spectrum and a subsequent application of the bosonization technique. Taking into account curvature one has to employ new methods. Recently, there has been considerable progress in calculating single-particle properties beyond the low-energy paradigm.^{1,10–14} In Ref. 11 edge singularities in the dynamic structure factor were found by performing a projection scheme in analogy to the x-ray edge singularity problem. The authors of Refs. 12 and 13 provided a framework for the calculation of response functions for pointlike interactions beyond the perturbative regime. In a combined Bethe ansatz and time-dependent density-matrix renormalization group (tDMRG) analysis it was shown that the edge behavior of the spectral function is indeed described by x-ray edge type effective Hamiltonians and the exact singularity exponents have been determined.¹⁴

For the calculation of the GF and the spectral function we employ two different methods that turn out to yield exactly

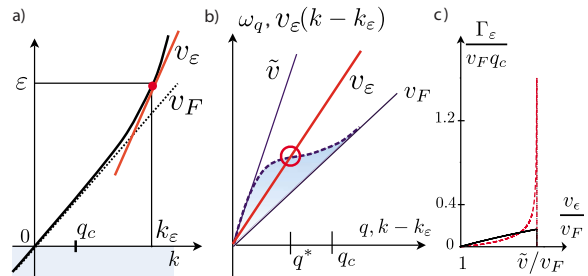


FIG. 1. (Color online) (a) High-energy fermion injected with energy $\varepsilon \gg q_c v_F$ on top of the Fermi sea. Due to the curvature of the dispersion it moves with an energy-dependent velocity $v_\varepsilon \geq v_F$. (b) Sketch of the dispersion relation of the density excitations of the Luttinger liquid (plasmons) ω_q with the plasmon velocity \tilde{v} (dashed blue line) and the dispersion of the high-energy fermion linearized in the vicinity of its initial energy ε (thick red line). The mode q^* denotes the intersection point of the two dispersion relations whose existence is responsible for momentum- and energy-conserving scattering between the injected electron and the plasmons. (c) Plot of the decay rate of the GF [cf. Eq. (3)] for an analytic interaction potential $U_q = 2\pi\alpha v_F e^{-|q/q_c|^2}$ (dashed line) and a nonanalytic one $U_q = 2\pi\alpha v_F e^{-|q/q_c|}$ (solid line), respectively (see main text).

the same result. On the one hand, we use a physically transparent semiclassical ansatz whose validity was proven earlier by comparison to the bosonization result.⁹ This ansatz is naturally extended to include curvature effects. Additionally, we derive an effective Hamiltonian for the description of the single-particle properties by extending the method of Pustilnik *et al.*¹¹ to include the full interaction potential. Based on the latter approach we also obtain the fermionic density after the injection of the high-energy electron.

II. MODEL AND GF

Consider a system of spinless chiral interacting 1D electrons described by the Hamiltonian

$$\hat{H} = \sum_k \varepsilon_k \hat{c}_k^\dagger \hat{c}_k + \frac{1}{2} \int dx dx' \hat{\rho}(x) U(x - x') \hat{\rho}(x'), \quad (1)$$

where $\hat{\psi}(x) = 1/\sqrt{L} \sum_k e^{ikx} \hat{c}_k$ and we normal order the Hamiltonian with respect to the vacuum (indicated by \dots) where all states with $k < 0$ are occupied and empty otherwise. We denote the fermionic density with $\hat{\rho}(x) = : \hat{\psi}^\dagger(x) \hat{\psi}(x) :$ and introduce an almost arbitrary interaction potential $U(x)$ with a Fourier transform $U_q = \int dx e^{-iqx} U(x)$. The latter is assumed to be cut off beyond some momentum scale q_c , and we introduce a dimensionless coupling strength $\alpha = U_{q=0}/2\pi v_F$. Whereas the following considerations, in principle, do not rely on a particular choice of ε_k , for simplicity, we deal with a dispersion relation of positive curvature as in the case of free fermions and assume a repulsive interaction, i.e., $\alpha > 0$.

It will be shown below that due to the finite interaction range the indistinguishability between the injected fermion and the Fermi sea at small temperatures is lifted if the injection energy $\varepsilon \gg v_F q_c$ is sufficiently large. This allows for the separation of high- and low-energy degrees of freedom, the single fermion propagating ballistically with the bare velocity v_ε and the remaining fermions constituting a Tomonaga-Luttinger liquid, respectively. The bosonic excitations of the latter evolve according to the plasmonic dispersion relation $\omega_q = v_F q (1 + U_q / 2\pi v_F)$ defining the velocity $\tilde{v} = v_F (1 + \alpha)$ of the fastest plasmon.

The fermion and the plasmons are coupled via a residual interaction. Due to the finite interaction range $1/q_c$ and as long as $v_F < v_\varepsilon < \tilde{v}$ there exists an intersection point q_* (with $\omega_{q_*} = v_\varepsilon q_*$) between the plasmonic spectrum and the dispersion relation of the single fermion $\varepsilon_k - \varepsilon \approx v_\varepsilon (k - k_*)$ linearized in the vicinity of its initial energy (see Fig. 1). The existence of the intersection point enables an electron-plasmon scattering mechanism conserving momentum and energy. This manifests in an exponential long-distance decay of the GF even at zero temperature $T=0$

$$|G^>(x, \varepsilon)| \sim x^{-\gamma_\varepsilon} e^{-\Gamma_\varepsilon x/v_\varepsilon}, \quad x q_c \gg 1 \quad (2)$$

with

$$\Gamma_\varepsilon = 2\pi^2 \frac{(v_\varepsilon - v_F)^2}{|U'_{q_*}|} \Theta(\tilde{v} - v_\varepsilon), \quad \gamma_\varepsilon = \left[\frac{\alpha v_F}{\tilde{v} - v_\varepsilon} \right]^2. \quad (3)$$

A plot of the decay rate Γ_ε is shown in Fig. 1. The appearance of the step function Θ in the expression for Γ_ε mirrors

the fact that for $v_\varepsilon > \tilde{v}$ the high-energy electron is faster than any plasmonic mode such that the intersection point q_* between the plasmonic and fermionic dispersion relation vanishes (cf. Fig. 1). In the limit of vanishing curvature, i.e., $v_\varepsilon \rightarrow v_F$ we have $\Gamma_\varepsilon \rightarrow 0$ and a power-law exponent $\gamma_\varepsilon \rightarrow 1$, which is independent of the coupling strength α as found earlier.⁹ Increasing the injection energy such that $v_\varepsilon \rightarrow \tilde{v}$, the decay rate diverges for analytic interaction potentials. In the limit of large energies, where $v_\varepsilon > \tilde{v}$ and $\Gamma_\varepsilon = 0$, the GF decays algebraically for long distances. This decay can be attributed to the Anderson Orthogonality catastrophe¹⁵ in view of the fact that the GF is the equivalent to the core hole Green's function in the x-ray edge singularity problem. In this context it is remarkable that the exponent $\gamma_\varepsilon = \Delta n^2$ can be related to the screening charge Δn , that is the charge displaced in the fermionic background by the injection of the high-energy fermion. In the remainder of this paper, we will sketch the derivation of Eq. (2) and discuss further quantities such as the spectral function and the density of the fermionic background after the injection of the high-energy electron.

III. SEMICLASSICAL ANSATZ FOR THE GF

Motivated by the earlier results in Ref. 9 we employ a semiclassical ansatz for the GF in the limit of large energies $\varepsilon \gg q_c v_F$. After its injection, the electron propagates chirally with its bare velocity v_ε , thereby experiencing a fluctuating potential landscape $\hat{V}(t) = \int dx' U(x' - v_\varepsilon t) \hat{\rho}_B(x', t)$ (see also Ref. 16) at its classical position $x = v_\varepsilon t$. Here, $\hat{\rho}_B(x, t)$ is the fermionic density $\hat{\rho}_B(x, t) = L^{-1} \sum_{q>0} \sqrt{n_q} (\hat{b}_{q,B} e^{iqx - i\omega_q t} + H.c.)$ [with $(n_q = qL/2\pi)$] of the bath electrons with bosonic operators $\hat{b}_{q,B} = 1/\sqrt{n_q} \sum_k \hat{c}_{k,B}^\dagger \hat{c}_{k+q,B}$ representing the plasmonic excitations evolving according to the plasmonic dispersion ω_q . It is assumed that the nonlinearity of the fermionic dispersion is small enough such that the velocity of the propagating fermion can be considered as constant and the remaining electrons can be treated by means of bosonization. Specifically, the change in velocity of an electron due to a scattering event with a typical momentum transfer q_c has to be small such that $q_c \partial^2 \varepsilon_k / \partial k^2 \ll \partial \varepsilon_k / \partial k$ for all momenta k near the Fermi momentum and near k_* . As a consequence of the fluctuating plasmonic quantum bath, the high-energy fermion accumulates a random phase and its noninteracting GF is multiplied by the average value of the corresponding phase factor

$$\frac{G^>(x, \varepsilon)}{G_0^>(x, \varepsilon)} = \left\langle \hat{T} \exp \left[-i \int_0^{x/v_\varepsilon} dt' \hat{V}(t') \right] \right\rangle. \quad (4)$$

Here, \hat{T} denotes the time-ordering symbol and $G_0^> = -ie^{ik_\varepsilon x}/v_\varepsilon$ is the noninteracting GF for $\varepsilon > 0$. Note that the whole influence of the finite curvature is contained in the energy dependence of $v_\varepsilon \geq v_F$. Employing the Gaussian nature of the plasmonic bath it is possible to express the rhs of Eq. (4) in terms of the autocorrelation function of the potential fluctuations $\langle \hat{V} \hat{V} \rangle_\omega = \int dt e^{i\omega t} \langle \hat{V}(t) \hat{V}(0) \rangle$ (cf. Ref. 9) experienced by the single electron in its comoving frame of reference. In particular, for the modulus of the GF one obtains

$$\left| \frac{G^>}{G_0^>} \right| = \exp \left[- \int_{-\infty}^{\infty} \frac{d\omega \sin^2(\omega x/2v_e)}{2\pi \omega^2} \langle \{\hat{V}, \hat{V}\} \rangle_\omega \right], \quad (5)$$

where only the symmetrized correlator $\langle \{\hat{V}, \hat{V}\} \rangle_\omega = \langle \hat{V}\hat{V} \rangle_\omega + \langle \hat{V}\hat{V} \rangle_{-\omega}$ enters. The asymptotic long-distance decay of the GF in Eq. (7) is governed by the low-frequency properties of the potential fluctuation spectrum $\langle \{\hat{V}, \hat{V}\} \rangle_{\omega \downarrow 0} = 2\pi\gamma_e|\omega| + 4\Gamma_e$ (here we took $T=0$). It consists of an Ohmic part responsible for the power-law decay and a constant offset which leads to an exponential decay of the GF. For intermediate energies where $v_F q_c \ll \epsilon$ but $v_e = v_F$, Eq. (4) reproduces exactly the GF from standard bosonization.⁹ Thus, our analysis is correct within the validity of the bosonization technique.

IV. EFFECTIVE HAMILTONIAN

In fact, the semiclassical ansatz for the GF in Eq. (4) matches precisely the result obtained by an extension of the approach in Ref. 11 to treat the full interaction potential. There, $G^>(x, t)$ is viewed as an impurity problem related to the x-ray edge singularity¹⁷ where a scatterer, the injected fermion in this case, is suddenly switched on. The Hamiltonian in Eq. (1) is projected onto two strips of states that capture the relevant degrees of freedom, an energy interval around the initial energy ϵ of the injected high-energy fermion labeled by ϵ and an energy window around the Fermi energy labeled by an index B . Under this projection, the fermionic field decomposes into $\hat{\psi}(x) \rightarrow \hat{\psi}_B(x) + e^{ik_e x} \hat{\psi}_e(x)$. Linearizing the dispersion relations within both strips of states, the Hamiltonian of the low-energy sector can be bosonized. Regarding correlation functions involving at most one high-energy electron one obtains

$$H = \sum_{q>0} \omega_q b_{q,B}^\dagger b_{q,B} + \int dx \hat{\psi}_e^\dagger(x) (\epsilon - iv_e \partial_x) \hat{\psi}_e(x) + \int dxdx' \hat{\rho}_B(x) U(x-x') \hat{\psi}_e^\dagger(x') \hat{\psi}_e(x'). \quad (6)$$

In the derivation of this effective Hamiltonian a contribution proportional to U_{k_e} has been neglected as $k_e \gg q_c$ and U_q rapidly decays for $q \gg q_c$ by assumption. The omitted term is responsible for exchange processes between high- and low-energy sectors lifting the distinguishability between the high-energy fermion and the low-energy degrees of freedom. In Eq. (6) a constant Fock shift $U(x=0)\hat{N}_e/2$ is omitted which drops out automatically if we take as a starting point the Coulomb interaction instead of the density-density interaction in Eq. (1). The Hamiltonian in Eq. (6) can be diagonalized by means of the unitary transformation $\hat{U} = \exp(\hat{S})$, where $\hat{S} = \int dx \hat{\psi}_e^\dagger(x) \hat{\psi}_e(x) \sum_{q \geq 0} \chi_q [\hat{b}_{q,B}^\dagger e^{-iqx} - \text{H.c.}]$ with $\chi_q = 2\pi U_q / (U_q - 2\pi(v_e - v_F)) \sqrt{n_q}$. From Eq. (6), one can calculate the golden rule rate for the excitation of plasmons by the high-energy fermion. It matches precisely the decay rate determining the exponential decay of the GF in Eq. (3).

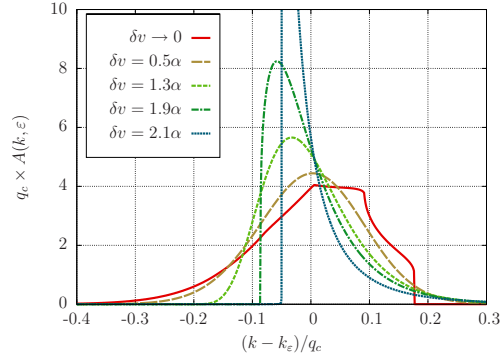


FIG. 2. (Color online) Spectral function $A(k, \epsilon)$ for different velocities v_e of the high-energy fermion where $\delta v = (v_e - v_F)/v_F$. For these plots we have chosen an analytic potential $U_q = 2\pi v_F \alpha \exp[-(q/q_c)^2]$ with $\alpha = 0.2$.

V. SPECTRAL FUNCTION

The spectral function $A(k, \epsilon)$ is connected to the GF via $A(k, \epsilon) = i/(2\pi) \int dx e^{-ikx} G^>(x, \epsilon)$ ($\epsilon > 0$ and $T=0$). It behaves qualitatively different whether the exponent γ_e appearing in the large distance behavior of the GF is bigger or smaller than one. Remarkably, this property is not connected to the distinction between $v_e \leq \tilde{v}$ that determines the threshold between exponential and algebraic large distance behavior for the GF. For $\gamma_e < 1$ or equivalently $\delta v = (v_e - v_F)/v_F > 2\alpha$, the spectral function shows a power-law singularity together with a threshold behavior for $k \rightarrow \kappa_e + k_e$

$$A(k, \epsilon) \sim \sin(\gamma_e \pi/2) (k - \kappa_e - k_e)^{\gamma_e - 1} \theta(k - \kappa_e - k_e), \quad (7)$$

where $\kappa_e = v_e^{-1} \mu_e$ and $\mu_e = \int_0^\infty dq (U_q/2\pi)^2 / (v_e - v_F - U_q/2\pi)$ denotes the energy that is needed to overcome the Coulomb interaction while injecting an electron with energy ϵ . In Fig. 2, the curve with $\delta v = 2.1\alpha$ shows the spectral function with a power-law singularity according to Eq. (7). Note that the support of the spectral function, $A(k, \epsilon) \neq 0$ only for $\epsilon + \mu_e < \epsilon_k$, is exactly opposite to the low-energy Tomonaga-Luttinger Liquid case where $A(\epsilon, k) \neq 0$ only for $\epsilon + \mu_e > \epsilon_k$. This is a consequence of the condition $v_e > \tilde{v}$ implying that an electron with wave vector k can excite plasmonic modes only by reducing the energy in the system (see Fig. 1). In the limit $\epsilon \rightarrow \infty$ where $\gamma_e \rightarrow 0$, one recovers the free particle, a δ function in the spectrum as $\lim_{\eta \rightarrow 0} \eta |x|^{\gamma_e - 1}/2 = \delta(x)$. As shown in Ref. 18 this is not the case for a linearized dispersion even in the limit $\epsilon \rightarrow \infty$.

For $\gamma_e > 1$, i.e., $v_F < v_e < 2\tilde{v} - v_F$, the spectrum changes drastically. The singularity vanishes and the spectral function merely becomes a skew Gaussian, compare Fig. 2. In the regime $\gamma_e > 1$ the GF, that is the Fourier transform of $A(k, \epsilon)$, is dominated by its initial Gaussian decay due to strong dephasing by the plasmonic background fluctuations. Thus, the spectrum itself is also dominated by the incoherent background such that no well-defined quasiparticle peak is visible in spite of the exponential decay of the GF. In the limit $v_e \rightarrow v_F$ and for a potential U_q with a sharp cutoff at q_c , one recovers the result by Ref. 18 as indicated in Fig. 2.

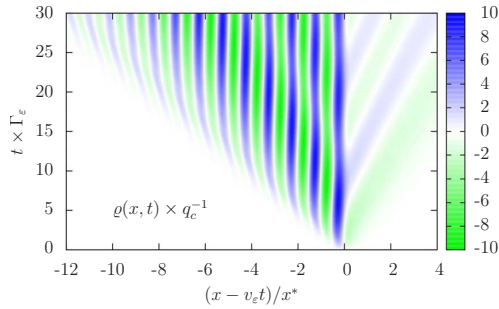


FIG. 3. (Color online) The fermionic density $\varrho(x,t)$ in the co-moving frame of the high-energy electron injected at time $t=0$. The period x^* of the oscillations is given by $x^*=2\pi/q_*$. For this plot we have chosen the same potential U_q as in Fig. 2 and $\delta v=0.5\alpha$.

VI. COHERENT EMISSION OF PLASMON WAVES

In order to investigate the influence of the electron-plasmon scattering mechanism onto the fermionic background, we analyze the fermionic density of the bath

$$\varrho(x,t) = \mathcal{N} \langle \psi_0 | \hat{\psi}_e(0) \hat{\rho}_B(x,t) \hat{\psi}_e^\dagger(0) | \psi_0 \rangle \quad (8)$$

in the presence of the high-energy electron. Here, $|\psi_0\rangle$ is the ground state of the Hamiltonian in Eq. (6) without the high-energy fermion and $\mathcal{N}=\langle \psi_0 | \hat{\psi}_e(0) \hat{\psi}_e^\dagger(0) | \psi_0 \rangle^{-1}$ a normalization constant. In the parameter regime $v_\varepsilon < \tilde{v}$ where electron-plasmon scattering takes place one observes the coherent emission of plasmon waves with wave vector q_* of the resonant plasmonic mode [see Fig. 3]. In the limit $t \rightarrow \infty$ and for distances $|x - v_\varepsilon t| \gg q_*^{-1}$ sufficiently far away from the position of the high-energy electron, we obtain the following analytic result:

$$\varrho(x,t) \rightarrow \Theta(v_\varepsilon t - x) \sin[q_*(x - v_\varepsilon t)] U_{q_*}/U'_{q_*}. \quad (9)$$

As can be seen in Fig. 3, the coherent density excitations buildup within a “light cone” $x \in [v_F t, \tilde{v} t]$ (Ref. 19) set by minimal and maximal plasmonic phase velocities. The wavelength of the oscillations in the density $\varrho(x,t)$ is tunable by the choice of an appropriate injection energy ε of the high-energy fermion.

For velocities $v_\varepsilon > \tilde{v}$, no scattering between electrons and plasmons is possible. In this case, the density $\varrho(x,t)$ can be separated into two contributions. The first one describes the initial excitation of plasmonic modes right after the injection of the high-energy fermion. This transient perturbation cannot follow the electron that is faster than any plasmonic mode. The second contribution traveling together with the high-energy electron is responsible for the screening of the injected charge and is reminiscent of viewing the GF as an impurity problem. Integrating over space then provides us with the screening charge Δn , the charge displaced by the introduction of the local scatterer. As mentioned before, it is directly related to the exponent $\gamma_e = \Delta n^2$ of the GF.

VII. CONCLUSIONS

We have discussed electron-plasmon scattering in systems of 1D chiral electrons. This scattering leads to an exponential decay of the single-particle Green’s function even at zero temperature and to a coherent monochromatic pattern in the fermionic density in the wake of the electron. This effect is absent in the low-energy limit and relies exclusively on the interplay between a finite interaction range and a nonlinear fermionic dispersion.

ACKNOWLEDGMENTS

We thank L. Glazman for fruitful discussions. Financial support by NIM, CeNS, the Emmy-Noether program, and the SFB/TR 12 is gratefully acknowledged.

-
- ¹M. Khodas, M. Pustilnik, A. Kamenev, and L. I. Glazman, *Phys. Rev. B* **76**, 155402 (2007).
- ²G. Feve, A. Mahe, J.-M. Berroir, T. Kontos, B. Placais, D. C. Glattli, A. Cavanna, B. Etienne, and Y. Jin, *Science* **316**, 1169 (2007).
- ³C. Altimiras, H. le Sueur, U. Gennser, A. Cavanna, A. Mailly, and F. Pierre, *Nat. Phys.* **6**, 34 (2010).
- ⁴Y. Ji, Y. Chung, D. Sprinzak, M. Heiblum, D. Mahalu, and H. Shtrikman, *Nature (London)* **422**, 415 (2003).
- ⁵I. Neder, M. Heiblum, Y. Levinson, D. Mahalu, and V. Umansky, *Phys. Rev. Lett.* **96**, 016804 (2006).
- ⁶L. V. Litvin, H.-P. Tranitz, W. Wegscheider, and C. Strunk, *Phys. Rev. B* **75**, 033315 (2007).
- ⁷P. Roulleau, F. Portier, D. C. Glattli, P. Roche, A. Cavanna, G. Faini, U. Gennser, and D. Mailly, *Phys. Rev. B* **76**, 161309(R) (2007).
- ⁸L. V. Litvin, A. Helzel, H.-P. Tranitz, W. Wegscheider, and C. Strunk, *Phys. Rev. B* **78**, 075303 (2008).
- ⁹C. Neuenhahn and F. Marquardt, *Phys. Rev. Lett.* **102**, 046806 (2009).
- ¹⁰A. V. Rozhkov, *Eur. Phys. J. B* **47**, 193 (2005).
- ¹¹M. Pustilnik, M. Khodas, A. Kamenev, and L. I. Glazman, *Phys. Rev. Lett.* **96**, 196405 (2006).
- ¹²A. Imambekov and L. I. Glazman, *Science* **323**, 228 (2009).
- ¹³A. Imambekov and L. I. Glazman, *Phys. Rev. Lett.* **102**, 126405 (2009).
- ¹⁴R. G. Pereira, S. R. White, and I. Affleck, *Phys. Rev. B* **79**, 165113 (2009).
- ¹⁵P. W. Anderson, *Phys. Rev. Lett.* **18**, 1049 (1967).
- ¹⁶K. Le Hur, *Phys. Rev. Lett.* **95**, 076801 (2005).
- ¹⁷P. Nozières and C. T. De Dominicis, *Phys. Rev.* **178**, 1097 (1969).
- ¹⁸K. Schönhammer and V. Meden, *Phys. Rev. B* **47**, 16205 (1993).
- ¹⁹P. Calabrese and J. Cardy, *Phys. Rev. Lett.* **96**, 136801 (2006).

2.3 Publication: Real-time energy dynamics in spin-1/2 Heisenberg chains

In case of the high-energy fermion injected into a Luttinger liquid as discussed before in Sec. 2.2 one observes ballistic behavior. The mobile impurity propagates through space at a fixed velocity without dispersing. The question whether propagation happens ballistically or diffusively is deeply related to the transport properties of the system of interest. One prototypical system with rich transport properties is the one-dimensional XXZ -chain. The XXZ -model

$$H_{XXZ} = J \sum_{l=1}^L [S_l^x S_{l+1}^x + S_l^y S_{l+1}^y + \Delta S_l^z S_{l+1}^z] \quad (2.9)$$

describes the properties of anisotropically coupled spins on a lattice with L sites. Here, S_l^μ , $\mu = x, y, z$, denotes the components of spin-1/2 operators acting on a site l . The degree of anisotropy in z -direction is encoded in the parameter Δ . The antiferromagnetic exchange coupling $J > 0$ sets the overall energy scale. The one-dimensional XXZ -chain shows a quantum phase transition from a gapless metallic ($\Delta < 1$) to a gapped insulating phase ($\Delta > 1$) at the isotropic Heisenberg point $\Delta = 1$.

Although H_{XXZ} is in principle exactly solvable by Bethe ansatz and therefore integrable for all values of Δ dynamical properties are typically difficult to access from this method. Below, the real-time properties of the XXZ -chain will be investigated on the basis of bosonization in the small Δ limit and on the basis of the time-dependent density matrix renormalization group (tDMRG) approach for the general case.

Via the Jordan-Wigner transformation the XXZ -chain can be mapped onto a system of interacting spinless fermions

$$H_{XXZ} = \frac{J}{2} \sum_{l=1}^L [c_l^\dagger c_{l+1} + c_{l+1}^\dagger c_l] + \Delta J \sum [c_{l+1}^\dagger c_{l+1} - \frac{1}{2}] [c_l^\dagger c_l - \frac{1}{2}] \quad (2.10)$$

where the strength of the interaction is set by the anisotropy parameter Δ . Note that for this mapping periodic boundary conditions have been imposed and the Hilbert space has been restricted to the subspace of even parity where $\mathcal{N} = \sum_{l=1}^L c_l^\dagger c_l$ can be replaced by an even number. Concerning the properties of this model sufficiently far away from the boundaries the precise choice of boundary conditions has no impact. The fermionic operators c_l obeying the anticommutation relation $\{c_l, c_{l'}^\dagger\} = \delta_{ll'}$ are related to the spin-1/2 operators via $c_l^\dagger = e^{-i\phi_l} S_l^+$ with $\phi_l = \pi \sum_{m=1}^{l-1} [S_m^z + 1/2]$ the phase counting operator. Here the spin ladder operators $S_l^\pm = S_l^x \pm iS_l^y$ are defined as usual. For weak interactions $\Delta \ll 1$ the main low-energy and low-momentum properties are captured by a Luttinger liquid theory which can be solved analytically via bosonization [58].

Below, the character of energy transport in the XXZ -model is studied beyond linear response. Specifically, two different nonequilibrium scenarios are investigated. First, the system is initially prepared in a state with localized energy excitations while simultaneously leaving the spin background constant. This is achieved by choosing the initial state as the

ground state of a XXZ -chain with a local variation of the exchange coupling J which yields for the local energy density of H_{XXZ} a localized energy perturbation without creating excitations in the local magnetization. The dynamics is characterized by analyzing the mean square displacement of the energy density profile during time evolution with the Hamiltonian in Eq. 2.9 as has been done for the spin case recently [103]. Remarkably, it is found that perturbations in the local energy always propagate ballistically irrespective of the presence of a gap on time scales accessible via tDMRG. The special isotropic point $\Delta = 1$ exhibits an additional $SU(2)$ symmetry. This can be used to drive the numerical simulations to substantially longer times without any qualitative or quantitative change in the results. The result of ballistic energy transport in the gapless phase $\Delta < 1$ agrees with the predictions of the universal low-energy Luttinger liquid theory. This is evidently true also for the noninteracting point $\Delta = 0$ as will be demonstrated below.

This differs from the case of spin transport that shows ballistic behavior in the gapless phase but on the other hand diffusive behavior in the gapped phase. For an initial configuration with localized spin excitations the energy density also exhibits a local perturbation. In this case spin as well as energy currents will flow due to time evolution. Even though the magnetization propagates diffusively in the gapped phase on the accessible time scales the energy does not and shows still ballistic behavior as for the previous case. The ballistic transport of spin in the gapless phase $\Delta < 1$ is again in precise agreement with the result of the low-energy Luttinger liquid theory.

Real-time energy dynamics in spin- $\frac{1}{2}$ Heisenberg chains

Stephan Langer,^{1,*} Markus Heyl,¹ Ian P. McCulloch,² and Fabian Heidrich-Meisner¹

¹*Department of Physics and Arnold Sommerfeld Center for Theoretical Physics, Ludwig-Maximilians-Universität München, DE-80333 München, Germany*

²*School of Physical Sciences, The University of Queensland, Brisbane, QLD 4072, Australia*

(Received 20 July 2011; revised manuscript received 23 September 2011; published 14 November 2011)

We study the real-time dynamics of the local energy density in the spin-1/2 XXZ chain starting from initial states with an inhomogeneous profile of bond energies. Numerical simulations of the dynamics of the initial states are carried out using the adaptive time-dependent density matrix renormalization group method. We analyze the time dependence of the spatial variance associated with the local energy density to classify the dynamics as either ballistic or diffusive. Our results are consistent with ballistic behavior both in the massless and the massive phase. We also study the same problem within Luttinger liquid theory and obtain that energy wave packets propagate with the sound velocity. We recover this behavior in our numerical simulations in the limit of very weakly perturbed initial states.

DOI: [10.1103/PhysRevB.84.205115](https://doi.org/10.1103/PhysRevB.84.205115)

PACS number(s): 75.10.Jm, 74.25.F-, 75.40.Mg

I. INTRODUCTION

The understanding of transport properties of low-dimensional systems with strong correlations still poses viable challenges to theorists. These include, on the one hand, the fundamental problem of calculating transport coefficients for generic models such as the Heisenberg chain,^{1,2} and on the other hand, the theoretical modeling of experiments that typically require the treatment of spin or electronic degrees of freedom coupled to phonons, in particular, in the case of the thermal conductivity.^{3,4} Most theoretical work is focused on the linear-response regime, in which the properties of current-current autocorrelation functions determine transport properties (see Refs. 1 and 2 for a review).

More recently, the out-of-equilibrium properties of one-dimensional systems have evolved into an active field of research, one reason being recent advances in experiments with ultracold atoms.⁵ These have paved the way for studying the dynamics of quantum many-body systems that are driven far away from equilibrium in a controlled manner, with little or no coupling to external degrees of freedom. Much attention has been paid to the question of thermalization, typically studied in so-called quantum quenches (see Ref. 6 and references therein). While global quantum quenches in homogeneous systems usually do not induce any finite net currents (of either spin, energy, or particles), we will be particularly interested in setups that feature finite net currents. Such situations are realized in, for instance, the sudden expansion of particles in optical lattices after the removal of trapping potentials.⁷ Further examples are spin and/or particle currents induced by connecting two regions with opposite magnetizations or by letting two particle clouds collide (see, for instance, Refs. 8–11).

Theoretical work in this context ranges from the expansion dynamics of bosons and fermions in optical lattices^{12–18} over the dynamics of wave packets in spin chains,^{19–28} to the demonstration of signatures of spin-charge separation in such setups.^{29,30} In the aforementioned examples, nonequilibrium situations were studied with either finite spin or particle currents. In our work, we address the energy dynamics for a

model that is prototypical for systems with strong correlations, namely, the spin-1/2 XXZ chain:

$$H_{XXZ} = \sum_{i=1}^{L-1} h_i \\ := J \sum_{i=1}^{L-1} \left[\frac{1}{2} (S_i^+ S_{i+1}^- + H.c.) + \Delta S_i^z S_{i+1}^z \right], \quad (1)$$

where S_i^μ and $\mu = x, y, z$ are the components of a spin-1/2 operator acting on site i and S_i^\pm are the corresponding lowering/raising operators. The global energy scale is set by the exchange coupling J , Δ is the exchange anisotropy in the z direction, and L denotes the number of sites. Equation (1) describes either interacting quantum spins or, via the Jordan-Wigner transformation,³¹ spinless fermions.

Specifically, we follow the time evolution of the local energy density $\langle h_i \rangle$ starting from initial states that are far away from the ground state of Eq. (1) and that feature an inhomogeneous profile in the local energy density (see Fig. 1 for a sketch). We emphasize that, in the main part of our work, we choose the initial conditions such that only finite energy currents exist, whereas the spin (particle) density is constant during the time evolution, hence all spin (particle) currents vanish. Obviously, an initial state with an inhomogeneous spin density profile leads to both finite spin and energy currents, and we revisit this case, previously studied in Refs. 20 and 28.

Our work is motivated by and closely related to a specific experiment on a spin-ladder material. Many low-dimensional quantum magnets are known to be very good thermal conductors with heat predominantly carried by magnetic excitations at elevated temperatures.^{32,33} Examples for materials that exhibit particularly large thermal conductivities are $(\text{Sr},\text{La},\text{Ca})_{14}\text{Cu}_{24}\text{O}_{41}$ (Refs. 34 and 35) and SrCuO_2 (Ref. 36). While these experiments are carried out under steady-state conditions and in the regime of small external perturbations, more recently, time-resolved measurements have been performed on $\text{La}_9\text{Ca}_5\text{Cu}_{24}\text{O}_{41}$ (Ref. 37). For this spin ladder material, two approaches have been implemented:

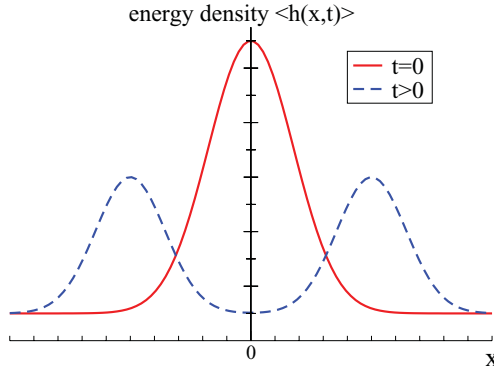


FIG. 1. (Color online) Sketch of our setup: we prepare initial states with an inhomogeneous distribution of local energies and then study the time evolution of the local energy density.

a time-of-flight measurement in which one side of the sample is heated up with a laser pulse and the time-dependent response is recorded on the other side. Second, a nonequilibrium local heat distribution was generated in the surface of the material by shining laser light on it. It is possible to record the heat dynamics via thermal imaging that uses the response of an excited thin fluorescent layer placed on top of the spin ladder material.

It is the latter case that we mimic in our work: the time evolution of local energy densities induced by inhomogeneous initial distributions. We utilize the time-dependent density matrix renormalization group (tDMRG)^{38–42} technique. It allows us to simulate the dynamics of pure states whereas in the experiment, temperature likely plays a role. Our work thus addresses qualitative aspects in the first place, while a direct comparison with experimental results is beyond the scope of this study. The goal is to demonstrate that in a spin-1/2 chain described by Eq. (1), the energy dynamics is ballistic, irrespective of how far from equilibrium the system is and also irrespective of the presence or absence of excitation gaps. To this end, we use the same approach as in Ref. 20. We classify the dynamics based on the behavior of the spatial variance $\sigma_E^2(t)$ of the local energy density. The ballistic case is $\sigma_E^2(t) \sim t^2$, whereas diffusion implies $\sigma_E^2 \sim t$. Our main result for the XXZ chain, based on numerical tDMRG simulations, is that energy propagates ballistically at sufficiently long times, independently of model parameters (such as Δ). One can then interpret the prefactor V_E in $\sigma_E^2(t) = V_E^2 t^2$ as a measure of the average velocity of excitations contributing to the expansion. The velocity V_E can be calculated analytically and exactly in noninteracting models, which (in the absence of impurities or disorder) typically have ballistic dynamics, and we consider two examples: (i) the noninteracting limit of the XXZ Hamiltonian ($\Delta = 0$), i.e., spinless fermions and (ii) the Luttinger liquid, which is the universal low-energy theory in the continuum limit of Eq. (1) for $|\Delta| < 1$. We show that our tDMRG results agree with the exactly known expansion velocity V_E in these two examples.

Our main result, namely, the numerical observation of $\sigma_E^2(t) \sim t^2$ independently of initial conditions or model parameters such as the exchange anisotropy Δ , is consistent with

the qualitative picture derived from linear-response theory. Within that theory, transport properties of the XXZ chain have intensely been studied in recent years, both the energy^{43–47} and the spin transport.^{1,2,47–62} Ballistic dynamics is associated with the existence of nonzero Drude weights. Since the total energy current of the anisotropic spin-1/2 chain is a conserved quantity for all Δ , the thermal conductivity $\kappa(\omega)$ diverges in the zero-frequency limit and is given by $\text{Re } \kappa(\omega) = D_E \delta(\omega)$, where D_E is the thermal Drude weight.^{43–46} This behavior is different from the spin conductivity $\sigma(\omega)$. This quantity takes the form $\text{Re } \sigma(\omega) = D_s \delta(\omega)$ only at the noninteracting point $\Delta = 0$, whereas for $0 < \Delta \leq 1$, many numerical studies^{1,2,60,61} indicate $D_s(T > 0) > 0$, with a finite weight at finite frequencies, though. Therefore, for $0 < \Delta \leq 1$, $\text{Re } \sigma(\omega) = D_s \delta(\omega) + \sigma_{\text{reg}}(\omega)$. Recent field-theoretical and numerical work suggests that the regular part $\sigma_{\text{reg}}(\omega)$ of $\sigma(\omega)$ in massless phases is consistent with diffusive behavior.^{54,56,62} A finite value of the current-current correlation function in the long time limit is associated with a finite Drude weight. Finite Drude weights can be traced back to the existence of conservation laws,^{43,60} and, in consequence, a potential relation between integrability⁶³ and ballistic behavior—in the sense of nonzero Drude weights—has been intensely discussed (see, e.g., Refs. 1, 2, 47, 60–62 and further references cited therein). Very recently, Prosen has presented results that provide a lower bound to the spin Drude weight that is non zero for $\Delta < 1$.⁶⁰ This is in qualitative agreement with earlier exact diagonalization studies.^{2,47,48} The particular point $\Delta = 1$ is still discussed controversially;^{47,49,52,54,59–61} first, no finite lower bound to the Drude weight is known,⁶⁰ and second, the qualitative results of exact diagonalization studies seem to depend on details of the extrapolation of finite-size data to the thermodynamic limit and the statistical ensemble that is considered.^{47,48,59}

Our approach that analyzes the time dependence of spatial variances, albeit restricted to the analysis of densities, is numerically easily tractable and is an alternative to the numerically cumbersome evaluation of current correlation functions. tDMRG has, for instance, been applied to evaluate current-current autocorrelation functions in the thermodynamic limit.⁵⁴ However, the accessible time scales are quite limited ($t \sim 10/J$), making an unambiguous interpretation of the results difficult and the approach is not applicable to nonequilibrium. Our approach allows us, at least in principle, to study the entire regime of weakly perturbed states to maximally excited ones. An earlier analysis of spin-density wave packets in various spin models has yielded the following picture (all based on the time-dependence of the spatial variance);²⁰ in massless phases, ballistic dynamics is seen, whereas in massive ones, examples of diffusive dynamics have been identified. It is important to stress that the observation of a variance that increases linear in time is a necessary condition for the validity of the diffusion equation.

Finally, to complete the survey of related literature, recent studies have addressed steady-state spin and energy transport in open systems coupled to baths with no restriction to the linear-response regime.^{28,61,64–66} These studies suggest spin transport to be ballistic in the gapless phase of the XXZ spin chain and to be diffusive in the gapped phase with a negative differential conductance at large driving strengths. The heat

current has been addressed in Ref. 64 where Fourier's law has been validated for the Ising model in a tilted field.

A byproduct of any tDMRG simulation is information on the time-evolution of the entanglement entropy. While this is not directly related to this article's chief case, it nevertheless provides valuable information on the numerical costs of tDMRG simulations. Qualitatively speaking (see the discussion in Ref. 42 and references therein), the faster the entanglement growth is the shorter are the time scales that can be reached with tDMRG. We here show that the quenches studied in this work generate a mild logarithmic increase of entanglement, which is why this problem is very well suited for tDMRG. Such a behavior is typical for so-called local quenches.⁶⁷ This result might be useful for tDMRG practitioners.

This paper is organized as follows. First, we introduce the model and the quantities used in our analysis in Sec. II. Section III A reviews the framework of bosonization, which is applied in Sec. III B to give an analytical derivation of ballistic spin and energy dynamics in the low-energy case, valid in the massless phase of Eq. (1). Sections IV and V contain our numerical results. First, we study the energy dynamics in the absence of spin currents in Sec. IV. To this end, we generate an initial state consisting of a variable number of ferromagnetic bonds in the center of an antiferromagnetic chain. We calculate the time evolution of these states under Eq. (1) finding ballistic energy dynamics independent of the phase and the strength of the perturbation. To supplement these findings we derive an observable, which depends on the local currents, and whose expectation value is time-independent whenever $\sigma_E^2(t) \sim t^2$. The numerical calculation of this quantity indicates ballistic dynamics as well. Section V revisits the scenario of Ref. 20 where local spin and energy currents are present during the dynamics as we start from states with an inhomogeneous spin density. In that case, the energy density shows ballistic dynamics in the massless phase with a velocity matching the bosonization result in the limit of small perturbations. In the massive phase, we observe a different behavior of the two transport channels, i.e., ballistic energy dynamics while the spin dynamics looks diffusive.²⁰ Finally, we summarize our findings in Sec. VI. Additionally, we discuss the entanglement growth induced by coupling two regions with an opposite sign of the exchange coupling in the Appendix.

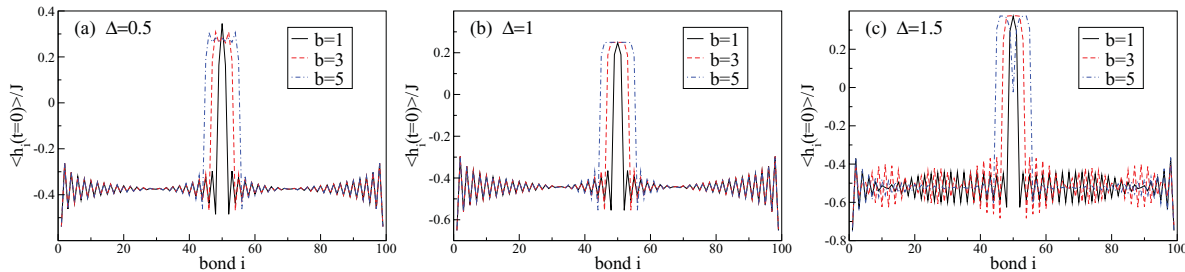


FIG. 2. (Color online) Profile of the local energy density $\langle h_i \rangle$ in the initial states induced by a J_i quench for $b = 1, 3, 5$ [compare Eq. (30)] for (a) $\Delta = 0.5$, (b) $\Delta = 1$, and (c) $\Delta = 1.5$. In all cases, the system forms a region with ferromagnetic nearest-neighbor spin correlations in the middle of the chain. In the regions with antiferromagnetic $J_i > 0$, the local energy density oscillates, reflecting the antiferromagnetic nearest-neighbor correlations.

II. SETUP AND DEFINITIONS

A. Preparation of initial states and definition of spatial variance

In this work, we focus on spin-1/2 XXZ chains of a finite length L given by Eq. (1) where our goal is to study the dynamics of an inhomogeneous distribution of the local energy density originating from a local quench of system parameters. The inhomogeneous distributions are generated by preparing the system in the respective ground states of the following Hamiltonians that are perturbations of H_{XXZ} from Eq. (1). First,

$$H_{\text{init}}^J = \sum_{i=1}^{L-1} \frac{J_i}{J} h_i, \quad (2)$$

where h_i is defined in Eq. (1), and second,

$$H_{\text{init}}^B = H_{XXZ} - \sum_i B_i S_i^z, \quad (3)$$

where

$$B_i = B_0 e^{-\frac{(i-L/2)^2}{2\sigma_0^2}}. \quad (4)$$

In the first case, we quench site-dependent exchange couplings. In this scenario, we obtain initial states with large local energy densities. Typical initial states that are ground states of Eq. (2) are shown in Fig. 2. These states have b bonds with ferromagnetic $J_i < 0$ in the center while the rest has antiferromagnetic $J_i > 0$. We refer to this setup as the J_i quench.

In the second case, the dynamics is driven by an inhomogeneous spin density, enforced by an external magnetic field applied in the initial state. This allows us to generate smooth spatial perturbations of $\langle h_i \rangle$ with small differences in energy compared to the ground state of Eq. (1). We refer to this setup as the B_0 quench. A more detailed discussion of the initial states generated by a J_i quench will be given in Sec. IV A. The B_0 quench was introduced in detail in Ref. 20.

The definition of the local energy density from the Hamiltonian Eq. (1) is not unambiguous. For instance, it is always possible to add local terms to the Hamiltonian whose total contribution by summation over all lattice sites vanishes. However, this seeming ambiguity can be resolved up to constants by requiring that any block of adjacent lattice sites $\sum_{i=l}^m h_i$ is Hermitian and yet to have the same structure as the

total Hamiltonian H . These details seem to be rather specific, yet for the definition of the appropriate local energy density within the Luttinger liquid description, see below, these formal considerations are important. For the XXZ chain the local energy density is therefore determined by the bond energies $\langle h_i \rangle$.

To classify the dynamics of a density e_i we study its spatial variance

$$\sigma_E^2(t) = \sum_{i=1}^{L-1} (i - \mu)^2 e_i(t), \quad (5)$$

where μ is the first moment of e_i . The e_i are the normalized distribution linked to the energy density via

$$e_i = \delta E^{-1} \langle \tilde{h}_i \rangle \quad (6)$$

where $\langle \tilde{h}_i \rangle = \langle h_i \rangle - \langle h_i \rangle_0$ denotes the expectation value of h_i in the initial state shifted by the ground state expectation value $\langle h_i \rangle_0 = \langle \psi_0 | h_i | \psi_0 \rangle$.

$$\delta E := E_{\text{init}} - E_0 = \sum_i \langle \tilde{h}_i \rangle \quad (7)$$

is the energy difference between the initial state $|\psi_{\text{init}}\rangle$ [i.e., the ground state of either H_{init}^J or H_{init}^B] and the ground state $|\psi_0\rangle$ of Eq. (1), both energies measured with respect to the unperturbed Hamiltonian from Eq. (1):

$$E_0 = \langle \psi_0 | H_{XXZ} | \psi_0 \rangle, \quad E_{\text{init}} = \langle \psi_{\text{init}} | H_{XXZ} | \psi_{\text{init}} \rangle. \quad (8)$$

On physical grounds, the energy density should be normalized by the amount of energy transported by the propagating perturbation. This is well approximated by the energy difference δE between the initial state and the ground state of Eq. (1), as we have verified in many examples. In some cases, though, the propagating energy is, on a quantitative level, better described by estimating the area under the perturbations, as δE may also contain contributions from static deviations from the ground state bond energies in the background. Nevertheless, δE does not depend on the overall zero of energy and is an obvious measure of how far the system is driven away from the ground state. This, all together, justifies our definition of the e_i .

To remove static contributions depending only on the initial distribution $e_i(t=0)$, we subtract $\sigma_E^2(t=0)$ and study $\delta\sigma_E^2(t) := \sigma_E^2(t) - \sigma_E^2(0)$. $\delta\sigma_E^2(t) \sim (V_E t)^2$ is expected to grow quadratically in time in the case of ballistic behavior, where V_E has the dimensions of a velocity. For diffusive behavior, we expect, from the fundamental solution of the diffusion equation,⁶⁹ that $\delta\sigma_E^2(t) \sim Dt$ grows linearly in time, where D is the diffusion constant (see, e.g., the discussion in Ref. 20). Within linear response theory the diffusion constant can be related to transport coefficients via Einstein relations, see, e.g., Ref. 70. To be clear, the observation of $\delta\sigma_E^2 \sim t^2$ or $\delta\sigma_E^2 \sim t$ is a necessary condition for the respective type of dynamics and time-dependent crossovers are possible.

B. Spatial variance in the noninteracting case

For pedagogical reasons and to guide the ensuing discussion, we next calculate the spatial variance in the noninteracting limit of Eq. (1), i.e., at $\Delta = 0$. Using the

Jordan-Wigner transformation, we can write the Hamiltonian as

$$H = \frac{J}{2} \sum_i (S_i^+ S_{i+1}^- + \text{H.c.}) = -\frac{J}{2} \sum_i (c_i^\dagger c_{i+1} + \text{H.c.}), \quad (9)$$

where c_i^\dagger creates a spinless fermion on site i . A subsequent Fourier transformation diagonalizes the Hamiltonian:

$$H = \sum_k \epsilon_k c_k^\dagger c_k. \quad (10)$$

Since we will compare with numerical results on systems with open boundary conditions, we obtain

$$\epsilon_k = -J \cos(k), \quad k = \frac{\pi n}{L+1}, \quad n = 1, \dots, L. \quad (11)$$

Next, we compute

$$\delta\sigma_E^2(t) = \sum_i e_i(t)(i - i_0)^2 - \sum_i e_i(t=0)(i - i_0)^2$$

with e_i from Eq. (6) and $h_i = -J(c_i^\dagger c_{i+1} + \text{H.c.})/2$. By expressing $c_i^{(\dagger)}$ through their Fourier transform and by plugging in the time evolution of $c_k^{(\dagger)}$, we finally obtain, after straightforward calculations:

$$\delta\sigma_E^2(t) = V_E^2 t^2, \quad (12)$$

i.e., ballistic dynamics independently of the initial state. Terms linear in t will be absent if in the initial state, the density is symmetric with respect to its first moment, i.e., $e_{\mu+\delta} = e_{\mu-\delta}$ and if the wave packet has no finite center-of-mass momentum at $t = 0$ already. In the remainder of the paper, we will work under these two additional assumptions that are valid for all initial states considered in our work. The prefactor V_E^2 is given by

$$V_E^2 = \frac{1}{\delta E} \sum_k \epsilon_k v_k^2 \delta n_k, \quad (13)$$

where $v_k = \partial \epsilon_k / \partial k$ and

$$\delta n_k = n_k^{\text{init}} - n_k$$

is the difference between the momentum distribution function (MDF) in the initial state and the one in the ground state of Eq. (1). Since we use open boundary conditions, we compute n_k from

$$n_k = \langle c_k^\dagger c_k \rangle := \frac{2}{L+1} \sum_{r,r'} \sin(kr) \sin(kr') \langle c_r^\dagger c_{r'} \rangle. \quad (14)$$

We can also express δE via δn_k :

$$\delta E = \sum_k \epsilon_k \delta n_k.$$

The expression (13) suggests that V_E is the average velocity of excitations contributing to the propagation of the wave packet. Characteristic for ballistic dynamics, V_E^2 is fully determined by the initial conditions through δn_k .

For completeness, we mention that an analogous calculation can be done for the spatial variance σ_S of the spin density. This quantity is defined as

$$\sigma_S^2(t) := \frac{1}{\mathcal{N}} \sum_{i=1}^L (i - \mu)^2 \langle S_i^z(t) + 1/2 \rangle. \quad (15)$$

The normalization constant \mathcal{N} measures the number of propagating particles. The spin density is, in terms of spinless fermions,

$$S_i^z = c_i^\dagger c_i - 1/2 = n_i - 1/2.$$

The result for the spatial variance of the spin density is

$$\delta\sigma_S^2(t) = \sigma_S^2(t) - \sigma_S^2(0) = V_S^2 t^2 \quad (16)$$

with

$$V_S^2 = \frac{1}{\mathcal{N}} \sum_k v_k^2 \delta n_k. \quad (17)$$

Although we started from the Hamiltonian for $\Delta = 0$, we stress that Eqs. (12), (16), (13), and (17) are valid for any dispersion relation ϵ_k , irrespective of the presence of a gap, provided that k has the meaning of a momentum.

C. Energy current

Another aspect worth noting is that the time-evolving state carries a nonzero energy current, a situation that usually does not appear in the case of a global quench. From the equation of continuity for the energy density, one can derive the well-known expression for the local energy current operator,⁴³

$$j_i^E = J^2 \tilde{\vec{S}}_{i-1} \cdot (\tilde{\vec{S}}_i \times \tilde{\vec{S}}_{i+1}), \quad (18)$$

where $\tilde{\vec{S}} = (S^x, S^y, \Delta S^z)$. With periodic boundary conditions, the total current $J_E = \sum_i j_i^E$ is a conserved quantity, i.e., $[H, J_E] = 0$ (see Ref. 43). On a system with open boundary conditions such as the ones that are well suited for DMRG, this property is lost, yet the dynamical conductivity still has a quasi-Drude peak at very low frequencies, reminiscent of the true Drude peak $\text{Re}\chi(\omega) = D_E \delta(\omega)$ of a system with periodic boundary conditions.⁶⁸ The latter form is recovered on a system with open boundary conditions as $L \rightarrow \infty$ (see Ref. 68), showing that ballistic dynamics due to the existence of globally conserved currents can still be probed on systems with open boundary conditions.

To connect the local energy currents to the spatial variance of the time-dependent density one can rewrite the time derivative of $\sigma_E^2(t)$ using the equation of continuity, assuming no current flow to sites at the boundary (this assumption is justified in our examples as long as we restrict ourselves to times before reflections occur at the boundary in our simulations):

$$\begin{aligned} \partial_t \sigma_E^2(t) &\sim \sum_{r=1}^L (r - \mu)^2 \partial_t \langle h_r(t) \rangle \\ &= -\langle j_1^E \rangle + \sum_{r=1}^L (2r - 2\mu + 1) \langle j_r^E(t) \rangle. \end{aligned} \quad (19)$$

If $\sigma_E^2(t) = V_E^2 t + b$ and $\mu \neq \mu(t)$, then using $\langle J_E \rangle = 0$ leads to

$$\sum_{r=1}^L r \partial_t \langle j_r^E(t) \rangle \sim \frac{1}{2} \partial_t^2 \sigma_E^2(t) = V_E^2 = \text{const.} \quad (20)$$

If we interpret this equation as an operator equation, then we see that we can define a quantity J_E^* via

$$J_E^* = \sum_{r=1}^L r \partial_t j_r^E. \quad (21)$$

If for a given initial state and over a certain time window, $\langle J_E^*(t) \rangle = \text{const}$, then we have identified a regime with ballistic dynamics, $\delta\sigma_E^2(t) \sim t^2$. If $\langle J_E^*(t) \rangle = \text{const}$ holds for all times and initial states, then J_E^* is a conserved quantity, $[H, J_E^*] = 0$. This is the case at $\Delta = 0$, the noninteracting limit of Eq. (1), where $\langle J_E^* \rangle = V_E^2 \delta E$ from Eq. (13).

We emphasize that we have here identified an operator that connects the phenomenological observation of a quadratic increase of $\sigma_E^2(t)$ to the local energy currents. In ballistic regimes, its expectation value becomes stationary.

For completeness, we mention an analogous result in the diffusive regime where $\sigma_E^2 \sim t$. Then, expectation values of the operator

$$J_E^D = \sum_{r=1}^L (r - \mu) j_r^E(t) \quad (22)$$

are time independent. Obviously, similar expressions can be written down for the spatial variance associated with the spin density.

III. PROPAGATING ENERGY AND SPIN WAVE PACKETS IN A LUTTINGER LIQUID

In the gapless phase, i.e., for $|\Delta| < 1$, the low-energy and low-momentum properties of the XXZ chain can be described by an effective Luttinger liquid theory.⁷¹ In the following, we want to analyze the energy density and the spin dynamics of the XXZ chain in this exactly solvable hydrodynamic limit. Specifically, we show that at least asymptotically for large times, the spatial variance always grows quadratically both in the case of spin and energy dynamics. In addition, we work out the precise dependence of the prefactor in front of the t^2 increase of the spatial variance on system parameters. Since our DMRG results to be presented in Secs. IV and V show that $\sigma_E^2(t) \sim t^2$ at any Δ , we did not investigate the influence of marginally relevant perturbations at $\Delta = 1$ on the wave-packet dynamics. In passing, we mention that in the massive phase, where the appropriate low-energy theory is the sine-Gordon model, the expansion velocity could also be derived at the Luther-Emery point (this case was studied in, e.g., Refs. 25 and 26).

A. Bosonization of the anisotropic spin-1/2 chain

The Hamiltonian (1) can be mapped onto a system of interacting spinless fermions via the Jordan-Wigner transformation.³¹ Within a hydrodynamic description in terms

of a linearized fermionic dispersion relation, the Hamiltonian can be represented in terms of a Luttinger liquid theory (LL),

$$H_{LL} = \frac{u}{4} \int \frac{dx}{2\pi} \left[K(\rho_L - \rho_R)^2 + \frac{1}{K}(\rho_L + \rho_R)^2 \right], \quad (23)$$

using the notation of Ref. 72. The sum of the two left- and right-moving densities $\rho_L(x) + \rho_R(x)$ of the spinless Jordan-Wigner fermions is proportional to the continuum approximation of the local magnetization S_i^z up to a constant. The sound velocity u can be related to the parameters of the XXZ chain in Eq. (1) via the group velocity⁷³

$$u = v_g = J \frac{\pi \sin(v)}{2v}, \quad (24)$$

with $\cos v = \Delta$. Similarly, the Luttinger parameter K is given by the relation $K = \pi/[2(1 - v)]$. In the noninteracting case, $\Delta = 0$, we have $K = 1$ and $u = J$.

B. Ballistic dynamics in the gapless phase

Within the Luttinger liquid description for $\Delta < 1$, an initially inhomogeneous local energy density profile always propagates ballistically independently of the details of the perturbation as can be seen from general arguments. For the effective low-energy Hamiltonian, the probability distribution $e(x,t)$ associated with the local energy density is given by

$$e(x,t) = \mathcal{E}^{-1} \langle \psi_{\text{init}} | \hat{h}(x,t) | \psi_{\text{init}} \rangle, \quad (25)$$

where $|\psi_{\text{init}}\rangle$ is the initial state,

$$\begin{aligned} \hat{h}(x) = u(K + K^{-1})/(8\pi) &\sum_{\eta} \partial_x \varphi_{\eta}^{\dagger}(x) \partial_x \varphi_{\eta}(x) \\ &- u(K - K^{-1})/(8\pi) [\partial_x \varphi_L^{\dagger}(x) \partial_x \varphi_R^{\dagger}(x) \\ &+ \partial_x \varphi_R(x) \partial_x \varphi_L(x)] \end{aligned} \quad (26)$$

and

$$\mathcal{E} = \int dx \langle \psi_{\text{init}} | \hat{h}(x,t=0) | \psi_{\text{init}} \rangle. \quad (27)$$

For the exact definition of the fields $\varphi_{\eta}^{(\dagger)}$, see, e.g., Ref. 72. The local energy density operator consists of decoupled left- and right-moving contributions in the basis in which the Hamiltonian for the time evolution is diagonal. This allows for a separation of $e(x,t)$ into left- and right-moving contributions, which both propagate with the sound velocity v_g : $e(x,t) = e_L(x + v_g t, t=0) + e_R(x - v_g t, t=0)$.

Assuming an $L \leftrightarrow R$ symmetry in the initial state, i.e., a state with zero total momentum, one obtains for the variance from Eq. (5):

$$\delta\sigma_E^2(t) = \sigma_E^2(t) - \sigma_E^2(t=0) = (V_E t)^2 \quad (28)$$

for all times t with $V_E = v_g = u$. This result can also be obtained from evaluating Eq. (13) in the continuum limit.

In the case of an initial $L \leftrightarrow R$ asymmetry in the initial state, we get $\delta\sigma_E^2(t) \rightarrow (v_g t)^2$ for $t \rightarrow \infty$, but the short-time behavior may differ. Thus within the validity of a Luttinger liquid description the energy transport is always ballistic for all initial conditions. This is evident from a physical point of view as all excitations propagate with exactly the same velocity v_g , the left movers to the left and the right movers

to the right. Note that the applicability of a Luttinger liquid description is manifestly restricted to cases in which the initial energy density profile is a smooth one in the sense that the associated excitations do not feel the nonlinearity of the fermionic dispersion relation. Thus, the time-evolution starting from initial profiles such as the ones shown in Fig. 2 is beyond the scope of this low-energy theory.

In analogy to the above arguments, the dynamics of spin-density wave packets is also ballistic in the XXZ chain for $\Delta < 1$ in the Luttinger liquid limit. In the bosonic theory, the spin density is proportional to $\rho_L(x) + \rho_R(x)$ up to a constant, see Sec. III A. The associated probability distribution $\rho(x,t) = \mathcal{Q}^{-1} \langle \rho_L + \rho_R \rangle / 2\pi$, with $\mathcal{Q} = \int dx \langle \rho_L + \rho_R \rangle / 2\pi$, can again be separated into a left- and a right-moving contribution, i.e.,

$$\rho(x,t) = \rho_L(x + v_g t, t=0) + \rho_R(x - v_g t, t=0). \quad (29)$$

Thus similar to the case of the energy dynamics, one finds ballistic behavior for $|\Delta| < 1$ consistent with the numerical results of Ref. 20.

IV. DMRG RESULTS FOR THE J_i QUENCH

Now we turn to the numerical simulations. Using the adaptive time-dependent DMRG^{38–42} method, we can access the real-time dynamics of initial bond-energy distributions. Within this approach, we can probe the microscopic dynamics including the time dependence of bond energies or the entanglement entropy starting from various initial states in an essentially exact manner without limitations in the range of parameters. We discuss the pure energy dynamics in the absence of spin currents induced by the J_i quench in this section. We detail the construction of initial states and their specific features, then move on to the analysis of the time evolution of the bond energies. We calculate the spatial variance and the related quantity J_E^* and discuss the emergent velocities of the energy dynamics. Within the numerical accuracy of our simulations we find a quadratic increase of $\sigma_E^2(t)$ in all cases studied. However, it seems that for a J_i quench a large number of different velocities contribute as opposed to the Luttinger liquid theory result, the latter valid at low energies. Our study of the energy current during the time evolution and the time evolution of the expectation value $\langle J_E^*(t) \rangle$, defined in Eq. (21), gives additional insights into short-time dynamics and further validates the conclusion of ballistic energy dynamics.

A. Initial states

Let us first describe the typical shape of initial states induced by a J_i quench on a few bonds in the middle of the spin chain. To be specific, in the Hamiltonian (2), we set

$$J_i = \begin{cases} J, & i < L/2 - b, \\ -J, & \text{for } L/2 - b \leq i \leq L/2 + b, \\ J, & i > L/2 + b, \end{cases} \quad (30)$$

which provides us with initial states with an inhomogeneous energy density profile with a width of $2b$ of the ferromagnetic region. Outside this ferromagnetic region, we obtain antiferromagnetic nearest-neighbor correlations.

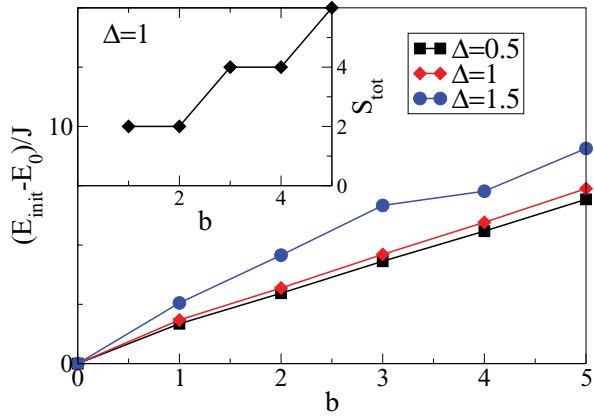


FIG. 3. (Color online) Energy difference δE between the initial state and the ground state for the J_i quench as a function of b for $\Delta = 0.5, 1, 1.5$. The inset shows the hierarchy of states with increasing total spin, which appear as initial states when the total spin is a good quantum number, i.e., at $\Delta = 1$.

Figure 2 shows the profile of the local energy density of XXZ chains with $L = 100$ sites with (a) $\Delta = 0.5$, (b) $\Delta = 1$, and (c) $\Delta = 1.5$, induced by a sign change of J_i on $b = 1, 3, 5$ bonds [compare Eq. (30)], obtained using DMRG with $m = 200$ states exploiting the U(1) symmetry to ensure zero global magnetization $S_{\text{tot}}^z = \sum_i \langle S_i^z \rangle = 0$ and, in consequence, $\langle S_i^z \rangle = 0$. In all cases shown in Fig. 2, the system forms a region with ferromagnetic nearest-neighbor correlations in the middle of the chain. Note that for $\Delta \neq 1$, $\langle h_i \rangle$ is the sum of the nearest-neighbor transverse and longitudinal spin correlations, the latter weighted with Δ . In the regions with antiferromagnetic $J_i > 0$, the local energy density oscillates, reflecting the antiferromagnetic nearest-neighbor correlations. Figure 3 shows the energy difference δE . As a function of b , the energy difference δE increases linearly once the smallest possible ferromagnetic region has been established. The minimum energy difference $\delta E = E_{\text{init}} - E_0$ is of the order of $2J$, i.e., initial states that are only weak perturbations of the respective ground state cannot be generated using a J_i quench.

At the isotropic point $\Delta = 1$, we can explain the dependence of the initial state on the width b in a transparent manner. The ground-state energy per site for the antiferromagnetic ground state is known from the Bethe Ansatz to be $\lim_{L \rightarrow \infty} E_0(L)/L = -\ln(2) + 1/4$,⁷⁴ while for the ferromagnetic ground state, $E_0/(L-1) = 1/4$, excluding the boundary sites, which gives rise to a very small system-size dependence. By growing the ferromagnetic region symmetrically with respect to the center of the chain and taking $E_0(L)$ from the unperturbed ground state with open boundaries, we obtain states with an energy that increases as

$$\delta E(b) = (2b-1)[E_0/(L-1) - 0.25] + \delta E^0, \quad (31)$$

for our finite system size (δE^0 is simply an offset). Equation (31) exactly reproduces the data for $\Delta = 1$ shown in Fig. 3.

Furthermore, at $\Delta = 1$, the total spin

$$S_{\text{tot}}^2 = \sum_i \vec{S}_i \cdot \sum_j \vec{S}_j \quad (32)$$

is a conserved quantity. Since the ground-state calculation only respects the conservation of magnetization ($S_{\text{tot}}^z = 0$), we obtain a hierarchy of states with $S > 0$. This can be easily understood by considering the block structure of the initial state. Taking, e.g., a total of $L = 100$ spins and assuming a ferromagnetic region of only two spins (i.e., $b = 1$), the two ferromagnetic spins are fully polarized with a total spin of $S = 1$, while each of the antiferromagnetic blocks has 49 spins and therefore a total spin of $S = 1/2$. Thus the total spin of the whole chain is $S_{\text{tot}} = 2$. Increasing the width of the ferromagnetic region by one, i.e., to $b = 2$, we have $S = 2$ in the middle, and the antiferromagnetic blocks are of even length, both having $S = 0$ in their ground state. This pattern repeats itself upon increasing the length $2b$ of the ferromagnetic region.

B. Time evolution of bond energies after a J_i quench

Now we focus on the time evolution of the local energy density induced by the aforementioned perturbation. At time $t = 0^+$, we set all $J_i = J$ and then evolve under the dynamics of Eq. (1). The DMRG simulations are carried out using a Krylov-space based algorithm^{75,76} with a time step of typically $0.25J$ and by enforcing a fixed discarded weight. We restrict the discussion to times smaller than the time needed for the fastest excitation to reach the boundary.

1. J_i quench: qualitative features

Figure 4 shows the time evolution of the bond energies $\langle h_i(t) \rangle$ as a contour plot for $\Delta = 0.5, 1, 1.5$ at $b = 1$. Despite the different ground states for the selected values of anisotropy, all features of the dynamics such as two distinct rays starting at the edges of the block of ferromagnetic correlations, are similar. The solid white lines for $\Delta = 0.5$ and $\Delta = 1$ indicate an excitation spreading out from the center of the ferromagnetic region with the group velocity given by Eq. (24) (these lines are parallel to the outer rays visible in the figure, i.e., the fastest propagating particles). Note that Eq. (24) holds only in the gapless phase ($|\Delta| \leq 1$). Besides the outer rays that define a light-cone structure, Fig. 4 unveils the presence of more such rays inside the light cone. Since our particular initial states have a sharp edge in real space, there ought to be many excitations with different momenta k contributing to the expansion.

2. J_i quench: spatial variance

Our main evidence for ballistic dynamics in both phases is based on the analysis of the spatial variance, shown in Fig. 5. Fitting a power law (straight lines) to the data, i.e., $\sigma_E^2(t) - \sigma_E^2(0) = \alpha t^\beta$ yields a quadratic increase with $\beta \approx 2$, classifying the dynamics as ballistic.

In order to estimate uncertainties in the fitting parameter α , we compare this to the results of fitting a pure parabola $\sigma_E^2(t) - \sigma_E^2(0) = V_E^2 t^2$ to the data. Typically, V_E^2 deviates from α by about 10% while the exponent of the power-law fit is

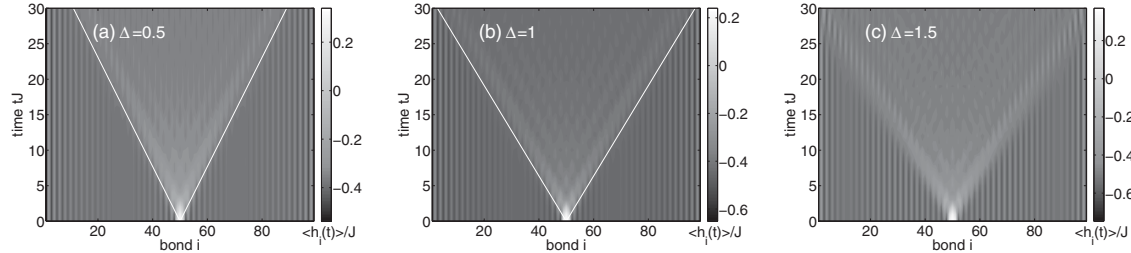


FIG. 4. Time evolution of the bond energy distribution starting from initial states with $b = 1$ from Fig. 2 for (a) $\Delta = 0.5$, (b) $\Delta = 1$, and (c) $\Delta = 1.5$. Despite the different ground-state phases, for the selected values of the exchange anisotropy Δ , main features of the dynamics such as two distinct rays extending from the edges of the perturbation are similar. The solid white lines for $\Delta = 0.5$ and $\Delta = 1$ indicate the propagation of a single excitation starting in the middle of the chain at time $t = 0$ moving with the group velocity v_g from Eq. (24). This is also the velocity in the outer rays.

usually different from 2 by 5%. As an example, for $\Delta = 0.5$ and $b = 1$, we obtain $\beta = 2.03$ and $\alpha = 0.53$ versus $V_E^2 = 0.6J^2$. The main reason for the deviation of β from two is, in fact, that the short-time dynamics is not well described by a power law at all over a b -dependent time window. We shall see later, in Sec. IV C, that the ballistic dynamics sets in

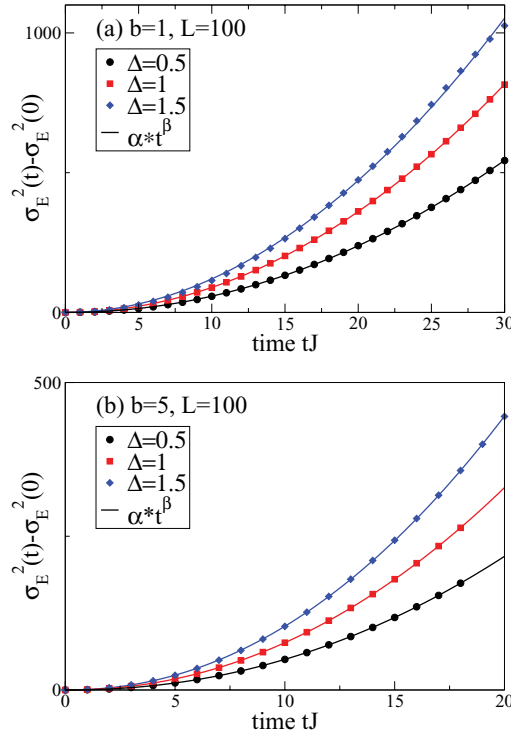


FIG. 5. (Color online) Spatial variance of the evolving energy distribution for (a) $b = 1$, (b) $b = 5$, and $\Delta = 0.5, 1, 1.5$. Fitting a power law (straight lines) to $\sigma_E^2(t) - \sigma_E^2(0) = \alpha t^\beta$ yields a quadratic increase with sufficient accuracy, classifying the dynamics as ballistic. For instance, we find $\alpha = 0.53$, $\beta = 2.03$ for $\Delta = 0.5$ and $b = 1$ [black circles in (a)]. We do not find any qualitative difference between the massless ($|\Delta| \leq 1$) and the massive ($\Delta > 1$) phases. The deviations between the fit and the tDMRG data in the $\Delta = 1.5$ curves at the largest times simulated are due to the boundaries.

only after the block of ferromagnetically correlated bonds has fully “melted.” Indeed, by excluding several time steps at the beginning of the evolution from the power-law fit, we observe that $\beta \rightarrow 2$ and $\alpha \rightarrow V_E^2$. Therefore we will present results for V_E^2 , obtained by fitting $\sigma_E^2(t) - \sigma_E^2(0) = V_E^2 t^2$ to our tDMRG data.

3. Exploiting SU(2) symmetry at $\Delta = 1$ for the J_i quench

Before proceeding to the discussion of the expansion velocity V_E^2 , we wish to discuss the long-time limit, which can be accessed in the case of $\Delta = 1$. Since our perturbation is proportional to the operators for the local energy density, global symmetries of the unperturbed Hamiltonian are respected by the initial states of the type in Eq. (30). Therefore, at $\Delta = 1$, we can exploit the conservation of total spin S , a non-Abelian symmetry. This can be used to push the simulations to much longer times, since we can perform the time evolution in an SU(2) invariant basis.⁷⁷ The number of states needed to ensure a given accuracy is reduced substantially compared to a simulation that only respects U(1) symmetry. Therefore we can work with larger system sizes and study the long-time dynamics of the energy density. As we can reach longer times, we can also analyze and discuss finite-size effects for $\Delta = 1$ here. Figure 6 shows our result for the time evolution respecting SU(2) symmetry (blue triangles) for a system of $L = 200$ sites and $\Delta = 1$, $b = 1$ compared to the result from Fig. 5 for $L = 100$ sites (red squares). We still find a quadratic increase of $\sigma_E^2(t)$ and thus ballistic dynamics for times up to $t \sim 60/J$ and in addition, the prefactor does not depend on the system size. Both simulations were carried out keeping the discarded weight below 10^{-4} , which requires at most $m = 900$ states using only U(1) symmetry on $L = 100$ sites versus a maximum of $m = 400$ using SU(2) for $L = 200$ sites.

4. Expansion velocity

The results for V_E^2 are collected in Fig. 7 and plotted as a function of δE for $\Delta = 0, 0.5, 1, 1.5$. In the noninteracting case, $\Delta = 0$, V_E^2 is constant for $b \geq 2$, while at $b = 1$ (the smallest possible δE), $V_E^2 = 0.5J^2$. For all $\Delta > 0$, V_E^2 slightly decreases with δE and V_E^2 is much smaller than v_g^2 given by Eq. (24), suggesting that indeed, many velocities contribute during the expansion of the energy wave packet.

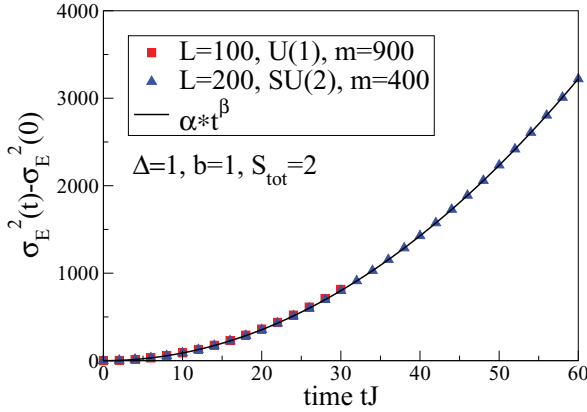


FIG. 6. (Color online) Long-time evolution exploiting the conservation of total spin S_{tot} at $\Delta = 1$ for $L = 200$ sites using an initial state with $b = 1$. For comparison, we plot the result for $L = 100$ sites using only $U(1)$ symmetry. Fixing the discarded weight to 10^{-4} , we need less than half the number of states. Furthermore, we find that the spatial variance is very robust against finite-size effects.

Intuitively, one might associate the decrease of V_E^2 , which is a measure of the average velocity of propagating excitations contributing to the expansion, to band curvature: the higher δE , the more excitations with velocities smaller than v_g are expected to factor in.

It is instructive to consider the noninteracting limit first by comparing the numerical results obtained from a time evolution with exact diagonalization to the analytical (and also exact result) from Eq. (13). To that end, we need to compute the MDF [see Eq. (14)] of the initial state. Our results for $\Delta = 0$, which are shown in Fig. 8, unveil a peculiar property: the J_i quench always induces changes at all k , i.e., the system is not just weakly perturbed in the vicinity of k_F . This is not surprising since our initial states have sharp edges in real space (compare Fig. 2). Moreover, the J_i quench changes the MDF in

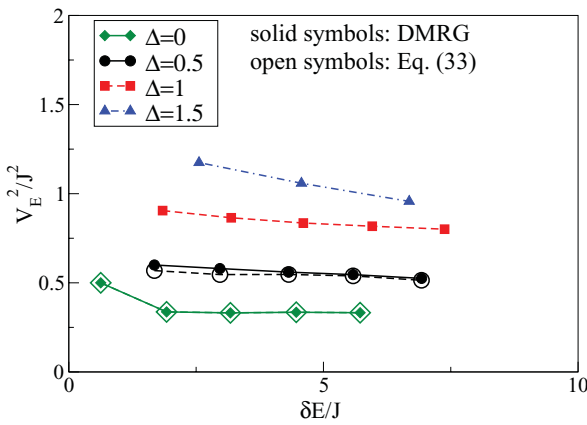


FIG. 7. (Color online) Prefactors V_E^2 of the fits $\sigma_E^2 - \sigma_E^2(0) = V_E^2 t^2$ as functions of δE for $\Delta = 0, 0.5, 1, 1.5$ and J_i quenches with $b = 1, 2, 3, 4, 5$ (for $\Delta = 1.5$, we show $b = 1, 2, 3$ only). For $\Delta > 0$, V_E^2 decreases slightly with b , while $V_E^2 < v_g^2$. At $\Delta = 0$, V_E^2 is roughly constant for $b > 2$.

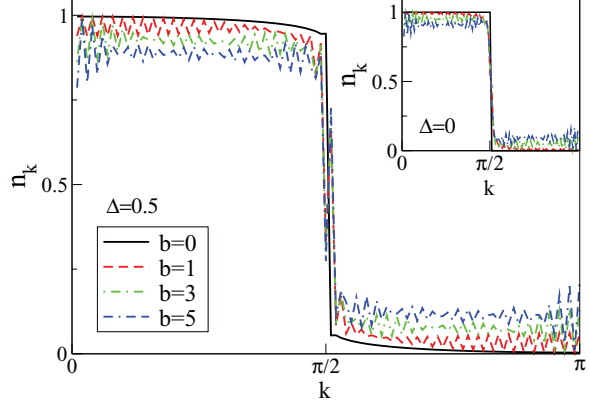


FIG. 8. (Color online) MDF of the initial states generated by a J_i quench at $\Delta = 0.5$ and $\Delta = 0$ (inset) with $b = 1, 3, 5$. For comparison, we include the MDF of the ground state (solid black line).

such a way that $\delta n_k(b) = n_k^{\text{init}}(b) - n_k$ is point symmetric with respect to $k_F = \pi/2$, where k_F is the Fermi wave vector. As Fig. 7 shows, V_E^2 as extracted from fits to $\delta \sigma_E^2$ (solid symbols) and V_E^2 from Eq. (13) (open symbols) perfectly agree with each other, as expected.

The MDF of initial states for the interacting systems are also such that $\delta n_k \neq 0$ at all momenta and we may therefore conclude that the observation $V_E < v_g$ is due to the fact that the J_i quench induces many excitations with velocities smaller than v_g (compare the data shown for $\Delta = 0.5$ shown in Fig. 8). Of course, Eq. (13) is not directly applicable to the interacting case since, first, it does not account for the correct eigenstates at $\Delta \neq 0$ and second, in general, $\langle h_i \rangle \neq \langle J(S_i^+ S_{i+1}^- + \text{H.c.})/2 \rangle$. Nevertheless, by numerically calculating δn_k for the interacting system and by using the renormalized velocity in Eq. (13) instead of J [i.e., $J \rightarrow v_g(\Delta)$], we obtain an estimate for V_E^2 from

$$V_E^2 \approx \frac{v_g^2}{\delta E} \sum_k \cos(k) \sin^2(k) \delta n_k. \quad (33)$$

This reproduces the qualitative trend of the tDMRG results for V_E^2 as we exemplify for $\Delta = 0.5$ in Fig. 7.

To summarize, the overall picture for the time evolution of the bond energies after a J_i quench is that energy propagates ballistically with an expansion velocity V_E that is approximately given by Eq. (33). Combined with the observation that on a finite system, a J_i quench induces changes in the MDF at all momenta k , we conclude that many excitations contribute to the wave-packet dynamics, resulting in $V_E < v_g$, both in the noninteracting and in the interacting case.

C. Energy currents

To conclude the discussion of the J_i quenches we present our results for the local energy currents at $\Delta = 1$ in Fig. 9. By comparison with Fig. 4(b), we see that the local current is the strongest in the vicinity of the wave packet. The energy current in each half of the system becomes a constant after a few time steps, i.e., $J_{L/2}^E := \sum_{i=1}^{L/2-1} j_i^E$ reaches a constant value. We

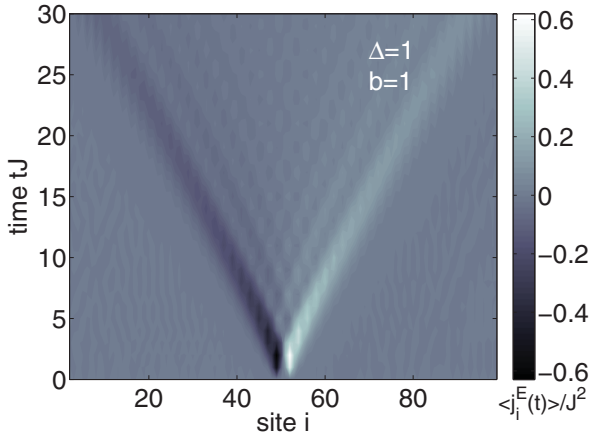


FIG. 9. (Color online) Real-time evolution of the local energy current, Eq. (18), at $\Delta = 1$ for a J_i quench with $b = 1$.

plot the absolute value of $\langle J_{L/2}^E \rangle$ for $\Delta = 0.5, 1, 1.5$ for $b = 1$ in Fig. 10(a). The qualitative behavior is independent of Δ : as soon as the initial perturbation has split up into two wave packets, we have prepared each half of the chain in a state with a constant, global current $\langle J_{L/2}^E \rangle = \text{const}$. For a system with periodic boundary conditions, the total current $J_E = \sum_i j_i^E$ is a conserved quantity.⁴³ Since the effect of boundaries only factors in once these are reached by the fastest excitations, we directly probe the conservation of a global current with our setup, after some initial transient dynamics. Therefore we can link the phenomenological observation of ballistic wave-packet dynamics to the existence of a conservation law in the system.

While the currents $\langle J_{L/2}^E \rangle$ clearly undergo some transient dynamics [see Fig. 10(a)], we have derived a quantity in Sec. II, called J_E^* , whose expectation value is stationary if $\sigma_E^2 \sim t^2$. We now numerically evaluate $\langle J_E^*(t) \rangle$ from Eq. (21), which provides an independent probe of ballistic dynamics. Figure 10(b) shows our results for $\Delta = 1$ and J_i quenches with $b = 1, 2, 3, 4, 5$. It turns out that $\langle J_E^*(t) \rangle$ is indeed constant at sufficiently large times, consistent with the observation of $\delta\sigma_E^2 \sim t^2$. In Sec. IV B, we have noted that $\delta\sigma_E^2 \not\sim t^2$ at short times $t \lesssim b/J$. This renders $\langle J_E^*(t) \rangle$ a time-dependent quantity over the same time window. Clearly, the time window over which $\langle J_E^*(t) \rangle \neq \text{const}$ depends on b [see Fig. 10(b)], which suggests that the deviation of ballistic dynamics is associated to the ‘‘melting’’ process of the region with ferromagnetic correlations. We have carefully checked that these observations are robust against errors in the calculation of time derivatives in Eq. (21) induced by the finite time step. Since $\langle J_E^*(t) \rangle$ is time dependent (at least at short times), we conclude that J_E^* is not a conserved quantity in the interacting case. Finally, within our numerical accuracy and as an additional consistency check, we find that $\langle J_E^* \rangle / \delta E = \alpha$ in the stationary state as expected from the discussion in Sec. II C.

To summarize, $\langle J_E^*(t) \rangle = \text{const}$ whenever $\delta\sigma_E^2 \sim t^2$ but $\langle J_E^* \rangle$ is very sensitive to the initial transient dynamics in the energy dynamics and becomes constant after a time $\approx bJ$. Furthermore, our setup serves to prepare each half of the system in a state with a finite global energy current $\langle J_{L/2}^E \rangle$.

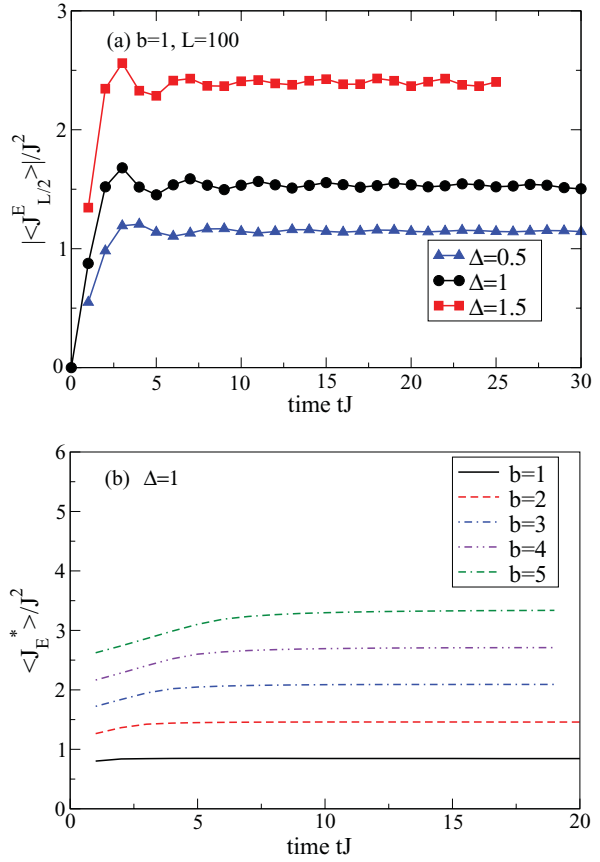


FIG. 10. (Color online) (a) Absolute value of the current in each half of the system. A constant value is reached after $t \approx 5/J$. (b) The quantity $\langle J_E^*(t) \rangle$ from Eq. (21) derived from a pure quadratic increase of the spatial variance for $\Delta = 1$ and $b = 1, 2, 3, 4, 5$. This quantity is constant, as expected from the discussion in Sec. IV C, except for the initial transient dynamics at $t < b/J$.

that, after some transient dynamics, does not decay since the global energy current operator is a conserved quantity.

V. COUPLED SPIN AND ENERGY DYNAMICS

After focusing on the energy dynamics in the absence of spin/particle currents we now revisit the case of spin dynamics starting from states with $\langle S_i^z(t=0) \rangle \neq 0$. Thus during the time evolution, the local spin and energy currents are both nonzero. In Ref. 20, the dynamics of the magnetization was studied, where the inhomogeneous spin-density profile was induced by a Gaussian magnetic field in the initial state. We take the initial state to be the ground state of Eq. (3) in the sector with zero global magnetization, i.e., $S_{\text{tot}}^z = \sum_i \langle S_i^z \rangle = 0$. Such a perturbation naturally also results in an inhomogeneous energy density in the initial state, which is coupled to the spin dynamics during the time evolution.²⁸

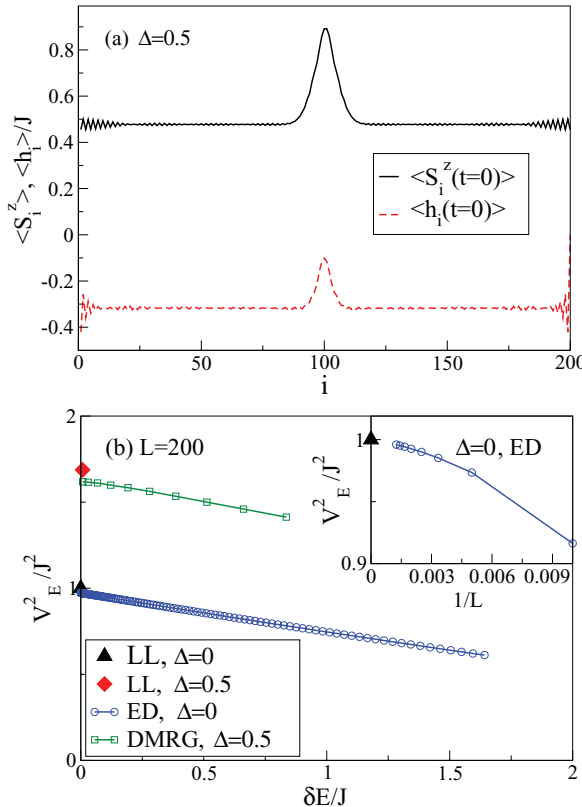


FIG. 11. (Color online) (a) Magnetization (solid black line) and energy density (dashed red line) in the initial state, for a B_0 quench with $B_0 = J$ and $\sigma_0 = 5$ for $\Delta = 0.5$ on a lattice of $L = 200$ sites. (b) Prefactor V_E^2 of $\delta\sigma_E^2(t) = V_E^2 t^2$ for the energy dynamics after a B_0 quench in the massless phase of the XXZ chain, compared to the group velocity [Eq. (24)] for $\Delta = 0, 0.5$ and $L = 200$. On this system size and in the limit of small perturbations, V_E^2 is approximately 5% smaller than the prediction from the Luttinger liquid theory for both Δ . For $\Delta = 0$, finite-size scaling of $V_E^2(\delta E \rightarrow 0)$ using $L = 100, 200, \dots, 800$ yields $V_E^2 \rightarrow v_g^2$ as shown in the inset.

A. Massless phase

In Fig. 11(a), we compare the initial magnetization (black solid line) and the local bond energies (dashed red line) induced by a Gaussian magnetic field with $B_0 = J$ and $\sigma_0 = 5$ at $\Delta = 0.5$ finding qualitatively the same pattern; both the spin and the energy density follow the shape of the magnetic field, resulting in a smooth perturbation with small oscillations in the background away from the wave packet.

For the time evolution of the bond energies at $0 < \Delta \leq 1$, we perform an analysis of their spatial variance analogous to the discussion of the J_i quench, finding ballistic dynamics in the massless phase. Since with a B_0 quench, initial states with very small δE can be produced, we next connect our numerical results to the predictions of LL theory, valid in the limit $\delta E \ll J$ (compare Sec. III).

Since we enforce zero global magnetization, we draw magnetization from the background into the peak.¹⁴ Therefore one has to carefully estimate the contributions to δE that

do not contribute to the time dependence of bond energies yet change the background density n_{bg} . The latter, in turn, affects the expected group velocity and we thus expect to recover the LL result derived for the half-filled case, i.e., propagation with v_g from Eq. (24), in the limit of large systems where $n_{bg} \rightarrow 1/2$. Furthermore, B_0 quenches induce $2k_F$ oscillations in the spin and energy density.²⁰ To account for this, we use coarse graining, i.e., averaging the energy density over neighboring sites, and we take the sum only over the area of the peak when estimating δE . We obtain $\delta E^{\text{peak}} := \sum_{L/2-x}^{L/2+x} (\langle h_i \rangle - \langle h_i \rangle_0)$, where $\langle h_i \rangle_0$ denotes the ground-state expectation value. From this quantity we calculate the velocity via $V_E^2 \rightarrow V_E^2 \cdot \delta E / \delta E^{\text{peak}}$, which is shown in Fig. 11(b). Note that while δE^{peak} is the correct normalization to obtain the correct velocities, we label our initial states via δE . At $\Delta = 0$ (blue circles), V_E^2 decreases linearly as a function of δE . Next we compare the result from the low-energy theory from Sec. III (solid symbols at $\delta E = 0$) to our tDMRG data. For both $\Delta = 0$ and $\Delta = 0.5$, V_E^2 for $L = 200$ sites is approximately 5% smaller than v_g^2 from Eq. (24), which is mainly due to the deviation of the background density from half filling. While it is hard to get results for larger systems than $L \sim 200$ in the interacting case, we can solve the $\Delta = 0$ case numerically exactly in terms of free spinless fermions, allowing us to go to sufficiently large L to observe $V_E^2(L) \rightarrow v_g^2$ as $L \rightarrow \infty$. The inset of Fig. 11(b) shows the finite-size scaling of $V_E^2(L)$ for $\Delta = 0$ using $L = 100, 200, \dots, 800$, which yields $V_E^2 \rightarrow v_g^2$ in the limit $L \rightarrow \infty$, taking first $\delta E \rightarrow 0$ for each system size. We thus, in principle, have numerical access to the dynamics in the low-energy limit well described by Luttinger liquid theory using a B_0 quench.

B. Massive phase

In Ref. 20, examples of a linear increase of the spatial variance of the magnetization $\sigma_S^2(t)$, defined in Eq. (16), were found in the massive phase, which were interpreted as an indication of diffusive dynamics. We now demonstrate that while the spin dynamics may behave diffusively, i.e., $\delta\sigma_S^2 \sim t$ over a certain time window, the energy dynamics in the same quench is still ballistic, i.e., $\delta\sigma_E^2 \sim t^2$.

In Fig. 12, we show the full time evolution of the bond energies for a Gaussian magnetic field with $B_0 = 1.5J$ and $\sigma_0 = 5$ on a chain of $L = 200$ sites at $\Delta = 1.5$. It consists of two rays propagating with opposite velocities. In Fig. 13, we compare the spatial variance of the magnetization $\sigma_S^2(t)$ to the one of the bond energies $\sigma_E^2(t)$ calculated in the same time evolved state. The main panel of Fig. 13 shows $\sigma_E^2(t) - \sigma_E^2(0)$, which is very well described by a power-law fit with an exponent $\beta = 2.03$ on the accessible time scales. The inset of Fig. 13 displays the data for $\delta\sigma_S^2(t) = \sigma_S^2(t) - \sigma_S^2(0)$ taken from Ref. 20. The spatial variance of the energy density is quadratic in time, even at times $t \gtrsim 12/J$ where the spatial variance of the magnetization increases only linearly. This example reflects the qualitative difference between spin and energy transport in the massive phase of the XXZ model at zero global magnetization. The conservation of the global energy current is consistent with the observation of ballistically propagating energy wave packets, while spin clearly does not propagate ballistically. Our result, obtained in the nonequilibrium case with a

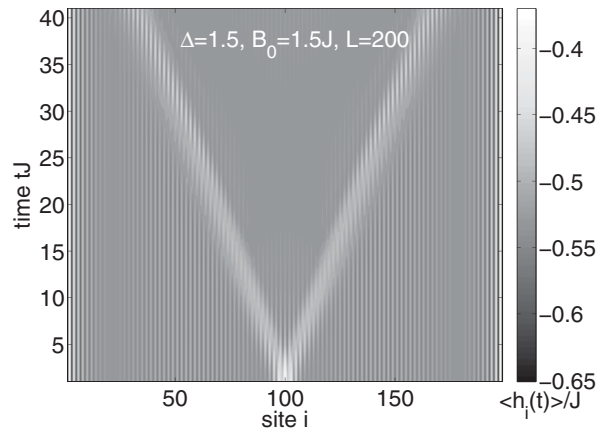


FIG. 12. (Color online) Time-dependent bond energies for the dynamics induced by a B_0 quench with $B_0 = 1.5J$, $\sigma_0 = 5$ on a chain of $L = 200$ sites at $\Delta = 1.5$. In this case, both local spin and local energy densities are perturbed and the corresponding local currents are nonzero.

zero-temperature background density, is consistent with the picture established from both linear-response theory^{51,55} and steady-state simulations.^{28,61,64}

Very recently, Jesenko and Žnidarič have also studied the time evolution of spin and energy densities induced by a B_0 quench.²⁸ They concentrate their analysis on the velocity of the fastest wave fronts, contrasting energy against spin dynamics. Based on the presence of these rays of fast propagating particles, they claim that the wave packet dynamics still has ballistic features. However, their analysis neglects the influence of slower excitations that also contribute to the dynamics of the wave packet, which is captured by the variance, and it ignores the decay of the intensity in the outer rays that we typically observe whenever $\delta\sigma_S^2 \sim t$.²⁰ The latter is, if at all, weak in a ballistic expansion characterized by

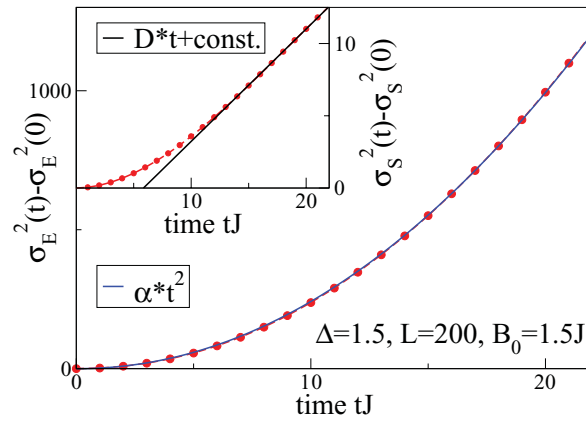


FIG. 13. (Color online) Spatial variance of the energy density (main panel) and the spin density (inset), induced by a B_0 quench with $B_0/J = 1.5$ and $\sigma_0 = 5$ [compare Eq. (3)] at $\Delta = 1.5$. In this case, both local spin and local energy densities are non zero during the time evolution. The inset was reproduced from Ref. 20.

$\delta\sigma_S^2 \sim t^2$. Therefore, while the analysis of Ref. 28 unveils interesting details of the time evolution of densities during a B_0 quench, we maintain that the variance is a useful quantity to identify candidate parameter sets for spin diffusion in, e.g., the nonequilibrium regime. Final proof of diffusive behavior then needs to be established by either demonstrating the validity of the diffusion equation or by computing correlation functions, see, e.g., Refs. 55 and 61. For instance, in Ref. 28, Jesenko and Žnidarič analyze the steady-state currents in the $\Delta > 1$ regime at finite temperature and obtain diffusive behavior.

VI. SUMMARY

We studied the real-time energy dynamics in XXZ spin-1/2 chains at zero temperature in two different scenarios. First, we investigated the energy dynamics in the absence of spin currents induced by a local sign change in the exchange interactions. The spatial variance behaves as $\delta\sigma_E^2(t) \propto t^2$ for all Δ , consistent with ballistic dynamics. In the gapless regime, the velocity of the fastest excitation present in the dynamics is the group velocity v_g of spinons, yet our particular quench also involves excitations with much smaller velocities resulting in expansion velocities $V_E < v_g$. Furthermore, the ballistic dynamics can be related to properties of energy currents. While the total current vanishes in our setup, i.e., $\langle J_E \rangle := \sum_i \langle j_i^E \rangle = 0$, the current in each half of the chain $\langle J_{L/2}^E \rangle > 0$ takes a constant value, after some transient dynamics. Therefore, in each half of the system, we prepared a state with a conserved global current, allowing us to make a direct connection to the predictions of linear-response theory where the existence of ballistic dynamics is directly linked to conservation laws that prohibit currents from decaying.⁴³ Moreover, we identified an observable J_E^* built from local currents whose expectation value $\langle J_E^*(t) \rangle$ is time independent if $\delta\sigma_E^2 \propto t^2$ and vice versa. This carries over to other types of transport as well and, in fact, the analysis of the time dependence of $\langle J_E^* \rangle$ can be used as an independent means to identify ballistic regimes, or to unveil the absence thereof.

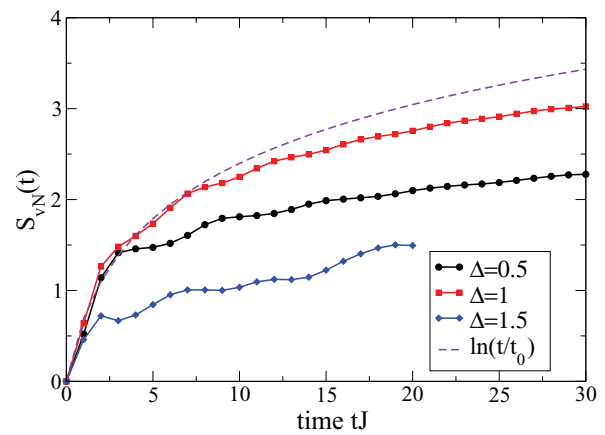


FIG. 14. (Color online) Time dependence of the von Neumann entropy S_{vN} for a bipartition that cuts the system across the central bond during the time evolution starting from a ferromagnetic region coupled to an antiferromagnetic one at $\Delta = 0.5, 1, 1.5$.

In the second part, we studied the energy dynamics induced by quenching a Gaussian magnetic field, with two main results. These quenches allow us to access the regime of weakly perturbed initial states and in that limit, we recover the predictions from Luttinger liquid theory for the wave-packet dynamics. Their variance simply grows as $\delta\sigma_E^2 = v_g^2 t^2$. In the massive phase, a very interesting phenomenon occurs, since the energy dynamics is ballistic on time scales over which the spin dynamics behaves diffusively although both are driven by the same perturbation. This resembles the picture established from linear-response theory,⁴³ there applied to the finite-temperature case, in the nonequilibrium setup studied here. While our numerical results cover spin chains on real-space lattices and initial states far from equilibrium, the extension of our work to a finite temperature of the background will be crucial to tackle the most important open questions.

ACKNOWLEDGMENTS

We thank W. Brenig, S. Kehrein, A. Kolezhuk, and R. Noack for very helpful discussions. S.L. and F.H.-M. acknowledge support from the Deutsche Forschungsgemeinschaft through FOR 912, M.H acknowledges support by the SFB TR12 of the Deutsche Forschungsgemeinschaft, the Center for Nanoscience (CeNS), Munich, and the German Excellence Initiative via the Nanosystems Initiative Munich (NIM). F.H.-M. acknowledges the hospitality of the Institute for Nuclear Theory at the University of Washington, Seattle, where part of this research was carried out during the INT program “Fermions from Cold Atoms to Neutron Stars: Benchmarking the Many-Body Problem.”

APPENDIX: ENTANGLEMENT GROWTH

Here, we want to study the growth of entanglement across a junction separating regions in a spin chain with ferromagnetic correlations from ones with antiferromagnetic ones.

To that end, we take initial states inspired by Ref. 19 where one half of the system has a positive and the other one a negative J . We obtain this configuration as a variation of J_i -quench choosing:

$$J_i = \begin{cases} J, & i < L/2, \\ 0, & \text{for } i = L/2, \\ -J, & i > L/2, \end{cases} \quad (\text{A1})$$

in Eq. (2). We then perform the time evolution under the antiferromagnetic Hamiltonian [Eq. (1)]. As a measure of the entanglement we calculate the von Neumann entropy

$$S_{\text{VN}} = -\text{Tr}(\rho_A \ln \rho_A) \quad (\text{A2})$$

of the reduced density matrix $\rho_A = \text{Tr}_B \rho$, where $\rho = |\psi(t)\rangle\langle\psi(t)|$ is the time-evolved wave function, for a bipartition in which we cut the chain into two halves of length $L/2$ across the central link. Our results are plotted in Fig. 14. We observe that the von Neumann entropy grows at most logarithmically (purple dashed line), in agreement with Ref. 21. The overall largest values of $S_{\text{VN}}(t)$ are found at the critical point $\Delta = 1$ (red squares). This behavior is very similar to the observations made in Ref. 19 for spin dynamics starting from a state with all spins pointing up (down) in the left (right) half.

*stephan.langer@physik.uni-muenchen.de

¹X. Zotos and P. Prelovšek, *Strong Interactions in Low Dimensions* (Kluwer, Dordrecht, 2004), Chap. 11.

²F. Heidrich-Meisner, A. Honecker, and W. Brenig, *Eur. J. Phys. Special Topics* **151**, 135 (2007).

³A. V. Rozhkov and A. L. Chernyshev, *Phys. Rev. Lett.* **94**, 087201 (2005).

⁴E. Boulat, P. Mehta, N. Andrei, E. Shimshoni, and A. Rosch, *Phys. Rev. B* **76**, 214411 (2007).

⁵I. Bloch, J. Dalibard, and W. Zwerger, *Rev. Mod. Phys.* **80**, 885 (2008).

⁶A. Polkovnikov, K. Sengupta, A. Silva, and M. Vengalattore, *Rev. Mod. Phys.* **83**, 863 (2011).

⁷U. Schneider, L. Hackermüller, J. P. Ronzheimer, S. Will, S. Braun, T. Best, I. Bloch, E. Demler, S. Mandt, D. Rasch, and A. Rosch, e-print arXiv:1005.3545 (unpublished).

⁸P. Medley, D. M. Weld, H. Miyake, D. E. Pritchard, and W. Ketterle, *Phys. Rev. Lett.* **106**, 195301 (2011).

⁹A. Sommer, M. Ku, and M. W. Zwierlein, *New J. Phys.* **13**, 055009 (2011).

¹⁰A. Sommer, M. Ku, G. Roati, and M. W. Zwierlein, *Nature (London)* **472**, 201 (2011).

¹¹J. Joseph, J. E. Thomas, M. Kulkarni, and A. G. Abanov, *J. Stat. Mech.: Theory Exp.* (2011) P04007.

¹²M. Rigol and A. Muramatsu, *Phys. Rev. Lett.* **93**, 230404 (2004).

¹³M. Rigol and A. Muramatsu, *Phys. Rev. Lett.* **94**, 240403 (2005).

¹⁴C. Kollath, U. Schollwöck, J. von Delft, and W. Zwerger, *Phys. Rev. A* **71**, 053606 (2005).

¹⁵F. Heidrich-Meisner, M. Rigol, A. Muramatsu, A. E. Feiguin, and E. Dagotto, *Phys. Rev. A* **78**, 013620 (2008).

¹⁶F. Heidrich-Meisner, S. R. Manmana, M. Rigol, A. Muramatsu, A. E. Feiguin, and E. Dagotto, *Phys. Rev. A* **80**, 041603(R) (2009).

¹⁷D. Karlsson, M. O. C. Verdozzi, and K. Capelle, *Europhys. Lett.* **93**, 23003 (2011).

¹⁸J. Kajala, F. Massel, and P. Törmä, *Phys. Rev. Lett.* **106**, 206401 (2011).

¹⁹D. Gobert, C. Kollath, U. Schollwöck, and G. Schütz, *Phys. Rev. E* **71**, 036102 (2005).

²⁰S. Langer, F. Heidrich-Meisner, J. Gemmer, I. P. McCulloch, and U. Schollwöck, *Phys. Rev. B* **79**, 214409 (2009).

²¹V. Eisler and I. Peschel, *J. Stat. Mech.: Theory Exp.* (2009) P02011.

²²J. Lancaster and A. Mitra, *Phys. Rev. E* **81**, 061134 (2010).

²³J. Lancaster, E. Gull, and A. Mitra, *Phys. Rev. B* **82**, 235124 (2010).

²⁴J. Mossel, G. Palacios, and J.-S. Caux, *J. Stat. Mech.: Theory Exp.* (2010) L09001.

²⁵M. S. Foster, E. A. Yuzbashyan, and B. L. Altshuler, *Phys. Rev. Lett.* **105**, 135701 (2010).

- ²⁶M. S. Foster, T. C. Berkelbach, D. R. Reichman, and E. A. Yuzbashyan, *Phys. Rev. B* **84**, 085146 (2011).
- ²⁷L. F. Santos and A. Mitra, *Phys. Rev. E* **84**, 016206 (2011).
- ²⁸S. Jesenko and M. Žnidarič e-print arXiv:1105.6340v1 (unpublished).
- ²⁹C. Kollath, U. Schollwöck, and W. Zwerger, *Phys. Rev. Lett.* **95**, 176401 (2005).
- ³⁰M. Polini and G. Vignale, *Phys. Rev. Lett.* **98**, 266403 (2007).
- ³¹P. Jordan and E. Wigner, *Z. Phys.* **47**, 631 (1928).
- ³²C. Hess, H. ElHaes, A. Waske, B. Büchner, C. Sekar, G. Krabbes, F. Heidrich-Meisner, and W. Brenig, *Phys. Rev. Lett.* **98**, 027201 (2007).
- ³³A. V. Sologubenko, T. Lorenz, H. R. Ott, and A. Freimuth, *J. Low Temp. Phys.* **147**, 387 (2007).
- ³⁴C. Hess, C. Baumann, U. Ammerahl, B. Büchner, F. Heidrich-Meisner, W. Brenig, and A. Revcolevschi, *Phys. Rev. B* **64**, 184305 (2001).
- ³⁵A. V. Sologubenko, K. Gianno, H. R. Ott, U. Ammerahl, and A. Revcolevschi, *Phys. Rev. Lett.* **84**, 2714 (2000).
- ³⁶N. Hlubek, P. Ribeiro, R. Saint-Martin, A. Revcolevschi, G. Roth, G. Behr, B. Büchner, and C. Hess, *Phys. Rev. B* **81**, 020405 (2010).
- ³⁷M. Otter, V. Krasnikov, D. Fishman, M. Pshenichnikov, R. Saint-Martin, A. Revcolevschi, and P. van Loodsrecht, *J. Mag. Mag. Mat.* **321**, 796 (2009).
- ³⁸A. Daley, C. Kollath, U. Schollwock, and G. Vidal, *J. Stat. Mech.: Theory Exp.* (2004) P04005.
- ³⁹S. R. White and A. E. Feiguin, *Phys. Rev. Lett.* **93**, 076401 (2004).
- ⁴⁰G. Vidal, *Phys. Rev. Lett.* **93**, 040502 (2004).
- ⁴¹U. Schollwöck, *Rev. Mod. Phys.* **77**, 259 (2005).
- ⁴²U. Schollwöck, *Ann. Phys. (NY)* **326**, 96 (2011).
- ⁴³X. Zotos, F. Naef, and P. Prelovšek, *Phys. Rev. B* **55**, 11029 (1997).
- ⁴⁴A. Klümper and K. Sakai, *J. Phys. A* **35**, 2173 (2002).
- ⁴⁵K. Sakai and A. Klümper, *J. Phys. A* **36**, 11617 (2003).
- ⁴⁶F. Heidrich-Meisner, A. Honecker, D. C. Cabra, and W. Brenig, *Phys. Rev. B* **66**, 140406(R) (2002).
- ⁴⁷F. Heidrich-Meisner, A. Honecker, D. C. Cabra, and W. Brenig, *Phys. Rev. B* **68**, 134436 (2003).
- ⁴⁸B. N. Narozhny, A. J. Millis, and N. Andrei, *Phys. Rev. B* **58**, R2921 (1998).
- ⁴⁹X. Zotos, *Phys. Rev. Lett.* **82**, 1764 (1999).
- ⁵⁰X. Zotos, *Phys. Rev. Lett.* **92**, 067202 (2004).
- ⁵¹P. Prelovšek, S. El Shawish, X. Zotos, and M. Long, *Phys. Rev. B* **70**, 205129 (2004).
- ⁵²J. Benz, T. Fukui, A. Klümper, and C. Scheeren, *J. Phys. Soc. Jpn. Suppl.* **74**, 181 (2005).
- ⁵³P. Jung, R. W. Helmes, and A. Rosch, *Phys. Rev. Lett.* **96**, 067202 (2006).
- ⁵⁴J. Sirker, R. G. Pereira, and I. Affleck, *Phys. Rev. Lett.* **103**, 216602 (2009).
- ⁵⁵R. Steinigeweg and J. Gemmer, *Phys. Rev. B* **80**, 184402 (2009).
- ⁵⁶S. Grossjohann and W. Brenig, *Phys. Rev. B* **81**, 012404 (2010).
- ⁵⁷R. Steinigeweg, *Phys. Rev. E* **84**, 011136 (2011).
- ⁵⁸R. Steinigeweg and W. Brenig, e-print arXiv:1107.3103 (unpublished).
- ⁵⁹J. Herbrych, P. Prelovšek, and X. Zotos, *Phys. Rev. B* **84**, 155125 (2011).
- ⁶⁰T. Prosen, *Phys. Rev. Lett.* **106**, 217206 (2011).
- ⁶¹M. Žnidarič, *Phys. Rev. Lett.* **106**, 220601 (2011).
- ⁶²J. Sirker, R. G. Pereira, and I. Affleck, *Phys. Rev. B* **83**, 035115 (2011).
- ⁶³J.-S. Caux and J. Mossel, *J. Stat. Mech.* (2011) P02023.
- ⁶⁴T. Prosen and M. Žnidarič, *J. Stat. Mech.: Theor. Exp.* (2009) P02035.
- ⁶⁵G. Benenti, G. Casati, T. Prosen, and D. Rossini, *Europhys. Lett.* **85**, 37001 (2009).
- ⁶⁶G. Benenti, G. Casati, T. Prosen, D. Rossini, and M. Žnidarič, *Phys. Rev. B* **80**, 035110 (2009).
- ⁶⁷P. Calabrese and J. Cardy, *J. Stat. Mech.: Theory Exp.* (2007) P10004.
- ⁶⁸M. Rigol and B. S. Shastry, *Phys. Rev. B* **77**, 161101(R) (2008).
- ⁶⁹S. Chandrasekhar *Rev. Mod. Phys.* **15**, 1 (1943).
- ⁷⁰R. Steinigeweg and R. Schnalle, *Phys. Rev. E* **82**, 040103(R) (2010).
- ⁷¹J. Solyom, *Adv. Phys.* **28**, 209 (1979).
- ⁷²J. von Delft and H. Schoeller, *Ann. Phys. (Leipzig)* **7**, 225 (1998).
- ⁷³J. des Cloizeaux and M. Gaudin, *J. Math. Phys.* **7**, 1384 (1966).
- ⁷⁴L. Hulthén, *Arkiv. Mat. Astron. Fysik* **26A** No. 11 (1938).
- ⁷⁵T. Park and J. Light, *J. Chem. Phys.* **85**, 5870 (1986).
- ⁷⁶M. Hochbruck and C. Lubich, *SIAM J. Numer. Anal.* **34**, 1911 (1997).
- ⁷⁷I. McCulloch and M. Gulasci, *Europhys. Lett.* **57**, 852 (2002).

Chapter 3

Work distribution functions and x-ray edge absorption spectra

One of the first examples of a nonequilibrium many-body quantum system beyond the linear response regime addressed in the literature dates back to the asymptotic solution of the so-called x-ray edge problem by Nozieres and De Domenicis [128]. In the 1930's sharp peaks in optical x-ray spectra have been observed for simple metals, for details and references to theoretical and experimental work see the review by Ohtaka and Tanabe [129]. Within a perturbative treatment Mahan [115] showed to leading logarithmic accuracy that the absorption of an x-ray edge photon can lead to power-law singularities in the optical spectra, see Fig. 3.1. Later, it was realized that this complicated linear response many-body problem of matter-light interaction can be mapped onto an exactly solvable nonequilibrium one [128].

Consider an x-ray beam incident on a simple metal, for a schematic picture see Fig. 3.1. The conduction band is filled up with electrons up to the Fermi level. At energies far below the Fermi energy very narrow bands appear corresponding to nearly localized electrons bound to the core atoms constituting the lattice. Associated with the in general complicated band structure there is a multitude of different imaginable processes where electrons are excited between different bands. Among all possible excitation processes, however, there is just one specific that is responsible for the sharp experimentally observed peaks in the x-ray edge spectra. The excitation of localized electrons from the narrow tight-binding bands into the vicinity of the Fermi energy is accompanied with the creation of a localized immobile hole that is left behind. Due to Coulomb interactions the positively charged hole establishes a potential scatterer for the other electrons constituting the electronic conduction band. Associated with the sudden absorption of a photon is then the sudden creation of a localized impurity to which the conduction band electrons have to adapt to.

In general, x-ray edge absorption spectra $A(\omega)$ show a power-law behavior at zero temperature $T = 0$

$$A(\omega) \stackrel{\omega \approx \omega_{\text{th}}}{\sim} \theta(\omega - \omega_{\text{th}})(\omega - \omega_{\text{th}})^{-\gamma}, \quad T = 0, \quad (3.1)$$

beyond a threshold frequency ω_{th} with an exponent γ that is solely determined by the

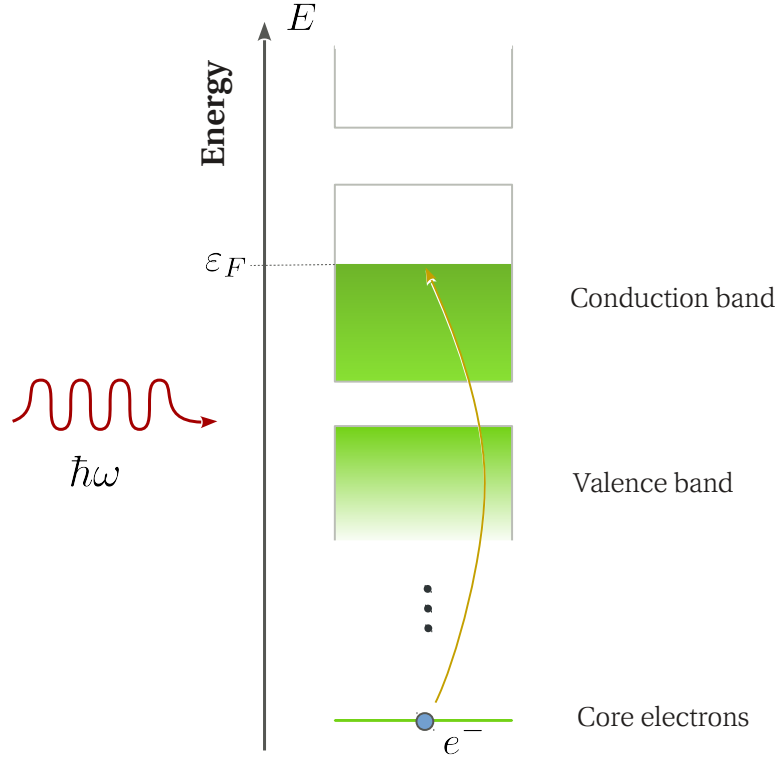


Figure 3.1: Schematic illustration of the band structure of a simple metal and the x-ray edge absorption process. All energy levels are filled up to the Fermi energy ε_F in the conduction band. Below the conduction band comes the valence band that is completely filled by electrons. For very low energies narrow tight-binding bands appear that are built out of strongly localized electrons bound to the core atoms. For an incoming x-ray beam of photons with angular frequency ω one can imagine a variety of different excitation processes. The x-ray edge singularity corresponds to a process where a core electron is excited to the Fermi energy. For details see the text.

phase shifts of the conduction band electrons at the Fermi level as argued by Hopfield [72]. For frequencies $\omega < \omega_{\text{th}}$ there are no available states for the excited core electron due to the Pauli principle such that no photon absorption can take place. By relating x-ray edge spectra to work distribution functions, see Sec. 3.1, the existence of the threshold frequency $\omega_{\text{th}} > 0$ can be traced back to the minimum work the photon has to perform on the system such that it can excite the core electron and to switch on the perturbation. The algebraic divergence as $\omega \rightarrow \omega_{\text{th}}$ signals that the absorption of a photon is most likely accompanied by the creation of a multitude of low-energy particle-hole excitations in the conduction band.

The power-law is valid on a scale set by the conduction bandwidth D , i.e., for $\omega \ll D$. In the simplest case of the switch on of a potential scatterer embedded in a sea of spinless fermions one obtains

$$\gamma = 1 - (1 - \delta/\pi)^2 \quad (3.2)$$

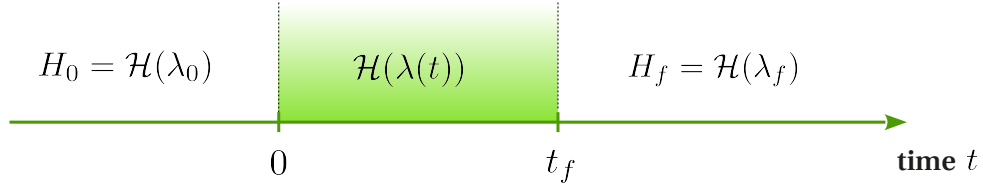


Figure 3.2: Schematic illustration of the general nonequilibrium protocol. The system is initially prepared in the canonical state of the Hamiltonian H_0 at a temperature T . In an interval from time $t = 0$ to $t = t_f$ an external force acts on the system leading to a time-dependent parameter $\lambda = \lambda(t)$ and a time-dependent Hamiltonian $\mathcal{H}(\lambda(t))$. At time t_f the protocol stops and the subsequent time evolution is governed by the final Hamiltonian H_f .

with δ the phase shift at the Fermi energy and $\delta/\pi = \Delta n$ is the screening charge Δn according to the Friedel sum rule. At finite temperatures $T > 0$ the singularity gets smeared and the absorption spectrum develops a Lorentzian form for frequencies $|\omega - \omega_{\text{th}}| \ll T$ [185, 20]

$$A(\omega) \stackrel{|\omega - \omega_{\text{th}}| \ll T}{\sim} \frac{\pi T \Delta n^2}{(\omega - \omega_{\text{th}})^2 + (\pi T)^2 \Delta n^4}, \quad T > 0. \quad (3.3)$$

At frequencies $T \ll \omega - \omega_{\text{th}} \ll D$, however, one still finds the power-law behavior as for the zero temperature limit, see Eq. (3.1). On the other side of the Lorentzian peak, $T \ll \omega_{\text{th}} - \omega \ll D$, the probability for photon absorption is nonzero in contrast to the zero temperature limit, but exponentially suppressed by temperature. This is a manifestation of the Crooks relation, a nonequilibrium fluctuation theorem which will be discussed in more detail in Sec. 3.2.2.

Although initially related to optical spectra, x-ray edge physics has been found in a variety of different scenarios but all sharing the same principle, namely that a fermionic many-particle system has to adapt to a suddenly created local perturbation. Recently, x-ray edge physics has regained particular interest since quantum dots in semiconductor heterostructures, see Sec. 3.4, provide the experimental framework for the implementation of quantum impurity models with a high control on the system parameters. Most notably in the present context, it has been demonstrated that optical spectra for specifically constructed quantum dots can be associated with x-ray edge spectra for the sudden switch on of a Kondo impurity [176, 104]. In the meantime the x-ray edge problem has been solved using a variety of different approaches, most notably bosonization in the weak scatterer limit [157] and by the Riemann-Hilbert approach [33] that will be used below for the calculation of optical quantum dot spectra.

3.1 Work distribution functions

From a thermodynamic perspective the work W performed on a system is an elementary quantity for the description of systems in a nonequilibrium process - especially when considering closed isolated system when there is no heat exchange with an environment as will

be the case for all examples studied in the following. Remarkably, the definition of work performed on a quantum system has been clarified only recently [167]. As a consequence of fundamental quantum mechanical principles work cannot be represented by a Hermitian operator leading to the notion of “work is not an observable”. The origin lies at the observation that two projective quantum mechanical measurements are required to actually determine the work performed. As a consequence the work W is a random variable with a probability distribution function $P(W)$ termed work distribution.

Consider a closed isolated quantum system with a Hamiltonian $\mathcal{H}(\lambda)$ that is prepared in a canonical state at temperature $T = \beta^{-1}$. Here and in the following we set Boltzmann’s constant $k_B = 1$. The system is supposed to depend on a classical parameter λ that can be manipulated by acting with some external force. The system is taken out of equilibrium by changing the parameter λ from a value λ_i to λ_f according to a prescribed protocol during a time interval from $t = 0$ to $t = t_f$, for a schematic picture see Fig. 3.2. Due to the inherent randomness in the initial mixed state its energy is not known with certainty but can be determined by a projective measurement that yields the energy E_n^i corresponding to the eigenstate $|E_n^i\rangle$ with a probability

$$p_n = \frac{e^{-\beta E_n^i}}{Z^i} \quad (3.4)$$

with $Z^i = \sum_n \exp[-\beta E_n^i] = \text{Tr} \exp[-\beta \mathcal{H}(\lambda_i)]$ the partition function of the initial state. Here, $|E_n^i\rangle$ denotes a complete set of eigenstates with eigenenergies E_n^i for the Hamiltonian $\mathcal{H}(\lambda_i)$. As a consequence of the measurement the mixed state is projected onto the eigenvector $|E_n^i\rangle$. Due the nonequilibrium protocol this state is time evolved with the operator $U(t_f)$ determined by its equation of motion

$$i \frac{d}{dt} U(t) = \mathcal{H}[\lambda(t)] U(t) \quad (3.5)$$

with $U(0) = 1$, $\lambda(0) = \lambda_i$, and $\lambda(t_f) = \lambda_f$. Here we set $\hbar = 1$. The probability that the time evolved state $|E_n^i(t_f)\rangle = U(t_f)|E_n^i\rangle$ has energy $E_m^f - |E_m^f\rangle$ denotes the full set of eigenstates for $\mathcal{H}(\lambda_f)$ - is given by the conditional probability

$$p(m, t_f | n) = |\langle E_m^f | U(t_f) | E_n^i \rangle|^2. \quad (3.6)$$

The two energy measurements for this single realization of the nonequilibrium protocol determine the corresponding work performed W via $W = E_n^f - E_n^i$. The associated probability distribution $P(W)$ for W is then given by summing over all possible initial and final states with the same energy difference W [167]

$$P(W) = \sum_{n,m} p_n p(m, t_f | n) \delta(W - E_n^f + E_n^i). \quad (3.7)$$

In the literature $P(W)$ as defined in this equation appears also in different contexts. In studies of quantum chaos $P(W)$ is termed strength function [47]. In work about nonequilibrium dynamics in quantum many-body systems $P(W)$ is associated with an energy

distribution function [136, 144, 116]. Concerning optical x-ray edge experiments $P(W)$ can be associated with absorption and emission spectra, see Secs. 3.3 and 3.5.

Work distribution functions are related to dynamical correlation functions via Fourier transformation [167]

$$P(W) = \int dt e^{iWt} G(t), \quad G(t) = \langle e^{i\mathcal{H}(\lambda_i)t} e^{-i\mathcal{H}_H(\lambda_f)t} \rangle, \quad \langle \dots \rangle = \text{Tr} \left[\frac{e^{-\beta\mathcal{H}(\lambda_i)}}{Z^i} \dots \right], \quad (3.8)$$

where $\mathcal{H}_H(\lambda_f) = U^\dagger(t_f)\mathcal{H}(\lambda_f)U(t_f)$ with U the full time evolution operator obeying the operator equation analogue to the Schrödinger equation, see Eq. (3.5). The simplest case and the most important one for what follows is that of a quench where a parameter of the Hamiltonian is changed suddenly. For such a particular protocol we have that $t_i = t_f = 0$ yielding a trivial time evolution operator $U = 1$. The dynamical correlation function $G(t)$ then reduces to the expectation value of two counter propagating time evolution operators

$$G(t) = \langle e^{i\mathcal{H}(\lambda_i)t} e^{-i\mathcal{H}(\lambda_f)t} \rangle. \quad (3.9)$$

Considering the contribution in the Hamiltonian that is suddenly switched on as a perturbation $G(t)$ may be interpreted as a measure for the “dynamical” strength of the perturbation and its influence on the system’s time evolution - $G(t)$ compares the dynamics of the unperturbed system with the perturbed one. This becomes even more transparent in the zero temperature limit when the system is initially prepared in the ground state $|\psi_0\rangle$ of the Hamiltonian $\mathcal{H}(\lambda_i)$

$$G(t) = \langle \psi_0 | e^{i\mathcal{H}(\lambda_i)t} e^{-i\mathcal{H}(\lambda_f)t} | \psi_0 \rangle. \quad (3.10)$$

where the dynamical correlation function $G(t)$ reduces to the overlap of two states time-evolved with different Hamiltonians. In this way it quantifies the stability of quantum motion [131]. The modulus $\mathcal{L}(t) = |G(t)|^2$ of $G(t)$ is termed the Loschmidt echo [78, 89, 162] and may be associated with a return probability in the spirit of Loschmidt’s *gedanken* experiment about microreversibility in all physical laws. For more details see Sec. 4.

3.2 Work fluctuation theorems

If an external force acting on the system under study is sufficiently weak for a perturbative treatment, the system’s properties are completely determined by linear response theory where the influence of the external perturbation is fully encoded in the equilibrium fluctuations. This manifests in the famous fluctuation-dissipation theorem [24]. For external forces that cannot be considered as weak the fluctuation dissipation theorem is violated and the system is driven out of equilibrium. It has been discovered recently that there exists a more general class of fluctuation theorems that are valid also for systems arbitrarily far away from equilibrium [25]. Among these are the so-called work fluctuation theorems such as the Jarzynski equality [80], the Crooks relation [32], and the Bochkov-Kuzovlev theorem [19, 27].

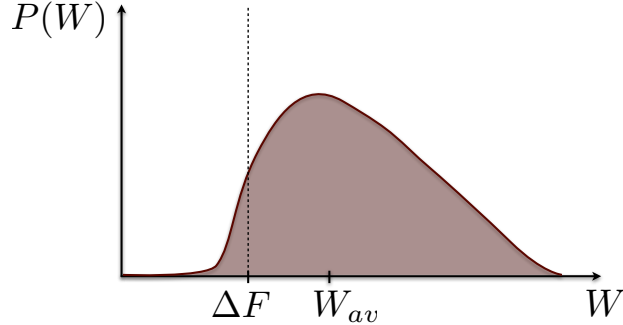


Figure 3.3: Schematic plot of a work distribution function $P(W)$. The average work performed $W_{av} \geq \Delta F$ is bounded from below by the free energy difference ΔF due to the second law of thermodynamics. There are individual but unlikely processes with $W < \Delta F$ where work can be extracted from the system. Note, however, that this does not correspond to a "violation" of the second law of thermodynamics, see text.

3.2.1 Jarzynski equality

Preparing the system of interest in a canonical state at a temperature T the second law of thermodynamics gives a lower bound on the average work performed

$$W_{av} = \int dW W P(W) \geq \Delta F. \quad (3.11)$$

set by ΔF where $\Delta F = F(\lambda_f, T) - F(\lambda_i, T)$ is determined by the difference in free energies of the system at the same temperature T but for different parameters λ_f and λ_i . The lower bound is reached for reversible processes. In Fig. 3.3 a schematic plot of a work distribution function is shown. Although the average work W_{av} is larger than ΔF there are individual processes with $W < \Delta F$ and a nonzero probability to extract work from the system. Note, however, that this does not correspond to a "violation" of the second law of thermodynamics as the average work still obeys Eq. (3.11).

There is, however, a much stronger result than the lower bound given by the second law of thermodynamics that is called the Jarzynski equality [80]

$$\langle e^{-\beta W} \rangle_P = e^{-\beta \Delta F}, \quad \langle \dots \rangle_P = \int dW \dots P(W). \quad (3.12)$$

It relates the work distribution function to free energy differences not by a lower bound but via an equality. First shown for classical systems [80], the Jarzynski equality has later been proven also for quantum systems [123]. It connects an inherently nonequilibrium quantity - the work distribution function $P(W)$ - with the purely equilibrium quantities temperature $T = \beta^{-1}$ and free energies ΔF . Weighting the work distribution with an exponential $\exp[-\beta W]$ washes out all the nonequilibrium details. This is even more remarkable because Eq. (3.12) is valid for arbitrary nonequilibrium protocols. The probability distribution $P(W)$ depends on the precise path in parameter space whereas its weighted integral only

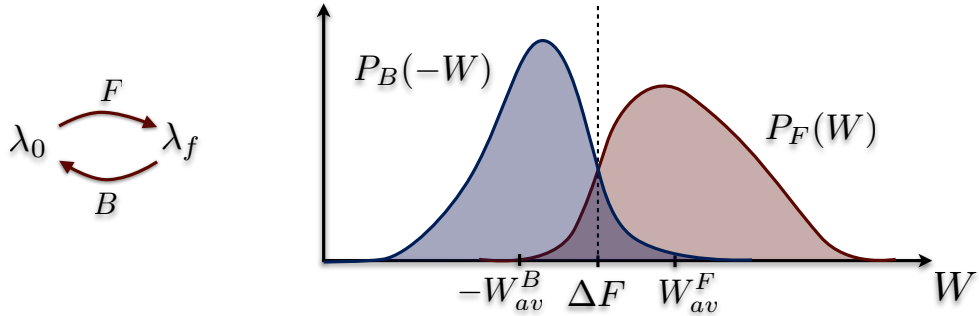


Figure 3.4: Within the protocol (F) of the forward process the system parameter λ is varied from λ_0 to a value λ_f . For the backward process (B) the protocol is executed in the time-reversed way. The right-hand side shows a schematic plot of the forward work distribution function $P_F(W)$ and the work distribution function $P_B(-W)$ for the backward process at minus the work performed. As a consequence of the Crooks relation both distributions intersect each other exactly at one point where $W = \Delta F$ irrespective of the nonequilibrium protocol. For more details see text.

about the initial preparation and a hypothetical equilibrium system at temperature T and value λ_f of the external parameter.

The Jarzynski equality allows to deduce equilibrium quantities, ΔF , from nonequilibrium measurements. The equilibrium information is hidden in the work distribution $P(W)$ and can be revealed by the appropriate average. Consequently, the Jarzynski equality has been used to determine free energy differences of classical systems in experiments [36, 110]. Concerning quantum systems, however, there has been no experimental verification due to difficulties to measure the corresponding work distribution function. Recently, there has been a proposal using cold ions in a harmonic traps [73]. This proposal has, however, not been realized yet. In Sec. 3.3 below it will be shown that work distributions of quantum impurity models have been measured for decades in terms of x-ray edge spectra which in principle allows for the study of the Jarzynski equality in experiments.

The second law of thermodynamics can be inferred from the Jarzynski equality using Jensen's inequality [168]. It should be noted, however, that this does not constitute a proof of the second law as the derivation of Eq. (3.12) already relies on basic thermodynamic principles through the initial canonical state. In contrast to the second law of thermodynamics the Jarzynski equality also holds for microscopic systems provided the initial state before the start of the nonequilibrium protocol can be described by a canonical ensemble. Therefore, Eq. (3.12) constitutes an extension of the second law to microscopic systems.

3.2.2 The Crooks relation

Consider now both the forward and backward nonequilibrium protocols. Within the backward process the system is initially prepared in the canonical state of the Hamiltonian $\mathcal{H}(\lambda_f)$ at the same temperature T . At time $t = 0$ the nonequilibrium protocol is started

where the parameter of the backward process $\lambda_B(t)$ changes according to $\lambda_B(t) = \lambda_F(t_f - t)$ where $\lambda_F(t)$ is the parameter dependence for the forward protocol. In the following the work distribution functions for the forward and backward protocols will be denoted by $P_F(W)$ and $P_B(W)$, respectively. From the second law of thermodynamics one can again deduce for the average work W_{av}^B of the backward process

$$W_{\text{av}}^B = \int dW W P_B(W) \geq -\Delta F \Rightarrow \int dW W P_B(-W) \leq \Delta F \quad (3.13)$$

where the free energy difference $\Delta F = F(\lambda_f, T) - F(\lambda_i, T)$ is defined as in Eq. (3.11). Based on this observation the mean of $P_B(-W)$ is located at a value smaller than ΔF as is schematically indicated in Fig. 3.4. As a consequence $P_F(W)$ and $P_B(-W)$ have to intersect each other at least in one point in case where their support is not too small as is typically the case for nonzero temperatures. As it turns out, however, see below, there cannot be more than one intersection point.

Independent of the details of the nonequilibrium protocol and the considered system the forward at backward work distributions are connected via a universal relation - the Crooks relation [32]

$$\frac{P_F(W)}{P_B(-W)} = e^{\beta(W - \Delta F)}. \quad (3.14)$$

First proven for classical systems [32] its validity has later been extended to closed [168, 166] and open quantum systems [26]. For open quantum systems however, the meaning of the free energy difference ΔF changes and contributions from the coupling to the environment have to be included [26].

As is the case for the Jarzynski equality, see Eq. (3.12), the Crooks relation establishes a connection between nonequilibrium ($P_F(W), P_B(W)$) and equilibrium quantities ($T = \beta^{-1}, \Delta F$). The Crooks relation is more general than the Jarzynski equality because the former can be deduced from the latter as its integral version [32]:

$$P_F(W)e^{-\beta W} = P_B(-W)e^{-\beta \Delta F} \Rightarrow \int dW e^{-\beta W} P_F(W) = e^{-\beta \Delta F}. \quad (3.15)$$

Despite of being more general, an additional advantage of the Crooks relation is that it is local in W in contrast to the Jarzynski equality for which $P(W)$ has to be known for all relevant values of W . This is especially important for experiments as due to the exponential weight $e^{-\beta W}$ in Eq. (3.12) $P(W)$ is amplified exponentially for negative values of W . Thus, the small values of $P(W)$ for negative W have to be resolved with a high precision in measurements. On the other hand, the Crooks relation requires the measurement of two different work distributions. For certain cases, however, as will be shown below, see Sec. 3.3, the Crooks relation can also manifest in a *single* work distribution.

For the value $W = \Delta F$ the two work distribution functions $P_F(\Delta F) = P_B(-\Delta F)$ have to intersect each other. As $e^{\beta W}$ is a monotonously increasing function there can only be this one intersection point. In case of zero temperature initial states the Crooks relation implies that $P_F(W) = 0$ for $W < \Delta E$ and $P_B(-W) = 0$ for $W > \Delta E$ with

$\Delta E = E_{\text{gs}}(\lambda_f) - E_{\text{gs}}(\lambda_i) = \lim_{T \rightarrow 0} \Delta F$ the ground state energy difference and thus restricts the support of the work distribution functions. At zero temperature the energy of the initial state - the respective ground state - is precisely known such that there are no fluctuations arising from the initial energy measurement. The minimum work that has to be performed on the system is thus the ground state energy difference yielding the restriction of the support. Note that for this special case it is possible to define a work operator, for the forward process this is $\hat{W}_F = \mathcal{H}(\lambda_f) - E_{\text{gs}}(\lambda_i)$, as it is not necessary to perform two energy measurements.

As in case of the Jarzynski equality, the Crooks relation has been used in experiments for the measurement of equilibrium free energy differences in classical systems [30, 83]. Moreover, the Crooks relation has been verified in electrical circuits in the linear response regime [53], mechanical oscillators [36], for small colloidal particles experiencing entropy changes when translated through surrounding water while captured in an optical trap [179] and for nonthermal systems, specifically a driven two-level system in a non-equilibrium steady state [158].

3.3 Publication: The Crooks relation in optical spectra

As already indicated before, work distributions have up to now only been measured for classical but not quantum systems. The main difficulty stems from the observation that work is not an observable as discussed in Sec. 3.1. Instead, two energy measurements are necessary to determine the work performed on the system where at least the first one has to be nondestructive which poses a great challenge on the experimental viability. Recently, a measurement scheme for cold ions in optical traps has been proposed [73] but not realized yet. Below, it is shown that work distribution functions have already been measured for decades. X-ray edge absorption and emission spectra can be identified with work distributions for the sudden switch on or off of a local perturbation embedded into a fermionic bath.

Using optical spectra for measuring work distributions the practical problem of implementing the sequence of a nondestructive first energy measurement, applying the perturbation, and performing the second energy measurement is carried out in a single step. A photon of angular frequency ω can be absorbed if and only if its energy $\hbar\omega$ precisely equals the energy difference between initial and final state. In this way the photon performs two energy measurements at the same time. It provides its energy $\hbar\omega$ to the system and thereby performs the work $W = \hbar\omega$. Moreover, for the X-ray edge type problems the absorption is associated with the sudden switch on of a local perturbation such that the absorption process incorporates all necessary and elementary ingredients for work distributions.

For the x-ray edge problem absorption and emission correspond to forward and backward processes allowing for the experimental verification of the Crooks relation, see Sec. 3.2.2, for quantum systems in experiments. This requires the measurement of two different spec-

tra, absorption and emission. For the particular case of a weak local perturbation, it is shown below that there exists an additional symmetry relating absorption and emission spectra such that the Crooks relation manifests already in a single spectrum. This result holds in second order renormalized perturbation theory and applies also to strongly-correlated impurity systems such as the Kondo model at sufficiently high temperatures.

Crooks Relation in Optical Spectra: Universality in Work Distributions for Weak Local Quenches

M. Heyl

*Department of Physics, Arnold Sommerfeld Center for Theoretical Physics, and Center for NanoScience,
Ludwig-Maximilians-Universität München, Theresienstrasse 37, 80333 Munich, Germany*

S. Kehrein

*Department of Physics, Arnold Sommerfeld Center for Theoretical Physics, and Center for NanoScience,
Ludwig-Maximilians-Universität München, Theresienstrasse 37, 80333 Munich,
Germany and Georg-August-Universität Göttingen, Friedrich-Hund-Platz 1, 37077 Göttingen*

(Received 28 June 2010; revised manuscript received 9 March 2012; published 7 May 2012)

We show that work distributions and nonequilibrium work fluctuation theorems can be measured in optical spectra for a wide class of quantum systems. We consider systems where the absorption or emission of a photon corresponds to the sudden switch on or off of a local perturbation. For the particular case of a weak local perturbation, the Crooks relation establishes a universal relation in absorption as well as in emission spectra. Because of a direct relation between the spectra and work distribution functions this is equivalent to universal relations in work distributions for weak local quenches. As two concrete examples we treat the x-ray edge problem and the Kondo exciton.

DOI: 10.1103/PhysRevLett.108.190601

PACS numbers: 05.70.Ln, 05.40.-a, 78.67.Hc, 78.70.Dm

Equilibrium thermodynamics provides the framework for the description of the equilibrium properties of macroscopically large systems. This includes the properties of systems in equilibrium states as well as the description of transitions between different equilibrium states even if the system is not in equilibrium in the meantime. Starting in 1997 with a seminal contribution from Jarzynski [1], the field of nonequilibrium work fluctuation theorems [2] opened up. These relate a measurable nonequilibrium quantity, the work performed, to equilibrium free energies even if the system is driven arbitrarily far away from equilibrium.

Suppose a system is prepared in a thermal state at inverse temperature β . If the Hamiltonian $H(t)$ of the system changes during a time interval from 0 to t_f according to a prescribed protocol, work is performed on the system. In order to determine the work done two energy measurements are necessary leading to the notion that work is not an observable [3]; the work W rather is a random variable with a probability distribution function [3]

$$P_F(W) = \int \frac{ds}{2\pi} e^{iWs} G(s), G(s) = \langle e^{iH(0)s} e^{-iH_H(t_f)s} \rangle. \quad (1)$$

Here $\langle \dots \rangle$ denotes the thermal average over the initial state and $H_H(t_f) = U^\dagger(t_f)H(t_f)U(t_f)$ with $U(t_f)$ the time-evolution operator obeying the differential equation $i\partial_t U(t) = H(t)U(t)$. In this Letter we set $\hbar = 1$.

Let $P_B(W)$ be the probability distribution function for the backward protocol. Then the Crooks relation, first shown for classical systems [4] and later extended to closed as well as open quantum systems [5–7]:

$$\frac{P_F(W)}{P_B(-W)} = e^{\beta(W - \Delta F)}, \quad (2)$$

establishes a universal connection between the forward and backward processes that only depends on the equilibrium free energy difference ΔF of the final and initial state independent of the details of the protocol. The Jarzynski relation [1] is a consequence of Eq. (2), see, e.g., Ref. [4].

Experimental tests of the Crooks relation have been performed in recent years for classical systems. Among these are folding-unfolding experiments of small RNA-hairpins where the free energy difference between the folded and unfolded state has been extracted using the Crooks relation [8,9]. Moreover, it has been verified in electrical circuits [10], for mechanical oscillators [11], small colloidal particles [12], and nonthermal systems [13].

In the quantum case a measurement of work distributions has not been performed up to now. Recently, a measurement scheme in optical traps has been proposed [14] that has not been realized yet. In the present Letter we show that work distributions of quantum systems have been measured for decades in terms of x-ray spectra of simple metals. We point out that there exists a large class of quantum systems associated with the x-ray edge problem where absorption spectra $A(\omega)$ and emission spectra $E(\omega)$ can be identified with forward and backward work distributions for a sudden switch on or off of a local perturbation. This allows for an experimental observation of nonequilibrium work fluctuation theorems such as the Crooks relation. For the particular case of a weak local perturbation, the Crooks relation manifests in the universal relations

$$\frac{A(\omega + \Delta F)}{A(-\omega + \Delta F)} = e^{\beta\omega}, \quad \frac{E(\omega + \Delta F)}{E(-\omega + \Delta F)} = e^{-\beta\omega} \quad (3)$$

that hold in second order renormalized perturbation theory. This is the central result of this Letter that will be proven below. Here ΔF is the free energy difference between the system with and without local perturbation at the same inverse temperature β . Notice that an independent measurement of ΔF is not required to establish Eq. (3) in an experiment. Actually, Eq. (3) permits a determination of ΔF similar to experiments in biophysics [8,9]. Because of the correspondence between spectra and work distributions, Eq. (3) implies universal relations for work distributions of weak local quenches:

$$\frac{P_F(W + \Delta F)}{P_F(-W + \Delta F)} = e^{\beta W}, \quad \frac{P_B(W - \Delta F)}{P_B(-W - \Delta F)} = e^{\beta W}. \quad (4)$$

Here, $P_F(W)$ is the work distribution for a protocol where the local perturbation is suddenly switched on and $P_B(W)$ the work distribution for the backward protocol.

Consider a system weakly coupled to a monochromatic light field of frequency ω where the absorption or emission of a photon corresponds to the sudden switch on or off of a local perturbation. Such systems have been discussed extensively in the literature. In the x-ray spectra of simple metals a system of free fermions has to adapt to a suddenly created or annihilated local potential scatterer [15–18]. For metals with incomplete shells the local perturbation is related to localized orbitals [18,19]. As has been shown recently, spectra of quantum dots allow for an idealized implementation of x-ray edge type problems [20,21]. In the remainder, H denotes the Hamiltonian with the local perturbation and H_0 without, respectively.

Crooks relation in absorption and emission spectra.—First, we concentrate on the absorption case, the related emission spectra will be discussed below. The absorption spectrum for incident light of frequency ω in second order of the system-light field coupling (Fermi's golden rule) is related to a dynamical correlation function via Fourier transformation

$$A(\omega) = \kappa_A \int \frac{dt}{2\pi} e^{i\omega t} G_A(t). \quad (5)$$

The constant κ_A contains parameters depending on the experimental details such as the intensity of the incident light beam or the system-light field coupling. Note that the photon energy ω in Eq. (5) is not the bare one, it is usually measured relative to a constant offset ω_0 , e.g., the core-hole binding energy in the x-ray edge problem. We consider those systems where the dynamical correlation function $G_A(t)$ appearing in Eq. (5) is of the structure

$$G_A(t) = \frac{1}{Z_A} \text{Tr}(e^{-\beta H_0} e^{iH_0 t} e^{-iHt}), \quad Z_A = \text{Tr}(e^{-\beta H_0}) \quad (6)$$

as in the case of x-ray edge type problems [15–21]. For a particular problem at hand, the question of whether $G_A(t)$ can be brought into the form in Eq. (6) has to be studied on a case by case basis. Regarding Eq. (6) $G_A(t)$ is the characteristic function of a work distribution for a quench from H_0 to H , cf. Eq. (1). This identification allows for an observation of the Crooks relation in an optics experiment. Recently, x-ray edge singularities have been found in work distributions for local quenches in an Ising chain at criticality [22].

The emission spectrum $E(\omega)$ corresponding to the same setup is given by

$$E(\omega) = \kappa_E \int \frac{dt}{2\pi} e^{-i\omega t} G_E(t) \quad (7)$$

with

$$G_E(t) = \frac{1}{Z_E} \text{Tr}(e^{-\beta H} e^{iHt} e^{-iH_0 t}), \quad Z_E = \text{Tr}(e^{-\beta H}). \quad (8)$$

Hence, $E(-\omega)$ is proportional to the work distribution for a protocol where the local perturbation is switched off, that is precisely the backward process to absorption. A direct application of the Crooks relation in Eq. (2) therefore yields

$$\frac{A(\omega)}{E(\omega)} = \frac{\kappa_A}{\kappa_E} e^{\beta(\omega - \Delta F)} \quad (9)$$

as an exact result. This relation depends on experimental details through the parameters κ_A and κ_E . The linear scaling of $\ln(A(\omega)/E(\omega))$ as a function of the frequency ω of the light beam, however, is universal with a slope β . Note that Eq. (9) is valid for an arbitrary strength of the local perturbation, we only assume a small coupling to the external light field.

Two different measurements, absorption and emission, are necessary to explore this relation in experiment. However, the Crooks relation can also be measured in a single experiment in case of weak local perturbations where Eq. (3) holds as will be shown below. This has the additional advantage as opposed to the exact relation in Eq. (9) that also the experiment specific constants κ_A and κ_E drop out.

Equations (1), (6), and (8), show the formal equivalence between work distribution functions and optical x-ray edge spectra. In conventional experiments the work distribution function is sampled by recording in each realization the work performed. The full distribution function is successively built up jointly over all work values. Optical spectra, however, are recorded differently. The outcome of a measurement is not the work performed. Instead one obtains directly the probability for photon absorption (or emission) at a given frequency ω (work performed). The full distribution function is then constructed by sweeping the laser through all relevant frequencies.

The advantage of measuring work distributions via optical spectra is that the absorbed photon carries out the sequence of measuring the energy in the initial state, applying the perturbation, and measuring the energy of the final state, in a single step. It can be absorbed or emitted only in case when its frequency ω matches precisely the energy difference between the system's initial and final state. The disadvantage is that only specific local perturbations and only specific protocols (sudden switchings) can be implemented.

Crooks relation in a single spectrum.—Suppose V is the unitary transformation that diagonalizes the Hamiltonian H . In the following we normal order Hamiltonians relative to the finite temperature initial mixed state [23]. For generic weak coupling impurity problems the diagonalized Hamiltonian can be represented as [24]

$$VHV^\dagger = H_0 + \Delta F \quad (10)$$

in the thermodynamic limit [25] where ΔF denotes the free energy difference between the systems described by H and H_0 at the same temperature T . The appearance of temperature in this equation can be understood from the normal ordering procedure [24]. As a consequence of Eq. (10), the dynamical correlation functions $G_{A/E}(t)$ can be written as

$$\begin{aligned} G_A(t) &= \frac{1}{Z_A} \text{Tr}(e^{-\beta H_0} V^\dagger(t) V) e^{-i\Delta F t}, \\ G_E(t) &= \frac{1}{Z_A} \text{Tr}(e^{-\beta H_0} V(t) V^\dagger) e^{i\Delta F t} e^{-\beta \Delta F}, \end{aligned} \quad (11)$$

where $V(t) = e^{iH_0 t} V e^{-iH_0 t}$ and $\Delta F = -\beta^{-1} \log(Z_E/Z_A)$. For all the relevant cases, it is possible to represent the unitary transformation V as an ordered exponential $V = O \exp[\chi]$ where χ is anti-Hermitian, $\chi^\dagger = -\chi$, and O denotes some ordering prescription. For generic weak coupling problems such as the Kondo model at nonzero temperature analyzed later, the flow equation approach provides a general prescription for the construction of the unitary transformation V as an ordered exponential of its generator $\eta(B)$ [26]

$$V = \mathcal{T}_B \exp \left[\int_0^\infty dB \eta(B) \right], \quad (12)$$

where $\eta(B)$ is determined by a set of differential equations. For $B > B'$, \mathcal{T}_B orders an $\eta(B)$ left of an $\eta(B')$. Expectation values of ordered exponentials such as in Eq. (11) can be related to the exponential of a cumulant average [27] that can be expanded in a power series in powers of χ . The first cumulant vanishes as χ can be chosen normal ordered relative to the initial state. For the x-ray edge problem the cumulant expansion stops at second order within the validity of the bosonization technique, see below. For more complicated problems such as the Kondo exciton the diagonalizing unitary transformation can be obtained by the flow equation framework, see Eq. (12). In this case, the generator $\eta(B)$ and thus the

operator χ is proportional to the strength of the local perturbation such that in the case of a weak local perturbation the expansion is controlled by a small parameter. For systems with significant renormalization effects, couplings have to stay small over the whole renormalization flow.

Performing this cumulant expansion up to second order one observes that $G_A(t)$ and $G_E(t)$ are directly related to each other via $G_A(t)e^{i\Delta F t} = G_E(t)e^{-i\Delta F t}e^{-\beta \Delta F}$. For the spectra this result implies $\kappa_A E(\omega + \Delta F)e^{-\beta \Delta F} = \kappa_E A(-\omega + \Delta F)$. Plugging this relation into the Crooks relation, see Eq. (9), one directly proves the main result, Eq. (3), in second order renormalized perturbation theory.

In the remainder of this Letter, we will discuss two examples for the Crooks relation in absorption spectra: the x-ray edge problem and the Kondo exciton.

The x-ray edge problem.—In the x-ray edge problem the absorption of a photon is accompanied by the sudden creation of a local potential scatterer in a sea of noninteracting fermions [16]. Hence, we have $H_0 = \sum_k \varepsilon_k : c_k^\dagger c_k :$ and $H = H(g) = H_0 + (2\pi/L)g \sum_{kk'} : c_k^\dagger c_{k'} :$ where the colons denote normal ordering, see [24]. We consider a linearized dispersion $\varepsilon_k = v_F k$ and set $v_F = 1$. The Fourier transform of the absorption spectrum is given by [16]

$$S(t) = \frac{1}{Z_A} \text{Tr}(e^{-\beta H_0} e^{iH_0 t} \psi(0) e^{-iH(g)t} \psi^\dagger(0)) \quad (13)$$

that is yet not in the desired form as in Eq. (6). Using the bosonization technique, the fermionic fields $\psi(x)$ can be represented in terms of bosonic ones, $\phi(x)$, via $\psi(x) = a^{-1/2} F e^{-i\phi(x)}$ with a^{-1} an ultraviolet cutoff [28]. The Klein factor F commutes with $H(g)$ and does not contribute to $S(t)$ due to its property $FF^\dagger = 1$. The bosonization identity allows us to regard the fermionic fields as a unitary transformation acting on $H(g)$ such that $S(t) \propto G_A(t)e^{-i\Delta t}$ with a constant energy shift Δ that can be absorbed into a redefinition of the constant offset ω_o and $G_A(t)$ is in the desired form:

$$G_A(t) = \frac{1}{Z_A} \text{Tr}(e^{-\beta H_0} e^{iH_0 t} e^{-iH(1+g)t}). \quad (14)$$

The diagonalizing transformation V of $H(1+g)$ equals $V = e^{i(1+g)\phi(0)}$ [17]. Although the effective strength of the scatterer $1+g$ is not small, the cumulant expansion stops at second order as the operator in the exponent is linear in bosonic operators. Hence, in the range of validity of the bosonization treatment, the Crooks relation in Eq. (3) holds exactly for the x-ray edge absorption spectrum. Comparing bosonization [17] with the exact treatment [16], it yields the correct result up to second order in g . This restriction originates from the linearization of the free fermionic spectrum [17].

The Kondo exciton.—Recently, Türeci *et al.* [21] proposed an experimental setup for a quantum dot where the absorption of a photon corresponds to the sudden

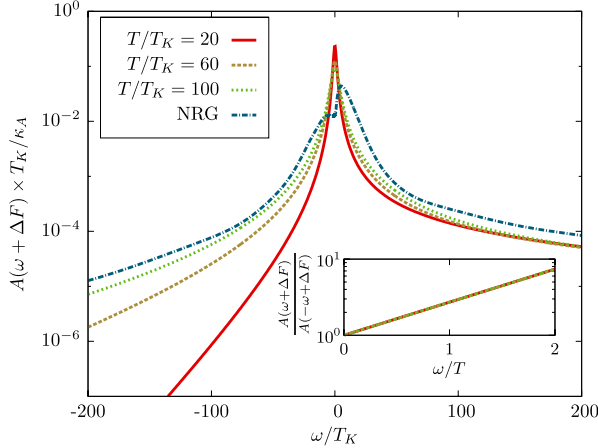


FIG. 1 (color online). Absorption spectrum of a Kondo exciton for different temperatures as a function of the light frequency. As a reference, a NRG curve for $T = 100T_K$ is shown taken from Türeci *et al.* [21]. In the regime $|\omega| \gtrsim T$ where the NRG data are accurate the agreement is excellent within the numerical accuracy. The inset exemplifies the validity of the Crooks relation in the absorption spectrum of the Kondo exciton, all curves for $T/T_K = 20, 60, 100$ lie on top of each other when plotted against ω/T .

switch on of a Kondo impurity. Hence, we have $H_0 = \sum_{k\sigma} \varepsilon_k : c_{k\sigma}^\dagger c_{k\sigma} :$ and $H = H_0 + \sum_{kk'} J_{kk'} : \vec{S} \cdot \vec{s}_{kk'} :$. For details about the Kondo problem, see, for example, Ref. [29]. The dynamical correlation function $G_A(t)$ for the absorption spectrum is given by Eq. (6). The diagonalizing unitary transformation V can be obtained by the flow equation approach [26], cf. Eq. (12), with $\eta(B) = \sum_{kk'} (\varepsilon_k - \varepsilon_{k'}) J_{kk'}(B) : \vec{S} \cdot \vec{s}_{kk'} :$ in 1-loop order. The couplings $J_{kk'}(B)$ are determined by a set of differential equations [30]. Importantly, the flow equation framework includes all the renormalization effects such as the emergence of a low-energy scale T_K , the Kondo temperature. The absorption spectrum is obtained via the cumulant expansion up to second order in the coupling strength. Its validity is restricted to weak coupling problems such that we have to require $T \gg T_K$ [31]. A plot of the absorption spectrum is shown in Fig. 1 for different temperatures. As a reference, a NRG curve for $T = 100T_K$ obtained by Türeci *et al.* [21] for an Anderson impurity model in the Kondo regime is included in this figure [32]. In the vicinity of the main peak at small $|\omega| < T$, the NRG calculation contains an unphysical double peak structure. For more details we refer to Ref. [21]. For frequencies $|\omega| \gtrsim T$, however, where the NRG data are accurate we observe excellent agreement with the results of the flow equation formalism. Asymptotic formulas for $A(\omega)$ in the limit $\omega \rightarrow \pm\infty$ can be found in Ref. [21]. The inset shows the validity of Eq. (3). The ratio $A(\omega + \Delta F)/A(-\omega + \Delta F)$ is the universal function $e^{\beta\omega}$ independent of any details.

Conclusions.—We have shown that work distributions and thus nonequilibrium work fluctuation theorems can be measured in optical spectra of quantum systems such as the x-ray edge problem or the Kondo exciton. For weak local perturbations, the Crooks relation establishes a universal relation within a single spectrum, absorption or emission, cf. Eq. (3).

We acknowledge fruitful discussions with Jan von Delft and Peter Hänggi. We thank Markus Hanl and Andreas Weichselbaum for providing us the NRG curve in Fig. 1. This work was supported by SFB TR12 of the Deutsche Forschungsgemeinschaft (DFG), the Center for Nanoscience (CeNS) Munich, and the German Excellence Initiative via the Nanosystems Initiative Munich (NIM).

- [1] C. Jarzynski, *Phys. Rev. Lett.* **78**, 2690 (1997).
- [2] M. Campisi, P. Hänggi, and P. Talkner, *Rev. Mod. Phys.* **83**, 771 (2011).
- [3] P. Talkner, E. Lutz, and P. Hänggi, *Phys. Rev. E* **75**, 050102(R) (2007).
- [4] G. E. Crooks, *Phys. Rev. E* **60**, 2721 (1999).
- [5] H. Tasaki, arXiv:cond-mat/0009244.
- [6] P. Talkner and P. Hänggi, *J. Phys. A* **40**, F569 (2007).
- [7] M. Campisi, P. Talkner, and P. Hänggi, *Phys. Rev. Lett.* **102**, 210401 (2009).
- [8] D. Collin *et al.*, *Nature (London)* **437**, 231 (2005).
- [9] I. Junier, A. Mossa, M. Manosas, and F. Ritort, *Phys. Rev. Lett.* **102**, 070602 (2009).
- [10] N. Garnier and S. Ciliberto, *Phys. Rev. E* **71**, 060101(R) (2005).
- [11] F. Douarche, S. Ciliberto, and A. Petrosyan, *J. Stat. Mech.* (2005) P09011.
- [12] G. M. Wang, E. M. Sevick, E. Mittag, D. J. Searles, and D. J. Evans, *Phys. Rev. Lett.* **89**, 050601 (2002).
- [13] S. Schuler, T. Speck, C. Tietz, J. Wrachtrup, and U. Seifert, *Phys. Rev. Lett.* **94**, 180602 (2005).
- [14] G. Huber, F. Schmidt-Kaler, S. Deffner, and E. Lutz, *Phys. Rev. Lett.* **101**, 070403 (2008).
- [15] G. D. Mahan, *Phys. Rev.* **163**, 612 (1967).
- [16] P. Nozieres and C. T. De Dominicis, *Phys. Rev.* **178**, 1097 (1969).
- [17] K. D. Schotte and U. Schotte, *Phys. Rev.* **182**, 479 (1969).
- [18] K. Ohtaka and Y. Tanabe, *Rev. Mod. Phys.* **62**, 929 (1990).
- [19] A. Kotani and Y. Toyozawa, *J. Phys. Soc. Jpn.* **35**, 1073 (1973).
- [20] M. Heyl and S. Kehrein, *Phys. Rev. B* **85**, 155413 (2012).
- [21] H. E. Türeci *et al.*, *Phys. Rev. Lett.* **106**, 107402 (2011).
- [22] A. Silva, *Phys. Rev. Lett.* **101**, 120603 (2008).
- [23] G. C. Wick, *Phys. Rev.* **80**, 268 (1950).
- [24] See Supplemental Material at <http://link.aps.org/supplemental/10.1103/PhysRevLett.108.190601> for details about the diagonal structure of locally perturbed Hamiltonians.
- [25] We restrict to situations without bound states.
- [26] S. Kehrein, *The Flow Equation Approach to Many-Particle Systems* (Springer, Berlin, 2006).
- [27] R. Kubo, *J. Phys. Soc. Jpn.* **17**, 1100 (1962).

- [28] J. von Delft and H. Schoeller, *Ann. Phys. (Leipzig)* **7**, 225 (1998).
- [29] A. C. Hewson, *The Kondo Problem to Heavy Fermions* (Cambridge University Press, Cambridge, 1993).
- [30] P. Fritsch and S. Kehrein, *Ann. Phys. (N.Y.)* **324**, 1105 (2009).
- [31] Details of this calculation will be presented elsewhere.
- [32] There is no fitting parameter since the Kondo temperatures from the $T = 0$ impurity contribution to the specific heat (T_K^{NRG}) and of the high temperature expansion via the flow equations ($T_K^{\text{f eq}}$) are linked by the Wilson number $w = 0.4128$ via $T_K^{\text{f eq}} = w T_K^{\text{NRG}}$ [29]. For the curves in Fig. 1 the temperatures are chosen according to T_K^{NRG} , i.e., $T_K = T_K^{\text{NRG}}$.

Supplementary Information

Markus Heyl¹ and Stefan Kehrein^{1,2}

¹*Department of Physics, Arnold Sommerfeld Center for Theoretical Physics, and Center for NanoScience, Ludwig-Maximilians-Universität München, Theresienstr. 37, 80333 Munich, Germany*

²*Georg-August-Universität Göttingen, Friedrich-Hund-Platz 1, 37077 Göttingen*

PACS numbers:

DETAILS ABOUT THE DIAGONAL STRUCTURE OF THE LOCALLY PERTURBED HAMILTONIAN

In this supplementary information we want to analyze the general statement about the diagonal structure of locally perturbed Hamiltonians in Eq. (10) of the main text for the case of a paradigmatic example, the potential scattering Hamiltonian H_p :

$$H_p = H_0 + g \frac{2\pi}{L} \sum_{kk'} c_k^\dagger c_{k'}, \quad H_0 = \sum_k \varepsilon_k c_k^\dagger c_k. \quad (1)$$

The fermionic operator c_k^\dagger creates a fermion in a state with wave vector k . For simplicity we restrict to the case of spinless fermions. The parameter g is the scattering amplitude and L is the system size.

Normal-ordering and energy offset

In the main text we normal-ordered the Hamiltonians relative the initial finite temperature mixed state at inverse temperature β . In the following, the normal ordered counterparts will be denoted by an additional superscript n

$$H_0^n = H_0 - \langle H_0 \rangle_0, \quad \langle \dots \rangle_0 = Z_0^{-1} \text{Tr} [e^{-\beta H_0} \dots], \quad Z_0 = \text{Tr} [e^{-\beta H_0}]. \quad (2)$$

In comparison with Eq. (1) the normal-ordered Hamiltonian H_0^n is shifted by a constant energy contribution $\langle H_0 \rangle_0$. In case of nonquadratic interacting systems such as the Kondo model in the main text the appropriate normal-ordering prescription is given by Wick [1].

In principle, temperature is a statistical property emerging on the macroscopic level, thus, it should not appear in the microscopic description of the system in terms of the Hamiltonian. However, there is a principal freedom of fixing the arbitrary global energy offset. In this work we choose the global offset in such a way that the thermal expectation value of the unperturbed system $\langle H_0^n \rangle_0 = 0$ vanishes in the initial state. The corresponding shifted potential scattering Hamiltonian is then given by

$$\tilde{H}_p = H_p - \langle H_0 \rangle_0 \quad (3)$$

Diagonalizing transformation

The potential scattering Hamiltonian in Eq. (1) can be diagonalized via a unitary transformation V

$$H_p^d = V H_p V^\dagger = \sum_k E_k c_k^\dagger c_k, \quad V = \exp [\chi], \quad \chi = \sum_{kk'} v_{kk'} c_k^\dagger c_{k'}, \quad (4)$$

for a suitably chosen matrix $v_{kk'}$ that is proportional to g for weak potential scatterers. As the potential scatterer is a local perturbation in a large system of size L the dispersion E_k coincides with ε_k up to finite-size corrections

$$E_k = \varepsilon_k + \frac{\pi}{L} \delta_k. \quad (5)$$

Thus $\lim_{L \rightarrow \infty} E_k = \varepsilon_k$. Note that we restrict to cases without bound states where contributions to the spectrum of $\mathcal{O}(1)$ can appear instead of $\mathcal{O}(L^{-1})$ as above. Concerning global system properties, the finite-size corrections given by

δ_k vanish in the thermodynamic limit, the local system properties, however, are determined by the δ_k 's. Regarding the time evolution of the single-particle operators

$$e^{iH_p^d t} c_k e^{-iH_p^d t} \xrightarrow{L \rightarrow \infty} c_k e^{-i\varepsilon_k t} \quad (6)$$

the finite-size effects can be neglected in the thermodynamic limit as we always have $L \gg t$. The unitary transformation V not only diagonalizes H_p but at the same time also \tilde{H}_p such that

$$V \tilde{H}_p V^\dagger = H_p^d - \langle H_0 \rangle_0 = H_0^n + \frac{\pi}{L} \sum_k \delta_k : c_k^\dagger c_k : + \frac{\pi}{L} \sum_k \delta_k f(\varepsilon_k) \quad (7)$$

Here, the colons $: \dots :$ denote normal-ordering which for the present quadratic Hamiltonian is a short-hand version for $: c_k^\dagger c_k : = c_k^\dagger c_k - \langle c_k^\dagger c_k \rangle_0$.

The last term in the above equality is the free energy difference ΔF between the system with and without local perturbation

$$\Delta F = -\beta^{-1} \sum_k \log [1 + e^{-\beta E_k}] + \beta^{-1} \sum_k \log [1 + e^{-\beta \varepsilon_k}] = \frac{\pi}{L} \sum_k \delta_k f(\varepsilon_k) + \mathcal{O}(L^{-1}) \quad (8)$$

with $f(\varepsilon_k) = 1/[1 + e^{\beta \varepsilon_k}]$ the Fermi-Dirac distribution. Note that for the internal energy difference ΔU we have $\Delta U = \sum_k E_k f(E_k) - \sum_k \varepsilon_k f(\varepsilon_k) = \Delta F + (\pi/L) \sum_k \delta_k \varepsilon_k f'(\varepsilon_k)$ with f' the derivative of the Fermi-Dirac distribution.

The second term on the right hand side of Eq. (7) denotes a finite-size correction to H_0^n . This correction vanishes when evaluated in the initial finite temperature Gibbs state. Concerning the time evolution of the single-particle operators the corresponding contribution vanishes in the thermodynamic limit, see Eq. (6). As we will show below in case of the absorption spectrum for the potential scattering Hamiltonian this part of the Hamiltonian gives no contribution at all. Note that this property strongly depends on the initial state. For the remainder of this supplementary information we will thus use the following identity

$$V H_p^n V^\dagger \xrightarrow{L \rightarrow \infty} H_0^n + \Delta F. \quad (9)$$

ABSORPTION SPECTRUM

In the following, we show that the approximate identity in Eq. (9) yields precisely the absorption spectrum one obtains from the exact solution.

Based on the knowledge of the diagonalizing transformation V one can calculate the Fourier transform $G_A(t)$ of the absorption spectrum, see Eq. (6) in the main text, also without the identity in Eq. (9). For $G_A(t)$ we have

$$G_A(t) = Z_A^{-1} \text{Tr} \left[e^{-\beta H_0} e^{-i(H_p^d - H_0)t} V^\dagger(t) V \right], \quad V^\dagger(t) = e^{iH_0 t} V^\dagger e^{-iH_0 t}. \quad (10)$$

where we have used that the finite-size effects for the time evolution can be neglected, see Eq. (6). The expressions for the emission spectrum can be obtained analogously. Using the exponential representation of V in Eq. (4) we perform a cumulant expansion in the expansion parameter g leading to

$$G_A(t) = \exp \left[-i \langle H_p^d - H_0 \rangle_0^c t + \langle \chi - \chi(t) \rangle_0^c + \frac{1}{2} \langle \chi \chi - \chi(t) \chi \rangle_0^c + \mathcal{O}(g^3) \right] \quad (11)$$

because χ is proportional to g for weak potential scatterers. The superscript c indicates a cumulant average. All higher cumulants $\langle (H_p^d - H_0)^n \rangle_0^c$ for $n > 1$ vanish in the thermodynamic limit. The same is true for the mixed cumulants $\langle (H_p^d - H_0)^n \chi^m \rangle_0^c$ for $n, m > 0$. As $\langle \chi(t) \rangle_0 = \langle \chi \rangle_0$ the lowest order contribution is of second order in g . The first term is the free energy difference as in Eq. (8)

$$\langle H_p^d - H_0 \rangle_0 = \frac{\pi}{L} \sum_k \delta_k f(\varepsilon_k) = \Delta F. \quad (12)$$

Concluding one obtains

$$G_A(t) = \exp \left[-i \Delta F t + \frac{1}{2} \langle \chi \chi - \chi(t) \chi \rangle_0 \right]. \quad (13)$$

Using normal-ordered Hamiltonians and Eq. (9) the absorption spectrum is determined by the generating function

$$G_A(t) = Z_A^{-1} \text{Tr} \left[e^{-\beta H_0^n} e^{iH_0^n t} e^{-i\tilde{H}_p t} \right]. \quad (14)$$

Based on Eq. (9) one can write

$$G_A(t) = Z_A^{-1} \text{Tr} \left[e^{-\beta H_0^n} V^\dagger(t) V \right] e^{-i\Delta F t} \quad (15)$$

with $V^\dagger(t) = e^{iH_0 t} V^\dagger e^{-iH_0 t}$ as before. Performing again the cumulant expansion one obtains the same result as in Eq. (13).

- [1] G. C. Wick, Phys. Rev. **80**, 268 (1950).

3.4 Absorption spectra of quantum dots

X-ray edge spectra in metals and other materials are by now a well-studied field, for an overview see, for example, the review [129]. As mentioned before x-ray edge spectra can be associated with local quenches in fermionic quantum impurity systems. Depending on the details of the material under investigation different types of quenches have been realized such as the switch on of a potential scatter or a resonant level for metals with incomplete shells. For each individual material, however, the properties of the respective x-ray edge processes are fixed. Recently, it has been realized that optical spectra of single quantum dots allow for the experimental implementation of x-ray edge type problems [68, 176, 104]. Contrary to experiments at bulk materials quantum dots offer a detailed control of the system parameters allowing for a detailed study of x-ray edge phenomena.

3.4.1 Minimal model for the description of quantum dots

Quantum dots are nanostructures in which electrons are confined similarly to a particle in a box yielding a discrete level structure of eigenstates with a spacing that can be controlled by the size of the dot. In most cases quantum dots are experimentally realized at the interface of semiconductor heterostructures such as GaAs/AlGaAs where two-dimensional electron gases (2DEG) are forming. One way of introducing the strong spatial confinement is to place metallic gates on top of the semiconductor material. By applying voltages on the gates they can be used to design a potential landscape for the electrons in the 2DEG. Irrespective of the experimental details there exists a minimal model for most applications that describes the properties of such a quantum dot connected to the 2DEG in terms of an extended Anderson impurity model that can be separated into three different contributions:

$$H = H_{\text{dot}} + H_{\text{tun}} + H_{\text{lead}}. \quad (3.16)$$

The first term H_{dot} covers the description of the isolated quantum dot typically involving a discrete spectrum and interactions between the electrons. The conduction band electrons in the 2DEG are approximated by a Fermi gas of noninteracting electrons yielding a simple representation of H_{lead} . Of course, real electrons do interact. In a two-dimensional system, however, it is possible to incorporate the presence of interactions by introducing renormalized effective parameters of a free theory within the validity of Fermi liquid theory. The lead and the quantum dot are coupled to each other typically by a tunneling mechanism. In most cases, it is assumed that the coupling term H_{tun} only affects the s -wave channel such that the description of the conduction band can be reduced to a one-dimensional of chiral scattering states.

In the most important case for the following analysis only two levels of the quantum dot are relevant for the dynamics of the respective nonequilibrium x-ray edge protocols. For a schematic picture see Fig. 3.5. For later convenience the upper level with energy ε_c will be termed the conduction band level of the quantum dot whereas the lower one with energy ε_v the valence band level following the notation in Ref. [68]. The position of the quantum dot levels can be shifted relative to the Fermi energy ε_F of the conduction

band via the external gate voltage V_g . In what follows it will be assumed that the gate voltage is chosen such that $\varepsilon_c > \varepsilon_F$ and $\varepsilon_v < \varepsilon_F$. Due to the strong spatial confinement electron-electron interactions on the quantum dot can in most cases not be neglected. This yields the following Hamiltonian for the quantum dot

$$H_{\text{dot}} = H_{\text{dot}}^c + H_{\text{dot}}^v + H_{\text{dot}}^{cv} \quad (3.17)$$

where

$$\begin{aligned} H_{\text{dot}}^c &= \sum_{\sigma=\uparrow,\downarrow} \varepsilon_c n_{c\sigma} + U n_{c\uparrow} n_{c\downarrow}, \\ H_{\text{dot}}^v &= \sum_{\sigma=\uparrow,\downarrow} \varepsilon_v n_{v\sigma} + U_v n_{v\uparrow} n_{v\downarrow}, \\ H_{\text{dot}}^{cv} &= -U_{\text{exc}} \sum_{\sigma,\sigma'} n_{c\sigma} (1 - n_{v\sigma'}). \end{aligned} \quad (3.18)$$

The operators $n_{c/v\sigma} = d_{c/v\sigma}^\dagger d_{c/v\sigma}$ measure the occupation of electrons with spin σ in the dot level c or v , respectively. The operator $d_{c/v\sigma}^\dagger$ creates an electron of spin σ in the level c/v on the dot. The interaction energy that has to be paid if one of the two levels is doubly occupied is given by U and U_v , respectively. The excitation of a valence electron to the upper level ε_c leaves behind a positively charged hole similarly as for the original x-ray edge problem, see the introduction of Ch. 3. This leads to an attractive capacitative interaction of strength U_{exc} shifting the upper level to lower energies as well as the lower level to higher energies. It is assumed, however, that the position of the lower level is still far below the Fermi surface.

The lead electrons of the 2DEG are described as an effectively one-dimensional system of noninteracting fermions

$$H_{\text{lead}} = \sum_{k\sigma} \varepsilon_k c_{k\sigma}^\dagger c_{k\sigma} \quad (3.19)$$

with a dispersion relation ε_k which for all examples below is approximated linearly in the vicinity of the Fermi surface via $\varepsilon_k \approx \hbar v_F (k - k_F)$ with v_F the Fermi velocity and k_F the Fermi momentum. The operator $c_{k\sigma}^\dagger$ creates an electron of spin $\sigma = \uparrow, \downarrow$ and momentum k in the conduction band.

The upper quantum dot level is tunnel coupled to the 2DEG via

$$H_t = V \sum_{k\sigma} \left[c_{k\sigma}^\dagger d_{c\sigma} + d_{c\sigma}^\dagger c_{k\sigma} \right] \quad (3.20)$$

with the amplitude V . As a consequence the local level hybridizes with the conduction band electrons yielding a level broadening of the order of the hybridization strength

$$\Gamma = \pi \rho_0 V^2 \quad (3.21)$$

with ρ_0 the noninteracting lead density of states at the Fermi energy ε_F . For the relevant experiments one can omit the hybridization of the quantum dot valence electrons [68, 104]

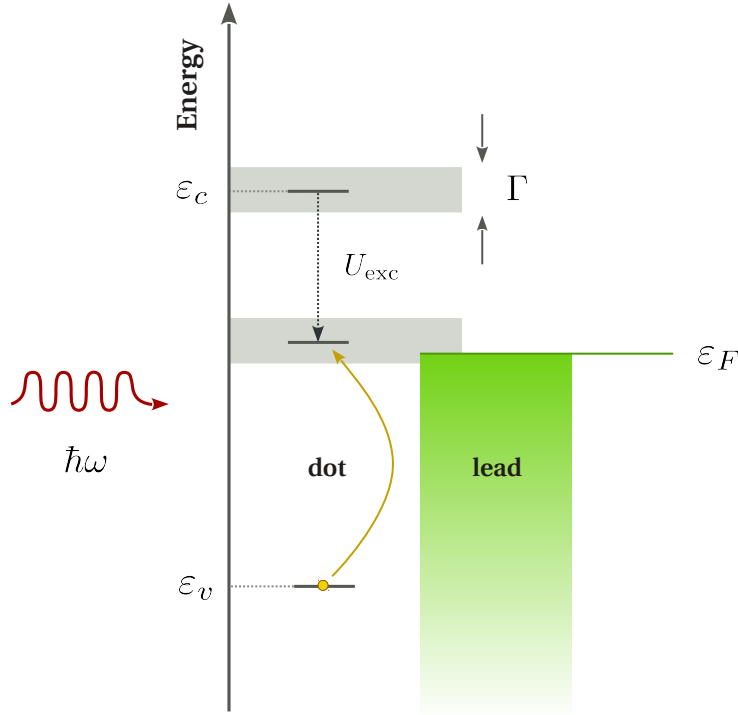


Figure 3.5: Schematic illustration for the implementation of x-ray edge spectra for quantum dots connected to a lead. Initially the system is prepared in a state in which the upper quantum dots level ε_c is unoccupied whereas the lower one ε_v occupied. This can be achieved by tuning the external gate voltage appropriately provided the level splitting of the quantum dot is large enough. Consider an incident light beam with photons of angular frequency ω . When a photon is absorbed by the quantum dot and excited from ε_v into ε_c the Coulomb interaction between the positively charged hole in ε_v and an electron in ε_c leads to a shift $\varepsilon_c \rightarrow \varepsilon_c - U_{\text{exc}}$ to lower energies. Provided $\varepsilon_c - U_{\text{exc}} - \varepsilon_F \leq \Gamma$ the upper level can hybridize with the conduction band. This effectively amounts to a sudden switch on of the coupling between quantum dot and conduction band. For details see text.

3.4.2 Description of x-ray absorption in quantum dots

Consider a quantum dot under the influence of an incident single mode laser beam of angular frequency ω_L , for a schematic picture see Fig. 3.5. Suppose that the quantum dot is initially prepared in such a way that the lower quantum dot level $\varepsilon_F - \varepsilon_v \gg T, \Gamma$ is occupied whereas the upper one unoccupied, i.e., $\varepsilon_c - \varepsilon_F \gg T, \Gamma$ where T is the temperature and Γ the hybridization strength, see Eq. (3.21). Note that this requires a large splitting $\varepsilon_c - \varepsilon_v \gg T, \Gamma$ of the single-particle spectrum in the dot that can be achieved for strong confinement. If the laser frequency ω_L is chosen appropriately one can induce optical excitations under the absorption of a photon. In case of circularly polarized light it is possible to address just one of the two electron species, spin- \uparrow say. This yields the following

coupling between dot and laser field

$$H_L(t) = \gamma \left[d_{c\uparrow}^\dagger d_{v\uparrow} a e^{-i\omega_L t} + a^\dagger d_{v\uparrow}^\dagger d_{c\uparrow} e^{i\omega_L t} \right]. \quad (3.22)$$

The operator a^\dagger creates a photon of frequency ω_L . The strength of the coupling is parametrized by the amplitude γ . Note that H_L is chosen in a gauge where the diagonal photonic part disappears from the Hamiltonian yielding a time-dependent coupling. The dynamics of the system in presence of the laser beam will be treated perturbatively in γ in the following.

The quantum dot valence level occupations $n_{v\sigma}$ are constants of motion of H . Initially we have $n_{v\sigma} = 1$ for $\sigma = \uparrow, \downarrow$. As a consequence of an absorption process generated by $H_L(t)$ the occupation of the \uparrow occupation changes to $n_{v\uparrow} = 0$. It turns out to be suitable to introduce projections of H onto the subspaces containing zero (H_f) or one (H_i) spin- \uparrow electron in the valence level corresponding to the system before and after absorption.

$$\begin{aligned} H_i &= \sum_{\sigma=\uparrow,\downarrow} \varepsilon_c n_{c\sigma} + U n_{c\uparrow} n_{c\downarrow} + 2\varepsilon_v + U_v + \sum_{k\sigma} \varepsilon_k c_{k\sigma}^\dagger c_{k\sigma} \\ H_f &= \sum_{\sigma=\uparrow,\downarrow} (\varepsilon_c - U_{\text{exc}}) n_{c\sigma} + U n_{c\uparrow} n_{c\downarrow} + \varepsilon_v + \sum_{k\sigma} \varepsilon_k c_{k\sigma}^\dagger c_{k\sigma} + V \sum_{k\sigma} \left[c_{k\sigma}^\dagger d_{c\sigma} + d_{c\sigma}^\dagger c_{k\sigma} \right] \end{aligned} \quad (3.23)$$

Note that $n_{v\downarrow} = 1$ always. For H_i tunneling processes are suppressed as $\varepsilon_c - \varepsilon_F \gg T, \Gamma$ such that H_{tun} can be neglected. Although the upper quantum dot level ε_c lies far above the Fermi surface the absorption of a photon yields a shift $\varepsilon_c \rightarrow \varepsilon_c - U_{\text{exc}}$ to lower energies due to the attractive capacitative coupling between hole and electron states in the quantum dot. For an appropriately chosen ε_c the excitonic binding energy U_{exc} can be sufficiently large in order to push the upper level into the vicinity of the Fermi energy allowing the level to hybridize with the continuum. In this regime the absorption of a photon is accompanied by complex local dynamics of the quantum dot. Depending on the precise parameters of H_f this can lead to the build of Kondo correlations [176] that have already been observed experimentally [104].

Suppose that the system is initially prepared in a mixed state at temperature T . Due to the specific choice of the location of the initial dot levels the hybridization can be neglected yielding a factorized density matrix

$$\rho = \rho_{\text{lead}} \otimes \rho_{\text{dot}} \quad (3.24)$$

where the conduction band state is given by

$$\rho_{\text{lead}} = \frac{1}{Z_{\text{lead}}} e^{-\beta H_{\text{lead}}}, \quad Z_{\text{lead}} = \text{Tr} e^{-\beta H_{\text{lead}}}, \quad (3.25)$$

and the dot state by

$$\rho_{\text{dot}} = d_{v\uparrow}^\dagger d_{v\downarrow}^\dagger | \rangle \langle | d_{v\downarrow} d_{v\uparrow} \quad (3.26)$$

with $| \rangle_{\text{dot}}$ the dot vacuum without any electron.

Suppose that the laser beam is switched on at time $t = 0$. The number of absorbed photons $\Delta\mathcal{N}(t)$ after a time t is then given by the change in photon occupation in the background field

$$\Delta\mathcal{N}(t) = \mathcal{N}(t = 0) - \mathcal{N}(t) \quad (3.27)$$

where $\mathcal{N}(t) = \langle a^\dagger(t)a(t) \rangle$. The dynamics of the system is governed by the time evolution operator $U(t)$ obeying the differential equation

$$\frac{d}{dt}U(t) = -i\mathcal{H}(t)U(t), \quad \mathcal{H}(t) = H + H_L(t), \quad (3.28)$$

see Eqs. (3.16, 3.22). In the Heisenberg picture the photonic operator is time evolved via $a(t) = U^\dagger(t) a U(t)$.

In second order time-dependent perturbation theory in H_L , see Eq. (3.22), the number of absorbed photons is related to a local correlation function

$$\Delta\mathcal{N}(t) = \gamma^2 |\phi|^2 \int_0^t dt' \int_0^t dt'' e^{i(\omega_L - \varepsilon_v - U_v)(t' - t'')} \text{Tr} [\rho d_{c\uparrow}(t') d_{c\uparrow}^\dagger(t'')] \quad (3.29)$$

with $d_{c\uparrow}(t) = \exp[iHt]d_{c\uparrow}\exp[-iHt]$. Here, it has been assumed that the laser field can be described by a coherent state with an amplitude ϕ . According to this result perturbation theory is valid not only in case of a small coupling γ . Additionally, one has to require a weak laser intensity given by $|\phi|^2$ such that the excitations due to absorption are rare and can be treated as independent from each other.

The corresponding absorption rate $\Gamma_L(\omega_L)$ at a frequency ω_L of the laser beam is given by the time derivative of the total number of absorbed photons in the asymptotic long-time limit

$$\Gamma_L(\omega_L) = \frac{d\Delta\mathcal{N}(t)}{dt} \xrightarrow{t \rightarrow \infty} 2\gamma^2 |\phi|^2 \text{Re} \int_0^\infty dt' e^{i(\omega_L - \varepsilon_v - U_v)(t-t')} \text{Tr} [\rho d_{c\uparrow}(t) d_{c\uparrow}^\dagger(t')] \quad (3.30)$$

Taking into account the subspaces corresponding to $n_{v\uparrow} = 0$ or $n_{v\uparrow} = 1$ associated with the respective Hamiltonians H_i and H_f , see Eq. (3.24), the absorption rate can be further simplified

$$\Gamma_L(\omega_L) = 2\gamma^2 |\phi|^2 \text{Re} \int_0^\infty dt e^{i(\omega_L - \omega_0)t} G(t), \quad G(t) = \frac{1}{Z_i} \text{Tr} [e^{-\beta H_i} e^{iH_i t} e^{-iH_f t}] \quad (3.31)$$

with $Z_i = \text{Tr} e^{-\beta H_i}$ the partition function for the system described by H_i at inverse temperature $\beta = T^{-1}$. This result again confirms the preceding analysis in Sec. 3.3 as the function $G(t)$ in the above equation precisely equals the moment generating function for the work distribution of a quench with initial Hamiltonian H_i and final Hamiltonian H_f , see Eq. (3.9). As a consequence the absorption rate $\Gamma_L(\omega_L)$ is identical to a work distribution up to a constant prefactor $\gamma^2 |\phi|^2$. The offset $\omega_0 = \varepsilon_c + \varepsilon_v + U_v$ is typically absorbed into a redefinition of ω_L via $\omega_L \rightarrow \omega_L + \omega_0$.

An analogous analysis can also be applied to the emission case. As for absorption the emission spectrum is proportional to a work distribution for the backward protocol of a quench from H_f to H_i .

3.5 Publication: The X-ray edge singularity in optical spectra of Quantum Dots

Depending on the details of the parameters in the final Hamiltonian H_f , see Eq. (3.24), different physical regimes can be addressed in the analysis of the x-ray edge absorption spectra. For large local interactions $U \gg \Gamma, T$ and appropriately tuned $\varepsilon_{cf} = \varepsilon_c - U_{\text{exc}}$ with $\varepsilon_F - \varepsilon_{cf} \gg T, \Gamma$ and $\varepsilon_{cf} + U - \varepsilon_F \gg T, \Gamma$ one ends up in the strongly correlated local moment regime associated with the Kondo effect. This regime has been studied both theoretically [176] as well as experimentally [104].

The low-energy properties of H_f in the local moment regime are dominated by spin fluctuations such that charge fluctuations on the quantum dot can be neglected. The opposite limit where the two spin channels are - at least approximately - decoupled yields a quadratic and in principle exactly solvable model. This can, for example, be achieved in the limit of a strong tunnel coupling between the quantum dot and the conduction band with $\Gamma \geq U$ where renormalization group studies have shown that the corresponding fixed point of the model is associated with the noninteracting limit $U = 0$ [100, 101]. For more details, see below.

For $U = 0$ the Hamiltonian H_f reduces to two independent resonant level models for both the spins species. In the context of the x-ray edge problem these systems have been associated with metals with incomplete shells and have been studied theoretically already in the literature [94, 98, 99]. The asymptotic analytical zero temperature solution near the absorption threshold has been determined perturbatively in the limit where the final local level ε_{cf} lies far below or far above the Fermi energy [98, 99]. For a system with additional potential scatterer - as it can be important, see below - analytical results have been obtained for the case where the final level energies $\varepsilon_{cf} > \varepsilon_F$ [94].

In contrast to the original x-ray edge problem solved by Mahan [115] and Nozieres [128] where the local perturbation is a potential scatterer the resonant level model establishes a *dynamical* local perturbation in the sense that the perturbation itself has dynamical internal degrees of freedom. Below, the absorption spectrum in the vicinity of the threshold is solved analytically for zero temperature on the basis of an auxiliary Riemann-Hilbert problem [33] thereby extending the known results to the whole parameter regime.

X-ray edge singularity in optical spectra of quantum dots

M. Heyl¹ and S. Kehrein^{1,2}

¹Physics Department, Arnold Sommerfeld Center for Theoretical Physics and Center for NanoScience, Ludwig-Maximilians-Universität, Theresienstrasse 37, 80333 Munich, Germany

²Georg-August-Universität Göttingen, Friedrich-Hund-Platz 1, 37077 Göttingen, Germany

(Received 31 July 2010; revised manuscript received 24 September 2011; published 5 April 2012)

In this work we investigate the x-ray edge singularity problem realized in noninteracting quantum dots. We analytically calculate the exponent of the singularity in the absorption spectrum near the threshold and extend known analytical results to the whole parameter regime of local level detunings. Additionally, we highlight the connections to work distributions and to the Loschmidt echo.

DOI: 10.1103/PhysRevB.85.155413

PACS number(s): 72.15.Qm, 85.35.Be, 73.50.Mx

I. INTRODUCTION

In condensed-matter theory the x-ray edge singularity constitutes one of the most important paradigms, appearing in a variety of different contexts. In the x-ray edge problem one probes the response of a fermionic system, interacting or noninteracting, subject to a sudden local perturbation. Its origin lies in the study of x-ray spectra of simple metals where it was shown that the absorption or emission of a photon corresponds to the sudden switch on or off of a local potential scatterer embedded in a noninteracting Fermi sea.^{1–4} Since then x-ray edge physics has been found in a variety of different systems, such as Luttinger liquids with impurity,⁵ Anderson impurity and Kondo models,^{6–10} resonant tunneling current-voltage characteristics through localized levels,^{11,12} fermionic systems with gapped spectra,¹³ decoherence in two-level systems,¹⁴ or work distributions.¹⁵

In quantum-dot experiments x-ray edge physics has been found in resonant tunneling current-voltage characteristics through localized levels¹⁶ where the I - V curves display edge singularities $I \sim \theta(V - V_0)(V - V_0)^{-\gamma}$ (Refs. 11 and 12) as a function of the applied bias voltage V at zero temperature, with an exponent γ that is determined by the associated local perturbation. At nonzero temperatures T the singularity gets smeared and IT^γ becomes a universal function of $eV/k_B T$,¹⁷ as has been demonstrated in numerous experiments.^{17,18}

In this work we focus on the realization of the x-ray edge problem in noninteracting quantum dots by means of optics experiments. The possibility of tuning the system parameters in quantum dots enables one to vary the relevant quantity in the x-ray edge problem: the phase shift δ of the conduction-band electrons. We analytically calculate the absorption line shape near the threshold of a suitably initialized quantum dot at zero temperature, extending the known analytical results^{6,7} to the whole parameter regime of local level detunings. This is an important generalization of x-ray edge physics to an experimentally accessible setup, and it constitutes one of the very few examples that allows for exact solutions. We show that the absorption spectrum can be identified with a work distribution¹⁹ for a local quench in a resonant level model. Moreover, we highlight the connection to the Loschmidt echo, which can be related to the Fourier transform of the absorption spectrum.^{15,20} Thus the presented setup allows for the measurement of the Loschmidt echo in a condensed-matter system by means of optical spectra.

The paper is organized as follows. First, we outline the experimental setup that allows us to mimic the x-ray edge problem in quantum dots. Then we calculate the absorption spectrum near the threshold via an associated Riemann-Hilbert problem.²¹ In the end we show the results and point out the relation to work distributions and to the Loschmidt echo.

II. MODELING THE ABSORPTION PROCESS AS A QUENCH IN AN EXTENDED RESONANT LEVEL MODEL

Below, we present a possible experimental realization of x-ray edge physics in noninteracting quantum dots coupled to an electronic reservoir following the ideas of Helmes *et al.*⁹ and Türeci *et al.*¹⁰ In Fig. 1 a schematic picture of the setup is shown. Consider a narrow quantum dot with a large splitting of the single-particle energies. In the following we will assume that the two spin channels are decoupled such that we can restrict ourselves to a single channel of spinless fermions. One possible realization of this decoupling is presented in the Appendix. The decoupling of the two spin degrees of freedom eliminates spin fluctuations that can lead to a strongly correlated low-energy state characterized by the Kondo resonance at the Fermi energy in the local density of states. This scenario has been investigated recently in Ref. 10. As argued in the Appendix, the formation of a Kondo resonance is avoided in the case where charge fluctuations on the quantum dot are sufficiently strong. This can be achieved through a strong coupling between the quantum dot and the conduction band.

By varying the back gate voltage V_g , the quantum dot can be tuned in such a way that the topmost occupied level lies far below the Fermi surface, $(\varepsilon_F - \varepsilon_h)/\Delta \gg 1$, provided the level splitting is large enough. Here, $\Delta = \pi\rho_0 V^2$ denotes the level broadening, with ρ_0 being the density of states at the Fermi level and V the hopping amplitude of electrons between dot and reservoir. Thus, the lower level can be considered occupied. If an incident laser beam with angular frequency ω excites the electron from the lower level into the upper one, a positively charged hole is left behind. Due to a capacitative coupling U_{eh} between the excited electron and the hole, the upper level ε_i is shifted to lower energies ε_f . The localized hole not only interacts with the dot electron, it also establishes a local potential for the conduction-band electrons. Assuming

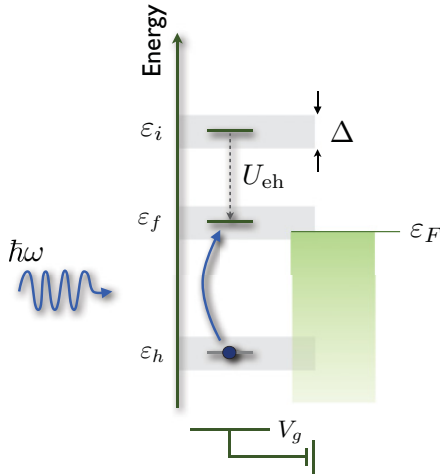


FIG. 1. (Color online) Schematic picture of a quantum dot coupled to a fermionic reservoir, which allows us to study x-ray edge physics in absorption spectra of quantum dots. The photon absorption of a suitably initialized quantum dot implements a sudden switch-on of the tunnel coupling between dot and fermionic reservoir due to a capacitative coupling between the excited electron and the residual hole. For details see the text.

that the hole is stable such that it can be considered static, at least compared to the other time scales in the problem, we can model this system by the following initial (before absorption) and final (after absorption) Hamiltonians:

$$\begin{aligned} H_i &= \sum_k \varepsilon_k :c_k^\dagger c_k: + \varepsilon_i c_d^\dagger c_d, \\ H_f &= \sum_k \varepsilon_k :c_k^\dagger c_k: - g \sum_{kk'} :c_k^\dagger c_{k'}: + \varepsilon_f c_d^\dagger c_d \\ &\quad + V \sum_k [c_k^\dagger c_d + c_d^\dagger c_k] + \Delta E. \end{aligned} \quad (1)$$

For one particular experimentally relevant realization of these model Hamiltonians, see the Appendix. The hole degree of freedom already has been integrated out and is contained in a constant energy shift ΔE of the final Hamiltonian. The operator c_k^\dagger creates an electron with wave vector k in the reservoir. Note that the quantum numbers k refer to an effective one-dimensional chiral description of the electronic degrees of freedom. Thus, we assume s -wave scattering, which allows for a reduction to a one-dimensional problem. For convenience, the wave vector k is measured relative to k_F . The colons $::$ denote normal ordering with respect to the Fermi sea. We measure the single-particle energies relative to the Fermi level, i.e., $\varepsilon_F = 0$. The operator c_d^\dagger creates an electron on the upper level of the quantum dot whose energy differs depending on if a photon has been absorbed or not.

The Hamiltonians in Eq. (1) without the potential scattering term have been introduced in the context of the x-ray edge problem by Kotani and Toyozawa^{6,22} to describe the x-ray spectra of metals with incomplete shells. They solved the problem analytically in the vicinity of the threshold for the case where the final local level lies far above or below the Fermi

energy. Moreover, they phenomenologically inferred from their analytical results the threshold behavior of the absorption spectrum over the whole parameter space. A similar problem at finite temperatures has been investigated in the context of decoherence in charge qubits.²³ The combined influence of a local potential scatterer and a virtual bound state was first discussed by Kita *et al.*,⁷ who solved the problem analytically for the case where the final local level energy lies above the Fermi level, i.e., $\varepsilon_f > 0$.

The aim of this work is to extend the known analytical zero-temperature results to the whole parameter regime of local level detunings with a general framework that can also be useful in other contexts. This includes, for example, decoherence in charge qubits coupled to a defect level.^{23,24}

III. ABSORPTION SPECTRUM

Assuming that the coupling between the system and the light field is small, one obtains for the absorption spectrum $A(\omega)$, the rate at which photons are absorbed, in second order of the coupling (Fermi's golden rule) at zero temperature,

$$A(\omega) = \kappa \sum_n |\langle e_n | c_d^\dagger | \psi_0 \rangle|^2 \delta[\omega - (e_n - e_{gs})]. \quad (2)$$

Here, $|\psi_0\rangle$ denotes the ground state of the initial Hamiltonian with energy e_{gs} and $|e_n\rangle$ is a complete orthonormal eigenbasis of the final Hamiltonian with corresponding energies e_n . The constant prefactor κ contains the experimental details such as the intensity of the incident laser beam and the system-light-field coupling. Representing the δ function by an integral over phase factors, one can relate $A(\omega)$ to a dynamical correlation function $G(t)$ via Fourier transformation,

$$A(\omega) = \kappa \int \frac{dt}{2\pi} e^{i(\omega - \varepsilon_i)t} G(t), \quad (3)$$

with

$$G(t) = \langle 0 | e^{iH_i t} e^{-iH_f t} | 0 \rangle. \quad (4)$$

Here, $|0\rangle = c_d^\dagger |\psi_0\rangle$ denotes a product state of the Fermi sea for the conduction-band electrons with a filled local d orbital. In view of the x-ray edge problem, $G(t)$ is the equivalent to the core-hole Green's function. The dynamical correlation function $G(t)$ in Eq. (4) is an important quantity also in other physical contexts. The quantity $\mathcal{L}(t) = |G(t)|^2$ is the Loschmidt echo that allows for a quantification of the irreversibility of a system,^{15,20} here H_i , under a perturbation, here $H_f - H_i$. Moreover, $G(t)$ is the characteristic function of a work distribution $P(\omega)$ for a quench from H_i to H_f , where $P(\omega) = \kappa^{-1} A(\omega)$ is the probability of having performed the work ω on the system under this protocol.¹⁹ The relation between absorption spectra and work distributions, which is evident from a physical point of view, has been worked out recently.²⁵ A photon when absorbed provides its energy ω to the system, which is equivalent to having performed the work ω .

Analytic results for the dynamical correlation function $G(t)$ in the asymptotic long-time limit $t \rightarrow \infty$ have been obtained for the case where the final energy ε_f of the local d level lies above the Fermi level, i.e., $\varepsilon_f > 0$.⁷ In the case without a potential scatterer, Kotani and Toyozawa⁶ calculated

analytically the characteristic function $G(t)$ in the limit where the final local energy level lies far above or far below the Fermi level. In both systems, the long-time behavior of the dynamical correlation function $G(t)$ is algebraic, $G(t) \xrightarrow{t \rightarrow \infty} (i\eta t)^{-\gamma}$, $\gamma = (1 - \delta/\pi)^2$, with an exponent γ that only depends on the phase shift δ of the conduction-band electrons at the Fermi level in the presence of the local perturbation. The prefactor η is a high-energy scale of the order of the bandwidth. Due to the Friedel sum rule, δ/π is the screening charge that determines the exponent according to the rule of Hopfield.²⁶

In the following, we will extend the known results to the whole parameter regime, including also the case where $\varepsilon_f \leq 0$. Although the problem is in principle quadratic, the mathematical difficulty stems from the fact that, in contrast to the original x-ray edge problem, an additional *dynamical* degree of freedom, the local *d* level, and its coupling to the fermionic reservoir are switched on. As a consequence the additional degree of freedom acquires a finite lifetime.

The absorption process creates two local perturbations: the potential scatterer as well as the coupling to a localized level. The time scale for the local level to hybridize with the conduction band is set by the inverse Δ^{-1} of the equilibrium level broadening Δ . Thus, for times $t \ll \Delta^{-1}$ the local level is effectively decoupled and the dynamics are controlled solely by the potential scatterer. This then leads to the following picture. For times smaller than the inverse bandwidth W^{-1} , $t \ll W^{-1}$, the time evolution of $G(t)$ is nonuniversal and is controlled mainly by high-energy excitations. In the intermediate regime $W^{-1} \ll t \ll \Delta^{-1}$, the dynamics is dominated by the local potential scatterer, with the local level still effectively decoupled. This is then equivalent to the original x-ray edge problem such that the amplitude $G(t)$ decays algebraically $G(t) \sim (i\eta t)^{-\alpha^2}$, with η being a high-energy scale of the order of the bandwidth. The exponent $\alpha = \delta^*/\pi$ is set by the phase shift δ^* for the potential scattering Hamiltonian in Eq. (1) with $V = 0$. The dynamics of the system for times $t \gg \Delta^{-1}$ are given by the full Hamiltonian and will be determined via the combined influence of the hybridization as well as the potential scatterer. In the following we will calculate the dynamics in the asymptotic long-time regime $t \gg \Delta^{-1}$ for all local level detunings ε_f , yielding that again $G(t) \sim (i\eta t)^{-(1-\delta/\pi)^2}$ decays algebraically with an exponent that is determined by the phase shift δ .

Due to the quadratic nature of the problem - the final and initial Hamiltonians are both bilinear in fermionic operators - the characteristic function $G(t)$, which is a thermal expectation value of exponentials in H_i and H_f , can be reduced to a single-particle problem. Functions such as $G(t)$ can be represented in terms of determinants^{12,27,28}

$$G(t) = \det M, \quad M = 1 - f + fR, \quad (5)$$

of matrices in the single-particle space due to the Slater determinant structure of the initial state. The matrix R with matrix elements

$$R_{ll'} = \langle |c_l \hat{R} c_{l'}^\dagger| \rangle, \quad \hat{R} = e^{iH_it} e^{-iH_{f'}t}, \quad l, l' = k, d, \quad (6)$$

where $| \rangle$ is the true vacuum without any fermion, is essentially determined by the single-particle subspace of \hat{R} . The operator \hat{R} can be identified as the time-evolution operator of $H = H_f$ in the interaction representation with respect to the free Hamiltonian $H_0 = H_i$. The matrix elements of R reduce to the retarded Green's functions of the final Hamiltonian up to a phase. The initial state is encoded in the matrix f :

$$f_{dd} = 1, \quad f_{dk} = f_{kd} = 0, \quad f_{kk'} = \delta_{kk'} \theta(-k). \quad (7)$$

It will be convenient to separate the dynamics of the additional dynamical degree of freedom, the local *d* level, from the dynamics of the conduction-band electrons. For that purpose, we write the matrix M in a block notation

$$M = \begin{pmatrix} A & B \\ C & D \end{pmatrix}, \quad (8)$$

where

$$A = M_{dd}, \quad B_k = M_{dk}, \quad C_k = M_{kd}, \quad D_{kk'} = M_{kk'}, \quad (9)$$

such that one obtains, by use of an elementary property of the determinant,

$$G(t) = \det M = (A - BD^{-1}C) \det D, \quad (10)$$

where $BD^{-1}C = \sum_{kk'} B_k D_{kk'}^{-1} C_{k'}$ is a scalar. Note that this separation of one degree freedom is formally similar to the treatment of a bound state in the x-ray edge problem in Ref. 21. However, in the present setup the additional *d* level is a dynamical degree of freedom, whereas a bound state is a static object. The matrix D now only includes reservoir states such that $\det D$ can be calculated with techniques known from the original x-ray edge problem. But the separation of the reservoir and *d*-level degrees of freedom comes at the cost of finding the inverse D^{-1} of an infinitely large matrix. Using the Riemann-Hilbert method by d'Ambrumenil and Muzykantskii,²¹ however, the evaluation of the determinant of D is equivalent to finding its inverse D^{-1} . In the context of the response of a fermionic system subject to a local perturbation, the auxiliary Riemann-Hilbert problem first appeared in Ref. 29. Subsequently, it has been used in the theory of full counting statistics³⁰ and for the x-ray edge problem^{21,31} even under nonequilibrium conditions.³² In the context of quantum inverse scattering problems, the Riemann-Hilbert problem is a well-established technique for evaluating determinants.³³

The inversion of the matrix D cannot be done exactly, but only asymptotically for large times $t \gg \Delta^{-1}$. For details, see Ref. 21. In this asymptotic limit it is well known that only the low-energy excitations in the vicinity of the Fermi level are relevant for the dynamics. Assuming that the scattering matrix $S(E)$ for the conduction-band electrons in presence of the local perturbation is only weakly dependent on energy, one can approximate $S(E)$ by its value at the Fermi level $S(E) \approx S(E_F) = e^{2i\delta}$. Here, δ is the corresponding phase shift. Within this approximation, the inversion of the matrix D is then equivalent to solving a singular integral equation with a Cauchy kernel.²¹ Such singular integral equations can be solved analytically due to their relation to Riemann-Hilbert problems.^{21,34} For the long-time limit of the generating function

$G(t)$, one thus obtains

$$G(t) \xrightarrow{t \gg \Delta^{-1}} (i\eta t)^{-\gamma}, \quad \gamma = (1 - \delta/\pi)^2, \quad (11)$$

in agreement with the known results for the case $\varepsilon_f > \varepsilon_F$ and consistent with the Hopfield rule of thumb.²⁶ Thus, the known asymptotic behavior extends to the whole parameter regime as already shown in numerous numerical calculations.^{7,22,35} This result constitutes one of the rare cases where it is possible to obtain exact analytical solutions.

Equation (11) expresses the asymptotic behavior of the generating function $G(t)$ in terms of the parameters η and δ . The quantity η , a high-energy scale of the order of the bandwidth, cannot be obtained analytically, as is usually the case for all the analytical treatments of the x-ray edge problem.^{1–4} The phase shift δ of the electrons at the Fermi level is a nonuniversal quantity that depends on a lot of details, such as the full free fermionic dispersion relation. Thus, in general it can only be determined numerically for a given system. Only in special cases it is possible to arrive at general statements about δ ; for the case of a weak potential scatterer, for example, see Ref. 4; for a far-detuned local level $|\varepsilon_f - \varepsilon_F| \gg \Delta$, see Ref. 6. If the final local level energy is resonant with the Fermi level, i.e., $\varepsilon_f = \varepsilon_F$, we have $\delta/\pi = 1/2$.

In the context of the initial problem, a quantum dot subject to a laser field, we have to bear in mind that the system actually exhibits two spin channels. If the laser excites electrons of both spins, the problem is still separable in the spin degree of freedom, i.e., $G(t) = G_{\uparrow}(t)G_{\downarrow}(t)$, and the dynamics of each spin component is governed by the Hamiltonians in Eq. (1). The exponent γ of the asymptotic long-time decay of the generating function $G(t)$ gets contributions from both spin channels, i.e., $\gamma = \gamma_{\uparrow} + \gamma_{\downarrow}$, with $\gamma_{\sigma} = (1 - \delta_{\sigma}/\pi)^2$ and δ_{σ} is the phase shift of the spin- σ electrons at the Fermi level. If the incident laser beam is circularly polarized it is possible to address just one of the two electronic spin species; spin- \uparrow for example. In this case, only one spin- \uparrow electron is excited from the core hole into the upper local level. Again, the total exponent $\gamma = \gamma_{\uparrow} + \gamma_{\downarrow}$ is given by two contributions. For $\gamma_{\uparrow} = (1 - \delta_{\uparrow}/\pi)^2$ we then get the same result as in Eq. (11). The spin- \downarrow contribution, however, is different as the absorption process does not excite a spin- \downarrow electron in the dot. Thus, we get an exponent $\gamma_{\downarrow} = (\delta_{\downarrow}/\pi)^2$ due to the presence of the local potential scatterer generated by the absorption of the spin- \uparrow electron.

Absorption lineshape. From Eq. (11), one can deduce the behavior of the absorption lineshape near the threshold analytically,

$$A(\omega) \xrightarrow{\omega \rightarrow \omega_{\text{th}}} \theta(\omega - \omega_{\text{th}})(\omega - \omega_{\text{th}})^{\gamma-1}, \quad (12)$$

which shows the typical power-law singularity. The singularity is a consequence of the singular behavior of the initial Fermi-Dirac distribution of the conduction-band electrons at zero temperature. Thus, at nonzero temperatures T the singularity is cut off;³⁷ see Ref. 31 for the finite-temperature generalization in the context of the Riemann-Hilbert method. In Fig. 2, numerical renormalization group (NRG) data for the absorption spectrum are shown. For light frequencies ω in the vicinity of the threshold, the analytical power-law results included as thin solid lines fit perfectly to the exact NRG

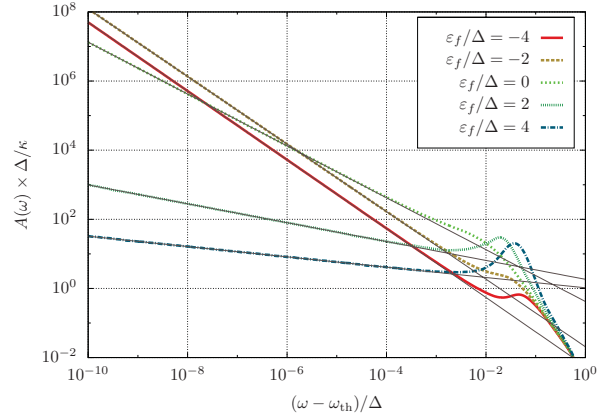


FIG. 2. (Color online) Absorption spectrum $A(\omega)$ as a function of the incident light frequency ω near the threshold frequency ω_{th} for different final energies ε_f of the quantum dot level at zero temperature. For simplicity we restrict ourselves to the case $g = 0$ without a potential scatterer. Here, $\Delta = \pi\rho_0 V^2$ denotes the half-width of the hybridized level in the quantum dot, with ρ_0 being the noninteracting density of states at the Fermi level. The thick lines are results obtained by NRG calculations.³⁶ The thin lines show the analytic power-law results, which fit perfectly the exact NRG data in the asymptotic low-frequency regime for $|\omega - \omega_{\text{th}}| \ll \Delta$. For details, see the main text.

results. The analytical curves in Fig. 2 are obtained by a fit of the high-energy scale η that cannot be obtained analytically by the present approach, as mentioned before. The phase shift δ , however, is not fitted; rather, it is obtained within the NRG independently of the absorption spectrum.

Work distribution. In view of the equivalence to a work distribution, the existence of the threshold in the absorption spectrum is evident. In the beginning, the system is prepared in the ground state of the initial Hamiltonian. The minimum energy, i.e., work, that has to be provided to the system by switching on the coupling to the resonant level, is the ground-state energy difference between initial and final Hamiltonians. Thus, it is impossible for a photon of energy less than the ground-state energy difference to be absorbed. The singular behavior of the absorption spectrum shows that the dominant excitations that are created by the absorption process are low-energy excitations in the vicinity of the Fermi level.

Loschmidt echo. As already mentioned before, the characteristic function $G(t)$ is also related to the Loschmidt echo,^{15,20}

$$\mathcal{L}(t) = |G(t)|^2 = |\langle 0 | e^{iH_i t} e^{-iH_f t} | 0 \rangle|^2. \quad (13)$$

The Loschmidt echo quantifies the stability of motion in time of a system; in this case the Hamiltonian H_i , under a perturbation $H_f - H_i$. Thus, for long times t , Eq. (11) states that, no matter how small the local perturbation is, the time evolution of the state $|0\rangle$ with the final Hamiltonian drives the system into a subspace of the Hilbert space that is orthogonal to the initial state. From the Anderson orthogonality catastrophe³⁸ it is known that the ground state of the final Hamiltonian is contained in this subspace. The

system as a whole, however, does not evolve into the ground state of the final Hamiltonian $|0_f\rangle$, as the overlap of both wave functions $|\langle 0_f | e^{-iH_f t} | 0 \rangle|^2 = |\langle 0_f | 0 \rangle|^2 \sim N^{-\alpha^2}$ with $\alpha = \delta/\pi$ being constant in time. Here, N is the particle number. Thus, the vanishing behavior of $G(t)$ for $t \rightarrow \infty$ cannot be simply traced back to the Anderson orthogonality catastrophe,³⁸ i.e., the vanishing overlap between ground-state wave functions. For the original x-ray edge model including only the potential scatterer, it has been shown that the characteristic scaling behavior of overlaps with system size is valid not only for the ground-state wave function overlap, but also for low-lying excited states $|\varepsilon\rangle$.³⁹ Here, the energies ε are measured relative to the ground-state energy of the final Hamiltonian. For a finite-size system it has been shown by the authors in Ref. 39 that, the function $\sigma(E_n = nW/N) = \sum_{\varepsilon=E_n}^{E_n+\Delta E} |\langle \varepsilon | 0 \rangle|^2$ [W is the bandwidth] has a scaling behavior similar to that in the Anderson orthogonality catastrophe, namely $\sigma(E_n) \sim (n/N)^{\alpha^2-1} \sim E_n^{\alpha^2-1}$, provided the energy E_n is small. This scaling behavior in energy is intimately connected to the scaling behavior with system size in the der Anderson orthogonality catastrophe; however, it is an extension to excited states. The asymptotic power-law behavior of $\mathcal{L}(t)$ is therefore not just a consequence of the vanishing ground-state overlap, but instead is due to the existence of a multitude of low-energy excitations satisfying the characteristic scaling behavior also found in the Anderson orthogonality catastrophe.

Due to the correspondence between absorption spectra and work distributions, we know that the average energy in the system $E_f = \langle 0 | H_f | 0 \rangle$ after the switch-on of the perturbation is larger than the ground-state energy E_f^{gs} of H_f . After the quench the system has (on average) an excess energy $w = E_f - E_f^{gs}$, in the context of the work distribution one can term w the dissipated work. The asymptotic long-time behavior of the Loschmidt echo $\mathcal{L}(t)$ suggests that in course of time the system redistributes this excess energy completely into a multitude of low-energy excitations.

IV. CONCLUSION

In this work we have discussed the x-ray edge singularity in optical spectra of quantum dots. We presented a general framework that allows one to determine analytically the singular threshold behavior of absorption spectra in quantum dots at zero temperature. This establishes an important generalization of x-ray edge physics to experimentally accessible environments that can be used to observe x-ray edge physics in a controlled setup. Moreover, we highlighted the correspondence of the spectra to work distributions and to the Loschmidt echo. The presented framework might also be useful in other contexts such as decoherence in charge qubits.

ACKNOWLEDGMENTS

We acknowledge valuable discussions with J. von Delft. We thank M. Hanl and A. Weichselbaum for providing us the NRG data. This work was supported through the SFB TR 12 of the Deutsche Forschungsgemeinschaft (DFG), by the Center for

Nanoscience (CeNS) Munich, and by the German Excellence Initiative via the Nanosystems Initiative Munich (NIM).

APPENDIX: MODEL AND EXPERIMENT

In this Appendix we present one possible absorption experiment whose effective description is governed by the Hamiltonians in Eq. (1). Consider a single semiconductor quantum dot embedded in a Schottky diode structure. Such quantum dots coupled to a fermionic reservoir can generically be described by Anderson impurity models:

$$H = \sum_{k\sigma} \varepsilon_k c_{k\sigma}^\dagger c_{k\sigma} + V \sum_{k\sigma} [c_{k\sigma}^\dagger d_\sigma + d_\sigma^\dagger c_{k\sigma}] \\ + \sum_\sigma \varepsilon_0 d_\sigma^\dagger d_\sigma + U d_\uparrow^\dagger d_\uparrow d_\downarrow^\dagger d_\downarrow. \quad (\text{A1})$$

The operator $c_{k\sigma}^\dagger$ creates an electron in the reservoir with spin σ and wave vector k that is measured relative to k_F . The quantum numbers k refer to an effective chiral one-dimensional description; see also the main text. The quantum dot is modeled by a single level with energy ε_0 in each spin channel. The operator d_σ^\dagger creates one electron of spin σ on the dot. The two spin channels are coupled via the local onsite interaction of strength U . The hybridization $\Delta = \pi \rho_0 V^2$, with ρ_0 being the noninteracting density of states, constitutes a second important energy scale. For a semiconductor quantum dot in such a Schottky diode structure, Δ can be tuned up to such large values that U and Δ are of the same order. For $\Delta > U$ renormalization group studies reveal that the physical properties of the system are dominated by fixed points that correspond to the noninteracting limit of the above Hamiltonian with $U = 0$.⁴⁰ In this regime it is therefore valid to assume that the two spin channels are decoupled, each of which can be modeled by a resonant level Hamiltonian \tilde{H} . Due to this decoupling we can restrict ourselves to a single channel of spinless electrons in the following:

$$\tilde{H} = \sum_k \varepsilon_k c_k^\dagger c_k + \varepsilon_0 d^\dagger d + V \sum_k [c_k^\dagger d + d^\dagger c_k]. \quad (\text{A2})$$

This is the effective description of the quantum dot before the absorption of a photon. As explained in the main text, one effect of the absorption is the shift of the local level energy $\varepsilon_0 \rightarrow \varepsilon_0 - U_{\text{eh}}$ via the attractive electron-hole interaction U_{eh} . Additionally, the absorption is associated with the switch on of a local potential scatterer for the electrons in the reservoir such that we have the following initial (\mathcal{H}_i) and final (\mathcal{H}_f) Hamiltonians:

$$\mathcal{H}_i = \sum_k \varepsilon_k c_k^\dagger c_k + \varepsilon_0 d^\dagger d + V \sum_k [c_k^\dagger d + d^\dagger c_k], \\ \mathcal{H}_f = \sum_k \varepsilon_k c_k^\dagger c_k + (\varepsilon_0 - U_{\text{eh}}) d^\dagger d \\ + V \sum_k [c_k^\dagger d + d^\dagger c_k] - g \sum_{kk'} c_k^\dagger c_{k'}. \quad (\text{A3})$$

Let W be the unitary transformation that diagonalizes \mathcal{H}_i , i.e.,

$$H_i = W \mathcal{H}_i W^\dagger = \sum_k \tilde{\varepsilon}_k c_k^\dagger c_k + \varepsilon_i d^\dagger d, \quad (\text{A4})$$

where the matrix elements of W are defined by the equations

$$\begin{aligned} W d W^\dagger &= W_{dd} d + \sum_k W_{dk} c_k, \\ W c_k W^\dagger &= W_{kd} d + \sum_{k'} W_{kk'} c_{k'}. \end{aligned} \quad (\text{A5})$$

It is straightforward to show that all matrix elements have a square-root scaling with system size, i.e., $W_{ll'} \sim L^{-1/2}$ with $l = k, d$. In the new basis the final Hamiltonian equals

$$\begin{aligned} H_f &= W \mathcal{H}_f W^\dagger = \sum_k \tilde{\varepsilon}_k c_k^\dagger c_k + \varepsilon_f d^\dagger d \\ &\quad + \sum_k [\tilde{V} c_k^\dagger d + \tilde{V}^* d^\dagger c_k] - \sum_{kk'} \tilde{g}_{kk'} c_k^\dagger c_{k'}, \end{aligned} \quad (\text{A6})$$

where the new coupling constants are given in terms of the matrix elements of W in the following way:

$$\begin{aligned} \varepsilon_f &= \varepsilon_i - g \left| \sum_k W_{kd} \right|^2, \quad \tilde{V} = -g \sum_k W_{kd}, \\ \tilde{g}_{kk'} &= -g \sum_{qq'} W_{qk}^* W_{q'k'} - U_{\text{eh}} W_{dk}^* W_{dk'}. \end{aligned} \quad (\text{A7})$$

Here, we have neglected all terms whose contribution vanishes in the thermodynamic limit. For the singular behavior of the absorption spectrum at the threshold, only low-energy excitations are relevant. For the description of the low-energy sector one can replace the coupling constants $\tilde{g}_{kk'} \rightarrow \tilde{g}_{00}$ by their values at the Fermi level. In conclusion, we have shown one possible experimental scenario that leads to the model Hamiltonians in Eq. (1).

-
- ¹G. D. Mahan, *Phys. Rev.* **163**, 612 (1967).
²P. Nozieres and C. T. De Dominicis, *Phys. Rev.* **178**, 1097 (1969).
³K. Ohtaka and Y. Tanabe, *Rev. Mod. Phys.* **62**, 929 (1990).
⁴K. D. Schotte and U. Schotte, *Phys. Rev.* **182**, 479 (1969).
⁵A. O. Gogolin, *Phys. Rev. Lett.* **71**, 2995 (1993).
⁶A. Kotani and Y. Toyozawa, *J. Phys. Soc. Jpn.* **35**, 1073 (1973).
⁷T. Kita, K. Ohtaka, and Y. Tanabe, *J. Phys. Soc. Jpn.* **56**, 4609 (1987).
⁸I. Affleck and A. W. W. Ludwig, *J. Phys. A: Math. Gen.* **27**, 5375 (1994).
⁹R. W. Helmes, M. Sindel, L. Borda, and J. von Delft, *Phys. Rev. B* **72**, 125301 (2005).
¹⁰H. E. Tureci, M. Hanl, M. Claassen, A. Weichselbaum, T. Hecht, B. Braunecker, A. Govorov, L. Glazman, A. Imamoglu, and J. von Delft, *Phys. Rev. Lett.* **106**, 107402 (2011).
¹¹K. A. Matveev and A. I. Larkin, *Phys. Rev. B* **46**, 15337 (1992).
¹²D. A. Abanin and L. S. Levitov, *Phys. Rev. Lett.* **93**, 126802 (2004).
¹³V. V. Mkhitaryan, E. G. Mishchenko, M. E. Raikh, and L. I. Glazman, *Phys. Rev. B* **80**, 205416 (2009).
¹⁴D. Segal, D. R. Reichman, and A. J. Millis, *Phys. Rev. B* **76**, 195316 (2007).
¹⁵A. Silva, *Phys. Rev. Lett.* **101**, 120603 (2008).
¹⁶A. K. Geim, P. C. Main, N. La Scala, L. Eaves, T. J. Foster, P. H. Beton, J. W. Sakai, F. W. Sheard, M. Henini, G. Hill, and M. A. Pate, *Phys. Rev. Lett.* **72**, 2061 (1994).
¹⁷H. Frahm, C. von Zobeltitz, N. Maire, and R. J. Haug, *Phys. Rev. B* **74**, 035329 (2006).
¹⁸E. E. Vdovin, Yu. N. Khanin, O. Makarovskiy, Yu. V. Dubrovskii, A. Patane, L. Eaves, M. Henini, C. J. Mellor, K. A. Benedict, and R. Airey, *Phys. Rev. B* **75**, 115315 (2007); N. Maire, F. Hohls, T. Lüdtke, K. Pierz, and R. J. Haug, *ibid.* **75**, 233304 (2007); M. Rüth, T. Slobodskyy, C. Gould, G. Schmidt, and L. W. Molenkamp, *Appl. Phys. Lett.* **93**, 182104 (2008).
¹⁹P. Talkner, E. Lutz, and P. Hänggi, *Phys. Rev. E* **75**, 050102(R) (2007).
²⁰A. Peres, *Phys. Rev. A* **30**, 1610 (1984).
²¹N. d'Ambrumenil and B. A. Muzykantskii, *Phys. Rev. B* **71**, 045326 (2005).
²²A. Kotani and Y. Toyozawa, *J. Phys. Soc. Jpn.* **35**, 1082 (1973).
²³A. Grishin, I. V. Yurkevich, and I. V. Lerner, *Phys. Rev. B* **72**, 060509(R) (2005).
²⁴B. Abel and F. Marquardt, *Phys. Rev. B* **78**, 201302(R) (2008).
²⁵M. Heyl and S. Kehrein, e-print arXiv:1006.3522 (unpublished).
²⁶J. J. Hopfield, *Comments Solid State Phys.* **2**, 40 (1969).
²⁷M. Combescot and P. Nozieres, *J. Phys. (France)* **32**, 913 (1971).
²⁸I. Kllich, in *Quantum Noise in Mesoscopic Systems*, edited by Yu. V. Nazarov (Kluwer, Dordrecht, 2003), p. 7.
²⁹Y. Adamov and B. A. Muzykantskii, *Phys. Rev. B* **64**, 245318 (2001).
³⁰B. A. Muzykantskii and Y. Adamov, *Phys. Rev. B* **68**, 155304 (2003).
³¹B. Braunecker, *Phys. Rev. B* **73**, 075122 (2006).
³²B. Muzykantskii, N. d'Ambrumenil and B. Braunecker, *Phys. Rev. Lett.* **91**, 266602 (2003).
³³V. E. Korepin, N. M. Bogoliubov, and A. G. Izergin, *Quantum Inverse Scattering Method and Correlation Functions* (Cambridge University Press, Cambridge, 1993).
³⁴N. I. Muskhelishvili, *Singular Integral Equations* (P. Noordhoff Ltd., Groningen, 1953).
³⁵L. N. Oliveira and J. W. Wilkins, *Phys. Rev. B* **32**, 696 (1985).
³⁶A. Weichselbaum and J. von Delft, *Phys. Rev. Lett.* **99**, 076402 (2007).
³⁷P. W. Anderson, G. Yuval, and D. R. Hamann, *Phys. Rev. B* **1**, 4464 (1970).
³⁸P. W. Anderson, *Phys. Rev. Lett.* **18**, 1049 (1967).
³⁹L. A. Feldkamp and L. C. Davis, *Phys. Rev. B* **22**, 4994 (1980).
⁴⁰H. R. Krishna-murthy, J. W. Wilkins, and K. G. Wilson, *Phys. Rev. B* **21**, 1003 (1980); **21**, 1044 (1980).

Chapter 4

Dynamical phase transitions

The nonequilibrium dynamics in quantum many-body systems can change its qualitative behavior abruptly as has been observed in a number of different systems [11, 40, 153, 159, 117] suggesting the existence of a dynamical equivalent to equilibrium phase transitions. Such a correspondence, however, has up to now not been established conceptually for closed quantum systems.

The staggered magnetization of one-dimensional anisotropic Heisenberg chains shows a change in its long-time behavior after a quench from purely exponential to damped oscillatory exactly at the equilibrium quantum critical point where relaxation also becomes most efficient [11]. Similar observations have been made for quenches in the Hubbard model [40, 153] where for a quench from an initial zero temperature Fermi sea the step in the Fermi distribution shows oscillatory contributions for interactions $U > U_c^{\text{dyn}}$ larger than a critical value $U_c^{\text{dyn}} \gtrsim U_c$ that, however, is close to but not precisely the value U_c of the equilibrium metal-Mott insulator phase transition [40]. For quenches in the bosonic mean-field version of the Hubbard model a similar shift in the value of the critical interaction U_c^{dyn} compared to U_c has been found [159]. A system of weakly interacting bosons in two dimensions can undergo a transition similar to an equilibrium Kosterlitz-Thouless one in consequence of a specific nonequilibrium protocol where the equilibrium order parameter correlation function shows a transition from algebraic to exponential behavior [117]. As a general observation for all the described examples the presence of an underlying equilibrium critical point seems to be important.

For classical systems a framework for dynamical phase transitions has been introduced, first in the context of glasses [67]. This phase transition happens in the space of trajectories. According to a measure for the activity of the system the dominant trajectories contributing to the dynamics are classified as either active or inactive. The dynamical order parameter of this transition is then given by the average activity of the dominant trajectories. This concept has been extended to small [57] and macroscopically large [10] *open* quantum systems. Up to now, however, a conceptual framework of a dynamical phase transition for *closed* quantum systems does not exist. In the following, a possible definition of such a transition will be introduced.

4.1 The concept of a dynamical quantum phase transition

The definition of a dynamical phase transition in the following will be studied for quantum quenches, for details see Sec. 2. For such protocols the system under study is prepared in the ground state $|\psi_0\rangle$ of a Hamiltonian H_0 . At time $t = 0$ a parameter λ of the Hamiltonian is suddenly switched from a value λ_0 to a new value λ_f corresponding to a Hamiltonian $H_f = H(\lambda_f)$ different from $H_0 = H(\lambda_0)$. For the generic case where $|\psi_0\rangle$ is not an eigenstate of H_f the initial state will show nontrivial dynamics.

For what follows, a dynamical phase transition will be defined on the basis of real-time nonanalyticities in the sense that the derivative at a given order of some measurable quantity shows a jump or a singularity in time. This implies the breakdown of short time expansions similar to the breakdown of, e.g., high-temperature, expansions at a critical point of an equilibrium phase transition. Thus, it is not possible to determine the system's dynamics by a short time expansion even in case where the expansion is known to all orders in time t . The time evolution of states in quantum mechanics is governed by the Schrödinger equation. This immediately poses the question whether these real-time nonanalyticities are compatible with general quantum mechanical principles. As it turns out, however, the respective dynamical phase transitions as analyzed below only occur in the thermodynamic limit again similar to the equilibrium case. In this way no fundamental and conceptual problems arise for the propagation of states in time as for finite-size or eventually large systems the Schrödinger equation always allows, in principle, for straightforward solutions by integration.

Expanding the time evolved initial state $|\psi_0(t)\rangle = \exp[-iH_ft]|\psi_0\rangle$ in the eigenbasis $|E_\nu\rangle$, $H_f|E_\nu\rangle = E_\nu|E_\nu\rangle$, of the final Hamiltonian one obtains the Lehmann representation

$$|\psi_0(t)\rangle = \sum_\nu e^{-iE_\nu t}|E_\nu\rangle\langle E_\nu|\psi_0\rangle. \quad (4.1)$$

How can such an object of rotating phases become nonanalytic? Clearly, if the Hilbert space has finite dimension such as for finite fermionic or spin lattice systems, this superposition will always result in an analytic expression. This signals the importance of the thermodynamic limit as emphasized before. Note that the dynamical phase transition in the space of trajectories as introduced in Ref. [67] can also happen for small systems [57] far beyond the thermodynamic limit. The expression as such in Eq. (4.1) is purely formal, the physically relevant quantities are expectation values, probabilities, etc., that are studied in what follows.

4.1.1 Loschmidt amplitude

The central quantity of the analysis will be termed the Loschmidt amplitude

$$\mathcal{L}(t) = \langle\psi_0|e^{iH_0t}e^{-iH_ft}|\psi_0\rangle \quad (4.2)$$

that establishes a measure of how far time evolution drives the system away from the initial state. In the following, the zero of energy will be chosen such that $H_0|\psi_0\rangle = 0$. In this gauge the propagator $\exp[-iH_0t]$ acting on the state $|\psi_0\rangle$ can be replaced by the identity. The Loschmidt amplitude can be decomposed into absolute value and phase contributions in its polar representation

$$\mathcal{L}(t) = |\mathcal{L}(t)|e^{i\varphi(t)}. \quad (4.3)$$

Its modulus squared

$$L(t) = |\mathcal{L}(t)|^2 = |\langle\psi_0|e^{-iH_f t}|\psi_0\rangle|^2 \quad (4.4)$$

is the Loschmidt echo and may be interpreted as a return probability [78]. The Loschmidt echo quantifies the stability of quantum motion and shares deep connections to the field of quantum chaos [131].

The quantity $\varphi(t)$ measures the phase acquired in consequence of the nonequilibrium protocol and may be viewed as the nonadiabatic equivalent to the Berry phase [14] that is associated with an *adiabatic* transport of a wave function along a parameter manifold.

In view of Sec. 3.1 and in particular Eq. (3.10) the Loschmidt amplitude is the moment generating function of the work distribution function of the respective quantum quench. This formal identification has the immediate consequence that, remarkably, the Loschmidt phase $\varphi(t)$ is gauge invariant. As such it is a measurable quantity, in principle [14]. Phases and phase differences are typically measured through interference experiments. From elementary quantum mechanics the outcome of a measurement in closed systems is associated with the eigenvalues of a Hermitian operator in the Hilbert space under study. For phases, however, no such observable exists; so how can a phase be measured then? This paradox can be resolved by noticing that the quantum quench requires the coupling to an environment, see the arguments in Sec. 1. Treating the influence of a classical force acting on the system through a Hamiltonian depending on an external parameter has the immediate advantage that the system can be considered as if it were isolated. As a consequence, however, some measurable quantities for which an observable exists in the full system may only appear as gauge-invariant quantities in the restricted subsystem [142].

4.1.2 Fisher zeros

Recalling that a dynamical phase transition has been defined on the basis of real-time nonanalyticities the question remains which quantities are potentially able to show nonanalyticities generically. The notion of generically in this context is supposed to mean as generic as there are equilibrium phase transitions. Below, it will be shown that the Loschmidt amplitude is such a quantity as has been demonstrated already for the specific case of magnetic field ramps in the Ising model [138]. Consider a generalized function

$$\mathcal{L}(z) = \langle\psi_0|e^{-iH_f z}|\psi_0\rangle, \quad z \in \mathbb{C}, \quad (4.5)$$

by extending time into the whole complex plane. The basic observation is that on the purely imaginary time axis $z = -i\tau$ the generalized Loschmidt amplitude becomes an

equilibrium boundary partition function

$$Z(\tau) = \mathcal{L}(-i\tau) = \langle \psi_0 | e^{-H_f \tau} | \psi_0 \rangle \quad (4.6)$$

of a system with boundaries separated by a distance τ with boundary conditions implemented by the boundary states $|\psi_0\rangle$ [105]. This identification is up to the present knowledge of purely formal nature. The equilibrium boundary partition function $Z(\tau)$ has no physical meaningful relationship to the nonequilibrium quench problem as it is known up to now.

The formal observation in Eq. (4.6) has a few important implications. First, it clarifies the appropriate scaling behavior in the thermodynamic limit. Note that the thermodynamic limit is of fundamental importance as already argued below Eq. (4.1). The free energy is extensive in system size V such that the Loschmidt amplitude has to be of large-deviation form [171]

$$\mathcal{L}(z) \xrightarrow{V \rightarrow \infty} e^{Vf(z)} \quad (4.7)$$

with $f(z)$ independent of V . Concluding, the proper quantity in order to study the behavior of the Loschmidt amplitude in the thermodynamic limit is the rate function $f(z)$. This is completely analogous to the equilibrium case where the appropriate quantity is the free energy density and not the partition function itself for large system sizes.

Let μ be a parameter of an equilibrium partition function Z of a system of size V such as magnetic field h or temperature T . Then Z and in particular the phase transitions of the model are determined by the zeros in the extended complex parameter plane of μ . In case of a magnetic field, i.e., $\mu = h$, the corresponding partition function zeros are called Lee-Yang zeros [106], for $\mu = \beta = T^{-1}$ they are called Fisher zeros [46]. Denoting those by μ_r the partition function Z can be represented in product form

$$Z(\mu) = e^{-G(\mu)} \prod_r \left[1 - \frac{\mu}{\mu_r} \right] \quad (4.8)$$

yielding the free energy F

$$F(\mu) = -T \sum_r \log \left[1 - \frac{\mu}{\mu_r} \right] + Tg(\mu). \quad (4.9)$$

Here, Boltzmann's constant $k_B = 1$ has been set to one such that temperature is measured in units of energy. The functions $G(\mu)$ and $g(\mu) = V^{-1}G(\mu)$ are smooth and analytic. Concerning phase transition they will therefore be unimportant such that they will not be considered in what follows. If $Z(\mu)$ is just a finite polynomial in μ the factorization of the partition function is obvious and $G(\mu)$ is a constant. In case of an infinite polynomial the factorization is guaranteed by the Weierstrass factorization theorem as long as the expression in Eq. (4.8) converges. In the general case this cannot be proven but as it turns out the convergence is always given for all practical purposes. In the above representation in Eq. (4.8) all the details and properties of the physical system are encoded in the location of the zeros μ_r .

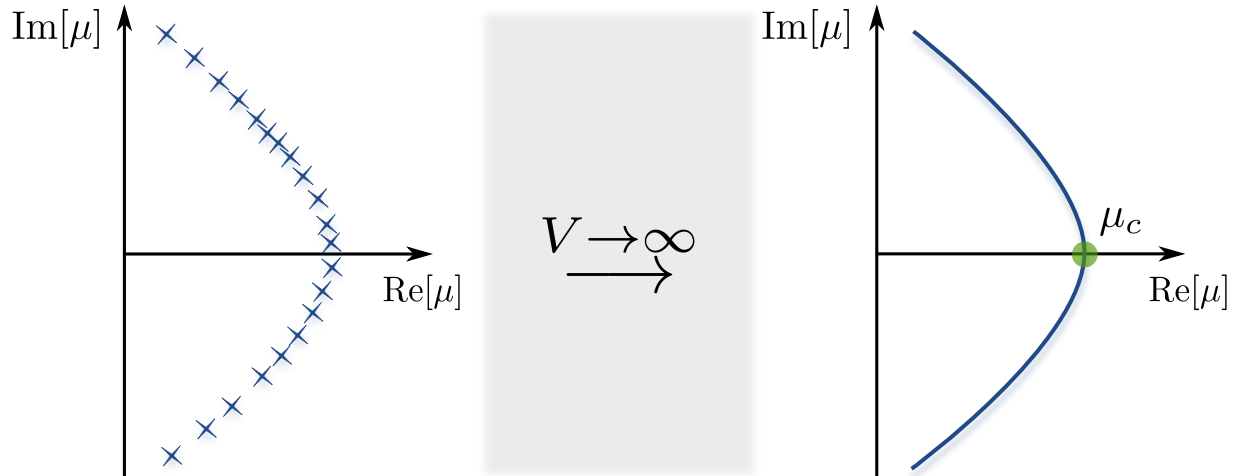


Figure 4.1: Schematic illustration of the partition function zeros of a parameter μ extended into the whole complex plane. The physical axis corresponds to real values of $\mu \in \mathbb{R}$. For a finite-size system the zeros are located at discrete and well-separated points as indicated by stars in the left picture. As the system size V increases the zeros accumulate on lines. At those points where such a line of zeros crosses the physical $\mu \in \mathbb{R}$ axis - in this schematic picture this corresponds to $\mu = \mu_c$ - the system undergoes a phase transition.

For a finite-size system the zeros are typically located at discrete points in the complex μ plane away from the physical $\mu \in \mathbb{R}$ axis. Increasing the system size the number of zeros increases and they typically accumulate on lines [46]. For a schematic picture see Fig. 4.1. Although for a finite-size system no zero lies directly on the real μ axis a line of accumulated zeros may cut the axis in the thermodynamic limit. In such case the partition function becomes nonanalytic and the system thus undergoes a phase transition. The character of this transition whether it is continuous or of first order as well as the respective exponents or the latent heat are all encoded in the line density of zeros at the transition point [79]. If the line density is a constant the phase transition is of first order and the respective constant is proportional to the latent heat. Provided the line density vanishes in a power-law fashion one obtains a continuous phase transition. For the case of Fisher zeros where $\mu = \beta = T^{-1}$ is the inverse temperature the exponent of the algebraic behavior of the density of zeros determines the critical exponent of the specific heat. Most importantly, for numerical simulations finite-size scaling of the zeros allows for the derivation of the latent heat or all the critical exponents [79].

As shown before the Loschmidt amplitude becomes an equilibrium partition function on the imaginary time axis such that it is possible to adopt the knowledge about the partition function zeros to the nonequilibrium quantum quench problem. As a function of time the Loschmidt amplitude is determined by its complex time zeros t_r such that it can be represented in the following way

$$\mathcal{L}(t) = e^{-G(t)} \prod_r \left[1 - \frac{t}{t_r} \right] \quad (4.10)$$

where the prefactor determined by the smooth function $G(t)$ will play no role in the following considerations. The complex time zeros will be termed Fisher zeros in the following due to the formal similarity of imaginary time and inverse temperature. If in the thermodynamic limit such a line of Fisher zeros crosses the real-time axis at a specific point t^* the Loschmidt amplitude becomes nonanalytic at $t = t^*$ defining the location of the dynamical phase transition.

Based on these general considerations about partition function zeros the Loschmidt amplitude can become nonanalytic generically in the sense of as generic as there are equilibrium phase transitions. It is therefore not just coincidence that the Loschmidt amplitude for magnetic field quenches in the transverse field Ising model studied below shows nonanalyticities. One may thus expect that nonanalyticities appear also in Loschmidt echoes of other model systems. In case of the Ising model there is a direct connection between real-time nonanalyticities and the quantum critical point of the underlying equilibrium theory. A general proof of such a relationship, however, does not exist. In Sec. 4.2 below lines of Fisher zeros as well as the nonanalyticities of the Loschmidt amplitude are investigated for magnetic field quenches in the one-dimensional transverse field Ising model.

Note that even though there seems to be formal relationship between the Loschmidt amplitude and an equilibrium partition function, the Loschmidt amplitude should not be viewed as a “dynamical partition function” because it is not possible to deduce the time evolution of thermodynamic quantities from it such as generalized forces or the expectation values of local observables. What can be deduced from the Loschmidt amplitude is the average work performed W_{av} , compare Ch. 3, via $W_{\text{av}} = i \frac{d\mathcal{L}(t)}{dt} |_{t=0}$.

4.1.3 Observables

Although it defines the location of a dynamical phase transition the Loschmidt amplitude is a rather abstract quantity and difficult to measure for large systems because of its exponential suppression due to its large-deviation scaling, see Eq. (4.7). In case of slow ramps instead of quenches the rate function $f(t)$ takes on small numerical values that the measurement of the Loschmidt amplitude is within the scope of experimental resolution. Apart from this special case, in experiments one is typically interested in local observables and correlation functions. As far as it is known in the literature there exists no example of a local observable with real-time nonanalyticities. A general proof of this property, however, does not exist. Even though local observables may be analytic it remains to clarify the potential impact of the dynamical phase transition onto them. The Loschmidt amplitude quantifies the deviations from the initial state $|\psi_0\rangle$ during time evolution. From a physical point of view one may expect that those properties of the system that are especially sensitive to the initial state may be influenced most by nonanalyticities in the Loschmidt amplitude and therefore by the dynamical phase transitions. One general class of observables that fall into this category may be equilibrium order parameters for the case where the initial state is chosen within the ordered phase of the model under study. But as will have become clear those are just physically motivated arguments without an explicit proof. Ultimately, this general statement has to be tested at least on the basis of

a sufficiently large class of examples to show its validity. Below, they will be verified for the one-dimensional Ising model. Another but structurally very similar model where the validity of these arguments can be shown is the one-dimensional XY -chain as investigated in the work of Ref. [11].

For the particular example of magnetic field quenches in the one-dimensional transverse field Ising model studied in Sec. 4.2 one such observable is the longitudinal magnetization that represents the equilibrium order parameter. In one dimension the ferromagnetic order only exists at zero temperature such that the nonzero energy pumped into the system by the quench will force the magnetization to vanish in the long-time limit. This always happens [22, 23], on intermediate time scales, however, the dynamics turn out to be particularly influenced by dynamical phase transitions. Here, just a short overview will be given, for details see Sec. 4.2. Suppose the Ising system is prepared in a ferromagnetically ordered state with a finite magnetization. For a final transverse magnetic field that still supports ferromagnetic order in equilibrium the Loschmidt amplitude is analytic for all times t . As soon, however, as the final magnetic field crosses the equilibrium quantum critical point the Loschmidt amplitude shows nonanalyticities that appear periodically on an emergent nonequilibrium time scale t^* not set by the mass of the theory but by an energy scale larger than the gap. Simultaneously, the equilibrium order parameter develops an oscillatory decay similar to the staggered magnetization in one-dimensional Heisenberg chains [11] mentioned in the beginning of this Chapter, see Ch. 4. Below, it is found numerically that the frequency of this oscillation of the equilibrium order parameter precisely coincides with the periodic appearance of nonanalyticities in the Loschmidt amplitude. Although no formal proof has been found establishing a relation between the Loschmidt amplitude and the equilibrium order parameter there is a connection between the two as demonstrated numerically. From the general physical argument given above one may expect that such a relation may be not restricted to this special case but to be rather generic.

4.2 Dynamical quantum phase transitions in the Ising model

The one-dimensional transverse field Ising chain constitutes the paradigmatic model for the study of continuous equilibrium phase transitions. Within the Ising model the z -components of $1/2$ -spins are coupled on a lattice of length L in presence of a transverse field

$$H_I(g) = -\frac{J}{2} \sum_{l=1}^L [\sigma_l^z \sigma_{l+1}^z + g \sigma_l^x]. \quad (4.11)$$

Here, σ_l^μ with $\mu = x, y, z$ denotes the Pauli matrices. The ferromagnetic coupling constant $J > 0$ sets the overall energy scale and will be set to $J = 1$ in the following. The strength of the transverse magnetic field is set by g . The Ising model exhibits a continuous quantum phase transition from a ferromagnetically ordered phase for $g < 1$ to a quantum paramagnet

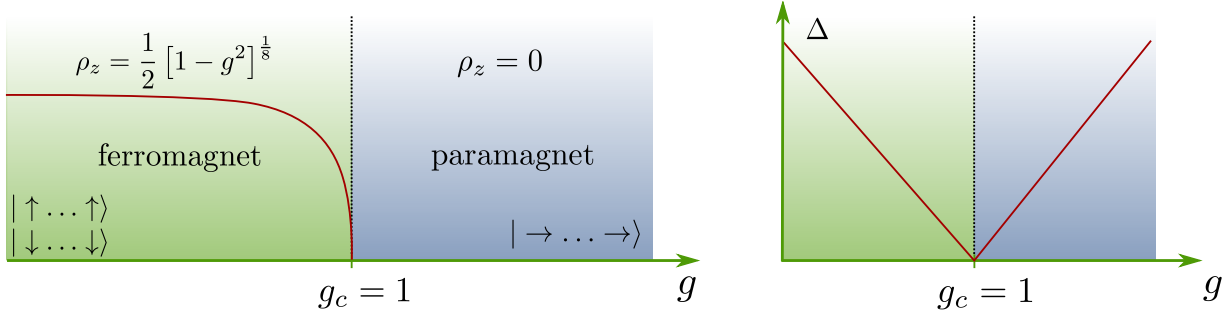


Figure 4.2: Equilibrium zero-temperature phase diagram of the one-dimensional transverse field Ising model. The critical point $g_c = 1$ separates a ferromagnetically ordered phase for $g < g_c$ from a quantum paramagnet for $g > g_c$. The associated local order parameter is the longitudinal magnetization ρ_z that vanishes as $\rho_z \sim (g_c - g)^{1/8}$ near the quantum critical point $g \rightarrow g_c$. The gap in the spectrum Δ vanishes linearly when the magnetic field g approaches the quantum critical point.

for $g > 1$ as is illustrated in a schematic phase diagram in Fig. 4.2. For details about the equilibrium properties see Ref. [149].

The Ising Hamiltonian in Eq. (4.11) exhibits an exact \mathbb{Z}_2 symmetry implemented by the unitary transformation

$$U = \prod_{l=1}^L \sigma_l^x \quad (4.12)$$

that maps the Pauli matrices according to the formulas

$$\sigma_l^x \mapsto \sigma_l^x, \quad \sigma_l^z \mapsto -\sigma_l^z. \quad (4.13)$$

In the ferromagnetically ordered phase for $g < g_c$ this \mathbb{Z}_2 symmetry is broken yielding a nonvanishing longitudinal magnetization as illustrated in Fig. 4.2. The spontaneous symmetry breaking can be demonstrated best for the particular case of zero transverse magnetic field $g = 0$. In this case the system reduces to a collection of spins with a ferromagnetic nearest-neighbor coupling of the spin- z components. In this limit there is an exact ground state degeneracy of the two fully polarized states

$$|\psi_1\rangle = |\uparrow \dots \uparrow\rangle, \quad |\psi_2\rangle = |\downarrow \dots \downarrow\rangle, \quad (4.14)$$

with opposite longitudinal magnetization in z -direction. The elementary excitations above the two respective ground states $|\psi_1\rangle$ and $|\psi_2\rangle$ are domain walls [149]. At small but finite magnetic field the exact degeneracy is lifted with an energy difference, however, exponentially suppressed by system size.

In the opposite limit of large magnetic fields $g \gg 1$ where the ferromagnetic coupling can be neglected to zeroth order the ground state of the system is unique. All spins point in one direction and the ground state factorizes into a product state

$$|\psi_0\rangle = |\rightarrow \dots \rightarrow\rangle = \prod_{l=1}^L |\rightarrow\rangle_l, \quad |\rightarrow\rangle_l = \frac{1}{\sqrt{2}} [|\uparrow\rangle_l + |\downarrow\rangle_l], \quad (4.15)$$

of states $|\rightarrow\rangle_l$ corresponding to the +1 eigenvalues of the Pauli matrices σ_l^x .

The Ising Hamiltonian can be solved exactly by a mapping onto a quadratic fermionic theory [132]. For that purpose it is convenient to perform a rotation around the y -spin axis about 90 degrees that effectively amounts to the replacement

$$\sigma_l^z \mapsto \sigma_l^x, \quad \sigma_l^x \mapsto -\sigma_l^z. \quad (4.16)$$

This transformation yields the following Hamiltonian

$$H_I(g) = \frac{J}{2} \sum_{l=1}^L [g\sigma_l^z - \sigma_l^x \sigma_{l+1}^x]. \quad (4.17)$$

For what follows this representation of the Ising model will be used throughout. Using the Jordan-Wigner transformation, see also Sec. 2.3, it is possible to represent the Ising Hamiltonian in terms of operators

$$c_l^\dagger = e^{-i\phi_l} S_l^+, \quad c_l = S_l^- e^{i\phi_l}, \quad \phi_l = \pi \sum_{m=1}^{l-1} \left[S_z^m + \frac{1}{2} \right], \quad (4.18)$$

that fulfill fermionic anticommutation relations

$$\{c_l, c_{l'}^\dagger\} = \delta_{ll'}, \quad \{c_l, c_{l'}\} = 0, \quad \{c_l^\dagger, c_{l'}^\dagger\} = 0. \quad (4.19)$$

In this fermionic representation the Ising Hamiltonian maps onto a quadratic fermionic theory

$$H(g) = \frac{J}{2} \sum_{l=1}^L [2gc_l^\dagger c_l - g + c_l^\dagger c_{l+1} + c_{l+1}^\dagger c_l + c_l^\dagger c_{l+1}^\dagger + c_{l+1} c_l]. \quad (4.20)$$

To arrive at this simple expression of the Hamiltonian antiperiodic boundary conditions have been imposed on the fermionic chain. The Hamiltonian does not conserve the number of fermionic particles. Parity, however, is conserved, i.e., starting in a sector with an even number of Jordan-Wigner fermions the action of the Hamiltonian can never yield a state with an odd number of them. This property has been used in the derivation of Eq. (4.20) where the Hamiltonian has been projected onto the even parity sector. The above Hamiltonian can be diagonalized exactly on the basis two transformations. First, introduce the momentum representation of the fermionic operators via

$$c_k = \frac{1}{\sqrt{L}} \sum_{l=1}^L e^{-ikl} c_l. \quad (4.21)$$

The momentum $k = 2\pi[n_k + 1/2]/L$ with $n_k = -L/2, \dots, L/2 \in \mathbb{N}$ takes on values in the interval $k \in [-\pi, \pi]$ in the thermodynamic limit. The precise discrete structure of the momentum values is a consequence of the antiperiodic boundary conditions chosen before. Note that the lattice spacing $a = 1$ has been set to one. In the Fourier transformed basis

only $\pm k$ momentum states are coupled to each other as a consequence of translational invariance

$$H(g) = J \sum_{k>0} \left[(g - \cos(k)) (c_k^\dagger c_k + c_{-k}^\dagger c_{-k}) + i \sin(k) (c_{-k}^\dagger c_k^\dagger + c_{-k} c_k) - \frac{g}{2} \right]. \quad (4.22)$$

The last step of the diagonalization procedure consists of performing a Bogoliubov rotation in the momentum basis of the fermionic Jordan-Wigner operators that mixes creation and annihilation operators of opposite momentum

$$\eta_k = u_k(g) c_k - i v_k(g) c_{-k}^\dagger, \quad \eta_{-k} = u_k(g) c_{-k} + i v_k(g) c_k^\dagger, \quad k > 0, \quad (4.23)$$

with inverse transformation

$$c_k = u_k(g) \eta_k + i v_k(g) \eta_{-k}^\dagger, \quad c_{-k} = u_k(g) \eta_{-k} - i v_k(g) \eta_k^\dagger, \quad k > 0. \quad (4.24)$$

Here, the functions $u_k(g) \in \mathbb{R}$ and $v_k(g) \in \mathbb{R}$ are supposed to be real. The unitarity of the transformation then requires that $u_k^2(g) + v_k^2(g) = 1$ allowing for the parametrization

$$u_k(g) = \cos(\theta_k(g)), \quad v_k(g) = \sin(\theta_k(g)). \quad (4.25)$$

Applying the Bogoliubov transformation to the Hamiltonian in Eq. (4.22) diagonalizes the problem provided the Bogoliubov angles $\theta_k(g)$ fulfill the following equation

$$\tan(2\theta_k(g)) = \frac{\sin(k)}{g - \cos(k)}. \quad (4.26)$$

For this choice the Hamiltonian becomes diagonal

$$H(g) = \sum_{k>0} E_k(g) \left[\eta_k^\dagger \eta_k - \eta_{-k}^\dagger \eta_{-k} \right]. \quad (4.27)$$

As $\tan(x)$ is a periodic function of its argument x Eq. (4.26) does not uniquely determine the Bogoliubov angles $\theta_k(g)$. Requiring that $\theta_k(g) \in [0, \pi/2]$ is an analytic function of k and that the final spectrum $E_k(g) > 0$ is positive fixes $\theta_k(g)$ to be

$$\theta_k(g) = \frac{1}{2} \arctan \left[\frac{\sin(k)}{g - \cos(k)} \right] + \frac{\pi}{2} \theta[\cos(k) - g] \quad (4.28)$$

with $\theta(x) = 1$ for $x > 0$ and $\theta(x) = 0$ for $x < 0$ the Heaviside step function. Even though the Heaviside step function is not analytic the full expression for $\theta_k(g)$ is. With this choice for the Bogoliubov angles the final spectrum $E_k(g)$ is given by the following expression

$$E_k(g) = \sqrt{[g - \cos(k)]^2 + \sin^2(k)}. \quad (4.29)$$

Here and for what follows, J as the overall energy scale has been set to $J = 1$. The ground state of the Hamiltonian is thus the Fermi sea $| \rangle_\eta$ without any η -fermion such that $\eta_k | \rangle = 0$. The associated gap $\Delta = E_{k=0}(g)$ of the single-particle spectrum is vanishes at the quantum critical point $g = g_c$ linearly as $\Delta(g) = |g - g_c|$.

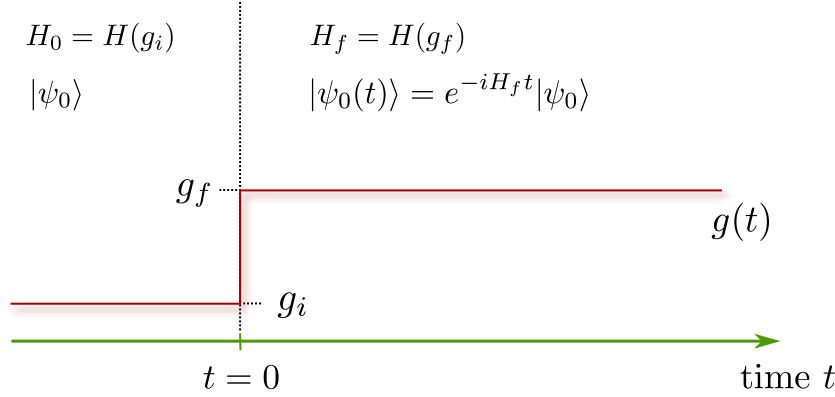


Figure 4.3: Schematic illustration of the transverse magnetic field quench in the one-dimensional Ising model. For times $t < 0$ the system is prepared in the ground state $|\psi_0\rangle$ according to a value g_i of the transverse field. At time $t = 0$ the magnetic field is suddenly switched to a new value g_f . This sudden quench induces dynamics of the initial state for times $t > 0$.

4.2.1 Quenches in the transverse magnetic field

In the following the nonequilibrium time evolution will be generated by a quantum quench in the transverse magnetic field as is illustrated in Fig. 4.3. For more details about quantum quenches and important related questions see the introduction to Ch. 2. For times $t < 0$ the system is supposed to be prepared in the ground state $|\psi_0\rangle$ of the Hamiltonian $H(g_i)$ in Eq. (4.17) at some initial magnetic field $g = g_i$. At time $t = 0$ the magnetic field g is suddenly switched to a new value $g = g_f$. As the initial state $|\psi_0\rangle$ is not an eigenstate of the final Hamiltonian $H_f = H(g_f)$ it will show nontrivial dynamics.

The nonequilibrium dynamics of magnetic field quenches in the transverse field Ising model have been analyzed in numerous works in the literature [146, 147, 22, 23, 138, 160, 74, 75]. Of most relevance for the dynamical phase transition discussed below is the time evolution of the equilibrium order parameter, the longitudinal magnetization

$$\rho_x(t) = \frac{1}{2} \langle \psi_0(t) | \sigma_l^x | \psi_0(t) \rangle. \quad (4.30)$$

that is independent of the location $l = 1, \dots, L$ on the chain due to translational invariance. Note that the representation of the Ising model in Eq. (4.17) is used in what follows instead of Eq. (4.11). In equilibrium, the longitudinal magnetization is known exactly [132]

$$\rho_x^{\text{eq}} = \frac{1}{2} [1 - g^2]^{\frac{1}{8}} \quad (4.31)$$

with an exponent $1/8$ demonstrating that the one-dimensional transverse quantum Ising model belongs to the universality class of the $2D$ classical Ising model [149].

Due to the quench a finite amount of energy is pumped into the system. The order in the one-dimensional Ising model only exists at zero temperature such that one may

expect that the longitudinal magnetization vanishes at least in the asymptotic long-time limit. This is indeed the case as demonstrated recently [22, 23]. Depending on the values of initial and final magnetic fields different cases have to be distinguished. For quenches starting and ending in the ordered phase, i.e., $g_i, g_f < 1$, the order parameter decays exponentially at long times at a rate that is known exactly [22, 23]

$$\rho_x(t) \xrightarrow{t \rightarrow \infty} \sqrt{C} e^{-\Gamma t}, \quad \Gamma = - \int_0^\pi \frac{dk}{\pi} \frac{dE_k(g_f)}{dk} \log |\cos(\theta_k(g_f) - \theta_k(g_i))| \quad (4.32)$$

with $\theta_k(g)$ the Bogoliubov angles defined through Eq. (4.26) and $E_k(g_f)$ the spectrum of the final Hamiltonian, see Eq. (4.29). The prefactor is a function of initial and final magnetic field and is also known analytically [23]

$$C = \frac{1 - g_i g_f + \sqrt{(1 - g_i^2)(1 - g_f^2)}}{2\sqrt{1 - g_i g_f}(1 - g_i^2)^{1/4}}. \quad (4.33)$$

In case where the final magnetic fields crosses the equilibrium quantum critical point the longitudinal magnetization acquires an additional oscillatory behavior. In this regime there exists no analytical solution to the problem, but a conjecture [23] that nicely fits to the numerical results

$$\rho_x(t) \xrightarrow{t \rightarrow \infty} \sqrt{C} [1 + \cos(2\varepsilon^* t + \alpha)]^{1/2} e^{-\Gamma t}. \quad (4.34)$$

The period of the oscillatory contribution is set by an energy scale $\varepsilon^* = E_{k^*}(g_f)$ given by the condition $\cos[\theta_{k^*}(g_f) - \theta_{k^*}(g_i)] = 0$. This energy scale will appear again below in the study of the dynamical phase transition. The shift α in the phase of the oscillatory contribution is not known as a function of the magnetic fields. The rate Γ of the decay is again given by the formula in Eq. (4.32). The prefactor, however, differs compared to quenches within the ferromagnetic phase

$$C = \sqrt{\frac{g_f \sqrt{1 - g_i^2}}{g_i + g_f}}. \quad (4.35)$$

For quenches starting in the disordered phase, i.e., $g_i > 1$, the order parameter remains zero during time evolution.

4.2.2 Loschmidt amplitude

As already argued in Sec. 4.1.1 the Loschmidt amplitude

$$\mathcal{L}(t) = \langle \psi_0 | e^{iH_0 t} e^{-iH_f t} | \psi_0 \rangle \quad (4.36)$$

plays the central role for the dynamical phase transition introduced in Sec. 4.1. For magnetic field quenches in the one-dimensional Ising model the Loschmidt amplitude is known exactly [162]

$$\mathcal{L}(t) = e^{-i\Delta E t} e^{-L_f(t)} \quad (4.37)$$

where $\Delta E = E_{\text{gs}}(g_f) - E_{\text{gs}}(g_i)$ is the ground state energy difference for the two Ising models at different magnetic fields $g = g_i$ and $g = g_f$. As already argued in Sec. 4.1.2 the Loschmidt amplitude has to satisfy a large-deviation principle such that the rate function $f(t)$ has to be independent of system size L . Due to the integrability of the model the Loschmidt amplitude factorizes into subspaces of different momentum yielding the following analytical expression for $f(t)$ [162]

$$f(t) = - \int_0^\pi \frac{dk}{2\pi} \log [\cos^2(\phi_k) + \sin^2(\phi_k)e^{-2iE_k(g_f)t}] . \quad (4.38)$$

In this equation a short-hand expression has been introduced for the difference of the two Bogoliubov angles $\theta_k(g_i)$ and $\theta_k(g_f)$ corresponding to the initial and final Hamiltonian, see Eq. (4.26),

$$\phi_k = \theta_k(g_i) - \theta_k(g_f) . \quad (4.39)$$

Before turning to the actual dynamical phase transition a different quantity will be analyzed first - the work distribution function for the quantum quench.

4.2.3 Work distribution function

A quantum quench changes the internal energy of the system and thereby work W is performed. As already analyzed in detail in Sec. 3.1 quantum work is not an observable but rather a random variable with a probability distribution function $P(W)$ termed work distribution function [167]. For a quantum quench the work distribution function is given by the following general expression

$$P(W) = \sum_\lambda |\langle E_\lambda | \psi_0 \rangle|^2 \delta [W - (E_\lambda - E_{\text{gs}}(g_i))] . \quad (4.40)$$

Here, $E_{\text{gs}}(g_i)$ denotes the ground state energy of the initial state $|\psi_0\rangle$ of the Ising model at initial transverse magnetic field $g = g_i$. In the following the zero of energy will be chosen such that $E_{\text{gs}}(g_i) = 0$. The states $|E_\lambda\rangle$ denote a complete set of eigenstates of the final Hamiltonian H_f with energies E_λ , i.e., $H_f|E_\lambda\rangle = E_\lambda|E_\lambda\rangle$. As already demonstrated in Eq. (3.10) the Fourier transform of the work distribution $P(W)$ of a quench is given by the Loschmidt amplitude such that there is a deep connection for those two quantities.

In the following a general framework will be presented that allows for the calculation of the work distribution functions. For that purpose define a function

$$G(\tau) = \sum_\lambda |\langle E_\lambda | \psi_0 \rangle|^2 e^{-E_\lambda \tau} = \langle \psi_0 | e^{-H_f \tau} | \psi_0 \rangle = \mathcal{L}(-i\tau) \quad (4.41)$$

that is the imaginary time extension of the Loschmidt amplitude. It may be interpreted as an equilibrium boundary partition function as already analyzed in Sec. 4.1.2. Using the definition of the work distribution in Eq. (4.40) the function $G(\tau)$ is related to $P(W)$ via Laplace transformation

$$G(\tau) = \int dW P(W) e^{-W\tau} . \quad (4.42)$$

Recall that on the real-time axis the relation between $P(W)$ and the Loschmidt amplitude $\mathcal{L}(t)$ is given by a Fourier transformation. Due to the exponential suppression of $\mathcal{L}(t)$ with system size, compare Eq. (4.37), even the numerical evaluation of the Fourier transformation is practically impossible. As the magnetic field g acts globally the work W performed is an extensive quantity such that it is suitable to change variables to intensive work densities $w = W/L$

$$G(\tau) = e^{-Lg(\tau)} = \int dw \mathcal{P}(w) e^{-Lw\tau}. \quad (4.43)$$

with $\mathcal{P}(w) = V^{-1}P(wV)$. Here, the large-deviation property of the Loschmidt amplitude $\mathcal{L}(t)$ in the whole complex time plane has been used such that $G(\tau) = \exp[-Lg(\tau)]$ with $g(\tau)$ the cumulant generating function of $P(W)$. The knowledge of the analytical result of the Loschmidt rate function $f(t)$ in Eq. (4.38) has the immediate consequence that also $g(\tau) = \Delta E\tau - f(-i\tau)$ is known exactly:

$$g(\tau) = \Delta E\tau - \int_0^\pi \frac{dk}{2\pi} \log [\cos^2(\phi_k) + \sin^2(\phi_k)e^{-2E_k(g_f)\tau}]. \quad (4.44)$$

In order to obtain the distribution function $\mathcal{P}(w)$ of the work density w from $G(\tau)$ the Laplace transform in Eq. (4.43) has to be inverted. For the general case this requires the knowledge of $G(\tau)$ in the whole complex τ plane which is, however, a difficult task. Provided the function $G(\tau)$ satisfies a large-deviation principle - as is the case in the present problem - the inversion of the Laplace transform simplifies drastically in the thermodynamic limit $L \rightarrow \infty$. In case where $g(\tau)$ is differentiable the Gärtner-Ellis theorem states that not only $G(\tau)$ but also $\mathcal{P}(w)$ has to be of large deviation form [171]

$$\mathcal{P}(w) = e^{-L\theta(w)}. \quad (4.45)$$

The work rate function $\theta(w)$ is again independent of system size L and is related to $g(\tau)$ via a Legendre transform

$$\theta(w) = -\inf_{\tau \in \mathbb{R}} [w\tau - g(\tau)] \quad (4.46)$$

with inverse

$$g(\tau) = \inf_{w \in \mathbb{R}} [w\tau + \theta(w)] \quad (4.47)$$

Here, \inf denotes the infimum. In this way $\theta(w)$ and $g(\tau)$ are related to each other in the same manner as the thermodynamic potentials in statistical mechanics such as energy and free energy. Moreover, work density w and separation of the boundaries τ , confirm Sec. 4.1.2, are conjugate variables such as volume and pressure. As further consequences of the Gärtner-Ellis theorem $g(\tau)$ is a concave and $\theta(w)$ a convex function [171]. Moreover, $\mathcal{P}(W)$ obeys a central limit theorem [171]. In the thermodynamic limit the work distribution can be approximated by a Gaussian that becomes a delta-function at the average work density $w_{av} = \int dw w \mathcal{P}(w)$ in the limit $L \rightarrow \infty$. Most importantly for practical purposes is that this prescription of calculating the work distribution function only requires the knowledge of $g(\tau)$ on the real- τ axis. This is of particular interest for numerical simulations as

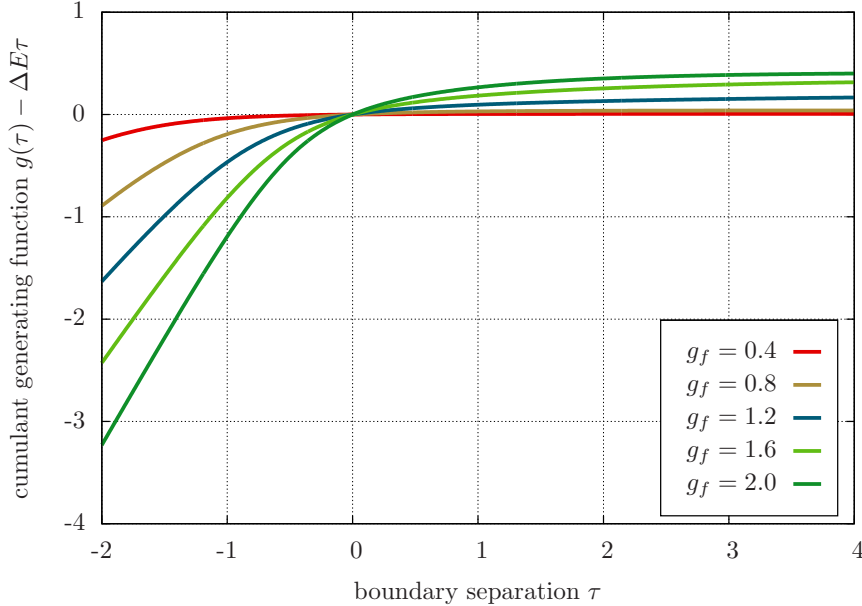


Figure 4.4: Cumulant generating function $g(\tau)$ for quenches in the transverse field Ising model from initial magnetic field $g_i = 0.1$ to different final g_f .

imaginary time propagation is way more efficient than the real-time one especially concerning Quantum Monte Carlo. The most probable values of $\mathcal{P}(w)$ are fortunately encoded in the small τ behavior of $g(\tau)$ that is easily accessible through perturbation expansions, for example. Although the Legendre transform formally requires to find the minimum over the whole real line it is in most cases not necessary to know the respective functions for all values of w or τ as the Legendre transform only acts locally in the variables [171].

If the cumulant generating function $g(\tau)$ is not differentiable then $\theta(w)$ is not a convex function and typically exhibits more than just one local maximum. But still $\mathcal{P}(w)$ obeys a large deviation principle and the Legendre transform yields a function $\theta(w)$ that is the convex envelope of the exact solution. Provided the nonanalyticity is not located at $\tau = 0$ the most probable values of $\mathcal{P}(w)$ still allow for an effective Gaussian description derived from the Gärtner-Ellis theorem while the nonanalyticities only effect the tails of the distribution. If, however, $g(\tau)$ is not analytic at $\tau = 0$ one most likely faces a situation where $\mathcal{P}(w)$ has two equally probable global maxima. But note that for all examples below the cumulant generating function is differentiable for all τ . In Fig. 4.4 the characteristic behavior of the function $g(\tau)$ is shown for different magnetic field quenches. The cumulant generating function is smooth and concave.

Based on these formal considerations it is the scope of the remainder of this section to compute the work distribution functions for magnetic field quenches in the one-dimensional Ising model.

Extreme quenches and coin tossing

Before coming to the general case two analytically solvable limits will be investigated, namely magnetic field quenches from $g_i = 0$ to $g_f \rightarrow \infty$ and vice versa. The associated Bogoliubov angles as defined in Eq. (4.26) appearing in the cumulant generating function $g(\tau)$ are given by

$$\theta_k(g=0) = \frac{\pi}{2} - \frac{k}{2}, \quad \theta_k(g \rightarrow \infty) = 0. \quad (4.48)$$

The corresponding spectra $E_k(g)$, see Eq. (4.29), become flat in both limits

$$E_k(g=0) = 1, \quad E_k(g \rightarrow \infty) = g \quad (4.49)$$

such that the cumulant generating function $g(\tau)$ in Eq. (4.44) for both extreme quenches can be represented in the following way:

$$g(\tau) = \Delta E \tau - \int_0^\pi \frac{dk}{2\pi} \log \left[1 + \cos^2 \left(\frac{k}{2} \right) (e^{-2\Delta\tau} - 1) \right] \quad (4.50)$$

The difference of the Bogoliubov angles $\phi_k = \theta_k(g_i) - \theta_k(g_f)$ is invariant under the exchange $g_i \leftrightarrow g_f$ only up to a sign change that, however, leaves the cumulant generating function invariant. The precise direction of the quench only enters through the gap Δ that takes two different values $\Delta = 1, g_f$ depending on whether $g_f = 0$ or $g_f \rightarrow \infty$. The above integral exhibits an exact analytical solution in terms of elementary functions:

$$g(\tau) = \Delta \varepsilon \tau - \log [1 + e^{-\Delta\tau}] + \log 2. \quad (4.51)$$

with $\varepsilon = \Delta E / L$ the ground state energy density difference. The work rate function $\theta(w)$ can be obtained from $g(\tau)$ through a Legendre transformation, see Eq. (4.46), yielding

$$\theta(w) = \hat{w} \log [\hat{w}] + [1 - \hat{w}] \log [1 - \hat{w}] + \log 2 \quad (4.52)$$

where a normalized variable

$$\hat{w} = \frac{w - \Delta E}{\Delta} \quad (4.53)$$

has been introduced which takes on values $\hat{w} \in [0, 1]$. The restriction to positive values is associated with the fact that the minimum work that has to be performed on the system is the ground state energy difference when starting from an initial zero temperature state. Recall that this is a consequence of the Crooks relation as already analyzed in Sec. 3.2.2. The property that \hat{w} and as well the work density w itself is bounded from above is a consequence of the bounded spectrum of the Ising Hamiltonian and as such a consequence of the lattice structure of the model.

The result for the work rate function $\theta(w)$ in Eq. (4.52) is identical to a coin tossing experiment when identifying \hat{w} with the fraction of either heads or tails in a sequence of L coin flips [171]. The relation between the extreme quenches and coin tossing becomes

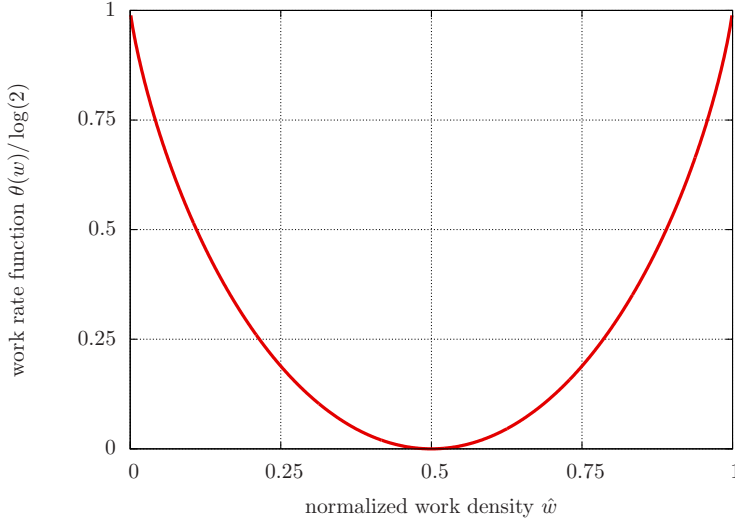


Figure 4.5: Work rate function $\theta(w)$ for the extreme quenches $g_i = 0 \mapsto g_f = \infty$ and $g_f = 0 \mapsto g_i = \infty$.

particularly evident for the quench from zero to infinite magnetic field. In this case, the final Hamiltonian

$$H_f = \frac{g_f}{2} \sum_{l=1}^L \sigma_l^z \quad (4.54)$$

equals a collection of L independent two state systems that one may identify with head and tail. As the work performed is measured by H_f work is equivalent to the number of heads and tails measured in the initial state. For $g_i = 0$ the initial state contains heads and tails with equal probability. This shows that the work distribution indeed can be viewed to measure the fraction of heads or tails in a coin tossing experiment with a coin flipping sequence of length L . Turning the initial magnetic field to nonzero values nonlocal correlations between the spins in the initial state will be generated. This is equivalent to correlations in the sequence of L coin flips.

The function $\theta(w)$ has a unique zero at $\hat{w} = 1/2$ implying that the probability distribution $\mathcal{P}(w) = \exp[-L\theta(w)]$ has a unique maximum at $\hat{w} = 1/2$ such that heads and tails are equally likely and that biased sequences with more heads or more tails are exponentially suppressed with L .

Work distributions for general quenches

After treating the special cases of zero and infinite magnetic field now the general case will be studied. Based on the exact solution of the cumulant generating function, see Eq. (4.44), and the subsequent Legendre transformation the work rate function $\theta(w)$ can be calculated exactly. In Fig. 4.6 the exact curves of the work distribution functions for specific magnetic field quenches are shown. As a common feature for all quenches $\theta(w)$ possesses a unique minimum. This implies that the associated work distribution $\mathcal{P}(w) = \exp[-L\theta(w)]$ exhibits

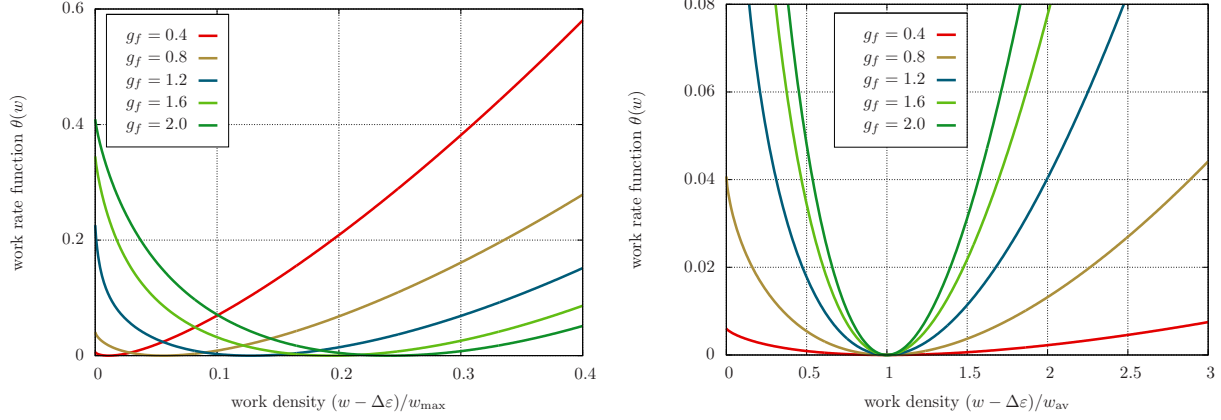


Figure 4.6: Work rate functions $\theta(w)$ for quenches from $g_i = 0.1$ to different final magnetic fields g_f in different phases. The work density w is shifted in all these plots by a constant $\Delta\epsilon = \Delta E/L$ that is the ground state energy difference between the final and initial zero temperature system per lattice site. The overall behavior is not changing qualitatively for different initial magnetic fields. In the left plot the work rate function is shown on a scale set by the maximum possible work performed w_{\max} . The right plot is scaled such that the most likely values w_{av} fall onto each other.

a single maximum that corresponds to the average work density performed w_{av} . Moreover, the dependence of $\theta(w)$ in the vicinity of the minimum is always quadratic yielding a Gaussian probability distribution $\mathcal{P}(w)$ that in the thermodynamic limit $L \rightarrow \infty$ obeys a central limit theorem. Note that this general behavior is also robust in case where the final or initial magnetic field are chosen at criticality.

Universality of small work asymptotics in the work distribution

The low work density $w \rightarrow \Delta\epsilon$ ($\Delta\epsilon = \Delta E/L$) asymptotics of the work rate function $\theta(w)$ shows universal behavior as will be discussed in what follows. The behavior of $\theta(w)$ in this limit only depends on the large distance limit $\tau \rightarrow \infty$ of the cumulant generating function $g(\tau)$. This can be seen in Fig. 4.4 where $g(\tau)$ is plotted for different quenches. The work rate function $\theta(w)$ and $g(\tau)$ are related via a Legendre transform, see Eq. (4.46) such that for a given w the function $\theta(w)$ is determined by the condition $w = g'(\tau)$ that has to be solved for $\tau = \tau(w)$. The function $g'(\tau)$ has a constant contribution $\Delta\epsilon$ that can be absorbed from $g'(\tau)$ into w by defining

$$\bar{w} = w - \Delta\epsilon, \quad \bar{g}(\tau) = g(\tau) - \Delta\epsilon\tau. \quad (4.55)$$

It is precisely the function $\bar{g}(\tau)$ that is plotted in Fig. 4.4. One observes that $\bar{g}(\tau)$ approaches quickly a constant signaling small values of the derivative and thereby small associated values of \bar{w} in the Legendre transform.

For the long distance behavior $\tau \rightarrow \infty$ of $\bar{g}(\tau)$ it is suitable to separate its asymptotic

value $\bar{g}_\infty = \bar{g}(\tau \rightarrow \infty)$ through

$$\delta\bar{g}(\tau) = \bar{g}(\tau) - \bar{g}_\infty = - \int_0^\pi \frac{dk}{2\pi} \log [1 + \tan^2(\phi_k) e^{-2E_k(g_f)\tau}] . \quad (4.56)$$

The large τ properties are solely determined by the long-wavelength $k \rightarrow 0$ behavior of both ϕ_k and $E_k(g_f)$. For that purpose one has to distinguish different cases.

If initial and final magnetic fields lie within one phase, i.e., either $g_i, g_f < 1$ or $g_i, g_f > 1$, the small momentum limit of the difference in Bogoliubov angles is given to leading order by

$$\phi_k \xrightarrow{k \rightarrow 0} \frac{1}{2} \frac{g_f - g_i}{|g_f - 1||g_i - 1|} k . \quad (4.57)$$

This translates into a large distance behavior of [162]

$$\delta\bar{g}(\tau) \xrightarrow{\tau \rightarrow \infty} -C [|g_f - 1|\tau]^{-3/2} e^{-2|g_f - 1|\tau} \quad (4.58)$$

with $C > 0$ a constant that depends on both initial and final magnetic field. Its precise value, however, will be of no importance in the following. This asymptotic result yields a small work \bar{w} dependence of the work rate function $\theta(w)$ in consequence of the Legendre transform

$$\theta(w) \xrightarrow{w \rightarrow \Delta\varepsilon} \bar{g}_\infty - \frac{\bar{w}}{|g_f - 1|} \log \left[\frac{\bar{w}}{|g_f - 1|} \right] \quad (4.59)$$

For quenches across the quantum critical point the long-wavelength scaling of the Bogoliubov angles is fundamentally different

$$\phi_k \xrightarrow{k \rightarrow 0} \pm \frac{\pi}{2} - \frac{1}{2} \frac{g_f - g_i}{|g_f - 1||g_i - 1|} k \quad (4.60)$$

where the $+$ sign refers to quenches that start in the disordered phase $g_i > 1$ and the $-$ sign to $g_f > 1$. The additional constant of $\pi/2$ has an important impact onto the large distance properties that now become [51]

$$\delta\bar{g}(\tau) \xrightarrow{\tau \rightarrow \infty} -D [|g_f - 1|\tau]^{-1/2} e^{-|g_f - 1|\tau} \quad (4.61)$$

with $D > 0$ again a constant. Note that the rate of decay is half as large as in the case of quenches within one phase. This then yields a modified behavior for $\theta(w)$:

$$\theta(w) \xrightarrow{w \rightarrow \Delta\varepsilon} \bar{g}_\infty - \frac{\bar{w}}{2|g_f - 1|} \log \left[\frac{\bar{w}}{2|g_f - 1|} \right] \quad (4.62)$$

Despite of the factor 2 the qualitative behavior of $\sim \bar{w} \log(\bar{w})$ is universal in the small \bar{w} limit for those type of quenches. This only differs in case where the final magnetic field is critical $g_f = 1$ and

$$\delta\bar{g}(\tau) \xrightarrow{\tau \rightarrow \infty} -\frac{\pi}{48\tau} \quad (4.63)$$

yielding an algebraic behavior of the work rate function

$$\theta(w) \xrightarrow{w \rightarrow \Delta\varepsilon} \bar{g}_\infty - \sqrt{\frac{\pi}{12}} \sqrt{\bar{w}} . \quad (4.64)$$

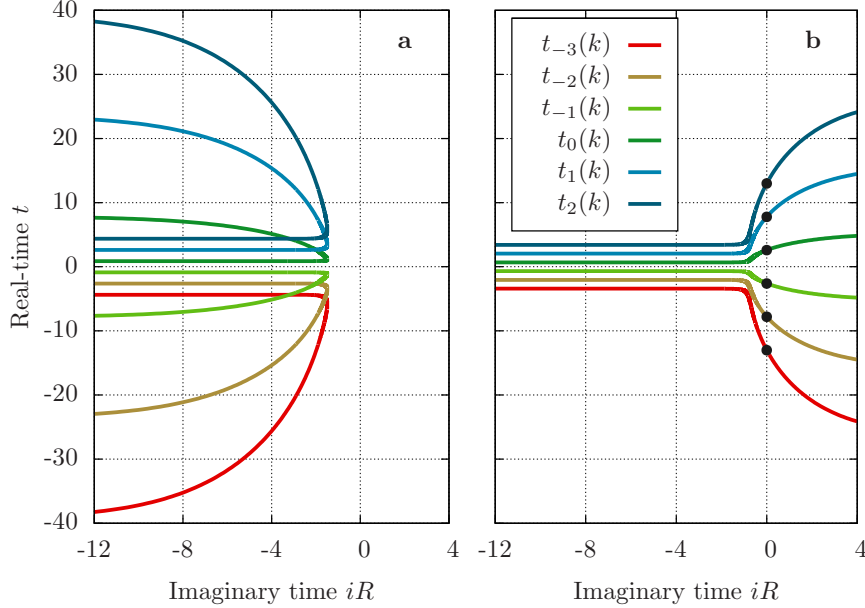


Figure 4.7: Lines of Fisher zeros for magnetic field quenches $g_i = 0.4 \mapsto g_f = 0.8$ in the left plot (a) and $g_i = 0.4 \mapsto g_f = 1.3$ in the right plot (b). Out of the infinite family of lines the first six in the vicinity of $t = 0$ are shown. For quenches within the same phase (a) the lines of Fisher zeros all lie in the negative imaginary time plane. For quenches across the equilibrium quantum critical point (b) the lines cross the real-time axis marked by the black circles. Every time such a curve hits the real-time axis the Loschmidt amplitude shows a real-time nonanalyticity yielding a dynamical phase transition.

4.2.4 Fisher zeros and real-time nonanalyticities

After analyzing the work distribution for the magnetic field quenches in the Ising model the focus in the following will be laid onto the real-time nonanalyticities and Fisher zeros for the Loschmidt amplitude. It will be demonstrated that the Loschmidt amplitude is analytic for quenches within one. In the opposite case for quenches across the equilibrium quantum critical point, however, the Loschmidt amplitude will develop real-time nonanalyticities that appear periodically on an emergent nonequilibrium time scale t^* .

For a finite-size system the Loschmidt amplitude $\mathcal{L}(t)$ can be rewritten in product form based on the exact result for the Loschmidt amplitude rate function $f(t)$ in Eq. (4.38):

$$\mathcal{L}(t) = e^{-i\Delta Et} \prod_{k>0} [\cos^2(\phi_k) + \sin^2(\phi_k)e^{-2iE_k(g_f)t}]. \quad (4.65)$$

In this representation the corresponding Fisher zeros t_r can be determined directly. The above product vanishes provided one factor becomes zero. Concentrating onto one momentum k the possible zeros have to fulfill the following formula

$$\cos^2(\phi_k) + \sin^2(\phi_k)e^{-2iE_k(g_f)t_r} = 0. \quad (4.66)$$

Note that provided t_r is a solution to this equation this is also the case for $t_r + n\pi/E_k(g_f)$ with $n \in \mathbb{Z}$. Thus, for each momentum k there is a whole family of solutions $t_n(k)$ that can be parametrized in the following way

$$t_n(k) = t(k) + \frac{n\pi}{E_k(g_f)}, \quad n \in \mathbb{Z}, \quad (4.67)$$

where $t(k)$ denotes the fundamental solution

$$t(k) = \frac{\pi}{2E_k(g_f)} + i \frac{1}{2E_k(g_f)} \log [\cot^2 \phi_k]. \quad (4.68)$$

In Fig. 4.7 plots of lines of Fisher zeros are shown for two paradigmatic cases. As already argued in Sec. 4.1.2 the Loschmidt amplitude becomes nonanalytic as a function of time provided a line of Fisher zeros crosses the real-time axis. In this case the system undergoes a dynamical phase transition according to the definition given in Sec. 4.1. This can happen when there is a mode k^* that satisfies

$$\cot^2 \phi_{k^*} = 1. \quad (4.69)$$

because only then the corresponding Fisher zero lies precisely on the real-time axis. This is equivalent to $\phi_{k^*} = \pi/4$. Using the definition $\phi_k = \theta_k(g_i) - \theta_k(g_f)$ and Eq. (4.26) for the Bogoliubov angles $\theta_k(g)$ this condition can be solved for k^* analytically

$$\cos(k^*) = \frac{1 + g_i g_f}{g_i + g_f}. \quad (4.70)$$

Recall that the momentum k^* is restricted to the real interval $k^* \in [0, \pi]$. Therefore, this equation can only be fulfilled provided g_i and g_f are chosen such that they correspond to different phases in equilibrium. In other words the nonanalyticities in the Loschmidt amplitude can only exist when the quench is performed across the equilibrium quantum critical point. This is illustrated in Fig. 4.7 where one can see that only for those quenches the lines of Fisher zeros cross the real-time axis.

The condition in Eq. (4.69) implies that the mode occupation n_{k^*} for k^* in the eigenbasis of the final Hamiltonian is precisely given by

$$n_{k^*} = \langle \psi_0 | \gamma_k^\dagger \gamma_k | \psi_0 \rangle = \sin^2(\phi_{k^*}) = \frac{1}{2}. \quad (4.71)$$

This corresponds to an infinite effective mode temperature. All modes $k < k^*$ have an occupation $n_k > 1/2$ signaling occupation inversion, see also Sec. 4.2.5.

As a consequence of this analytical analysis the Loschmidt amplitude shows a periodic sequence of real-time nonanalyticities for quenches across the quantum critical point at times

$$t_n^* = t^* \left(n + \frac{1}{2} \right), \quad t^* = \frac{\pi}{E_{k^*}(g_f)} = \pi \sqrt{\frac{g_i + g_f}{|g_f^2 - 1| |g_f - g_i|}}. \quad (4.72)$$

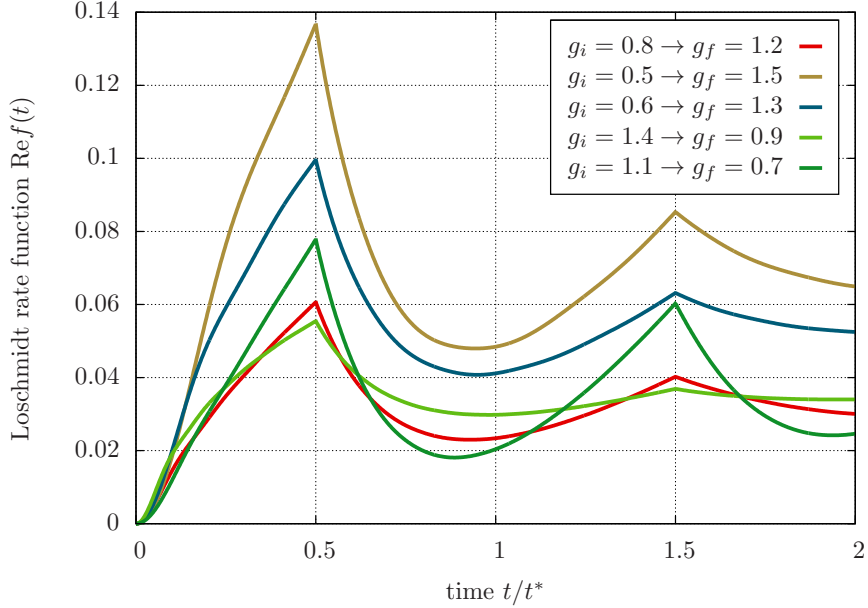


Figure 4.8: Nonanalytic behavior of the Loschmidt rate function for various quenches across the equilibrium quantum critical point. For simplicity only its real part is shown. The imaginary part shows similar kinks.

The new nonequilibrium time scale t_n^* is emergent and depends on the final and initial magnetic fields. This time scale t^* will later also appear in the order parameter dynamics, see Sec. 4.2.6. In Fig. 4.8 the Loschmidt rate function $f(t)$ is shown for several quenches across the equilibrium quantum critical point. The nonanalyticities manifest in kinks as has already been observed for the case of slow ramps [138]. These kinks imply that the derivative of the Loschmidt rate function $f'(t)$ exhibits jumps at times $t = t_n^*$. Note that in case of $g_f = 1$ the time scale $t^* \rightarrow \infty$ diverges.

As a consequence of these nonanalyticities the transverse field Ising model undergoes a periodic series of dynamical phase transition for quenches across the quantum critical point according to the definition given in Sec. 4.1.

4.2.5 Topological quantization: Chern number

Topological quantum numbers play an important role in the characterization and classification of ground state properties such as in the field of topological insulators [88, 66]. The quantization of the conductance in the quantum Hall effect is related to a Chern number [169]. Topological quantum numbers result from intrinsic geometrical properties of the physical system under study. One of the most prominent manifestations of geometric concepts in physical systems is the Berry phase associated with the adiabatic transport of wave functions along a parameter manifold [14, 163]. For adiabatic transport along closed two-dimensional parameter manifolds M^2 there naturally exists a topological quantum number, the so-called Chern number, that can be computed explicitly by integrating

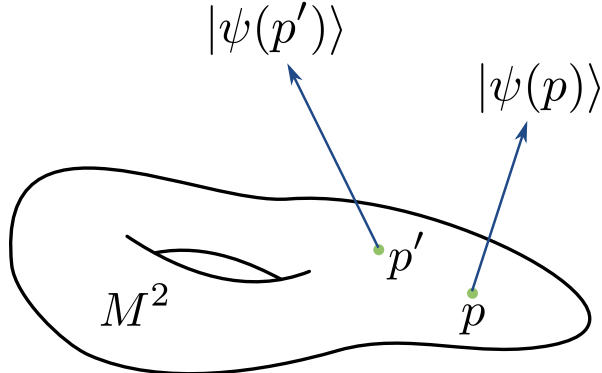


Figure 4.9: Schematic illustration of a compact two-dimensional manifold M^2 without boundaries. In the present context M^2 is the manifold of a set of parameters that the Hamiltonian under study depends on. To each point $p \in M^2$ a state $|\psi(p)\rangle$ of the Hilbert space \mathcal{H} is attached. In the context of adiabatic transport $|\psi(p)\rangle$ is the ground state of the Hamiltonian when the parameter takes a value p .

the related Berry curvature.

Berry curvature and Chern numbers

Consider a two-dimensional parameter manifold M^2 such that with each point $p \in M^2$ one associates a wave function $|\psi(p)\rangle$ in the Hilbert space under study. This is illustrated in Fig. 4.9. Note that there is no relation between the dimensionality of the manifold M^2 and the Hilbert space of the physical system. One natural way to associate points on M^2 with wave functions is the following. Suppose the Hamiltonian $H = H(\lambda, \mu)$ of the system depends on two external parameters λ and μ . To each value of λ and μ corresponds a unique ground state $|\psi_0(\lambda, \mu)\rangle$ up to a $U(1)$ symmetry due to the invariance of physical properties under the multiplication of states with phases. The assignment of states to points $p \in M^2$ is, however, not restricted to ground state properties. Another possibility where this assignment emerges is the time evolution of generalized forces of slowly driven systems in the linear response regime [64], for example.

Suppose that for the system under study such an assignment between points $p \in M^2$ and states $|\psi(p)\rangle$ exists. Moving along the manifold M^2 the associated states vary gradually from point to point. The infinitesimal change in the wave function $|\psi(p)\rangle$ for nearby points can be quantified via an appropriate differential ∇ [48]

$$\nabla|\psi(\mu, \lambda)\rangle = A_\lambda|\psi(\mu, \lambda)\rangle d\lambda + A_\mu|\psi(\mu, \lambda)\rangle d\mu \quad (4.73)$$

that may be interpreted as the usual derivative of wave functions projected back onto the space of states $|\psi(\lambda, \mu)\rangle$ [48]. Here A_λ and A_μ denote the derivatives in the two respective directions μ and λ and are called Berry connections because they appear naturally in the

context of the Berry phase [14, 163]

$$A_\lambda = i\langle\psi(\lambda, \mu)|\frac{d}{d\lambda}|\psi(\lambda, \mu)\rangle, \quad A_\mu = i\langle\psi(\lambda, \mu)|\frac{d}{d\mu}|\psi(\lambda, \mu)\rangle. \quad (4.74)$$

Note that the Berry connections and thus the differential ∇ are not gauge invariant. Multiplying the states by a λ -dependent phase, for example, gives an additional additive contribution. The curl of the Berry connection called Berry curvature, however, is gauge invariant. This is completely equivalent to the gauge dependent vector potential $\vec{A}(\vec{r})$ in the theory of electromagnetism where its curl, the magnetic field $\vec{B}(\vec{r}) = \vec{\nabla} \times \vec{A}(\vec{r})$, is a measurable quantity and therefore gauge independent. The Berry curvature is then given by

$$\theta^2 = \text{Im} \left\langle \frac{d\psi}{d\mu} \middle| \frac{d\psi}{d\lambda} \right\rangle. \quad (4.75)$$

When the Berry curvature is integrated over the whole manifold M^2 and provided the manifold is closed - this means compact without boundary - the outcome is an integer number called the Chern index $ch_{|\psi\rangle}$ corresponding to the states $|\psi\rangle$ [48]

$$ch_{|\psi\rangle} = \int_{M^2} d\lambda d\mu \theta^2 \in \mathbb{Z}. \quad (4.76)$$

Geometrically, Chern numbers classify complex vector bundles [48] that can be thought of as complex vector spaces attached to each point of a manifold. In the present context of the Berry phase this vector space is one-dimensional and consists just of one state $|\psi(p)\rangle$ and multiplications of it with complex phases. The Chern indices are invariant under continuous deformations of the underlying manifold and are therefore called topologically protected. Only drastic changes of the structure of the underlying space can alter their values.

Topology of the time-evolved initial state

The aim of what follows is to characterize the time evolved initial state $|\psi_0(t)\rangle$ of the quantum quench protocol via a topological quantum number. Denote by γ_k the fermionic operators that diagonalize the final Hamiltonian

$$H_f = \sum_{k>0} E_k(g_f) \left[\gamma_k^\dagger \gamma_k - \gamma_{-k}^\dagger \gamma_{-k} \right] \quad (4.77)$$

after the quench, for details see the beginning of Sec. 4.2. For a finite-size system the time evolved initial state $|\psi_0(t)\rangle$ factorizes into contributions from the different momentum sectors [162]

$$|\psi_0(t)\rangle = e^{-i\Delta Et} \prod_{k>0} |u_k(t)\rangle, \quad |u_k(t)\rangle = \left[\cos(\phi_k) + \sin(\phi_k) \gamma_k^\dagger \gamma_{-k}^\dagger e^{-i2E_k(g_f)t} \right] |\rangle_{\gamma_k} \quad (4.78)$$

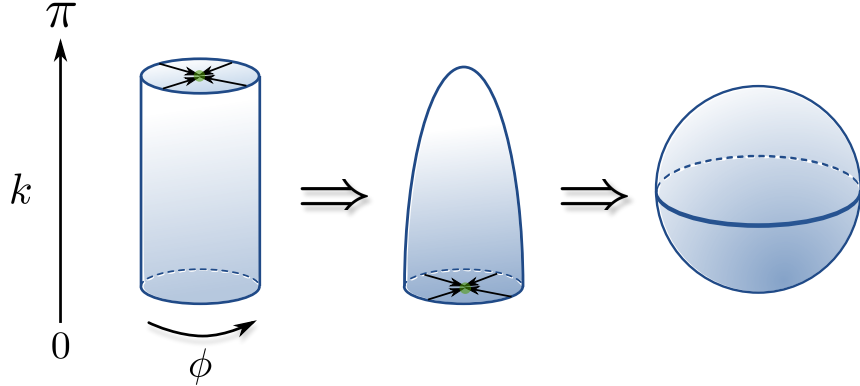


Figure 4.10: Topological equivalence of the effective Brioullin zone and the S^2 -sphere after two mappings.

up to a multiplicative phase that contains the ground state energy difference ΔE corresponding to the initial and final Hamiltonians. The state $|\rangle_{\gamma_k}$ denotes the vacuum for the γ -operators in the subspace of momentum k and $-k$ such that $\gamma_k|\rangle_{\gamma_k} = \gamma_{-k}|\rangle_{\gamma_k} = 0$. Formally similar to the BCS theory of superconductivity this state contains on top of the fermionic vacuum ‘‘Cooper-pairs’’, i.e., fermions of opposite momentum. The final Hamiltonian H_f obeys a global $U(1)$ symmetry

$$\gamma_k \mapsto e^{-i\phi}\gamma_k \quad (4.79)$$

as a consequence of particle number conservation. This symmetry is, however, not respected by the time-evolved initial state due to the spontaneous creation of ‘‘Cooper pairs’’ resulting in fluctuations of the particle number. Under this $U(1)$ transformation the states in the k -momentum subspaces change according to

$$|u_k(t)\rangle \mapsto |u_k(t, \phi)\rangle, \quad |u_k(t, \phi)\rangle = \left[\cos(\phi_k) + \sin(\phi_k)\gamma_k^\dagger\gamma_{-k}^\dagger e^{-2i\phi}e^{-i2E_k(g_f)t} \right] |\rangle_{\gamma_k}. \quad (4.80)$$

If $\phi = \pi$ the state is mapped back onto itself. Let $(k, \phi) \in M^2 = [0, \pi] \times [0, \pi]$ be the parameter manifold for the study of the Berry curvature and the related Chern number. This manifold is rectangular and thus has boundaries. For topological quantization, however, compact manifolds without boundaries are required. In the following it will be shown that M^2 can be identified with the 2-sphere S^2 . The basic steps are illustrated in Fig. 4.10.

For each k the states $|u_k(t, \phi)\rangle$ have the property that $|u_k(t, 0)\rangle = |u_k(t, \pi)\rangle$ that allows to wrap up the interval $\phi \in [0, \pi]$ and to identify the points at $\phi = 0$ and $\phi = \pi$ such that M^2 can effectively be thought of as a cylinder

$$M^2 \simeq [0, \pi] \times S^1. \quad (4.81)$$

Here, the \simeq is to be understood as topologically equivalent. But still the manifold has boundaries at $k = 0$ and $k = \pi$. The difference in Bogoliubov angles ϕ_k is directly linked to the mode occupation of the γ -fermions in the time-evolved initial state

$$n_k = \langle \psi_0(t) | \gamma_k^\dagger \gamma_k | \psi_0(t) \rangle = \sin^2(\phi_k). \quad (4.82)$$

The modes at $k = \pi$ can be associated with high-energy excitations. On general physical grounds one may expect that there are no modes occupied in the ultraviolet limit. For the quench in the transverse field Ising model this expectation holds precisely such that

$$\sin(\phi_{k=\pi}) = 0 \quad (4.83)$$

implying that

$$|u_{k=\pi}(t, \phi)\rangle = |\rangle_{\gamma\pi}, \quad (4.84)$$

see Eq. (4.80). Thus, at $k = \pi$ the state $|u_{k=\pi}(t, \phi)\rangle$ is independent of the angle ϕ . As all states on the ϕ circle at $k = \pi$ are identical one can identify all points on the top of the cylinder as illustrated in Fig. 4.10. In this way one gets rid of the top boundary of the manifold.

In the infrared limit at $k \rightarrow 0$ a similar procedure can be adopted. Depending on the quench parameters, however, one has to distinguish two different cases. Note that an analysis at $k = 0$ is not suitable even though it would simplify the discussion because of the property $\gamma_0^\dagger \gamma_0^\dagger = 0$. It is rather necessary to determine the limiting behavior $k \rightarrow 0$.

For quenches within the same phase the mode occupations in the infrared limit are identical to that of the high-energy case:

$$\sin(\phi_{k \rightarrow 0}) = 0. \quad (4.85)$$

Using the same arguments as before this allows to identify all points at $k = 0$ yielding the desired object, the 2-sphere S^2 , as illustrated in Fig. 4.10.

For quenches across the equilibrium quantum critical point the infrared behavior is completely different:

$$\sin(\phi_{k \rightarrow 0}) = 1. \quad (4.86)$$

This implies the following limiting behavior of the respective states

$$|u_{k \rightarrow 0}(t, \phi)\rangle = e^{-2i\phi} e^{-2i\Delta t} \gamma_{k \rightarrow 0}^\dagger \gamma_{-k \rightarrow 0}^\dagger |\rangle_{\gamma\pi} \quad (4.87)$$

with $\Delta = E_{k \rightarrow 0}(g_f)$ the gap of the final Hamiltonian. Varying the angle ϕ the states depend on ϕ via a total phase. Thus, up to a gauge transformation also all points at $k = 0$ can be identified yielding again the topological equivalence

$$M^2 \simeq S^2. \quad (4.88)$$

These considerations about the topological structure of the manifold M^2 immediately imply that the integral over the associated Berry curvature yields a Chern number and thus topological quantization according to Eq. (4.76). The next step is thus the actual computation of the Berry curvature, see Eq. (4.75). The derivative with respect to the angle ϕ is straightforward and gives

$$\frac{d}{d\phi} |u_k(t, \phi)\rangle = -2i \sin(\phi_k) e^{-2i\phi} e^{-2iE_k(g_f)t} \gamma_k^\dagger \gamma_{-k}^\dagger |\rangle_{\gamma k}. \quad (4.89)$$

For the derivative of the state $|u_k(t, \phi)\rangle$ with respect to momentum k the derivatives of the states $|\rangle_{\gamma k}$ and $\gamma_k^\dagger |\rangle_{\gamma k}$ have to be known. Those can be computed by means of elementary perturbation theory [142]. Consider the state $|\rangle_{\gamma k + \delta k}$ with δk a small parameter. Then

$$|\rangle_{\gamma k + \delta k} = |\rangle_{\gamma k} + \frac{d}{dk} |\rangle_{\gamma k} \delta k + \mathcal{O}[\delta k^2]. \quad (4.90)$$

Provided there is a gap in the spectrum as is always the case when the quench does not start or end at the quantum critical point perturbation theory shows that

$$\frac{d}{dk} |\rangle_{\gamma k} = \frac{d}{dk} \gamma_k^\dagger |\rangle_{\gamma k} = 0. \quad (4.91)$$

This is the consequence of a particular choice of gauge implicitly taken in the outlined perturbative treatment, the so-called parallel-transport gauge [142]. Based on this result it is straightforward to determine the full derivative

$$\begin{aligned} \frac{d}{dk} |u_k(t, \phi)\rangle &= \\ &\left[-\sin(\phi_k) \frac{d\phi_k}{dk} + \left(\cos(\phi_k) \frac{d\phi_k}{dk} - 2i \sin(\phi_k) \frac{dE_k(g_f)}{dk} \right) e^{-2i\phi} e^{-2iE_k(g_f)t} \gamma_k^\dagger \gamma_{-k}^\dagger \right] |\rangle_{\gamma k}. \end{aligned} \quad (4.92)$$

This yields for the Berry curvature $\theta^2 = -\partial_k \sin^2(\phi_k)$ and thus for the Chern number

$$\mathbb{Z} \ni ch_{|\psi_0(t)\rangle} = \sin^2(\phi_0) = \begin{cases} 0 & , \text{ quenches within the same phase} \\ 1 & , \text{ quenches across the quantum critical point} \end{cases} \quad (4.93)$$

This Chern number quantifies the difference between quenches within the same phase and across the quantum critical point. The topological protection manifests itself in such a way that as long as no gap closes, i.e., as long as either the initial magnetic field g_i and the final magnetic field g_f stay in their respective equilibrium phases, the Chern number is constant. Only in case where g_i or g_f cross the equilibrium quantum critical point with an associated gapless spectrum this topological quantum number can be altered.

Recalling that $\sin^2(\phi_0)$ is the zero-momentum occupation $n_{k=0}$ of the γ_k modes, see Eq. (4.82), that diagonalize the final Hamiltonian, the Chern number also expresses the thermal or athermal nature of the low-energy excitations. In equilibrium at zero temperature the zero-mode occupation $n_{k=0} = 0$ vanishes due to the presence of a gap. Thus a value $ch_{|\psi_0\rangle} = 1$ of the Chern index indicates a occupation inversion as a consequence of the quantum quench. The most important consequence of this property is that a value of $n_{k=0} = 1$ directly leads to the existence of the critical mode k^* , see Eq. (4.70), under the natural assumption of continuity of n_k as a function of k . Thus, a nontrivial Chern number automatically implies that the Loschmidt amplitude has real-time nonanalyticities and the system undergoes a dynamical phase transition. In this way the Chern number quantifies the difference between quenches within one phase and across the critical point in terms of a *single* natural number that can take either zero or one.

Both the initial and final Hamiltonians are time-reversal invariant. In the Ising model the time-reversal operation is just complex conjugation in the real-space basis without an additional unitary contribution. In general, time-reversal symmetry connects anti-podal points $k \leftrightarrow -k$ in the in this case one-dimensional Brioullin zone as $\Theta H_{i/f}(k)\Theta^{-1} = H_{i/f}(-k)$. In the present case of the Ising model also the relation $H_{i/f}(-k) = H_{i/f}(k)$ holds. Here, $H_{i/f}(k)$ denotes the Hamiltonian in the subspace of momentum k and Θ is the antiunitary implementation of the time-reversal operator that in the present case is given by $\Theta = \mathcal{K}$ with complex conjugation \mathcal{K} . Note that because Θ does not involve an additional unitary transformation to complex conjugation the situation is different from the case of topological insulators or Quantum Hall systems. In particular, there is no Kramers degeneracy. Time-reversal symmetry connects the $k \leftrightarrow -k$ subspaces of the Hamiltonian yielding an effective Brioullin zone $k \in [0, \pi]$ that contains all information [121]. This is important because topological quantum numbers involving the whole Brioullin zone are trivial [121]. Time reversal symmetry of the Hamiltonians is mirrored in the state $|\psi_0(t)\rangle$ by the fact that it can be written as a product involving only positive $k > 0$ from the effective Brioullin zone. In the context of time-reversal symmetry it is interesting to note that the Loschmidt amplitude can be identified with an expectation value of the time-reversal operator Θ

$$\mathcal{L}(t) = \langle \psi_0 | e^{-iH_f t} | \psi_0 \rangle = \langle \psi_0(-t/2) | \Theta | \psi(-t/2) \rangle. \quad (4.94)$$

Using the factorization of the time-evolved state $|\psi_0(t)\rangle$ into the different momentum subspaces this is equivalent to

$$\mathcal{L}(t) = \prod_{k>0} \langle u_k(-t/2) | \Theta | u_k(-t/2) \rangle. \quad (4.95)$$

A dynamical phase transition is associated with zeros of the Loschmidt amplitude as analyzed in detail in Sec. 4.1.2. In the representation in the last equation this is equivalent that for $k = k^*$ at time $t = t^*$ the corresponding expectation value of Θ vanishes

$$\langle u_{k^*}(-t^*/2) | \Theta | u_{k^*}(-t^*/2) \rangle = 0. \quad (4.96)$$

This means that for this specific momentum k^* at time t^* the subspaces to which $|u_{k^*}(-t^*/2)\rangle$ and $\Theta|u_{k^*}(-t^*/2)\rangle$ belong are orthogonal to each other. Note that a similar criterion has been used to determine the \mathbb{Z}_2 index in the topological classification of quantum spin Hall systems [88].

4.2.6 Equilibrium order parameter

In the previous part of this thesis the dynamical quantum phase transition in the Ising model has been analyzed in terms of the Loschmidt amplitude and topological quantum numbers. Although in principle measurable quantities in experiments local observables and correlation functions are more easily accessible. In the following, the dynamics of the local order parameter of the continuous equilibrium phase transition will be analyzed.

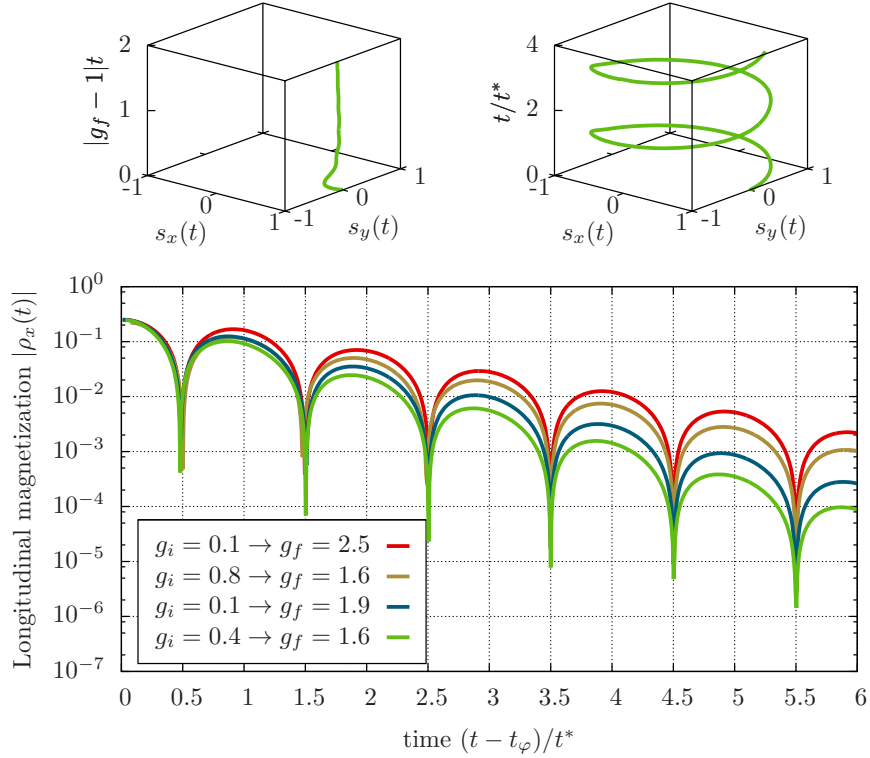


Figure 4.11: Dynamics of the longitudinal magnetization after quenches across the quantum critical point starting in the ferromagnetic phase. The lower plot shows the damped oscillatory decay of the longitudinal magnetization for different quenches from the ferromagnetic to the disordered phase. The period of the oscillation is entirely determined by the nonequilibrium time scale t_n^* as can be clearly seen from this graph. Note that the zeros of the order parameter are not precisely located at $t = t_n^*$. The curves have been shifted by a magnetic field dependent constant t_φ . The dynamics of the normalized local spin expectation values $s_x(t)$ and $s_y(t)$ in the xy -plane are illustrated in the upper two graphs. For quenches within one phase the ferromagnetic order is so rigid that the change in the external magnetic field is not able to induce a significant displacement in the xy -plane. In the opposite case of quenches across the quantum critical point as shown in the upper right plot the magnetization starts to precess with a frequency $\Omega^* = \pi/t^*$.

The longitudinal magnetization $\rho_x(t)$ is the local observable that measures the ferromagnetic order in the Ising ordering direction. Its equilibrium and already known nonequilibrium properties have been summarized already in Sec. 4.2.1. Formally, the longitudinal magnetization after the quench is given by

$$\rho_x(t) = \frac{1}{2} \langle \psi_0(t) | \sigma_l^x | \psi_0(t) \rangle. \quad (4.97)$$

As the operator σ_l^x connects states with different fermionic parity, compare the introduction to Sec. 4.2, its expectation value cannot simply be evaluated in terms of the Jordan-Wigner

fermions. This technical detail can be circumvented by alternatively analyzing the spin-spin correlation function

$$\rho_{xx}(t, r) = \frac{1}{4} \langle \psi_0(t) | \sigma_l^x \sigma_{l+r}^x | \psi_0(t) \rangle \quad (4.98)$$

from which the value of the order parameter can be deduced in the limit of large distances $r \rightarrow \infty$ [118]:

$$\rho_x^2(t) = \lim_{r \rightarrow \infty} \rho_{xx}(t, r). \quad (4.99)$$

This is called the Cluster decomposition. Most importantly, the fermion parity is conserved by evaluating $\rho_{xx}(t, r)$ such that the Jordan-Wigner representation of the Ising model can be used. Expressing the Pauli matrices in terms of Jordan-Wigner fermions it is possible to write $\rho_{xx}(t, r)$ [109]

$$\rho_{xx}(t, r) = \langle \psi_0 | B_l(t) A_{l+1}(t) B_{l+1}(t) \dots B_{l+r-1}(t) A_{l+r}(t) | \psi_0 \rangle \quad (4.100)$$

with the (up to a prefactor) Majorana operators

$$A_l = c_l^\dagger + c_l, \quad B_l = c_l^\dagger - c_l. \quad (4.101)$$

Each of the $A_l(t)$ and $B_l(t)$ are linear combinations of fermionic operators and $|\psi_0\rangle$ is the ground state of a quadratic operator allowing to use Wicks theorem [181]. As a consequence the spin-spin correlation function can be related to a Pfaffian [147] that can be evaluated numerically.

For quenches within one phase the longitudinal magnetization decays exponentially in time [22, 23], see Eq. (4.32). On the other hand, for large transverse magnetic fields where the coupling between the neighboring spins can be neglected one may expect that the spin expectation values precess in the xy -plane. The transition from exponential decay to a damped Larmor precession happens precisely at that point where the final magnetic field g_f crosses the quantum critical point $g_f = 1$. At this value the external force becomes strong enough to overcome the rigidity of the ferromagnetic order.

In Fig. 4.11 numerical data for the longitudinal magnetization is shown for quenches from the ordered into the disordered phase. The upper three-dimensional plots exemplify the different qualitative behavior for quenches within the ferromagnetic phase and across the quantum critical point. In equilibrium the magnetization in y -direction

$$\rho_y(t) = \frac{1}{2} \langle \psi_0(t) | \sigma_l^y | \psi_0(t) \rangle \quad (4.102)$$

vanishes as a consequence of time-reversal symmetry which is, however, broken in the nonequilibrium scenario. Instead it acquires a nonzero value as one can directly deduce from the equation of motion of the order parameter $\partial_t \rho_y(t) = -g_f \rho_y(t)$. To analyze the precession in the xy -plane it is suitable to introduce normalized functions $s_x(t) = \mathcal{N}^{-1}(t) \rho_x(t)$ and $s_y(t) = \mathcal{N}^{-1}(t) \rho_y(t)$ on the unit circle with $\mathcal{N}(t) = \sqrt{\rho_x^2(t) + \rho_y^2(t)}$. In

this way the exponential decay is eliminated making the precession visible in Fig. 4.11. As one can see in Fig. (4.11) quenches within the ferromagnetic phase do not lead to a significant dynamics in the spin orientation in the xy -plane. This is a consequence of the rigidity of the ferromagnetic order. The external magnetic field does not provide enough energy to overcome its stability.

In contrast, for quenches across the quantum critical point the spin expectation values in the xy -plane start to precess as is expected for large transverse magnetic fields. Remarkably, the frequency Ω^* of this precession is not set by the mass of the final Hamiltonian or the Larmor frequency. Instead $\Omega^* = \pi/t^*$ is solely given by the emergent nonequilibrium time scale t^* that marks the periodicity with which the real-time nonanalyticities in the Loschmidt amplitude appear, see Sec. 4.2.4. This finding is purely numerical and up to the present moment there is no analytic proof for a connection of the dynamics between the Loschmidt amplitude and the longitudinal magnetization. As the data shows, however, there is a deep relationship between the dynamical quantum phase transition and physical quantities. But note that there are other observables such as the transverse magnetization $\rho_z(t)$ that do not show an influence of the dynamical quantum phase transition. From a physical point of view one may expect that those quantities that are especially sensitive to the initial state are most likely influenced by the nonanalyticities in the Loschmidt amplitude and thus the dynamical quantum phase transition as discussed in more detail in Sec 4.1.3.

Chapter 5

Periodically driven many-body quantum systems

One important aspect in the study of nonequilibrium systems is the possibility to generate dynamically new states with properties not accessible through equilibrium thermodynamics. For quenches and ramps as investigated in Sec. 2 systems can be trapped dynamically in intermediate states with long lifetimes that are associated with a regime termed prethermalization [13, 120]. The dynamics of integrable systems is restricted by the presence of conservation laws leading to the expectation that they do not thermalize in the long-time limit [137]. Instead, the asymptotic steady state is supposed to be described by generalized Gibbs ensembles that bear some similarity to canonical states but require the maximization of the entropy constrained by more constants of motion than just energy [145]. As shown for a restricted class of systems there is a deep connection between prethermalization plateaus, generalized Gibbs ensembles, and the proximity to integrable theories [95].

Another possibility for the dynamical generation of new quantum states is provided by a periodic driving. Periodically time-dependent electric fields can lead to a dynamical localization of noninteracting particles on a chain [37]. This takes over to interacting particles on a lattice where it has been demonstrated that the periodic driving can yield effective renormalized microscopic parameters for time-averaged quantities allowing to manipulate and design model Hamiltonians dynamically [38, 134, 175]. As shown below in Sec. 5.1 fast periodic driving can generate nonequilibrium steady states showing time-translational invariance as equilibrium states but with violated fluctuation-dissipation theorem and properties not accessible within equilibrium thermodynamics [71].

Through a periodic driving energy is continuously pumped into the system. For local perturbations the increase in energy can be typically redistributed among the system's internal degrees of freedom provided the whole system is infinitely large signaling the importance of the thermodynamic limit, see for example Sec. 5.1. If the periodic perturbation acts globally the increase in energy can lead to a substantial heating of the system provided there is no external dissipation mechanism included in the description. This is especially important for effective low-energy models such as the Luttinger liquid, see Sec. 5.3 below, as the continuous heating will drive the model description beyond its limits of validity at

some point in time. For the periodically driven Luttinger liquid the absence of dissipation mechanisms manifests in a parametric instability with exponentially growing perturbations. This sets an intrinsic time scale beyond which other internal or external perturbations have to be included for a realistic description.

Compared to quenches or ramps periodically driven systems, especially interacting ones, pose new challenges in terms of methodology. Most theories for interacting many-body systems are based on low-energy approximations whose extension including the periodic driving beyond the linear response regime is not straightforward. Concerning strongly-correlated systems only a restricted class has been addressed. As for the quench or ramp case one can distinguish local periodic perturbations that only act on a small subsystem and global ones. The former has been studied in a number of works for periodically driven Anderson impurity models [126, 113, 1, 114, 124, 69] and related Kondo models [87, 86, 60, 61, 152] using different approaches. The latter for Bose-Hubbard [38, 134], Fermi-Hubbard [82, 42, 41, 175, 9], and Falicov-Kimball models [50, 49, 173, 174].

Despite of these fundamental questions it is important and instructive to study those particular models that exhibit exact and nonperturbative solutions. Below, three different examples will be investigated such as a Kondo model with periodically switched exchange interaction in Sec. 5.1, transport through a noninteracting quantum dot in presence of a periodic bias voltage in Sec. 5.2, and a Luttinger liquid with periodically modulated interaction strength in Sec. 5.3.

5.1 Publication: Periodically driven Kondo model

The Kondo model is the paradigm for strongly correlated quantum impurity systems, for details about its equilibrium and interaction quench properties see Sec. 2.1. The most important feature of the Kondo model is the emergence of a low-energy and temperature scale, the Kondo temperature T_K , see Eq. (2.4), resulting from a multitude of coherent low-energy spin excitations in the vicinity of the local spin. The most prominent manifestation of the Kondo effect at zero temperature is the Kondo resonance, a sharp peak in the local density of states of width T_K , that is pinned precisely at the Fermi energy of the conduction band.

At temperatures $T \gg T_K$ much larger than the intrinsic low energy scale T_K the Kondo effect gets smeared and disappears eventually [70]. Through a periodic driving energy is continuously pumped into the system leading to the natural question whether the Kondo effect survives this nonequilibrium scenario especially regarding the limit when the driving frequency $\Omega \gg T_K$ exceeds the Kondo temperature. There have been attempts to introduce effective temperatures to describe the properties of nonequilibrium Kondo models [112, 125]. If it were possible to assign an effective temperature to a specific *periodically* driven Kondo model one may expect that for sufficiently fast driving the temperature may be so large to suppress the Kondo effect.

Below, the consequences of a periodic switch on and off of the Kondo exchange interaction is studied in the Toulouse limit. As it turns out it is not possible in this case to

define an effective temperature because the excitations generated by the periodic driving are fundamentally different from those induced by temperature. The dominant processes in a periodically driven system are not just the energy conserving ones but rather those where the energy is conserved up to multiples of the driving frequency Ω . This can be associated with the absorption or emission of photons. Consequently, the respective excitations are of a discrete structure rather than equivalent to a smearing of the Fermi surface as for finite temperatures excluding the possibility to describe the system's properties via an effective temperature.

In experiments it has been demonstrated that microwave fields of sufficient intensity can destroy the Kondo effect in quantum dots [44]. One mechanism for its suppression is the generation of substantial charge fluctuations in the system [126] leading to ionization of the quantum dot. Recall that the Kondo effect results from coherent spin excitations in the vicinity of the local magnetic moment, compare Sec. 2.1, and requires a strictly conserved local occupation up to virtual processes. Ionization of the quantum dot changes the local occupancy thereby destroying the Kondo effect. Another mechanism for its suppression that appears already for smaller driving frequencies than for the case of ionization is attributed to spin-flip cotunneling [87, 86] when studying transport through a quantum dot in the local moment regime.

The anisotropic version of the Kondo model exhibits an exact solution using bosonization and refermionization for a specific line in parameter space, the so-called Toulouse limit [172]. The model stays exactly solvable even under nonequilibrium conditions [111, 112]. For the periodically driven case the corresponding Hamiltonian is given by

$$\begin{aligned} H(t) = & \sum_{k,\eta=\uparrow\downarrow} v_F k : c_{k\eta}^\dagger c_{k\eta} : + \frac{J_\parallel(t)}{2} \frac{2\pi}{L} \sum_{kk'} \left[c_{k\uparrow}^\dagger c_{k'\uparrow} - c_{k\downarrow}^\dagger c_{k'\downarrow} \right] S^z \\ & + \frac{J_\perp(t)}{2} \frac{2\pi}{L} \sum_{kk'} \left[c_{k\uparrow}^\dagger c_{k\downarrow} S^- + c_{k\downarrow}^\dagger c_{k\uparrow} S^+ \right]. \end{aligned} \quad (5.1)$$

The operator $c_{k\eta}^\dagger$ creates an electron with spin $\eta = \uparrow, \downarrow$ in a state of momentum k . The fermionic dispersion relation has been linearized around the Fermi energy such that v_F is the Fermi velocity. The colons $: \dots :$ denote normal ordering relative to the noninteracting zero temperature Fermi sea. The zero of energy has been chosen such that $k = 0$ corresponds to the Fermi energy. In contrast to Eq. (2.3) a generalized version of the Kondo Hamiltonian is studied where the coupling in z -direction of the spin J_\parallel does not have to equal the coupling in the xy -plane J_\perp . The exactly solvable Toulouse limit corresponds to the line in parameter space where $J_\parallel = 2 - \sqrt{2}$.

In the following, the local spin dynamics is analyzed analytically for a nonequilibrium protocol where the exchange interaction in the Kondo model is switched on and off periodically. Initially the system is prepared in the ground state of the model without exchange coupling, i.e., $J_\parallel(t < 0) = J_\perp(t < 0) = 0$, and a local spin polarization. For times $t > 0$ the couplings are periodically switched on and off

$$J_\parallel(t) = J_\parallel \theta[\sin(\Omega t)], \quad J_\perp(t) = J_\perp \theta[\sin(\Omega t)] \quad (5.2)$$

with $J_{\parallel} = 2 - \sqrt{2}$ in the Toulouse limit and J_{\perp} is set by the precise value of the Kondo temperature in the model, see below. An experimental implementation for such a protocol in quantum dots is presented below. This case, however, always yields an isotropic model $J_{\perp} = J_{\parallel}$. Nevertheless, the Toulouse limit shows many generic and universal features of the strongly-correlated Kondo model especially concerning the local spin dynamics. Other universal quantities such as the Wilson ratio explicitly depend on the anisotropy.

Remarkably the Kondo effect can be stable even in the limit $\Omega \gg T_K$. For the case of a periodic switch on and off of the Kondo exchange interaction in the Toulouse limit the Kondo effect survives even in the limit $\Omega \gg T_K$ and gets renormalized associated with a new value $T_K \rightarrow T_K/2$ of the Kondo temperature. But note that an important observation of the analysis is that the dynamics in the fast driving limit cannot be associated with an effective equilibrium Hamiltonian. This is a consequence of the inapplicability of the Trotter formula in the present problem. For more details see below.

In the slow driving limit the system's dynamics becomes essentially equivalent to that of a single interaction quench because the system is able to relax during the time until the next switching. In the opposite limit of very fast switching one may expect generally on the basis of the Trotter formula that the dynamics becomes equivalent to that of a time-averaged Hamiltonian [43]. Physically speaking, the system cannot follow the fast external perturbation and only experiences its average contribution. This is true as long as the system exhibits a mechanism that prevents the absorption of high-energy excitations such as a finite bandwidth. But as will be shown below, for the Kondo model in the Toulouse limit this is not the case yielding a time-translational invariant state that, however, violates the fluctuation-dissipation theorem. If the Trotter formula were applicable the steady state would be an equilibrium state corresponding to the time-averaged value of the exchange interaction which, however, is not the case here.

Nonequilibrium steady state in a periodically driven Kondo model

M. Heyl and S. Kehrein

*Physics Department, Arnold Sommerfeld Center for Theoretical Physics and Center for NanoScience,
Ludwig-Maximilians-Universität, Theresienstraße 37, 80333 Munich, Germany*

(Received 7 December 2009; revised manuscript received 2 February 2010; published 9 April 2010)

We investigate the Kondo model with time-dependent couplings that are periodically switched on and off. On the Toulouse line we derive exact analytical results for the spin dynamics in the steady state that builds up after an infinite number of switching periods. Remarkably, the universal long-time behavior of the spin-spin correlation function remains completely unaffected by the driving. In the limit of slow driving the dynamics becomes equivalent to that of a single interaction quench. In the limit of fast driving it is shown that the steady state cannot be described by some effective equilibrium Hamiltonian due to the observation that an incautious implementation of the Trotter formula is not correct. As a consequence, the steady state in the limit of fast switching serves as an example for the emergence of new quantum states not accessible in equilibrium.

DOI: [10.1103/PhysRevB.81.144301](https://doi.org/10.1103/PhysRevB.81.144301)

PACS number(s): 72.15.Qm, 85.35.Be, 73.50.Mx

I. INTRODUCTION

Recent progress in experiments stimulated the interest in nonequilibrium phenomena of interacting many-particle systems. Cold atoms trapped in optical lattices offer the possibility of studying the time evolution of quantum many-body systems with time-dependent system parameters.¹ Due to the excellent isolation from the environment the nonequilibrium dynamics of these systems are accessible with negligible decoherence over long times.

Nanostructures such as quantum dots provide the framework to examine experimentally the nonequilibrium dynamics in quantum impurity models. Most importantly for the present work, quantum dots can act as magnetic impurities displaying Kondo physics.² In contrast to impurities in a bulk sample, unscreened electrical or magnetic fields can be applied directly such that the local system parameters can be varied in time by choosing appropriate time-dependent fields.³

The possibility to experimentally study the properties of interacting many-body systems out of equilibrium motivated numerous analytical and numerical theoretical treatments. Most of the activities have been concentrating on interaction quenches in various model systems.^{4–7} For periodically driven interacting many-body systems, however, less results are known. Recently, periodic time-dependent Falicov-Kimball models have been investigated in the limit of infinite dimensions by using dynamical mean-field theory.⁹ Considerable activity in the field of time-dependent quantum impurity models led to a number of works on periodically driven Anderson impurity^{3,10} and Kondo models.^{11–14}

As the Kondo model is the paradigm model for strongly correlated impurity systems, it is of particular interest in the field of nonequilibrium phenomena. In equilibrium, the Kondo effect emerges from the interaction of a localized spin degree of freedom with a bath of surrounding electrons. At sufficiently low temperatures, this bath of itinerant electrons develops a localized spin polarization cloud in the vicinity of the local spin, the so-called Kondo cloud, providing a mechanism to screen the local magnetic moment. In the zero temperature limit, the screening becomes dominant leading to the emergence of a bound state. The surrounding spin polarization cloud is tied to the local spin establishing

the so-called Kondo singlet with an associated binding energy T_K , the Kondo temperature. The Kondo effect manifests itself most prominently in the Kondo resonance, a sharp peak in the local density of states that is pinned exactly at the Fermi energy. As the Kondo effect is a coherent many-body phenomenon, the question arises how it is affected in a non-equilibrium setting.

Due to the complexity of many-body systems out of equilibrium, it is instructive to investigate those cases where exact nonperturbative solutions are accessible. In this context, it is of particular interest that the Kondo model as a paradigm model for strongly correlated impurity systems exhibits a special line in parameter space, the Toulouse limit, where it becomes exactly solvable.¹⁵ The Toulouse limit displays many generic and universal properties of the strong coupling limit of the Kondo model in equilibrium as well as for interaction quenches.⁴ The local spin dynamics, for example, that is also investigated in this work, is well described whereas other universal quantities such as the Wilson ratio explicitly depend on the anisotropy.

The exact solvability of the Kondo model in the Toulouse limit is used in this work to investigate nonperturbatively a steady state that is generated by periodically switching on and off the interaction at zero temperature. This steady state is characterized by analyzing exact analytical results for the local dynamical quantities, that is, the magnetization of the impurity spin, the spin-spin correlation function, and the dynamical spin susceptibility.

A system that is driven by an external force approaches a steady state if the amount of energy that is provided to the system does not lead to an overheating, as it may happen for systems with an unbounded spectrum. Since these steady states emerge from a nonequilibrium setting, equilibrium thermodynamics is not applicable for their description. As a consequence, these states display new properties that are not accessible by exciting the system thermally. Their characterization, however, poses a new challenge. Recently, there have been attempts to assign effective thermodynamic quantities such as effective temperatures to describe the properties of systems in a nonequilibrium setup.^{3,5,7,8} As will be shown in this paper, a characterization of the present steady state in terms of an effective temperature is not possible. The excitations that are created by the periodic driving are fundamen-

tally different from those induced by temperature. A finite temperature smears the Fermi surface whereas the periodic driving leads to an excitation spectrum of discrete character with excitations of multiples of the driving frequency.

Another question arising in the context of driven systems is whether the universality in equilibrium systems such as the Kondo model extends to the nonequilibrium case, whether new universal properties emerge and whether equilibrium quantities remain meaningful. Kaminski *et al.*,^{11,12} for example, proposed a universal description for the conductance through a Kondo impurity for a periodically driven Kondo model. In the present setting, the spin-spin correlation function displays a universal long-time behavior that is completely independent of the driving. This universality originates from the fact that the low-energy excitations in the immediate vicinity of the Fermi level that are relevant for the long-time behavior are unaffected by the periodic driving due to the discrete character of the excitation spectrum.

This paper is organized as follows. In Sec. II, the model Hamiltonian, a time-dependent Kondo model in the Toulouse limit, is introduced and mapped onto a quadratic effective Hamiltonian. The method used to determine the time evolution in the periodic driving setup is presented in Sec. III. The result for the magnetization of the impurity spin is shown in Sec. IV. Section V is devoted to a detailed analysis of the spin-spin correlation function and the results for the dynamical spin susceptibility are presented in Sec. VI.

II. PERIODIC TIME-DEPENDENT KONDO MODEL

Consider a local spin whose exchange interaction with the surrounding electrons is switched on and off periodically, which generates a Kondo Hamiltonian with time-dependent couplings. For convenience we allow for an anisotropy in the exchange interaction leading to different couplings in z direction, $J_z=J_{\parallel}$, and in the xy plane, $J_x=J_y=J_{\perp}$

$$H = \sum_{k\alpha} k :c_{k\alpha}^\dagger c_{k\alpha}: + \sum_i \frac{J_i(t)}{2} \sum_{\alpha, \alpha'} : \Psi_\alpha^\dagger(0) \sigma_i^{\alpha, \alpha'} S_i \Psi_{\alpha'}(0) : \quad (1)$$

The operator $c_{k\alpha}^\dagger$ creates an electron with wave vector k and spin $\alpha=\uparrow, \downarrow$ in the reservoir. The colons $:::$ denote normal ordering relative to the Fermi sea. The local spin operator S_i with components $S_i, i=x, y, z$, is coupled to the local spin density of the conduction-band electrons whose components are determined by the Pauli matrices σ_i . The electron's dispersion relation has been linearized around the Fermi level and energies are measured in units of v_F relative to the Fermi energy, i.e., $v_F=1$ and $\epsilon_F=0$. As the local scatterer is assumed to be pointlike, only s -wave scattering occurs rendering the problem to be effectively one-dimensional.¹⁶

For negative times, the system is prepared in one of the ground states $|\Psi_0\rangle$ of the noninteracting problem that are product states of the Fermi sea for the conduction-band electrons and a wave function for the local spin. As depicted in Fig. 1, at time $t=0$, the periodic driving process starts by switching on the interaction. After half of the period τ , $t=\tau/2$, the interaction is switched off until $t=\tau$. Afterwards,

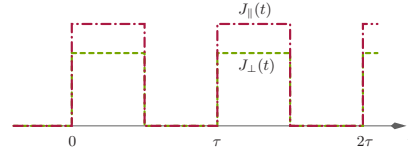


FIG. 1. (Color online) Time dependence of the perpendicular $J_{\perp}(t)$ and parallel coupling $J_{\parallel}(t)$ in the anisotropic Kondo Hamiltonian. For times $t < 0$ all couplings are zero whereas for $t > 0$ they are switched on and off periodically with period τ .

this procedure is continued, until after an infinite number of periods a steady state builds up, a state in which all real-time correlation functions are invariant under a discrete time shift of one period in all their time arguments. The energy scale associated with the periodic switching is the driving frequency $\Omega=2\pi/\tau$.

Due to the time-dependence of the Hamiltonian, energy is not a conserved quantity. Moreover, each quench that is performed excites the system such that one can expect that after an infinite number of switchings, in the steady state, an infinite amount of energy is pumped into the system. This is indeed the case in the present setup. Therefore, a dissipation mechanism is needed that prevents the system from overheating. As has been shown by Doyon and Andrei,¹⁷ the conduction band in the Kondo model itself can serve as a bath if and only if it is taken as infinitely large. Therefore, a definite order of taking limits has to be prescribed, namely, the thermodynamic limit has to be taken before the limit of long times

$$\lim_{t \rightarrow \infty} \lim_{L \rightarrow \infty} \quad (2)$$

In this way, as expected the conduction band is prevented from overheating induced by a single impurity.

One possible way of experimentally realizing the periodic switch on and off of the Kondo interaction in a quantum dot is the following: consider a quantum dot with a local single-particle level at energy ϵ_d and a large on-site interaction U in the Kondo regime where $\epsilon_d \ll \epsilon_F$, $\epsilon_d+U \gg \epsilon_F$ and $|\epsilon_d - \epsilon_F|, |\epsilon_d + U - \epsilon_F| \gg \Gamma, T$. Here, Γ denotes the broadening of the local level ϵ_d in the quantum dot and T the temperature. Via the Schrieffer-Wolff¹⁸ transformation, the corresponding Anderson impurity model can be mapped onto a Kondo model with an exchange coupling $J \propto \Gamma [\frac{1}{\epsilon_F - \epsilon_d - U} + \frac{1}{\epsilon_F + \epsilon_d}]$. Following a suggestion by Nordlander *et al.*,⁷ consider the case where the local single-particle level ϵ_d alternates between two different values ϵ_{d1} and ϵ_{d2} with $|\epsilon_{d2} - \epsilon_F| \gg |\epsilon_{d1} - \epsilon_F|$ where for each ϵ_{d1} and ϵ_{d2} the quantum dot is assumed to be in the Kondo regime. Then, the Kondo exchange coupling J_2 corresponding to ϵ_{d2} is much smaller than J_1 . The associated Kondo temperature $k_B T_{K2} = D \sqrt{\rho_0 J_2 e^{-1/(J_2 \rho_0)}}$, ρ_0 is the density of state at the Fermi level and D a high-energy cutoff, vanishes exponentially such that J_2 can be set equal to zero. As a result, the corresponding Kondo model becomes time dependent with an exchange interaction J_1 that is switched on and off periodically. This can be shown rigorously by performing a

time-dependent Schrieffer-Wolff transformation.^{11–13}

The periodic driving in a quantum dot sets an upper bound on the driving frequency Ω . As the Kondo Hamiltonian requires strict single occupancy, the driving has to be small enough not to induce charge fluctuations on the dot caused by hopping processes between the central region and the conduction band by absorbing or emitting quanta of the driving frequency, i.e., $\Omega \ll |\varepsilon_d|$, $\varepsilon_d + U$.^{11–13}

At zero temperature in equilibrium, the screening of the local magnetic moment by the conduction-band electrons becomes dominant leading to the emergence of a bound state called the Kondo singlet. Many universal features of the equilibrium Kondo model in this strong coupling limit are well described by the anisotropic Kondo Hamiltonian in the Toulouse limit that corresponds to a special line in parameter space of the Hamiltonian in Eq. (1) where $J_{\parallel} = 2 - \sqrt{2}$. For this value of the parallel coupling, the Hamiltonian can be mapped onto an exactly solvable quadratic noninteracting resonant-level model using bosonization and refermionization.¹⁶ Recently, it was shown by Lobaskin and Kehrein⁴ that these methods can also be adopted to an exact solution of an interaction quench scenario. The only difference is an additional potential scattering term in the effective Hamiltonian.

The bosonization technique establishes a bosonic representation of fermionic fields $\Psi_{\alpha}(x)$ in one dimension called the bosonization identity, see Ref. 19 for a recent review. In the thermodynamic limit, the bosonization identity reduces to

$$\Psi_{\alpha}(x) = \frac{1}{\sqrt{a}} F_{\alpha} e^{-i\phi_{\alpha}(x)}, \quad \alpha = \uparrow, \downarrow, \quad (3)$$

where the bosonic field $\phi_{\alpha}(x) = -\sum_{q>0} [e^{-iqx} b_{q\alpha} + e^{iqx} b_{q\alpha}^{\dagger}] e^{-aq/2}/\sqrt{n_q}$ is related to the fermionic densities $\rho_{\alpha}(x) := \Psi_{\alpha}^{\dagger}(x)\Psi_{\alpha}(x) := \partial_x \phi_{\alpha}(x)$ and a^{-1} is an ultraviolet cut-off. The bosonic operators $b_{q\alpha}^{\dagger} = i/\sqrt{n_q} \sum_k c_{k+q\alpha}^{\dagger} c_{k\alpha}$ create a superposition of particle-hole pairs with momentum transfer $q = 2\pi n_q/L > 0$. Here, L denotes the system size. The Klein factor F_{α} accounts for the annihilation of one electron as this cannot be achieved by the bosonic field $\phi_{\alpha}(x)$.

By performing a sequence of unitary transformations, the Kondo Hamiltonian in the Toulouse limit can be simplified tremendously. First, the spin and charge (s, c) degrees of freedom are separated by defining the bosonic fields $\phi_s(x) = [\phi_{\uparrow}(x) - \phi_{\downarrow}(x)]/\sqrt{2}$ and $\phi_c(x) = [\phi_{\uparrow}(x) + \phi_{\downarrow}(x)]/\sqrt{2}$. The charge sector of the anisotropic Kondo Hamiltonian is decoupled from the local spin and reduces to a collection of uncoupled harmonic oscillators. Therefore it will be omitted from now on. In the first half period, the interaction part in the spin sector $J_{\parallel}/\sqrt{2}\partial_x\phi_s(x)S_z + J_{\perp}/(2a)[F_{\uparrow}^{\dagger}F_{\downarrow}e^{i\sqrt{2}\phi_s(0)}S_- + \text{H.c.}]$ is modified by an Emery-Kivelson transformation $U = e^{i\gamma\phi_s(x)S_z}$, $\gamma = \sqrt{2} - 1$, to $J_{\perp}/(2a)[F_{\uparrow}^{\dagger}F_{\downarrow}e^{i\phi_s(0)}S_- + \text{H.c.}]$ in the Toulouse limit where $J_{\parallel} = 2 - \sqrt{2}$. For the second half period, the Emery-Kivelson transformation generates a scattering term $\propto \langle S_z(t) \rangle \partial_x \phi_s(0)$, whose strength depends on the instantaneous magnetization of the impurity spin $\langle S_z(t) \rangle$.⁴ The exponentials appearing in the transformed interaction part can be refermionized by introducing new spinless fermionic

fields $\Psi(x) = a^{-1/2} F_s e^{-i\phi_s(x)}$ using the inverse of the bosonization identity where $F_s = F_{\downarrow}^{\dagger} F_{\uparrow}$.²⁰ One may think of the $\Psi^{\dagger}(x)$ fields as creating spin excitations at point x in the reservoir. Moreover, another unitary transformation $U_2 = e^{i\pi N_s S_z}$ has to be imposed in order to arrive at a completely refermionized Hamiltonian and to ensure correct anticommutation relations for all operators.²⁰ Here, $N_s = \frac{1}{2}[N_{\uparrow} - N_{\downarrow}]$ measures the total spin polarization of the conduction-band electrons. By defining the operator $d = e^{-i\pi[N_s - S_z]S_-}$ and its Hermitian conjugate d^{\dagger} as well as by performing a mode expansion for the new fermionic fields $c_k = (2\pi L)^{-1/2} \int dx \Psi(x) e^{ikx}$, one arrives at the following Hamiltonian:

$$H = \sum_k :c_k^{\dagger} c_k: + g(t) \langle S_z(t) \rangle \sum_{kk'} :c_k^{\dagger} c_{k'}: + V(t) \sum_k [c_k^{\dagger} d + d^{\dagger} c_k], \quad (4)$$

where $g(t) = g[\theta[-\sin(\Omega t)]]$, $V(t) = V[\sin(\Omega t)]$, $V = J_{\perp} \sqrt{\pi/2aL}$, $g = (1 - \sqrt{2})\pi/L$ for $t > 0$, and $g(t) = g$, $V(t) = 0$ for $t < 0$. For times $N\tau < t < N\tau + \tau/2$ the Hamiltonian is a resonant-level model. For times $N\tau + \tau/2 < t < N\tau + \tau$ the dynamics are governed by a potential scattering Hamiltonian and the local d operators do not evolve in time such that $\langle S_z(t) \rangle = \langle S_z(N\tau + \tau/2) \rangle$. As it will turn out in the following analysis, the intermediate time evolution with the potential scattering Hamiltonian has no influence on the local spin dynamics such as the magnetization $\langle S_z(t) \rangle$ at all. Therefore, it is not necessary to solve the dynamics in a self-consistent way.

The Kondo scale can be connected to the parameters of the resonant-level model via the impurity contribution to the Sommerfeld coefficient in the specific heat:⁴ $C_{\text{imp}} = \gamma_{\text{imp}} T$ where $\gamma_{\text{imp}} = w\pi^2/3T_K$ and $w = 0.4128$ is the Wilson number. In this way, the Kondo temperature T_K is determined by $T_K = \pi w \Delta$ where $\Delta = V^2 L/2$ is the hybridization function.

The functional dependence between the spinless fermions c_k and the conduction-band electrons $c_{k\alpha}$ is highly nonlinear and nontrivial. The local spin observable S_z , however, commutes with all unitary transformations and can be connected to operators of the effective Hamiltonian in a simple way

$$S_z = d^{\dagger} d - \frac{1}{2}. \quad (5)$$

This relation allows to analytically calculate correlation functions that involve the S_z observable such as the magnetization of the impurity spin $P(t) = \langle S_z(t) \rangle$, the spin-spin correlation function $\langle S_z(t)S_z(t') \rangle$ and the dynamical spin susceptibility $\chi''(t, \varepsilon)$, as it will be done in this work for the periodic driving setup.

III. TIME EVOLUTION

As the Hamiltonian in Eq. (4) is quadratic, the time evolution of the single-particle operators c_k and d is entirely determined by the Green's functions $G_{ll'}(t) = \theta(t) \langle \{c_l(t), c_{l'}^{\dagger}\} \rangle$

$$c_l(t) = \sum_{l'} G_{ll'}(t) c_{l'}, \quad l, l' = k, d \quad (6)$$

with a unitary matrix G . Despite the complexity of time evolution for time-dependent Hamiltonians, the periodic driving

as it is considered in this work involves two time slices, during which the Hamiltonian is constant. For each half period, the dynamics is determined by the Green's functions for a potential scattering $\mathcal{G}^{(n)}$ and a resonant level model \mathcal{G} . The Green's function for the potential scattering Hamiltonian varies for different periods as the strength of the scatterer depends on the instantaneous magnetization of the impurity spin. Therefore, the Green's functions are labeled by an additional superscript where n stands for the number of the period after starting the periodic driving. The time evolution over one period transforms the single-particle operators in the following way:

$$c_l(\tau) = \sum_{l'} \mathcal{M}_{ll'}(n) c_{l'}, \quad \mathcal{M}_{ll'}(n) = \left[\mathcal{G}\left(\frac{\tau}{2}\right) \mathcal{G}^{(n)}\left(\frac{\tau}{2}\right) \right]_{ll'} \quad (7)$$

defining the unitary matrices $\mathcal{M}(n)$ that are obtained by matrix multiplication. Note that the order of time evolution in the Heisenberg picture is opposite to the order of time evolution in the Schrödinger picture: the operators are first evolved according to the potential scattering Hamiltonian although it acts in the second half period. In this formulation, the problem of long-time evolution reduces to a matrix multiplication problem since the long-time evolution is completely determined by evolving the single-particle operators over multiple periods

$$c_l(N\tau) = \sum_{l'} \mathcal{M}_{ll'}^{(N)} c_{l'}, \quad \mathcal{M}_{ll'}^{(N)} = [\mathcal{M}(1) \dots \mathcal{M}(N)]_{ll'}. \quad (8)$$

Finding the matrix elements of an arbitrary multiplication of some matrices can be a difficult task. The matrices $\mathcal{M}(n)$, however, display nice mathematical properties such that an analytical calculation can be carried out as is shown in the Appendix. The goal is to derive solvable recursion formulas by partially performing summations over intermediate indices. This yields the following relations:

$$\begin{aligned} \mathcal{M}_{dd}^{(N)} &= e^{-N\Delta\pi/2}, \quad \mathcal{M}_{dk}^{(N)} = \mathcal{M}_{dk} \frac{e^{-iNk\tau} - e^{-N\Delta\pi/2}}{e^{-ik\tau} - e^{-\Delta\pi/2}}, \\ \mathcal{M}_{kd}^{(N)} &= \mathcal{M}_{kd} \frac{e^{-iNk\tau} - e^{-N\Delta\pi/2}}{e^{-ik\tau} - e^{-\Delta\pi/2}}, \\ \mathcal{M}_{kk'}^{(N)} &= \delta_{kk'} e^{-iNk\tau} + \mathcal{L}_{kk'} \frac{e^{-iNk\tau} - e^{-iNk'\tau}}{e^{-ik\tau} - e^{-ik'\tau}} \\ &\quad + \mathcal{M}_{kd} \mathcal{M}_{dk} \left[\frac{e^{-iNk\tau}}{(e^{-ik\tau} - e^{-ik'\tau})(e^{-ik\tau} - e^{-\Delta\pi/2})} \right. \\ &\quad \left. + \frac{e^{-N\Delta\pi/2}}{(e^{-ik\tau} - e^{-\Delta\pi/2})(e^{-ik'\tau} - e^{-\Delta\pi/2})} \right. \\ &\quad \left. + \frac{e^{-iNk'\tau}}{(e^{-ik'\tau} - e^{-ik\tau})(e^{-ik'\tau} - e^{-\Delta\pi/2})} \right] + \mathcal{K}_{kk'}^{(N)}. \end{aligned} \quad (9)$$

The precise definition of the functions appearing in these relations can be found in the Appendix. The matrix elements $\mathcal{M}_{ll'}^{(N)}$ can be interpreted as the probability amplitudes for a

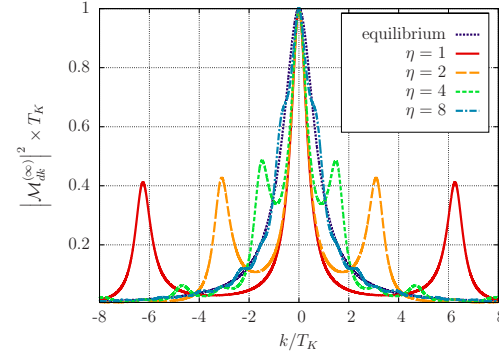


FIG. 2. (Color online) Probability $|\mathcal{M}_{dk}^{(\infty)}|^2$ for a local d fermion to decay into a bath state k after an infinite number of periods. As a reference, the equilibrium curve for a resonant level model with the same Kondo temperature T_K is included. The parameter $\eta = \tau T_K = \tau / t_K$ compares the speed of switching τ with the internal time scale $t_K = 1 / T_K$.

fermion in a single-particle state $|l\rangle = c_l^\dagger |0\rangle$ to transform into $|l'\rangle$ after N periods τ . Here, $|0\rangle$ denotes the true vacuum without any fermion. In Fig. 2, plots for $|\mathcal{M}_{dk}^{(\infty)}|^2$ are shown, that is, the probability for a d fermion to decay into a k fermion after an infinite number of periods, i.e., as the steady state has developed. For large periods, the probability distribution approaches its equilibrium shape of a resonant-level model whereas for decreasing the period τ side peaks appear located at odd multiples of the driving frequency Ω . This corresponds to hopping processes under the absorption or emission of an odd number of quanta Ω . Regarding the c_d^\dagger and c_k^\dagger as creating a spin excitation of energy k in the fermionic reservoir, one can deduce from Fig. 2 that the elementary excitations caused by the periodic driving are those where the local spin is flipped by simultaneously creating spin excitations of energy $n\Omega$, n odd. A Fourier series expansion of the $\theta[\sin(\Omega t)]$ -function in the interval $[0, \tau]$ reveals why mostly the odd frequencies contribute

$$\theta[\sin(\Omega t)] = - \sum_{n \in 2\mathbb{Z}+1} \cos(n\Omega t). \quad (10)$$

Therefore, the switch on and off driving can be thought of as a nonmonochromatic driving including all odd multiples of the driving frequency.

As an aside, one can deduce from Eq. (9) that the periodic switching only leads to the enhancement of certain fluctuations that are already present in the corresponding equilibrium Hamiltonians. The periodic time dependence of the Hamiltonian leads to a selection of certain transitions that correspond to the absorption or emission of an odd number of energy quanta Ω .

IV. MAGNETIZATION

The dynamics of all quantities is determined by the Hamiltonian in Eq. (4). Due to the Emery-Kivelson transformation, the instantaneous value of the magnetization $P(t)$ of the impurity spin

$$P(t) = \langle S_z(t) \rangle \quad (11)$$

itself appears in the Hamiltonian. Therefore, the magnetization provides the full access to the time evolution in the present time-dependent setup. As it will turn out in the following, this does not imply that the problem has to be solved self-consistently. In contrast, the time evolution of the magnetization is independent of the potential scattering term appearing in the effective Hamiltonian as already mentioned below Eq. (4). Due to Eq. (5), the magnetization is connected to the occupation $n_d(t) = \langle d^\dagger(t)d(t) \rangle$ of the local d level

$$P(t) = n_d(t) - \frac{1}{2}. \quad (12)$$

As a consequence of the periodicity of the Hamiltonian, it is convenient to represent time coordinates in the following way:

$$t = n\tau + s, \quad n \in \mathbb{N}, \quad s \in [0, \tau/2]. \quad (13)$$

For $s \in [\tau/2, \tau]$ the S_z operator is constant due to the switch off of the spin dynamics. Therefore, the formulas in the following will always be presented for $s \in [0, \tau/2]$. Using the formulas in Eq. (9) and the fact that the matrices $\mathcal{M}^{(\mathbb{N})}$ are unitary, it can be shown that the magnetization decays exponentially in time

$$P(t) = P(0)e^{-n\Delta\tau}e^{-2\Delta s}, \quad (14)$$

where the time scale is set by the Kondo scale $t_K = 1/T_K = 1/(\pi w\Delta)$. For a single interaction quench, the magnetization $P_{\text{qu}}(t)$ equals^{4,16,21,22}

$$P_{\text{qu}}(t) = P(0)e^{-2\Delta t}. \quad (15)$$

Comparison with the result in Eq. (14) reveals that the periodic driving affects the impurity spin orientation only by reducing the total time during which the spin dynamics in the Kondo Hamiltonian is switched on. The initial local spin polarization is transferred to the conduction band and flows away from the central region to infinity. Note that the magnetization is independent of the intermediate time evolution generated by the potential scattering Hamiltonian.

In the limit of fast switching, $\tau \rightarrow 0$, the magnetization decays exponentially in time

$$P_{\tau \rightarrow 0}(t) = P(0)e^{-\Delta t}. \quad (16)$$

The associated rate Δ , however, is smaller compared to the single quench case where it is equal to 2Δ , see Eq. (15). This is surprising, as one might expect that the additional energy provided to the system by the periodic driving may open additional phase space for relaxation processes. The decrease in the rate by one half occurs simply because the spin dynamics that are the only source of relaxation of the magnetization are switched on only during half of the time.

The exact result in Eq. (16) for the magnetization, however, contrasts the dynamics one obtains by a naive implementation of the Trotter formula. Following a suggestion by Eisler and Peschel,²³ the dynamics of a periodically quenched system in the limit $\tau \rightarrow 0$ is identical to that of an

effective equilibrium Hamiltonian that can be obtained by applying the Trotter formula²⁴ to the time evolution operator U over one period

$$U = e^{-iH_1\pi/2}e^{-iH_2\pi/2} \approx e^{-i(H_1+H_2)\pi/2} + \mathcal{O}(\tau^2). \quad (17)$$

As a result, the effective Hamiltonian equals the time-averaged one, that is a resonant level model with a hopping amplitude $V/2$ plus a potential scattering term. The potential scattering term, however, does not affect the spin dynamics. Therefore, it will be omitted in the following. A resonant-level model with hopping amplitude $V/2$ generates a decay of the magnetization at a rate $\Delta/2$ as $\Delta \propto V^2$, compare Eq. (15), in contrast to the exact value Δ .

From a mathematical point of view, the Trotter formula fails as both Hamiltonians H_1 and H_2 have to be self-adjoint in a mathematical sense, that is, a stronger requirement than Hermitian. For bounded operators (in fact, all realistic models are equipped with a high-energy cutoff), self-adjointness is guaranteed, in contrast to unbounded operators as considered in this work. In fact, regarding a resonant-level model with a nontrivial hopping element $V_k(t) = V(t)e^{-(k/k_c)^2}$ where $V(t) = \theta[\sin(\Omega t)]$ and k_c a high-energy cutoff, one indeed observes that in the limit $\tau \rightarrow 0$ the magnetization converges to the result obtained by applying the Trotter formula, see Eq. (17).

Physically speaking, the inapplicability of the Trotter formula is a consequence of the creation of high-energy excitations in the fast driving limit. The typical excitations generated by the periodic driving are on the order of $\Omega = 2\pi/\tau$ corresponding to the absorption and emission of quanta of the driving frequency, compare Fig. 2. As $\Omega \rightarrow \infty$ for $\tau \rightarrow 0$, the typical excitations carry high energies. If the system is not provided with a mechanism, such as a finite bandwidth, that suppresses or cuts off these high-energy excitations, they will exist in the system even for $\tau \rightarrow 0$. Clearly, such excitations are not present in equilibrium systems leading to the conclusion that this fast-driven system cannot be described by an equilibrium Hamiltonian reflecting the mathematical statement above.

Summing up, the Trotter formula is not applicable in this model with a flat hybridization function. Despite the fact that realistic models actually exhibit a bounded spectrum, the results presented in this work describe correctly the dynamics in the limit $\Omega \gg T_K$, provided that the physical cutoff D is still much bigger than Ω .

V. SPIN-SPIN CORRELATION FUNCTION

A dynamical quantity that carries more information about the local properties of the Kondo model is the spin-spin correlation function

$$\langle S_z(t)S_z(t') \rangle = C(t,t') - \frac{i}{2}\chi(t,t'), \quad (18)$$

where $C(t,t') = \frac{1}{2}\langle \{S_z(t), S_z(t')\} \rangle$ denotes the symmetrized part and $\chi(t,t') = i\theta(t-t')\langle [S_z(t), S_z(t')] \rangle$ the response function for $t > t'$. After an infinite number of periods τ , a steady state develops in which all real-time correlation functions are

invariant under a discrete time shift τ in all their time arguments. For the spin-spin correlation function this implies

$$\langle S_z(t + \tau)S_z(t' + \tau) \rangle = \langle S_z(t)S_z(t') \rangle. \quad (19)$$

Therefore, the time coordinate t' can be restricted to the interval $[0, \tau]$. The average $\langle \dots \rangle$ in the steady state is to be understood as

$$\langle S_z(t)S_z(t') \rangle = \lim_{N \rightarrow \infty} \langle \Psi_0(N\tau) | S_z(t)S_z(t') | \Psi_0(N\tau) \rangle, \quad (20)$$

where $|\Psi_0\rangle$ denotes the initial state. In the steady state where $\langle S_z(t) \rangle = \langle S_z(t') \rangle = 0$, the spin-spin correlation function equals

$$\langle S_z(t)S_z(t') \rangle = \langle \hat{n}_d(t)\hat{n}_d(t') \rangle - \frac{1}{4}. \quad (21)$$

Using the formulas in Eq. (9), the spin-spin correlation function, that is a four-point function in terms of the fermionic operators of the effective Hamiltonian, can be related to a two-point function

$$\langle S_z(t)S_z(t') \rangle = \langle d^\dagger(t)d(t') \rangle^2, \quad (22)$$

where

$$\begin{aligned} \langle d^\dagger(t)d(t') \rangle &= \frac{1}{\pi} \int_0^\infty d\omega \frac{e^{-i\omega\Delta\tau}}{1+\omega^2} \left[e^{-\Delta(s+t')} \frac{1-2\cos(\omega\Delta\tau/2)e^{-\Delta\pi/2}+e^{-\Delta\tau}}{1-2\cos(\omega\Delta\tau)e^{-\Delta\pi/2}+e^{-\Delta\tau}} + (e^{-i\omega\Delta s}-e^{-\Delta s})(e^{i\omega\Delta t'}-e^{-\Delta t'}) \right. \\ &\quad \left. + e^{-\Delta s}(e^{-i\omega\Delta t'}-e^{-\Delta t'}) \frac{e^{-i\omega\Delta\pi/2}-e^{-\Delta\pi/2}}{e^{-i\omega\Delta\tau}-e^{-\Delta\pi/2}} + e^{-\Delta t'}(e^{i\omega\Delta s}-e^{-\Delta s}) \frac{e^{i\omega\Delta\pi/2}-e^{-\Delta\pi/2}}{e^{i\omega\Delta\tau}-e^{-\Delta\pi/2}} \right]. \end{aligned} \quad (23)$$

Remarkably, the real part of the $\langle d^\dagger(t)d(t') \rangle$ correlator can be calculated analytically

$$\langle \{d^\dagger(t), d(t')\} \rangle = e^{-n\Delta\pi/2} e^{-\Delta(s-t')} \quad (24)$$

matching precisely the result of Langreth and Nordlander²⁵ who derived a general formula of this correlator for an arbitrarily time-dependent resonant-level model. Inserting the time dependence of the hopping amplitude $V(t)$ of the present setup into their result shows perfect agreement. As the anticommutator of two time-evolved fermionic single-particle operators is independent of the state if the Hamiltonian is quadratic, the full information about the influence of the steady state onto the spin-spin correlation function is contained in the imaginary part of the $\langle d^\dagger(t)d(t') \rangle$ correlator. The imaginary part is not accessible analytically but can be evaluated numerically. A representative plot of $C(t, t')$ and $\chi(t, t')$ is shown in Fig. 3. A detailed discussion will be given below.

Due to the appearance of a new scale in the present periodic driving setup, the universal description of the spin-spin correlation function gets modified in comparison to its equilibrium form

$$\langle S_z(t)S_z(t') \rangle = F\left(\frac{t}{t_K}, \frac{t'}{t_K}, \frac{\tau}{t_K}\right) \quad (25)$$

as one can expect by dimensional analysis. As a consequence, the Kondo scale, though an equilibrium quantity, remains the only relevant time and energy scale as it was shown for the conductance through a Kondo impurity in the work by Kaminski *et al.*^{11,12} The period τ only appears in combination with the Kondo time scale $t_K = 1/T_K$ defining the ratio

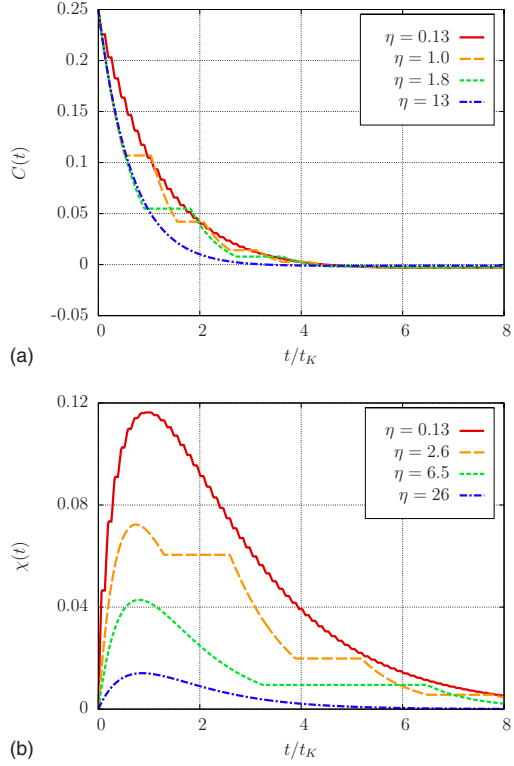


FIG. 3. (Color online) Universal curves for the symmetrized correlation function $C(t)=C(t,0)$ and the response function $\chi(t)=\chi(t,0)$ for different values of the driving rate η at zero waiting time $t'=0$. The parameter $\eta = \tau/t_K$ compares the speed of the external driving τ with the internal Kondo time scale $t_K = 1/T_K$.

$$\eta = \frac{\tau}{t_K} = \tau T_K. \quad (26)$$

Therefore, it is only important how fast the system is driven compared to the internal time scale t_K .

The limit of long switching times: in the limit of large periods τ , the behavior of the local correlation functions is accessible by general arguments. Roughly speaking, the system is able to relax during each half period. Initially, the system is prepared in one of the ground states $|\Psi_0\rangle$ of the noninteracting Hamiltonian that are product states of the Fermi sea for the conduction-band electrons and a spin wave function for the local level. Switching on the interaction in the Kondo model creates local excitations in the vicinity of the local spin and the Kondo singlet forms. The excitations generated by the quench delocalize and flow away from the central region to infinity such that they cannot contribute to local properties any more. Therefore, the time-evolved state looks like the ground state for local observables after a sufficiently long time. As was emphasized in Ref. 4, however, the state $|\Psi_0\rangle$ can never develop into the true ground state of the Kondo model as the overlap of both wave functions is constant in time. Nevertheless, the time evolved state $|\Psi_0\rangle$ is essentially equivalent to the true ground state as far as expectation values of local observables such as the S_z operator are concerned. All statements about relaxation of the state itself in the following are to be understood in this sense. After half of the period, the interaction in the Kondo model is switched off, thereby destroying the Kondo singlet. The excitations that are created by breaking up the Kondo singlet delocalize as argued before and the system evolves into the ground state of the noninteracting Hamiltonian, that is, a product state of the Fermi sea and a spin wave function with zero magnetization. Therefore, the system at the moment of the second switch on of the interaction is prepared as initially up to a change in the local spin wave function. As a result, the system behaves as for a single interaction quench, a situation that has already been addressed by Lobaskin and Kehrein.^{4,5} Analytically, the spin-spin correlation function transforms into

$$\langle S_z(t)S_z(t')\rangle \xrightarrow{\tau \rightarrow \infty} \left\{ \frac{1}{2}e^{-\Delta(t-t')} - i[s(t-t') - e^{-\Delta t'}s(t) + e^{-\Delta t}s(t')] \right\}^2, \quad (27)$$

where $s(t) = \pi^{-1} \int_0^\infty d\omega \sin(\omega\Delta t) / (\omega^2 + 1)$. This result matches precisely the result obtained by Lobaskin and Kehrein⁴ for a single interaction quench.

The limit of fast switching: in the opposite limit $\tau \rightarrow 0$, there exists no general argument capturing the dynamics in the resulting steady state. The sole reason for this is that the Trotter formula is not applicable in this model as explained in Sec. IV. Otherwise, the dynamics in the steady state would be governed by an effective equilibrium Hamiltonian. Nevertheless, the fast driving generates dynamics similar to equilibrium as the system is not able to follow the fast externally prescribed perturbation.

Performing the limit $\tau \rightarrow 0$, the spin-spin correlation function reduces to

$$\langle S_z(t)S_z(t')\rangle \xrightarrow{\tau \rightarrow 0} \left\{ \frac{1}{2}e^{-\Delta(t-t')/2} - i\frac{1}{2}s[(t-t')/2] \right\}^2. \quad (28)$$

Thus, it only depends on the time difference signaling the similarity to an equilibrium problem in the sense that time-translational invariance is restored. The equilibrium spin-spin correlation function equals⁴

$$\langle S_z(t)S_z(t')\rangle_{eq} = \left[\frac{1}{2}e^{-\Delta(t-t')} - is(t-t') \right]^2. \quad (29)$$

Comparing the result of Eq. (28) with the equilibrium case, one first observes that the time argument is scaled by a factor of 1/2. As for the magnetization, this can be understood by the fact that the spin operators evolve nontrivially only during half of the time. Additionally, a prefactor of 1/2 appears in front of the function s such that the real and imaginary part of the $\langle d^\dagger(t)d(t')\rangle$ correlator transform qualitatively different in the limit $\tau \rightarrow 0$. Thus, the fluctuation-dissipation theorem, a signature of equilibrium systems, is violated. This then leads to the conclusion that it is impossible to find an equilibrium Hamiltonian generating the same dynamics.

Nevertheless, other quantities such as the dynamical spin susceptibility, as it will be shown in Sec. VI, can be related to equilibrium Hamiltonians. The inapplicability of the Trotter formula does not exclude the possibility to find equilibrium behavior, it only excludes the possibility to find a unique equilibrium Hamiltonian describing the correct dynamics for all observables. Concluding, the steady state in the limit $\tau \rightarrow 0$ provides an example for the emergence of new quantum states similar to equilibrium states but with new properties that are not accessible by equilibrium thermodynamics.

The asymptotic long-time behavior: in equilibrium, the spin-spin correlation function exhibits a characteristic algebraic long-time behavior at zero temperature

$$\langle S_z(t)S_z(t')\rangle_{eq} \xrightarrow{t-t' \rightarrow \infty} -w^2 \left[\frac{t_K}{t-t'} \right]^2. \quad (30)$$

At finite temperatures, the decay is exponential due to the smearing of the Fermi surface. Therefore, the long-time behavior of the spin-spin correlation function can serve as a measure whether the excitations that are created by the periodic driving are equivalent to those induced by a finite temperature. In this case, the steady state may be characterized by relating it to an equilibrium system at an effective temperature, a concept that has been widely used recently.^{3,5,7,8}

In the present periodic time-dependent setup, the asymptotic long-time behavior of the spin-spin correlation function can be determined analytically

$$\langle S_z(t)S_z(t')\rangle \xrightarrow{t-t' \rightarrow \infty} -w^2 \left[\frac{t_K}{t-t'} \right]^2. \quad (31)$$

Surprisingly, the long-time behavior of the spin-spin correlation function is universal in the sense that it is completely independent of the external driving. Moreover, it precisely

matches the equilibrium behavior at zero temperature. As the algebraic decay in equilibrium is caused by the sharp Fermi surface at zero temperature, one can conclude that the periodic driving is not able to smear the Fermi surface or to at least locally heat up the system excluding the concept of effective temperature. Furthermore, the low-energy excitations in the immediate vicinity of the Fermi level that are relevant for the long-time behavior are unaffected by the periodic driving. The excitation spectrum involves excitations of multiples of the driving frequency that emerge from processes where the local spin is flipped by simultaneously creating collective spin excitations in the fermionic reservoir with energies of odd multiples of the driving frequency Ω , as can be seen in Fig. 2. Therefore, the excitation spectrum is of discrete character, in contrast to the excitation spectrum induced by temperature.

VI. DYNAMICAL SPIN SUSCEPTIBILITY

In the steady state, the magnetization of the impurity spin vanishes due to Eq. (14). A local spin polarization can be induced by applying a magnetic field to the local spin. In the linear response regime one obtains

$$\langle S_z(t) \rangle_h = \langle S_z(t) \rangle + \int_{-\infty}^{\infty} dt' \chi(t, t') h(t'). \quad (32)$$

Expectation values without an index h are to be evaluated with respect to the unperturbed Hamiltonian. In the steady state, the magnetization vanishes such that the expectation value for the local spin polarization is solely determined by the response function

$$\chi(t, t') = i\theta(t - t') \langle [S_z(t), S_z(t')] \rangle. \quad (33)$$

In equilibrium, the response function $\chi(t, t')$ only depends on the time difference thereby establishing a spectral representation of only one frequency argument whose imaginary part $\chi''(\epsilon)$ is called the dynamical spin susceptibility. It shows a peak located near the Kondo temperature T_K that can be associated with the Kondo singlet. The existence of such a peak in a nonequilibrium setting can also be interpreted as a signature for the presence of the Kondo effect as a whole, as the Kondo singlet is just one manifestation of this coherent many-body phenomenon. Moreover, in equilibrium, the fluctuation-dissipation theorem holds that connects the dynamical spin susceptibility with the local spin-fluctuation spectrum. In systems out of equilibrium, the fluctuation-dissipation theorem is violated, as can be seen explicitly for a single interaction quench scenario in the Kondo model.⁵

For periodic time-dependent Hamiltonians there also exists a preferable spectral decomposition. Due to the periodicity property in Eq. (19), it is suitable to define two new time arguments

$$t_{\text{av}} = \frac{t + t'}{2}, \quad t_{\text{rel}} = t - t'. \quad (34)$$

Expressing $\chi(t, t')$ in these coordinates, $\chi(t_{\text{av}}, t_{\text{rel}})$ is invariant under the transformation $t_{\text{av}} \rightarrow t_{\text{av}} + \tau$ such that a Fourier series expansion in the coordinate t_{av} can be performed. There-

fore, one can spectrally decompose χ in the following way that is usually referred to as the Wigner representation

$$\begin{aligned} \chi_n(\epsilon) &= \frac{1}{\tau} \int_0^\tau dt_{\text{av}} e^{in\Omega t_{\text{av}}} \int dt_{\text{rel}} e^{i\epsilon t_{\text{rel}}} \chi\left(t_{\text{av}} + \frac{t_{\text{rel}}}{2}, t_{\text{av}} - \frac{t_{\text{rel}}}{2}\right) \\ &= \frac{1}{\tau} \int_0^\tau dt_{\text{av}} e^{in\Omega t_{\text{av}}} \int dt_{\text{rel}} e^{i\bar{\epsilon} t_{\text{rel}}} \chi(t_{\text{av}} + t_{\text{rel}}, t_{\text{av}}) \\ &= \frac{1}{\tau} \int_0^\tau dt_{\text{av}} e^{in\Omega t_{\text{av}}} \chi(t_{\text{av}}, \bar{\epsilon}), \end{aligned} \quad (35)$$

where $\bar{\epsilon} = \epsilon + n\Omega/2$. With each component n , one can associate the behavior of the quantity χ due to processes where n quanta of the driving frequency Ω are absorbed ($n > 0$) or emitted ($n < 0$). The quantity $\chi(t_{\text{av}}, \epsilon)$ can be interpreted as the spectral decomposition of χ at a given point t_{av} in time. The $n=0$ component of χ_n simply is the time average of the quantity $\chi(t_{\text{av}}, \epsilon)$.

Applying a small sinusoidal magnetic field $h(t) = h_0 \sin(\Omega_0 t)$ to the local spin in the steady state, linear response theory predicts for the magnetization of the impurity spin $\langle S_z(t) \rangle_h$ in the presence of the small perturbation h

$$\begin{aligned} \langle S_z(t) \rangle_h &= h_0 \sum_n \{ \chi'_n(\Omega_0 + n\Omega/2) \sin[(\Omega_0 + n\Omega)t] \\ &\quad - \chi''_n(\Omega_0 + n\Omega/2) \cos[(\Omega_0 + n\Omega)t] \}. \end{aligned} \quad (36)$$

Remarkably, this expression contains a static contribution if $\Omega_0 = m\Omega$, $m \in \mathbb{Z} \setminus \{0\}$. Therefore, it is possible to align the local spin on average by applying a sinusoidal magnetic field that itself contains no static contribution

$$\overline{\langle S_z(t) \rangle_h} = \chi''_m(m\Omega/2). \quad (37)$$

Here, $\overline{\langle \dots \rangle}$ denotes the time average. As the spin dynamics are switched off during the second half period, the external magnetic field is not able to influence the local spin magnetization in this time window regardless of its time dependence. Therefore, the magnetic field must be capable of polarizing the local spin during the first half period in order to induce a static component. This can be achieved by $h(t) = h_0 \sin(\Omega_0 t)$ with $\Omega_0 = m\Omega$.

Note that a definite order of taking limits is implicitly prescribed in this linear response calculation. First, the system is evolved into the steady state that is established after an infinite number of periods. Afterwards, an additional sinusoidal magnetic field is applied that acts for an eventually infinite amount of time. Therefore, linear response theory only provides the information of how an additional infinitesimal magnetic field influences the local spin properties after the steady state has already been established. It does not necessarily describe the properties of a system whose interaction is periodically switched on and off in presence of a magnetic field, as the two involved limiting processes may not commute.

Results for $\chi''(t_{\text{av}}, \epsilon)$: in Fig. 4, results for the dynamical spin susceptibility $\chi''(t_{\text{av}}, \epsilon)$ are shown for different values of the driving frequency Ω . The first plot displays the case of slow driving, i.e., $\tau \gg t_K$, and reveals again the single-quench dynamics as argued before. After a transient regime on a

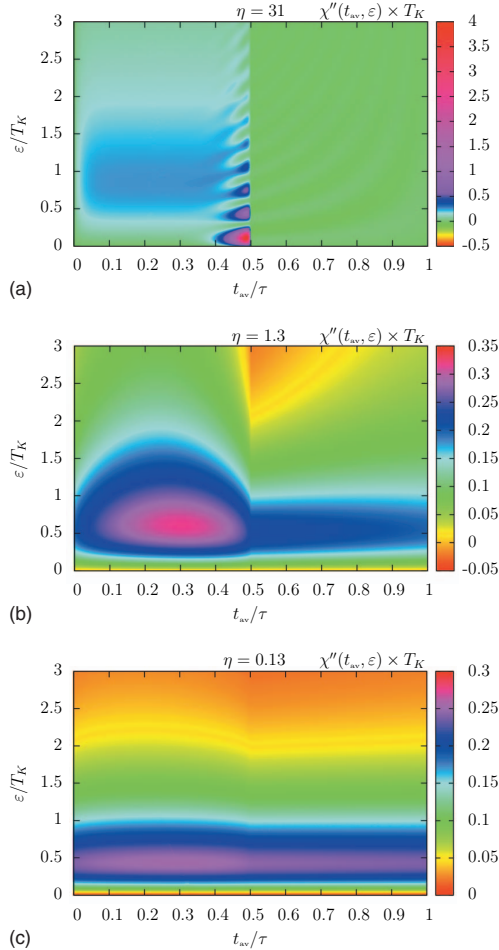


FIG. 4. (Color) False color plots of the dynamical susceptibility $\chi''(t_{av}, \varepsilon)$ at a given point t_{av} in time for different values of the parameter η . The upper plot shows the behavior for slow driving consistent with a single interaction quench picture. The lower plot displays the fast-driving behavior that is similar to an equilibrium problem. The plot in the middle shows the intermediate regime of competing time scales.

time scale t_K , that is the time scale for the buildup of the Kondo effect,⁷ the dynamical spin susceptibility approaches its equilibrium shape with a peak located at $\varepsilon \approx T_K$ representing the buildup of the Kondo singlet and therefore of the Kondo effect. Near the half period boundary, however, a new structure emerges. At $t_{av} \approx \tau/2 - t_K$, a whole sequence of strong peaks appears that cannot be explained by the simple single interaction quench picture as this coherent phenomenon is solely caused by the periodic driving. Approaching $t_{av} = \tau$ these peaks rapidly decrease and disappear. Note, that the dynamical spin susceptibility is not discontinuous at $t_{av} = \tau/2$ as it might seem. The collapse near $\tau/2$, however, is so fast that it cannot be resolved by the pictures presented here.

In the case of fast switching, the lower plot in Fig. 4, the dynamical spin susceptibility stays nearly constant over the whole period. The system is not able to adapt to the fast

external perturbation, as it is faster than the internal time scale t_K , on which the system is able to react. Remarkably, the shape of the spectral decomposition at any time point t_{av} resembles the shape of an equilibrium dynamical spin susceptibility with a reduced Kondo temperature $T_K/2$. It was shown in Eq. (28) that the response function $\chi_{\tau \rightarrow 0}(t, T_K)$ in the limit $\tau \rightarrow 0$ is identical to half of an equilibrium response function $\chi_{eq}(t/2, T_K)/2$ at a rescaled time argument $t/2$ and identical Kondo temperature T_K . Here, the Kondo temperature has been included explicitly for convenience. Such a relation for functions in time implies the following relation for the corresponding Fourier transforms:

$$\chi_{\tau \rightarrow 0}(\varepsilon, T_K) = \chi_{eq}(2\varepsilon, T_K). \quad (38)$$

For the dynamical spin susceptibility, this statement can be rewritten in terms of a modified Kondo temperature

$$\chi''_{\tau \rightarrow 0}(\varepsilon, T_K) = 2\chi''_{eq}(\varepsilon, T_K/2). \quad (39)$$

The equilibrium dynamical susceptibility at zero temperature is known exactly, such that^{16,26}

$$\chi''_{\tau \rightarrow 0}(\varepsilon) = \frac{\Delta^2}{2\pi\varepsilon^2 + \Delta^2} \left\{ \frac{1}{2\varepsilon} \ln \left[1 + \left(\frac{2\varepsilon}{\Delta} \right)^2 \right] + \frac{1}{\Delta} \arctan \left(\frac{2\varepsilon}{\Delta} \right) \right\}. \quad (40)$$

A Kondo singlet is present even for fast periodic driving with a reduced binding energy $T_K/2$. Therefore, one can speculate that the Kondo effect itself survives with a rescaled Kondo temperature $T_K/2$.²⁷ Although this analogy suggests the equivalence to an effective equilibrium problem, this is not valid in a strict sense, since it was shown, compare Eq. (28), that one cannot find an effective equilibrium Hamiltonian that generates the same dynamics. Nevertheless, it is remarkable that the dynamical spin susceptibility, that is a measurable quantity in principle, shows an equilibriumlike behavior of a Kondo model with reduced Kondo temperature in this limit.

The robustness of the Kondo effect even for $\Omega \gg T_K$ has also been observed by Nordlander *et al.*³ where the time-averaged local spectral density shows a Kondo resonance in the limit $\Omega \gg T_K$. The plot in the middle of Fig. 4 shows the intermediate regime where both the external time scale τ and the internal time scale t_K are of the same order. In this case, the system is able to adapt partially to the externally prescribed perturbation. For small times t_{av} , one observes that the Kondo singlet tries to form, the dynamical spin susceptibility tends to approach its equilibrium profile. Near the half period boundary where the interaction is switched off, however, the dynamical spin susceptibility collapses onto a curve with a peak located approximately at $T_K/2$ as in the fast driving case.

Results for $\chi''_n(\varepsilon)$: in Fig. 5, universal curves for the modes $\chi''_n(\varepsilon)$ are shown. In the upper plot of the $n=0$ component, one can nicely see the crossover from the fast to the slow driving regime. For fast driving, small η , one observes a peak located at $\varepsilon \approx T_K/2$, whose height and position decreases by increasing η . This signals a decrease in the binding energy as well as the stability of the associated Kondo singlet. For large η , this peak vanishes according to the

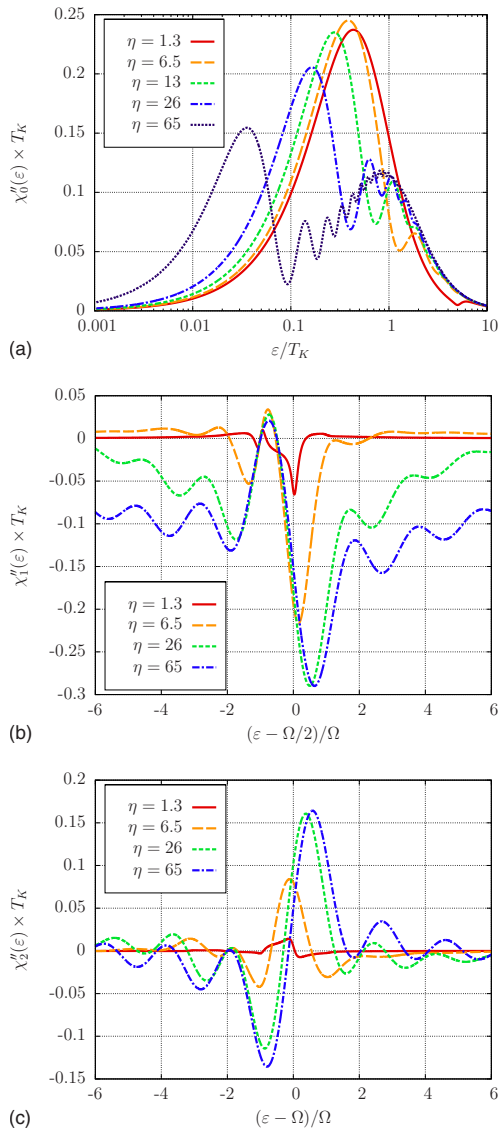


FIG. 5. (Color online) Universal curves of the zeroth, first, and second mode $\chi''_n(\varepsilon - n\Omega/2)$ for different values of the parameter η .

single-quench dynamics for $\tau=\infty$ where only a Kondo singlet of energy T_K exists. Indeed, for intermediate η , a second peak emerges at T_K with a height of only half of its equilibrium value, as half of the time the interaction is switched off. Thus, the $n=0$ component of the dynamical susceptibility shows the crossover from a Kondo singlet of binding energy T_K at $\tau=\infty$ to a Kondo singlet with binding energy $T_K/2$ for $\tau=0$. The oscillations appearing for large η originate in the periodic structure near the half period boundary of $\chi(t_{av}, \varepsilon)$ that can be seen in Fig. 4.

The $n=1$ and $n=2$ modes that correspond to processes where one or two energy quanta Ω are absorbed are shown in the lower two plots of Fig. 5. Due to the relation

$$\chi''_n(\varepsilon) = -\chi''_{-n}(-\varepsilon) \quad (41)$$

these results can be extended straightforwardly to the $n=-1, -2$ modes.

For small periods τ , all modes $n \neq 0$ vanish due to the equilibriumlike dynamics where absorption and emission of photons is not taking place. As $\Omega \rightarrow \infty$ for $\tau \rightarrow 0$, the absorption or emission of an energy quantum Ω involves high energy transfers that are cut off by the finite width of the local hybridized d level. The equilibrium spin fluctuations of the conduction-band electrons in the Kondo model at large energies are suppressed due to energy conservation. As mentioned in Sec. III, the only influence of the periodic driving is the enhancement of certain fluctuations that are present in the equilibrium versions of the involved Hamiltonians. If the equilibrium fluctuations already vanish, their enhancement due to the periodic driving is negligible, too.

The larger the parameter η , the larger becomes the response for processes under absorption and emission, as the excitations generated by the periodic driving now turn out to be excitations of lower energy as Ω decreases. In the limit $\tau \rightarrow \infty$, however, the $n \neq 0$ components are expected to vanish as in the $\tau \rightarrow 0$ limit, since the system is able to relax during each half period and locally behaves as in equilibrium nearly all of the time. The behavior for the $n=1$ and $n=2$ components is qualitatively different for energies above or below $n\Omega/2$. The absorption or emission of one photon is likely for the $n=1$ mode whereas the $n=2$ mode decays to zero much faster away from its maximum. The different properties of the even and odd modes can be traced back to Eq. (10), stating that the square-wave driving can be thought of as a nonmonochromatic driving including all frequencies of odd multiples of Ω .

VII. CONCLUSIONS

In this work, the steady state in a periodically driven Kondo model in the Toulouse limit has been investigated by analyzing exact analytical results for the local spin dynamics at zero temperature. Remarkably, the analysis revealed a universal asymptotic long-time behavior of the spin-spin correlation function, compare Eq. (31), independent of the driving matching precisely the zero temperature equilibrium result. This universality originates in the discrete character of the excitation spectrum that leaves the low-energy excitations in the immediate vicinity of the Fermi level unchanged.

For large switching times, $\tau/t_K \rightarrow \infty$ where t_K is the equilibrium Kondo time scale, the local observables behave as for a single-interaction quench since the system is able to relax during each half period. In the opposite limit, $\tau/t_K \rightarrow 0$, the system is not able to follow the fast externally prescribed perturbation. Although the dynamics is “equilibrium-like” [in the sense that time-translational invariance is restored, e.g., Eq. (28)], it is impossible to find an effective equilibrium Hamiltonian generating the same dynamics. This can be seen in the discussion below Eq. (29) were it was shown that the fluctuation-dissipation theorem is violated for the local spin observable. Consequently, the steady state created by the periodic time-dependent setup provides an ex-

ample for the possibility to reach new quantum states in systems out of equilibrium that are not accessible by equilibrium thermodynamics. The reason for the existence of this unusual steady state is the inapplicability of the Trotter formula in the present periodic time-dependent setup. This observation might also be useful for other periodically driven systems.

Remarkably, in the Toulouse limit the Kondo effect is robust against the periodic driving as long as the driving frequency is unable to induce charge fluctuations in the quantum dot. Even in the case of fast driving $\Omega \gg T_K$ the Kondo singlet survives. The associated binding energy $T_K/2$ is reduced to half of its equilibrium value. For intermediate τ , a crossover is observed from a Kondo singlet of binding energy $T_K/2$ in the fast switching limit to a Kondo singlet of binding energy T_K for long switching times.

It would be interesting to investigate related questions for the Kondo model away from the Toulouse limit, where one also expects that the flow to the strong-coupling fixed point itself is affected by the periodic switching. Likewise it would be important to understand whether other periodically driven quantum impurity models show similar dynamics. Work along these lines is in progress. The exact analytical results derived in this work will be important benchmarks for these investigations.

ACKNOWLEDGMENTS

This work was supported under Grant No. SFB 484 of the Deutsche Forschungsgemeinschaft (DFG), the Center for Nanoscience (CeNS) Munich, and the German Excellence Initiative via the Nanosystems Initiative Munich (NIM).

APPENDIX

In this appendix, the procedure to obtain the solution to the matrix multiplication problem is presented. For that purpose, the Green's functions for the resonant-level model \mathcal{G} and the potential scattering Hamiltonian $\mathcal{G}^{(n)}$ have to be derived, for example, by using the equations of motion approach. The matrices $\mathcal{M}(n)=\mathcal{G}\mathcal{G}^{(n)}$ obey the following formulas:

$$\begin{aligned}\mathcal{M}_{dd}(n) &= e^{-\Delta\pi/2}, \\ \mathcal{M}_{dk}(n) &= \frac{V}{k-i\Delta}[e^{-ik\pi/2} - e^{-\Delta\pi/2}], \\ \mathcal{M}_{kd}(n) &= \frac{Ve^{-ik\pi/2}}{k-i\Delta}[e^{-ik\pi/2} - e^{-\Delta\pi/2}], \\ \mathcal{M}_{kk'}(n) &= \delta_{kk'}e^{-ik\tau} + \mathcal{L}_{kk'} + \mathcal{K}_{kk'}(n),\end{aligned}\quad (\text{A1})$$

where the matrices \mathcal{L} and $\mathcal{K}(n)$ are determined by

$$\begin{aligned}\mathcal{L}_{kk'} &= V^2 e^{-ik\pi/2} \left[\frac{e^{-ik\pi/2}}{(k-k')(k-i\Delta)} + \frac{e^{-\Delta\pi/2}}{(k-i\Delta)(k'-i\Delta)} \right. \\ &\quad \left. + \frac{e^{-ik'\pi/2}}{(k'-k)(k'-i\Delta)} \right], \\ \mathcal{K}_{kk'}(n) &= \frac{g\langle S_z(n\tau) \rangle e^{-ik\pi/2}}{1+ig\langle S_z(n\tau) \rangle L/2} \frac{e^{-ik\pi/2} - e^{-ik'\pi/2}}{k-k'}.\end{aligned}\quad (\text{A2})$$

For simplicity, the method to obtain $\mathcal{M}^{(N)}$ will be displayed by calculating the matrix element $\mathcal{M}_{dd}^{(N)}$. Using its definition in Eq. (8) one can write

$$\begin{aligned}\mathcal{M}_{dd}^{(N)} = \sum_{l_1, \dots, l_{N-1}} \mathcal{M}_{dl_1}(1), \dots, \mathcal{M}_{l_{N-1}d}(N) &= \mathcal{M}_{dd}^{(N-1)} \mathcal{M}_{dd} + \sum_{l_1, \dots, l_{N-3}, k_{N-1}} \mathcal{M}_{dl_1}(1), \dots, \mathcal{M}_{l_{N-3}d}(N-2) \mathcal{M}_{dk_{N-2}} \mathcal{M}_{k_{N-2}d} \\ &\quad + \sum_{l_1, \dots, l_{N-3}, k_{N-2}, k_{N-1}} \mathcal{M}_{dl_1}(1), \dots, \mathcal{M}_{l_{N-3}k_{N-2}}(N-2) \mathcal{M}_{k_{N-2}k_{N-1}}(N-1) \mathcal{M}_{k_{N-1}d}.\end{aligned}\quad (\text{A3})$$

To proceed further, the following relations are required:

$$\begin{aligned}\sum_{k'} \mathcal{M}_{kk'}(n) \mathcal{M}_{k'd} e^{-i\lambda k' \tau} &= e^{-i(\lambda+1)k\tau} \mathcal{M}_{kd}, \\ \sum_k \mathcal{M}_{dk} \mathcal{M}_{kd} &= 0\end{aligned}\quad (\text{A4})$$

that originate in elementary properties of the matrix \mathcal{M} , namely, that \mathcal{M} as a function of k exhibits no poles and that the exponentials $e^{-ik\pi/2}$ always allow to deform integration contours into the lower half plane. Using these formulas, one can directly show that the two sums appearing in Eq. (A3) vanish. The resulting recursion formula is solved by

$$\mathcal{M}_{dd}^{(N)} = e^{-N\Delta\pi/2}. \quad (\text{A5})$$

Analogously, the other matrix elements of $\mathcal{M}^{(N)}$ can be derived although the evaluation of $\mathcal{M}_{kk'}^{(N)}$ is quite involved. Remarkably, all matrix elements with an index d are independent of the potential scatterer. Only $\mathcal{M}_{kk'}^{(N)}$ includes a term that can be traced back to the potential scattering

$$\mathcal{K}_{kk'}^{(N)} = g\langle S_z(0) \rangle \sum_{n=0}^{N-1} \frac{e^{-ink\tau} e^{-i(N-n)k' \tau}}{e^{n\Delta\tau} + ig\langle S_z(0) \rangle L/2}. \quad (\text{A6})$$

Here, the result for the magnetization, see Eq. (14), has been used.

- ¹B. P. Anderson and M. A. Kasevich, *Science* **282**, 1686 (1998); M. Greiner, O. Mandel, T. W. Hänsch, and I. Bloch, *Nature (London)* **419**, 51 (2002).
- ²D. Goldhaber-Gordon, H. Shtrikman, D. Mahalu, D. Abusch-Magder, U. Meirav, and M. A. Kastner, *Nature (London)* **391**, 156 (1998); S. M. Cronenwett, T. H. Oosterkamp, and L. P. Kouwenhoven, *Science* **281**, 540 (1998); J. Schmid, J. Weis, K. Eberl, K. von Klitzing, *Physica B* **256-258**, 182 (1998); W. G. van der Wiel, S. De Franceschi, T. Fujisawa, J. M. Elzerman, S. Tarucha, and L. P. Kouwenhoven, *Science* **289**, 2105 (2000).
- ³P. Nordlander, N. S. Wingreen, Y. Meir, and D. C. Langreth, *Phys. Rev. B* **61**, 2146 (2000).
- ⁴D. Lobaskin and S. Kehrein, *Phys. Rev. B* **71**, 193303 (2005).
- ⁵D. Lobaskin and S. Kehrein, *J. Stat. Phys.* **123**, 301 (2006).
- ⁶M. Moekkel and S. Kehrein, *Phys. Rev. Lett.* **100**, 175702 (2008); M. Eckstein, M. Kollar, and P. Werner, *ibid.* **103**, 056403 (2009); P. Calabrese and J. Cardy, *ibid.* **96**, 136801 (2006); C. Kollath, A. M. Läuchli, and E. Altman, *ibid.* **98**, 180601 (2007); A. Faribault, P. Calabrese, and J.-S. Caux, *J. Stat. Mech.* **2009**, P03018; M. Eckstein and M. Kollar, *Phys. Rev. Lett.* **100**, 120404 (2008); M. Rigol, *ibid.* **103**, 100403 (2009); S. R. Manmana, S. Wessel, R. M. Noack, and A. Muramatsu, *ibid.* **98**, 210405 (2007); M. A. Cazalilla, *ibid.* **97**, 156403 (2006).
- ⁷P. Nordlander, M. Pustilnik, Y. Meir, N. S. Wingreen, and D. C. Langreth, *Phys. Rev. Lett.* **83**, 808 (1999).
- ⁸A. Mitra and A. J. Millis, *Phys. Rev. B* **76**, 085342 (2007).
- ⁹A. V. Joura, J. K. Freericks, and Th. Pruschke, *Phys. Rev. Lett.* **101**, 196401 (2008); N. Tsuji, T. Oka, and H. Aoki, *ibid.* **103**, 047403 (2009); *Phys. Rev. B* **78**, 235124 (2008).
- ¹⁰R. López, R. Aguado, G. Platero, and C. Tejedor, *Phys. Rev. Lett.* **81**, 4688 (1998); T. K. Ng, *ibid.* **76**, 487 (1996); M. H. Hettler and H. Schoeller, *ibid.* **74**, 4907 (1995); B. H. Wu and J. C. Cao, *Phys. Rev. B* **77**, 233307 (2008).
- ¹¹A. Kaminski, Y. V. Nazarov, and L. I. Glazman, *Phys. Rev. Lett.* **83**, 384 (1999).
- ¹²A. Kaminski, Y. V. Nazarov, and L. I. Glazman, *Phys. Rev. B* **62**, 8154 (2000).
- ¹³Y. Goldin and Y. Avishai, *Phys. Rev. Lett.* **81**, 5394 (1998); *Phys. Rev. B* **61**, 16750 (2000).
- ¹⁴A. Schiller and S. Hershfield, *Phys. Rev. Lett.* **77**, 1821 (1996).
- ¹⁵G. Toulouse, C. R. Seances Acad. Sci., Ser. B **268**, 1200 (1969).
- ¹⁶A. J. Leggett, S. Chakravarty, A. T. Dorsey, M. P. A. Fisher, A. Garg, and W. Zwerger, *Rev. Mod. Phys.* **59**, 1 (1987).
- ¹⁷B. Doyon and N. Andrei, *Phys. Rev. B* **73**, 245326 (2006).
- ¹⁸J. R. Schrieffer and P. A. Wolff, *Phys. Rev.* **149**, 491 (1966).
- ¹⁹J. von Delft and H. Schoeller, *Ann. Phys.* **7**, 225 (1998).
- ²⁰G. Zaránd and J. von Delft, *Phys. Rev. B* **61**, 6918 (2000).
- ²¹F. Lesage and H. Saleur, *Phys. Rev. Lett.* **80**, 4370 (1998).
- ²²F. Guinea, V. Hakim, and A. Muramatsu, *Phys. Rev. B* **32**, 4410 (1985).
- ²³V. Eisler and I. Peschel, *Ann. Phys.* **17**, 410 (2008).
- ²⁴H. F. Trotter, *Proc. Am. Math. Soc.* **10**, 545 (1959); M. Suzuki, *Commun. Math. Phys.* **51**, 183 (1976).
- ²⁵D. C. Langreth and P. Nordlander, *Phys. Rev. B* **43**, 2541 (1991).
- ²⁶F. Guinea, *Phys. Rev. B* **32**, 4486 (1985).
- ²⁷Note that the time-averaged effective Hamiltonian would generate a Kondo model with a Kondo temperature $T_K/4$ in contrast to the exact value $T_K/2$.

5.2 Publication: Nonlinear ac transport through a resonant level model

As a consequence of the successive miniaturization of electronic devices it is now within the scope of future developments that quantum effects such as the quantization of the electronic charge become relevant in electronic circuits. According to Moore's law the number of transistors on consumer computer chips doubles every 18 months. Along with an increase of the number of transistors on an approximately fixed area comes a successive decrease in their size as well as in the number of electrons used for operations. The ultimate limit corresponds to single-electron devices as already realized by quantum dots or single-electron transistors. In this context the study of transport through single-electron devices is of fundamental importance.

In contrast to bulk materials where transport is essentially captured by linear response theory transport through nanostructures can readily drive the system far beyond equilibrium and far beyond linear response. Within the present experimental technology it is conceivable or even feasible to study such scenarios with a high control over the system's properties. In this context transport under the influence of periodic time-dependent applied bias voltages is of particular interest as alternating currents dominate electronic functional devices.

For ac currents through nanostructures where quantum effects become important the conductance can be enhanced by a mechanism termed photon-assisted tunneling [170]. Most importantly, in presence of an ac-voltage the current through the system is not dominated by energy conserving processes alone. Instead, the dominant processes are those where the energy is conserved up to multiples of the driving frequency Ω . Pictorially speaking, electrons can tunnel through the system by absorbing or emitting multiple photons of frequency Ω . Note that this process is of fundamental quantum nature. The externally applied electric ac field provides an energy reservoir that the system can use to overcome energy barriers.

Below, transport through a quantum dot is investigated in presence of a particularly chosen ac driving. For the minimal model of a quantum dot coupled to a fermionic reservoir see Sec. 3.4.1. For simplicity only one spin channel will be considered yielding the Hamiltonian

$$H = \sum_{k,\alpha=L/R} [\varepsilon_k + \mu_\alpha(t)] c_{k\alpha}^\dagger c_{k\alpha} + \varepsilon_d d^\dagger d + \frac{g}{\sqrt{2}} \sum_{k,\alpha=L/R} [d^\dagger c_{k\alpha} + c_{k\alpha}^\dagger d]. \quad (5.3)$$

The index $\alpha = L/R$ refers to the left and right conduction band. The operator $c_{k\alpha}^\dagger$ creates a fermion in the $\alpha = L/R$ lead with momentum k . Note that the conduction band is modeled as a one-dimensional system. This is based on the assumption that the scattering of fermions in the, in principle, higher-dimensional fermionic reservoir by the impurity only affects the s -wave channel allowing an effective dimensional reduction. A fermion with energy ε_d is created in the quantum dot via the operator d^\dagger . The coupling between the fermionic reservoirs and the quantum dot in terms of the hopping amplitude g is chosen to

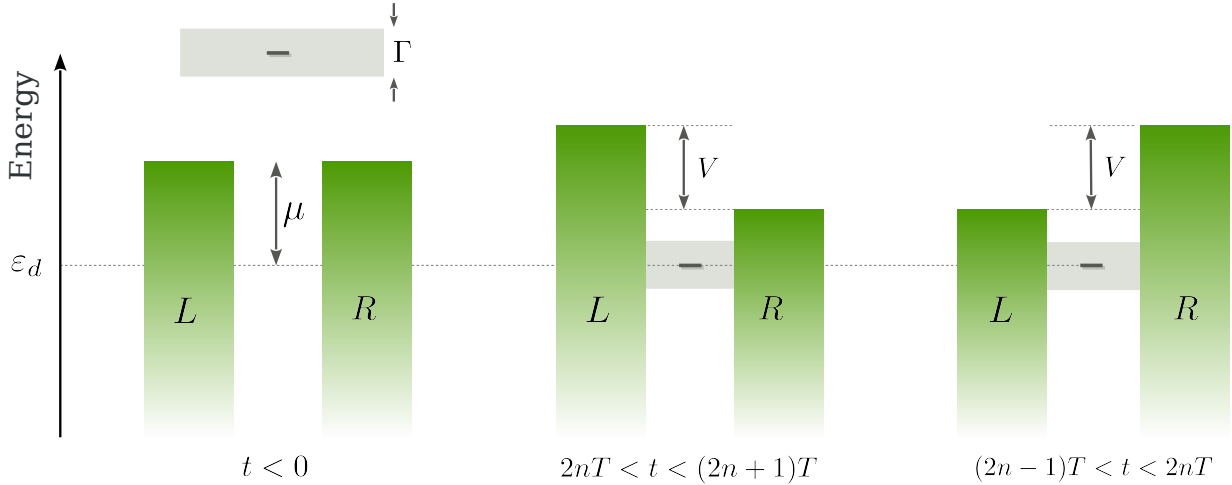


Figure 5.1: Schematic illustration of the nonequilibrium protocol. The system is initially prepared in the ground state of the decoupled system with two Fermi seas at the same chemical potential. The initial quantum dot level $\varepsilon_d - \varepsilon_F \gg \Gamma$ lies far above the Fermi energy ε_F of both conduction bands such that the hybridization characterized by Γ can be neglected. The periodic driving starts at time $t = 0$. In the first half period for times $2nT < t < (2n+1)T$ with $n \in \mathbb{N}$ a natural number the chemical potentials of the two leads are chosen in such a way to establish a potential difference $u_R - u_L = V$. In the second half period the potential difference is interchanged yielding $u_R - u_L = -V$. For more details see main text.

be of the same strength for both channels for simplicity. The corresponding hybridization strength $\Gamma = \pi\rho_0g^2$ is determined by the noninteracting density of states ρ_0 of the two conduction bands that is also taken to be independent of the channel index $\alpha = L/R$. The chemical potentials $\mu_\alpha(t)$ of the left and right lead are chosen to be time-dependent which generates the nonequilibrium scenario that will be investigated in this part of the thesis. Note that the whole analysis is based on the assumption that the level spacing in the quantum dot is sufficiently large to ignore the influence of the other electronic levels.

Below, the zero of energy will be set such that the value of the local level energy $\varepsilon_d = 0$ vanishes yielding the following parametrization of the Hamiltonian

$$H = \sum_{k,\alpha=L/R} [\varepsilon_k - u_\alpha(t)] c_{k\alpha}^\dagger c_{k\alpha} + \frac{g}{\sqrt{2}} \sum_{k,\alpha=L/R} [d^\dagger c_{k\alpha} + c_{k\alpha}^\dagger d]. \quad (5.4)$$

The nonequilibrium ac protocol will be chosen as follows. For a schematic picture see Fig. 5.1. For times $t < 0$ the system is supposed to be prepared in the ground state of a decoupled system. The initial state of the system is taken as a product state of two Fermi seas for the left and right lead with the same chemical potential μ and of an unoccupied quantum dot level. This can be achieved by adjusting the gate voltage in such a way that initially $\varepsilon_d - \varepsilon_F \gg \Gamma$. In this regime the hybridization of the local level can be neglected yielding an unoccupied quantum dot. At time $t = 0$ the driving is started by periodically

switching the chemical potentials of the left and right lead asymmetrically

$$u_R(t) = \frac{V}{2} \text{sgn} [\sin(\Omega t)], \quad u_R(t) = -u_L(t). \quad (5.5)$$

where $\text{sgn}(x)$ is the sign-function with $\text{sgn}(x) = 1$ for $x > 0$ and $\text{sgn} = -1$ for $x < 0$. The parameter Ω denotes the driving frequency $\Omega = \pi/T$ with T the time span for one half period which should not be confused with temperature. This yields $u_R(t) = V/2 = -u_L(t)$ in the first half period T and $u_R(t) = -V/2 = -u_L(t)$ in the second one.

The restriction to one channel of spinless fermions neglects the influence of local interactions on the quantum dot. In an experimental implementation interactions will always be present. Depending on the experimental details, however, there is a regime where interactions become irrelevant in a renormalization group sense and the physics is dominated by the noninteracting limit [100, 101]. This is the case when the local interaction strength $U \leq \Gamma$ is smaller than the hybridization Γ between the local level and the conduction band. In this limit it is thus possible to decouple the two spin channels and to restrict oneself to spinless fermions.

The most important advantage of treating the noninteracting limit despite of its experimental relevance in the limit $\Gamma \geq U$ is the possibility to derive exact analytical solutions. This serves as a benchmark for more advanced studies including also interactions. This, however, poses a great challenge on methodology such that it is instructive to study the exactly solvable cases first. Below, the current and the conductance of this system is studied based on the analytical solution.

Exact results for nonlinear ac transport through a resonant level model

This article has been downloaded from IOPscience. Please scroll down to see the full text article.

2010 J. Phys.: Condens. Matter 22 275604

(<http://iopscience.iop.org/0953-8984/22/27/275604>)

View [the table of contents for this issue](#), or go to the [journal homepage](#) for more

Download details:

IP Address: 129.187.254.47

The article was downloaded on 27/11/2011 at 08:34

Please note that [terms and conditions apply](#).

Exact results for nonlinear ac transport through a resonant level model

P Wang, M Heyl and S Kehrein

Physics Department, Arnold Sommerfeld Center for Theoretical Physics, and Center for NanoScience, Ludwig-Maximilians-Universität, Theresienstrasse 37, D-80333 Munich, Germany

E-mail: pei.wang@physik.lmu.de

Received 15 April 2010, in final form 31 May 2010

Published 23 June 2010

Online at stacks.iop.org/JPhysCM/22/275604

Abstract

We obtain exact results for the transport through a resonant level model (noninteracting Anderson impurity model) for rectangular voltage bias as a function of time. We study both the transient behavior after switching on the tunneling at time $t = 0$ and the ensuing steady state behavior. Explicit expressions are obtained for the ac current in the linear response regime and beyond for large voltage bias. Among other effects, we observe current ringing and PAT (photon-assisted tunneling) oscillations.

(Some figures in this article are in colour only in the electronic version)

1. Introduction

The recent advances in nanotechnology created a lot of interest in transport through correlated quantum impurities. While the linear response regime essentially probes the ground state properties of the system, transport beyond the linear response regime explores genuine non-equilibrium quantum many-body phenomena. However, theoretical calculations beyond the linear response regime are challenging since the steady state cannot be constructed via a variational principle like equilibrium states. Even for dc bias only recently exact numerical methods have been developed that permit such investigations for interacting systems, notably the time-dependent numerical renormalization group [1], Monte Carlo methods [2, 3] and the time-dependent density matrix renormalization group [4, 5]. Some of the analytical methods that have been applied successfully are perturbative Keldysh calculations [6], extensions of the renormalization group [7, 8], flow equations [9] and generalizations of the NCA (non-crossing approximation) to non-equilibrium [11, 10]. A comparative review of theoretical methods can be found in [12].

For ac bias beyond the linear response regime still much less is known since, for example, the numerical methods cannot easily be generalized to time-dependent bias. Interesting ac phenomena are, for example, the photon-assisted tunneling effect (PAT) [13] that has been observed in experiments [14], or the ‘current ringing’ after a step-like

bias pulse [15]. Non-equilibrium Green’s function methods can be employed [16, 15, 17] when the correlation effects are not too strong. In the strongly correlated regime of the Kondo model the non-crossing approximation was found to be reliable [11, 19, 18, 20]. At a specific point of the two-lead Kondo model it can be solved exactly [21], which permits exact results for the current in the steady state [22], after a rectangular pulse [23] or under sinusoidal bias [21]. Unfortunately, this special point is not generic for a Kondo impurity that can be derived from an underlying Anderson impurity model, which is experimentally the most relevant situation.

A closely related direction of current research is quantum pumping, where an ac gate voltage is applied to some central levels of a nanostructure, which are coupled to several leads. In this manner a direct current can be generated, see, for example, [24–30].

In our paper we study the response of a resonant level model (noninteracting Anderson impurity model) under rectangular ac voltage bias after switching on the tunneling at time $t = 0$.¹ We derive exact analytical results for the transient and steady state current by diagonalizing the Hamiltonian. This exact solution contains both dc and ac bias in and

¹ It should be mentioned that our model cannot be mapped to the model in [26] by the gauge transformation introduced there because the left and right leads are coupled to the same central level in our model. Therefore the hybridization functions after the gauge transformation become time-dependent, which is different from the situation studied in [26].

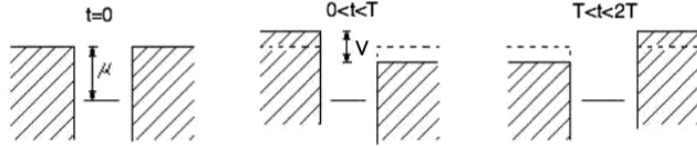


Figure 1. A schematic diagram of our model: a step-like voltage bias is applied to the two leads coupled to the quantum dot.

beyond the linear response regime. While dc results and ac results with sinusoidal bias have been obtained previously in the literature [15], rectangular ac driving beyond the linear regime seems not to have been studied before. Besides being experimentally relevant, our results are also helpful for exploring the various crossovers in this important model and serve as an exact benchmark for future work.

2. Model and diagonalization

The resonant level model coupled to two leads is defined by the following Hamiltonian:

$$\hat{H} = \sum_{k\alpha} \epsilon_k \hat{c}_{k\alpha}^\dagger \hat{c}_{k\alpha} + \sum_{k\alpha} \frac{g}{\sqrt{2}} (\hat{c}_{k\alpha}^\dagger \hat{d} + \text{h.c.}), \quad (1)$$

where $\alpha = L, R$ denotes the leads, $\hat{c}_{k\alpha}^\dagger$ creates an electron in lead α with energy ϵ_k and \hat{d}^\dagger creates an electron at the impurity site. The spin index can be omitted since the model is noninteracting and we work with spinless fermions. All energies are measured with respect to the single-particle energy of the impurity orbital ($\epsilon_d \equiv 0$). We take a wide band limit with a linear dispersion relation, $\epsilon_k = k\eta$, where η denotes the level spacing and k an integer number. The hybridization is defined by $\Gamma = \rho\pi g^2$, where $\rho = 1/\eta$. The impurity orbital spectral function in equilibrium is then given by

$$\rho_d(\epsilon) = \frac{\Gamma}{\pi(\epsilon^2 + \Gamma^2)}, \quad (2)$$

which is a Lorentzian with width Γ as defined above.

Our strategy to obtain exact results is to first diagonalize the discretized Hamiltonian and to then take the thermodynamic limit $\eta \rightarrow 0$. We introduce the hybridized basis $\hat{c}_s = \sum_k \frac{g}{\epsilon_s - \epsilon_k} B_s \hat{c}_{k+} + B_s \hat{d}$. It is then straightforward to diagonalize the Hamiltonian

$$\hat{H} = \sum_k \epsilon_k \hat{c}_{k-}^\dagger \hat{c}_{k-} + \sum_s \epsilon_s \hat{c}_s^\dagger \hat{c}_s, \quad (3)$$

where $\hat{c}_{k\pm} = \frac{1}{\sqrt{2}}(\hat{c}_{kL} \pm \hat{c}_{kR})$. The inverse transformation is $\hat{d} = \sum_s B_s \hat{c}_s$ and $\hat{c}_{k+} = \sum_s \frac{g}{\epsilon_s - \epsilon_k} B_s \hat{c}_s$. The eigenvalues are determined as solutions of the equation

$$\frac{\epsilon_s}{g^2} = \frac{\pi}{\eta} \cot \frac{\pi \epsilon_s}{\eta}. \quad (4)$$

B_s is given by (for details see [31])

$$B_s^2 = \frac{g^2}{\epsilon_s^2 + \Gamma^2 + g^2}, \quad (5)$$

which in the thermodynamic limit yields

$$B_s^2 = \frac{g^2}{\epsilon_s^2 + \Gamma^2}. \quad (6)$$

From the diagonalization one also derives the following set of equations:

$$\begin{aligned} \sum_s B_s^2 &= 1, \\ \sum_s \frac{g^2 B_s^2}{(\epsilon_s - \epsilon_k)^2} &= 1, \\ \sum_s \frac{B_s^2}{\epsilon_s - \epsilon_k} &= 0, \\ \sum_s \frac{B_s^2}{(\epsilon_s - \epsilon_k)(\epsilon_s - \epsilon_{k'})} &= 0, \quad k' \neq k. \end{aligned}$$

which will be important for calculating various summations below.

An ac voltage bias leads to time-dependent potentials $u_\alpha(t)$ in the leads and the Hamiltonian takes the form

$$\hat{H} = \sum_{k\alpha} (\epsilon_k - u_\alpha(t)) \hat{c}_{k\alpha}^\dagger \hat{c}_{k\alpha} + \sum_{k\alpha} \frac{g}{\sqrt{2}} (\hat{c}_{k\alpha}^\dagger \hat{d} + \text{h.c.}). \quad (7)$$

We suppose that initially (at time $t < 0$) the left and right lead chemical potentials are the same, $\mu_L = \mu_R = \mu$, the hybridization is switched off and that there is no electron in the dot, $n_d = 0$. At time $t = 0$ the hybridization is switched on and a rectangular voltage bias with period $2T$ (see figure 1) is applied: $u_R(t) = -u_L(t) = V/2$ for $2NT < t < (2N+1)T$ and $u_R(t) = -u_L(t) = -V/2$ for $(2N+1)T < t < 2(N+1)T$, where N is an integer denoting the number of switching periods². μ therefore gives the energy difference of the impurity orbital to the ‘average’ Fermi energy of the leads for time $t > 0$ (figure 1).

The current operator is defined as

$$\hat{I}_\alpha = s_\alpha e \frac{d\hat{N}_\alpha}{dt} = \frac{iges_\alpha}{\sqrt{2}} \sum_k (\hat{d}^\dagger \hat{c}_{k\alpha} - \hat{c}_{k\alpha}^\dagger \hat{d}), \quad (8)$$

where \hat{N}_α denotes the total number of electrons in lead α and $s_L \stackrel{\text{def}}{=} 1$, $s_R \stackrel{\text{def}}{=} -1$.

In the first half-period $2NT < t < (2N+1)T$ the Hamiltonian is

$$\begin{aligned} \hat{H}_a &= \sum_k \left(\epsilon_k + \frac{V}{2} \right) \hat{c}_{kL}^\dagger \hat{c}_{kL} + \sum_k \left(\epsilon_k - \frac{V}{2} \right) \hat{c}_{kR}^\dagger \hat{c}_{kR} \\ &+ \sum_{k\alpha} \frac{g}{\sqrt{2}} (\hat{c}_{k\alpha}^\dagger \hat{d} + \text{h.c.}). \end{aligned} \quad (9)$$

² For mathematical simplicity we assume that $V/2$ is an integer multiple of the level spacing η . In other words, $\epsilon_k \pm \frac{V}{2}$ can be written as some $\epsilon_{k'}$. This condition will, of course, play no role in the thermodynamic limit.

Because the dispersion relation is linear and k runs from $-\infty$ to ∞ (wide band limit), we can simply relabel the fermion operators, $\hat{c}_{k\alpha} = \hat{c}_{k+\frac{s\alpha V}{2\eta}, \alpha}$. The potentials in the leads are eliminated by this transformation and the Hamiltonian can be diagonalized as before: $\hat{H}_a = \sum_s \epsilon_s \hat{a}_s^\dagger \hat{a}_s + \sum_k \epsilon_k \hat{a}_k^\dagger \hat{a}_k$, where $\hat{a}_s = \sum_k \frac{g B_s}{\epsilon_s - \epsilon_k} \hat{a}_{k+} + B_s \hat{d}$ and $\hat{a}_{k\pm} = \frac{1}{\sqrt{2}} (\hat{c}_{k-\frac{\alpha V}{2}, L} \pm \hat{c}_{k+\frac{\alpha V}{2}, R})$. Similarly, in the second half-period $(2N+1)T < t < 2(N+1)T$ the Hamiltonian is diagonalized as $\hat{H}_b = \sum_s \epsilon_s \hat{b}_s^\dagger \hat{b}_s + \sum_k \epsilon_k \hat{b}_{k+}^\dagger \hat{b}_{k-}$, where $\hat{b}_s = \sum_k \frac{g B_s}{\epsilon_s - \epsilon_k} \hat{b}_{k+} + B_s \hat{d}$ and $\hat{b}_{k\pm} = \frac{1}{\sqrt{2}} (\hat{c}_{k+\frac{\alpha V}{2}, L} \pm \hat{c}_{k-\frac{\alpha V}{2}, R})$.

In the Heisenberg picture the current operator at time $t = 2NT + \tau$, $\tau \in [0, T]$ (first half-period) can be expressed as

$$\hat{I}_\alpha(t) = (\mathrm{e}^{i\hat{H}_a T} \mathrm{e}^{i\hat{H}_b T})^N \mathrm{e}^{i\hat{H}_a \tau} \hat{I}_\alpha \mathrm{e}^{-i\hat{H}_a \tau} (\mathrm{e}^{-i\hat{H}_b T} \mathrm{e}^{-i\hat{H}_a T})^N, \quad (10)$$

and in the second half-period ($t = (2N+1)T + \tau$, $\tau \in [0, T]$)

$$\begin{aligned} \hat{I}_\alpha(t) = & (\mathrm{e}^{i\hat{H}_a T} \mathrm{e}^{i\hat{H}_b T})^N \mathrm{e}^{i\hat{H}_a T} \mathrm{e}^{i\hat{H}_b \tau} \hat{I}_\alpha \mathrm{e}^{-i\hat{H}_b \tau} \mathrm{e}^{-i\hat{H}_a T} \\ & \times (\mathrm{e}^{-i\hat{H}_b T} \mathrm{e}^{-i\hat{H}_a T})^N. \end{aligned} \quad (11)$$

To find $\hat{I}_\alpha(t)$ we first calculate the time evolution of the single-fermion operator \hat{d}^\dagger and $\hat{c}_{k\alpha}^\dagger$ under \hat{H}_a or \hat{H}_b by expressing \hat{d}^\dagger and $\hat{c}_{k\alpha}^\dagger$ in the hybridized basis, next applying the diagonal time evolution and finally transforming back to the original basis. The calculation is straightforward but one needs to pay attention when encountering summations with respect to the eigenenergies ϵ_s . In the thermodynamic limit the summation can be transformed into an integral when there is no pole in the integrand, for example, $\sum_s B_s^2 e^{-i\epsilon_s t} = \int d\epsilon_s \rho B_s^2 e^{-i\epsilon_s t} = e^{-\Gamma t}$. If there are poles in the integrand we first calculate the time derivative to get rid of the pole terms. Key formulae are

$$\sum_s \frac{B_s^2 e^{-i\epsilon_s t}}{\epsilon_s - \epsilon_k} = \frac{e^{-i\epsilon_k t} - e^{-\Gamma t}}{\epsilon_k + i\Gamma} \quad (12)$$

$$\begin{aligned} \sum_s \frac{B_s^2 e^{-i\epsilon_s t}}{(\epsilon_s - \epsilon_k)^2} = & \left(\frac{1}{g^2} + \frac{-1 - (i\epsilon_k - \Gamma)t}{(\epsilon_k + i\Gamma)^2} \right) e^{-i\epsilon_k t} \\ & + \frac{e^{-\Gamma t}}{\left(\epsilon_k + i\Gamma \right)^2}. \end{aligned} \quad (13)$$

By using these two formulae we get

$$\mathrm{e}^{i\hat{H}_{(a,b)} T} \hat{d}^\dagger \mathrm{e}^{-i\hat{H}_{(a,b)} T} = e^{-\Gamma T} \hat{d}^\dagger + \sum_{k\alpha} \frac{g}{\sqrt{2}} W_{k\alpha}^{(a,b)} \hat{c}_{k\alpha}^\dagger \quad (14)$$

$$\begin{aligned} \mathrm{e}^{i\hat{H}_{(a,b)} T} \hat{c}_{k\alpha}^\dagger \mathrm{e}^{-i\hat{H}_{(a,b)} T} = & \frac{g}{\sqrt{2}} W_{k\alpha}^{(a,b)} \hat{d}^\dagger \\ & + \sum_{k'\alpha'} \left(\frac{g^2 (W_{k\alpha}^{(a,b)} - W_{k'\alpha'}^{(a,b)})}{2(\epsilon_{k\alpha}^{(a,b)} - \epsilon_{k'\alpha'}^{(a,b)})} + \delta_{\alpha,\alpha'} \delta_{k,k'} \mathrm{e}^{i\epsilon_{k\alpha}^{(a,b)} T} \right) \hat{c}_{k'\alpha'}^\dagger, \end{aligned} \quad (15)$$

where $W_{k\alpha}^{(a,b)}(T) = \frac{\mathrm{e}^{i\epsilon_{k\alpha}^{(a,b)} T} - e^{-\Gamma T}}{\epsilon_{k\alpha}^{(a,b)} - i\Gamma}$, $\epsilon_{kL}^a = \epsilon_{kR}^b = \epsilon_k + V/2$ and $\epsilon_{kR}^a = \epsilon_{kL}^b = \epsilon_k - V/2$. Employing this formula twice gives

the evolution over a full period:

$$\begin{aligned} \mathrm{e}^{i\hat{H}_a T} \mathrm{e}^{i\hat{H}_b T} \hat{d}^\dagger \mathrm{e}^{-i\hat{H}_b T} \mathrm{e}^{-i\hat{H}_a T} &= e^{-2\Gamma T} \hat{d}^\dagger + \sum_{k\alpha} \frac{g}{\sqrt{2}} D_{k\alpha}^a \hat{c}_{k\alpha}^\dagger, \\ \mathrm{e}^{i\hat{H}_a T} \mathrm{e}^{i\hat{H}_b T} \hat{c}_{k\alpha}^\dagger \mathrm{e}^{-i\hat{H}_b T} \mathrm{e}^{-i\hat{H}_a T} &= \sum_{k'\alpha'} (K_{k'\alpha', k\alpha} \\ &+ \delta_{k,k'} \delta_{\alpha,\alpha'} \mathrm{e}^{2i\epsilon_k T}) \hat{c}_{k'\alpha'}^\dagger + \frac{g}{\sqrt{2}} D_{k\alpha}^b \hat{d}^\dagger, \end{aligned} \quad (16)$$

where

$$\begin{aligned} D_{k\alpha}^{(a,b)} &= \mathrm{e}^{i\epsilon_{k\alpha}^{(a,b)} T} W_{k\alpha}^{(b,a)} + \mathrm{e}^{-\Gamma T} W_{k\alpha}^{(a,b)}, \\ K_{k'\alpha', k\alpha} &= \mathrm{e}^{i\epsilon_{k'\alpha'}^{(a,b)} T} \frac{g^2 (W_{k'\alpha'}^b - W_{k\alpha}^b)}{2(\epsilon_{k'\alpha'}^b - \epsilon_{k\alpha}^b)} \\ &+ \mathrm{e}^{i\epsilon_{k\alpha}^b T} \frac{g^2 (W_{k'\alpha'}^a - W_{k\alpha}^a)}{2(\epsilon_{k'\alpha'}^a - \epsilon_{k\alpha}^a)} + \frac{g^2}{2} W_{k'\alpha'}^a W_{k\alpha}^b. \end{aligned} \quad (17)$$

We perform the summation over k by transforming it into an integral and then employing the residue theorem. Applying the above formula recursively N times yields

$$\begin{aligned} &(\mathrm{e}^{i\hat{H}_a T} \mathrm{e}^{i\hat{H}_b T})^N \hat{d}^\dagger (\mathrm{e}^{-i\hat{H}_b T} \mathrm{e}^{-i\hat{H}_a T})^N = e^{-2N\Gamma T} \hat{d}^\dagger \\ &+ \sum_{k\alpha} \frac{g}{\sqrt{2}} D_{k\alpha}^a \gamma_N(k) \hat{c}_{k\alpha}^\dagger, \\ &(\mathrm{e}^{i\hat{H}_a T} \mathrm{e}^{i\hat{H}_b T})^N \hat{c}_{k\alpha}^\dagger (\mathrm{e}^{-i\hat{H}_b T} \mathrm{e}^{-i\hat{H}_a T})^N = \sum_{k\alpha} \frac{g}{\sqrt{2}} D_{k\alpha}^b \gamma_N(k) \hat{d}^\dagger \\ &+ \sum_{k'\alpha'} (\alpha_N(k', k) K_{k'\alpha', k\alpha} + \delta_{k,k'} \delta_{\alpha,\alpha'} \mathrm{e}^{2N\mathrm{i}\epsilon_k T} \\ &+ \frac{g^2}{2} \beta_N(k', k) D_{k'\alpha'}^a D_{k\alpha}^b) \hat{c}_{k'\alpha'}^\dagger, \end{aligned} \quad (18)$$

where $\alpha_0 = \beta_0 = \gamma_0 = 0$ and the recursion relations are

$$\alpha_{N+1}(k', k) = \alpha_N(k', k) \mathrm{e}^{2i\epsilon_{k'} T} + \mathrm{e}^{2N\mathrm{i}\epsilon_k T},$$

$$\beta_{N+1}(k', k) = \beta_N(k', k) \mathrm{e}^{2i\epsilon_{k'} T} + \gamma_N(k),$$

$$\gamma_{N+1}(k) = \gamma_N(k) \mathrm{e}^{-2\Gamma T} + \mathrm{e}^{2N\mathrm{i}\epsilon_k T}.$$

It is easy to find

$$\alpha_N = \frac{\mathrm{e}^{2N\mathrm{i}\epsilon_k T} - \mathrm{e}^{2N\mathrm{i}\epsilon_{k'} T}}{\mathrm{e}^{2i\epsilon_k T} - \mathrm{e}^{2i\epsilon_{k'} T}} \quad (19)$$

$$\gamma_N = \frac{\mathrm{e}^{2N\mathrm{i}\epsilon_k T} - \mathrm{e}^{-2N\Gamma T}}{\mathrm{e}^{2i\epsilon_k T} - \mathrm{e}^{-2\Gamma T}}. \quad (20)$$

In the first half-period the current evaluates to

$$I_\alpha(t) = s_\alpha \frac{e\Gamma}{h} \int d\epsilon_k n_k \left(\sum_{\alpha'} \Gamma |\xi_{k\alpha'}^{(1)}|^2 - 2 \mathrm{Im}(\xi_{k\alpha}^{(1)} \mathrm{e}^{-2N\mathrm{i}\epsilon_k T - i\epsilon_{k\alpha}^a \tau}) \right), \quad (21)$$

where $\xi_{k\alpha}^{(1)} = D_{k\alpha}^a \gamma_N(k) \mathrm{e}^{-\Gamma \tau} + \mathrm{e}^{2N\mathrm{i}\epsilon_k T} W_{k\alpha}^a(\tau)$, n_k is the Fermi-Dirac distribution function. In the following we will always specialize to the zero temperature case ($n_k = 1$ for $k < 0$, $n_k = 0$ for $k \geq 0$). In the second half-period the current evaluates to

$$\begin{aligned} I_\alpha(t) = & s_\alpha \frac{e\Gamma}{h} \int d\epsilon_k n_k \left(\sum_{\alpha'} \Gamma |\xi_{k\alpha'}^{(2)}|^2 \right. \\ & \left. - 2 \mathrm{Im}(\xi_{k\alpha}^{(2)} \mathrm{e}^{-2N\mathrm{i}\epsilon_k T - i\epsilon_{k\alpha}^a T - i\epsilon_{k\alpha}^b \tau}) \right) \end{aligned} \quad (22)$$

where $\xi_{k\alpha}^{(2)} = D_{k\alpha}^a \gamma_N(k) e^{-\Gamma(T+\tau)} + e^{2N\epsilon_k T} (W_{k\alpha}^a e^{-\Gamma\tau} + e^{i\epsilon_{k\alpha}^a T} W_{k\alpha}^b(\tau))$. To simplify notation in lengthy expressions we will frequently employ Γ as the unit of energy and current, and $1/\Gamma$ as the unit of time. In the final results we always reintroduce all dimensionful parameters.

3. Buildup of the steady state

There is a transient time regime after the coupling of the dot to the leads is switched on at time $t = 0$ before a steady state has built up. Initially, the left lead current is opposite to the right one and the initially empty dot is being charged. We will see that these transient effects decay exponentially (proportional to $e^{-\Gamma t}$) to the steady state.

Let us explicitly look at the two limits of period $T \rightarrow \infty$ (dc bias) and $T \rightarrow 0$ (very fast driving). For $T \rightarrow \infty$ one finds from equation (21)

$$I_\alpha(t) = s_\alpha \frac{e}{h} \int d\epsilon_k n_k \left(\sum_{\alpha'} \frac{1 + e^{-2t} - e^{i\epsilon_{k\alpha'}^a t-t} - e^{-i\epsilon_{k\alpha'}^a t-t}}{(\epsilon_{k\alpha'}^a)^2 + 1} - 2 \text{Im} \left[\frac{1 - e^{-i\epsilon_{k\alpha'}^a t-t}}{\epsilon_{k\alpha'}^a - i} \right] \right). \quad (23)$$

The steady limit ($t \rightarrow \infty$) is

$$I = \frac{e\Gamma}{h} \int d\epsilon \left(n\left(\epsilon + \frac{eV}{2}\right) - n\left(\epsilon - \frac{eV}{2}\right) \right) \frac{\Gamma}{\epsilon^2 + \Gamma^2} \quad (24)$$

which, of course, coincides with the well-known result for the stationary dc current [15], e.g. for zero temperature

$$I = \frac{2e\Gamma}{h} \arctan \left(\frac{eV}{2\Gamma} \right). \quad (25)$$

In the fast driving limit $T \rightarrow 0$ we keep $t = 2NT$ invariant and let $N \rightarrow \infty$. According to the Trotter formula, the evolution then becomes equivalent to zero voltage bias [32], $\lim_{T \rightarrow 0} (e^{i\hat{H}_a T} e^{i\hat{H}_b T})^N = e^{i(\hat{H}_a + \hat{H}_b)T N}$. We find

$$I_\alpha(t) = s_\alpha \frac{2e\Gamma e^{-t}}{h} \int d\epsilon n(\epsilon) \frac{e^{-t} - \cos \epsilon t - \epsilon \sin \epsilon t}{\epsilon^2 + 1}. \quad (26)$$

In figure 2 we show the transient currents in the left and right leads for different periods T when $\mu = 0$. The current oscillations are suppressed when the frequency goes to infinity. The $I(t)$ curves gradually change from the dc limit to the high frequency limit described by equation (26) when the period T decreases. In the fast driving limit the left and right currents are opposite to each other and both decay to zero with increasing time.

4. Steady state behavior

When the time is much larger than $1/\Gamma$, the current reaches its steady state behavior. By taking $N \rightarrow \infty$ we find this steady state limit given by

$$I_\alpha(\tau) = s_\alpha \frac{e\Gamma}{h} \int d\epsilon_k n_k (|\tilde{\xi}_{kL}|^2 + |\tilde{\xi}_{kR}|^2 - 2 \text{Im} \tilde{\xi}_{k\alpha}), \quad (27)$$

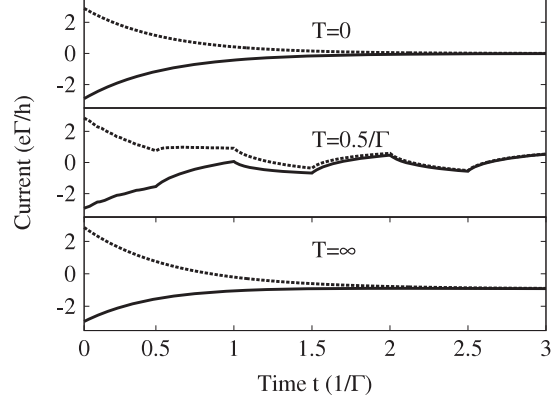


Figure 2. Time-dependent current for different switching periods T of the ac voltage bias (top: infinitely fast driving, middle: intermediate fast driving, bottom: dc case). Zero temperature and ac voltage bias $V = \Gamma$ in all graphs. The full lines denote the left lead current, while the dashed lines the right lead current. The hybridization is switched on at time $t = 0$. Notice the discontinuous onset of the current at $t = 0$, which is due to the wide band limit for the conduction band (a detailed discussion can be found in [2]).

where $0 \leq \tau \leq T$. In the first half-period we have

$$\tilde{\xi}_{k\alpha} = \frac{1}{\epsilon_{k\alpha}^a - i} + \frac{s_\alpha V (e^{2i\epsilon T - i\epsilon_{k\alpha}^a \tau - \tau} - e^{i\epsilon_{k\alpha}^a (T-\tau) - T - \tau})}{(e^{2i\epsilon T} - e^{-2T})(\epsilon_{k\alpha}^a - i)(\epsilon_{k\alpha}^b - i)}, \quad (28)$$

and in the second half-period

$$\tilde{\xi}_{k\alpha} = \frac{1}{\epsilon_{k\alpha}^b - i} + \frac{s_\alpha V (e^{i\epsilon_{k\alpha}^b (T-\tau) - T - \tau} - e^{2i\epsilon T - i\epsilon_{k\alpha}^b \tau - \tau})}{(e^{2i\epsilon T} - e^{-2T})(\epsilon_{k\alpha}^a - i)(\epsilon_{k\alpha}^b - i)}. \quad (29)$$

From equations (28) and (29) one immediately verifies that the steady state current satisfies $I_\alpha(\tau) = -I_{\bar{\alpha}}(\tau + T)$ as expected intuitively, where $\bar{\alpha}$ denotes the opposite lead.

4.1. Linear response regime

In the linear response regime of small voltage bias a sinusoidal signal drives a sinusoidal current with the same frequency, and signals with different frequencies can be superimposed linearly. Therefore we can factorize the rectangular signal into a series of sinusoidal components and find the frequency-dependent complex admittance of the system.

In the linear response regime the left lead current is equal to the right lead one and can be expressed as a Landauer-Büttiker-like formula:

$$\lim_{V \rightarrow 0} \frac{I(\tau)}{V} = \frac{e^2}{h} \int d\epsilon n(\epsilon) T(\epsilon), \quad (30)$$

where

$$T(\epsilon) = \frac{2\epsilon\Gamma^3}{(\epsilon^2 + \Gamma^2)^2} - \text{Im} \left[\frac{2\Gamma^2 e^{i\epsilon T - i\epsilon \tau - \tau}}{(e^{i\epsilon T} + e^{-T})(\epsilon - i\Gamma)^2} \right]. \quad (31)$$

We Fourier-transform both the ac voltage signal and the current. We define $I(\omega_n) = \int_0^{\tilde{\omega}T} dt e^{i\omega_n t} I(t) =$

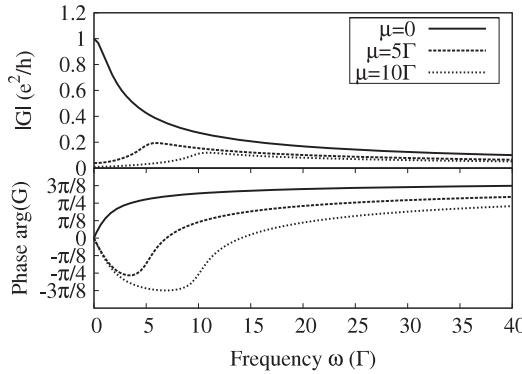


Figure 3. The linear admittance of a resonant level model for various level positions μ (energy of the dot level with respect to the Fermi energy in the leads) at zero temperature. The top graph shows the absolute value of the admittance, the bottom one its phase.

$2 \int_0^T d\tau e^{i\omega_n \tau} I(\tau)$, where we use the property $I(\tau + T) = -I(\tau)$ and $V(\omega_n) = \int_0^{2T} dt e^{i\omega_n t} V(t)$. Here $\omega_n = \frac{n\pi}{T}$ and n is an odd number. The voltage bias is $-V$ for $0 \leq t \leq T$ and V for $T \leq t \leq 2T$, leading to $V(\omega_n) = \frac{4V}{i\omega_n}$. By adjusting T the frequency ω_n can be an arbitrary real number and the linear response admittance $G(\omega) = I(\omega)/V(\omega)$ at zero temperature is given by

$$G(\omega) = \frac{e^2}{h} \left(\frac{\arccot \frac{\omega-\mu}{\Gamma} - \arccot \frac{\omega+\mu}{\Gamma}}{2\omega/\Gamma} - \frac{i\Gamma}{4\omega} \ln \frac{(\mu^2 + \Gamma^2)^2}{((\mu + \omega)^2 + \Gamma^2)((\mu - \omega)^2 + \Gamma^2)} \right), \quad (32)$$

where μ denotes the position of the dot level with respect to the average Fermi energy of the leads, see figure 1. Equation (32) agrees with previous ac calculations in the linear response regime, see [33]. Figure 3 depicts $G(\omega)$ for different level positions μ . The admittance goes to zero for fast driving,

$\omega \rightarrow \infty$. For $\omega \rightarrow 0$ one recovers the well-known dc conductance $G = \frac{e^2}{h} \frac{\Gamma^2}{\mu^2 + \Gamma^2}$. For asymmetric dot positions the resonance peak is around $\omega = \mu$, showing the PAT (photon-assisted tunneling) effect [14]: when the frequency of the ac signal is equal to the energy difference of the dot level from the Fermi energy in the leads, electrons in the leads can absorb a photon and jump into the dot. Notice from figure 3 that the symmetric dot always acts like an inductor, as already explained in [33]. For asymmetric dots there is a crossover from capacitive to inductive behavior around $\omega = \mu$ [33].

4.2. Beyond the linear response regime

For a voltage bias beyond the linear response regime it is impossible to calculate $G(\omega)$ by performing a Fourier transformation since the different frequency components interact with each other nonlinearly. Therefore we now depict the behavior of the current $I(t)$ as a function of time t during one full period in the steady state situation. Due to the nonlinearities we need to discuss this separately for different driving periods T . We will always take zero temperature in the following, so the generalization to nonzero temperature is straightforward.

We first look at fast driving, $T \ll \Gamma^{-1}$. For the symmetric situation the $I-t$ curve becomes triangulated: the current decreases from maximum to minimum in the first half-period, and then increases from minimum to maximum in the second half-period, see figure 4. In the opposite slow driving limit $T \gg \Gamma^{-1}$, the $I-t$ curve becomes rectangled. The saturated current in each half-period is simply given by the corresponding steady dc current (25). For intermediate driving speed, $T \sim \Gamma^{-1}$, we observe ringing oscillations [15] of the current with period $4\pi/V$ (see figure 5).

For asymmetric dot positions $\mu \neq 0$ the current also has characteristics of PAT and ringing, which are, however, not easily visible in a plot like figure 6. Clear signatures can be found in the differential conductance with respect to the gate voltage, which we denote as *gate differential*

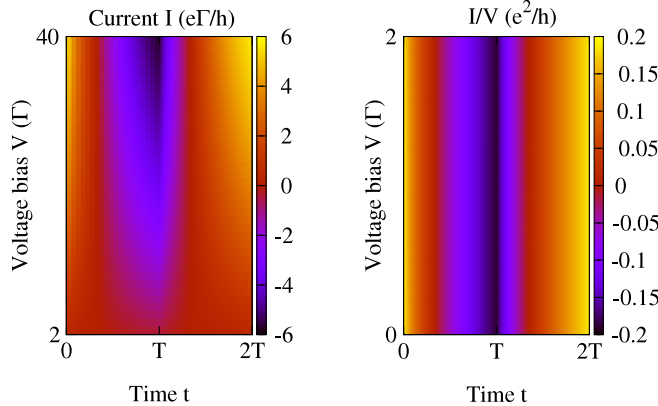


Figure 4. The steady state current in one period for fast driving (here $T = 0.1/\Gamma$ and zero temperature) in a symmetric resonant level model ($\mu = 0$). The left figure depicts the current I (units $e\Gamma/h$) in the nonlinear regime and the right figure shows I/V (units e^2/h) for smaller voltage bias (linear response regime). Because the driving period is shorter than the time required to establish stationarity in one period, the time-dependent current looks triangular.

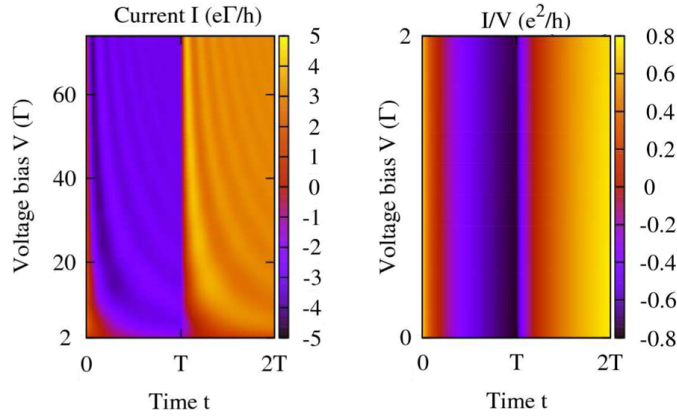


Figure 5. The steady state current in one period for intermediate driving (here $T = 1/\Gamma$ and zero temperature) in a symmetric resonant level model ($\mu = 0$). The left figure depicts the current I (units $e\Gamma/h$) in the nonlinear regime, and the right figure shows I/V (units e^2/h) for smaller voltage bias (linear response regime). The oscillations of the current with period $4\pi/V$ ('current ringing' [15]) are clearly visible for large bias.

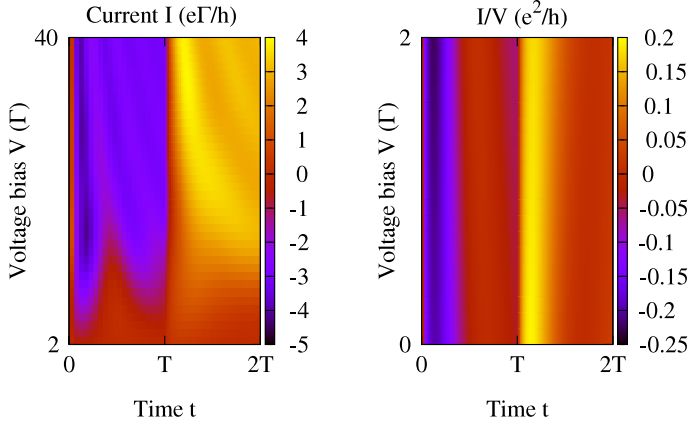


Figure 6. The steady state current in one period for intermediate driving (here $T = 1/\Gamma$ and zero temperature) in an asymmetric resonant level model ($\mu = 5\Gamma$). The left figure depicts the current I (units $e\Gamma/h$) in the nonlinear regime and the right figure shows I/V (units e^2/h) for smaller voltage bias (linear response regime). The crossover from capacitive to inductive response (compare figure 3) leads to a complicated behavior of the current in the first half-period.

conductance G^{gate} to distinguish it from the usual definition of differential conductance with respect to the voltage bias between the leads. We define

$$G_\alpha^{\text{gate}}(\epsilon, \tau) \stackrel{\text{def}}{=} \frac{dI_\alpha(\tau)}{d\mu} \Big|_{\mu=\epsilon} \quad (33)$$

and the current can then be expressed as $I_\alpha(\tau) = \int_{-\infty}^\mu d\epsilon G_\alpha^{\text{gate}}(\epsilon, \tau)$.

Figures 7 and 8 show G^{gate} in the first half-period (G^{gate} in the second half-period follows via $G_{2\text{nd}}^{\text{gate}}(\epsilon) = G_{1\text{st}}^{\text{gate}}(-\epsilon)$). In the linear response regime we find a pair of bright PAT lines at $\epsilon = \pm\pi/T$ (see figure 7). In the regime far from equilibrium, high order PAT lines at $\epsilon = n\pi/T$ ($|n| \geq 2$) can be observed (see figure 8), indicating multiple photon-assisted tunneling processes. These PAT lines combine and are replaced

by a pair of bright resonance lines at $\epsilon = \pm V/2$ when the period increases. This demonstrates that ac transport for high frequencies is dominated by photon-assisted tunneling, and by resonance tunneling for low frequencies.

5. Conclusions

We have investigated a resonant level model driven by rectangular ac bias in and beyond the linear response regime. Even this simple model shows surprisingly rich behavior in its transport properties. One can observe specific non-equilibrium effects like the buildup of the steady state, current ringing and photon-assisted tunneling, and the crossover to the well-studied limiting cases of dc bias and linear response regime. The results are exact and based on an explicit diagonalization

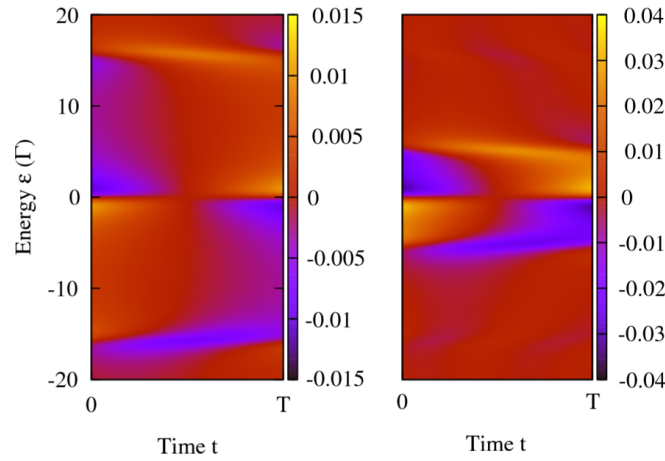


Figure 7. The gate differential conductance $G_L^{\text{gate}}(\epsilon, \tau)$ (units e^2/h) in the linear response regime ($V = 0.2\Gamma$ and zero temperature) for period $T = 0.2/\Gamma$ in the left figure and $T = 0.6/\Gamma$ in the right figure. The pair of bright lines symmetric to $\epsilon = 0$ are the PAT lines at $\epsilon = \pm\pi/T$.

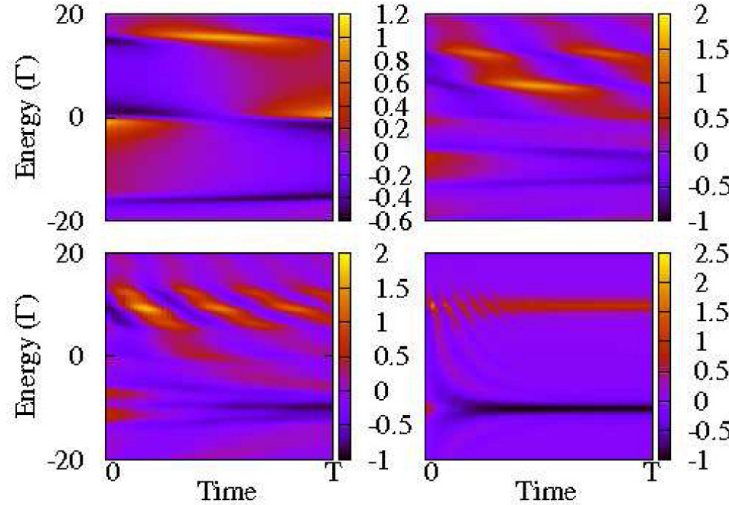


Figure 8. The gate differential conductance $G_L^{\text{gate}}(\epsilon, \tau)$ (units e^2/h) for large voltage bias ($V = 20\Gamma$) and zero temperature. The top left figure shows fast driving ($T = 0.2/\Gamma$), $T = 0.5/\Gamma$ in the top right figure, intermediate driving ($T = 1/\Gamma$) bottom left and slow driving ($T = 5/\Gamma$) bottom right. The y axis denotes the energy ranging from -20Γ to 20Γ . For fast driving ($T < 0.8/\Gamma$) the higher-order PAT lines are clearly visible. For slower driving ($T > 0.8/\Gamma$) the PAT lines away from $\epsilon = \pm V/2$ disappear with increasing T .

of the Hamiltonian in the first and second half-periods of the rectangular voltage bias driving. Within the flow equation framework, this approach can easily be generalized to an interacting quantum impurity model exposed to ac driving beyond the linear regime. Much less is known about such systems, which provides another motivation for this work and will be studied in a subsequent publication.

Acknowledgments

We acknowledge support through SFB 484 of the Deutsche Forschungsgemeinschaft, the Center for NanoScience (CeNS)

Munich and the German Excellence Initiative via the Nanosystems Initiative Munich (NIM).

References

- [1] Anders F B 2008 *Phys. Rev. Lett.* **101** 066804
Anders F B 2008 *J. Phys.: Condens. Matter* **20** 195216
- [2] Schmidt T, Werner P, Mühlbacher L and Komnik A 2008 *Phys. Rev. B* **78** 235110
- [3] Werner P, Oka T and Millis A J 2009 *Phys. Rev. B* **79** 035320
- [4] White S R and Feiguin A E 2004 *Phys. Rev. Lett.* **93** 076401
- [5] Schmitteckert P 2004 *Phys. Rev. B* **70** 121302
- [6] Fujii T and Ueda K 2003 *Phys. Rev. B* **68** 155310

- [7] Rosch A, Kroha H and Woelfle P 2001 *Phys. Rev. Lett.* **87** 156802
- [8] Schoeller H and Reininghaus F 2009 *Phys. Rev. B* **80** 045117
Schoeller H and Reininghaus F 2009 *Phys. Rev. B* **80**
209901(E)
- [9] Kehrein S 2005 *Phys. Rev. Lett.* **95** 056602
Fritsch P and Kehrein S 2009 *Ann. Phys. NY* **324** 1105
- [10] Meir Y, Wingreen N S and Lee P 1993 *Phys. Rev. Lett.* **70** 2601
- [11] Nordlander P, Pustilnik M, Meir Y, Wingreen N S and Langreth D C 1999 *Phys. Rev. Lett.* **83** 808
- [12] Eckel J, Heidrich-Meisner F, Jakobs S G, Thorwart M, Pletyukhov M and Egger R 2010 arXiv:[1001.3773](#)
- [13] Tien P K and Gordon J P 1963 *Phys. Rev.* **129** 647
- [14] Kouwenhoven L P, Jauhar S, Orenstein J and McEuen P L 1994 *Phys. Rev. Lett.* **73** 3443
- [15] Jauho A P, Wingreen N S and Meir Y 1994 *Phys. Rev. B* **50** 5528
- [16] Wingreen N S, Jauho A P and Meir Y 1993 *Phys. Rev. B* **48** 8487
- [17] Maciejko J, Wang J and Guo H 2006 *Phys. Rev. B* **74** 085324
- [18] Goker A 2008 *Solid State Commun.* **148** 230
- [19] Pilhal M and Langreth D C 2000 *Phys. Rev. B* **61** R13341
- [20] Nordlander P, Wingreen N S, Meir Y and Langreth D C 2000 *Phys. Rev. B* **61** 2146
- [21] Schiller A and Hershfield S 1996 *Phys. Rev. Lett.* **77** 1821
- [22] Schiller A and Hershfield S 1995 *Phys. Rev. B* **51** 12896
- [23] Schiller A and Hershfield S 2000 *Phys. Rev. B* **62** R16271
- [24] Moskalets M and Büttiker M 2002 *Phys. Rev. B* **66** 205320
- [25] Moskalets M and Büttiker M 2004 *Phys. Rev. B* **70** 245305
- [26] Kohler S, Lehmann J and Hänggi P 2005 *Phys. Rep.* **406** 379
- [27] Martinez D F, Molina R A and Hu B 2008 *Phys. Rev. B* **78** 045428
- [28] Kwapinski T 2004 *Phys. Rev. B* **69** 153303
- [29] Kwapinski T, Kohler S and Hänggi P 2009 *Phys. Rev. B* **79** 155315
- [30] Arrachea L 2005 *Phys. Rev. B* **72** 125349
- [31] Moekel M 2005 Application of the flow equation method to the out-of-equilibrium Anderson impurity model *Diploma Thesis* Universität München
- [32] Eisler V and Peschel I 2008 *Ann. Phys. (Berlin)* **17** 410
- [33] Fu Y and Dudley S C 1993 *Phys. Rev. Lett.* **70** 65

5.3 Parametric instability in periodically driven Luttinger Liquids

As the Kondo model for strongly correlated quantum impurity systems the Luttinger liquid constitutes the paradigm for strongly correlated and interacting electron systems in low dimensions. For some details about the equilibrium properties see Sec. 2.2. For interaction quenches the dynamics of Luttinger liquids exemplifies the properties of integrable systems in the sense of absence of thermalization in the long-time limit. Instead of being equivalent to a canonical state the asymptotic steady state is equivalent to a generalized Gibbs ensemble [29]. For details about interaction quenches and the question of thermalization see the introduction in Ch. 2.

As already emphasized in the beginning of Ch. 5 there are only a few examples in the literature where the properties of interacting strongly correlated many-body systems in the presence of periodic driving are addressed. Below, the impact of a periodic time-dependence of the interaction strength onto the properties of a system of spinless fermions in one dimension is investigated. The Hamiltonian of the periodically driven Luttinger liquid is given by:

$$H(t) = H_0 + H_{\text{int}}(t). \quad (5.6)$$

The kinetic energy remains unchanged compared to the equilibrium situation

$$H_0 = v_F \sum_{k,\eta=L/R} k : c_{k\eta}^\dagger c_{k\eta} : \quad (5.7)$$

whereas the interaction part acquires a time-dependence

$$\begin{aligned} H_{\text{int}}(t) &= \sum_{\eta=L/R} \int_{-L/2}^{L/2} dx \int_{-L/2}^{L/2} dx' \rho_\eta(x) \frac{1}{2} U(x - x'; t) \rho_\eta(x') + \\ &\quad + \int_{-L/2}^{L/2} dx \int_{-L/2}^{L/2} dx' \rho_L(x) U(x - x'; t) \rho_R(x'). \end{aligned} \quad (5.8)$$

For details about the Hamiltonian and its derivation see Sec. 2.2. This Hamiltonian differs from the equilibrium case only through the periodic time dependence of the interaction $U(x - x'; t)$ with an associated Fourier transform $U_q(t) = \int dx e^{-iqx} U(x; t)$. Throughout the analysis below a repulsive interaction potential $U_q(t) > 0$ is considered. The colons $: \dots :$ denote normal ordering relative to the Fermi sea and v_F is the Fermi velocity. The fermionic density $\rho_\eta(x)$ with $\eta = L/R$ is determined by the fermionic fields $\psi_\eta(x) = \sqrt{2\pi/L} \sum_k e^{-ikx} c_{k\eta}$ via $\rho_\eta(x) = : \psi_\eta^\dagger(x) \psi_\eta(x) : .$ The operator $c_{k\eta}^\dagger$ creates a fermion of the species $\eta = L/R$ with wave vector $k .$

In the nonequilibrium scenario under investigation the system is initially prepared in the ground state $|\psi_0\rangle$ at some fixed interaction strength such that $U_q(t < 0) = V_q(1 + \nu)$ is chosen to be time-independent for times $t < 0$. At time $t = 0$ the periodic driving is started with the following parametrization of the time-dependence of the interaction potential

$$U_q(t) = V_q[1 + \nu \cos(\Omega t)]. \quad (5.9)$$

Throughout the following analysis only repulsive interactions will be studied such that $V_q > 0$ and $0 < \nu < 1$. The interaction potential is supposed to be of finite range and cut off beyond a momentum scale q_c . This turns out to be important, see below. Note that for the experimental realization in an optical lattice it is not the interaction strength itself that is under direct control. Instead it is possible to vary the hopping amplitude $J(t) = J_0[1 - \nu \cos(\Omega t)]$ periodically as has been done for spectroscopy [165, 178]. Regarding the time evolution operator this, however, maps onto a problem with time-independent hopping $J = J_0$ and an interaction strength $U \rightarrow U(t) = U/[1 - \nu \cos(\Omega t)]$. For small amplitudes $\nu \ll 1$ this then approximately gives $U(t) \approx V[1 + \nu \cos(\Omega t)]$ in first order in ν as desired with respect to Eq. (5.9). Note that the precise value of ν has no influence on the qualitative results of the discussion below such that the restriction $\nu \ll 1$ for a realization in optical lattices would have no impact on the main conclusions.

Note that only the case of spinless fermions is considered. This reduced model system already incorporates most of the characteristic features of interacting fermions in 1D. For a system of fermions with spin in equilibrium, for example, the dynamics separates into two independent sectors of spin and charge, a phenomenon called spin-charge separation, each of which can be modeled by a Hamiltonian of the form in Eq. (5.6). Note that the influence of a periodic modulation of the Fermi velocity onto the momentum distribution in case of fermions with spin has been investigated recently [62].

The interaction strength is characterized by the dimensionless number

$$\alpha = \frac{V_0}{2\pi v_F} \quad (5.10)$$

which within the validity of the Luttinger model is always chosen $\alpha < 1$. The interaction potential V_q is assumed to be cut off beyond the momentum scale q_c . In the numerical simulations a Gaussian is chosen for simplicity, i.e., $V_q/(2\pi v_F) = \alpha \exp[-(q/q_c)^2]$.

Although the Hamiltonian in Eq. (5.6) is quartic in fermionic operators it can be mapped onto a quadratic and exactly solvable problem using the bosonization technique [34]. Introducing bosonic operators [34]

$$\begin{aligned} b_{q\eta} &= -i\sqrt{\frac{2\pi}{Lq}} \sum_k c_{k-q\eta}^\dagger c_{k\eta}, \quad q > 0, \\ b_{q\eta}^\dagger &= i\sqrt{\frac{2\pi}{qL}} \sum_k c_{k+q\eta}^\dagger c_{k\eta}, \quad q > 0, \end{aligned} \quad (5.11)$$

for each right- and left-moving branch $\eta = L/R$, the Hamiltonian in Eq. (5.6) can be mapped onto a quadratic but time-dependent bosonic problem

$$H = \sum_{q>0, \eta=L/R} \omega_q(t) b_{q\eta}^\dagger b_{q\eta} - \sum_{q>0} q \frac{U_q(t)}{2\pi} \left[b_{qL}^\dagger b_{qR}^\dagger + b_{qR} b_{qL} \right] + \Delta(t). \quad (5.12)$$

The dispersion of the diagonal part of the above Hamiltonian is given by

$$\omega_q(t) = qv_F \left(1 + \frac{U_q(t)}{2\pi v_F} \right). \quad (5.13)$$

The overall constant $\Delta(t) = (2\pi)^{-1} \sum_{q>0} q U_q(t)$ has no effect on the time evolution of observables except the internal energy density itself as discussed below. In principle, it is possible to diagonalize this Hamiltonian using a time-dependent unitary transformation. However, it turns out to be suitable to determine the dynamics in the untransformed basis, see Sec. 5.3.1 below.

Irrespective of the details the periodically driven Luttinger liquid develops a parametric instability [84, 62, 133]. Along with the instability comes an exponential growth in the internal energy of the system. The periodic driving leads to an “overheating” in the long-time limit. On intermediate time scales, however, set by the interaction strength and the finite range of the interaction meta-stable states with long lifetimes can form. These meta-stable states are characterized by approximately constant time-averaged internal energies. The overheating signals that beyond the onset of the instability additional internal perturbations or external dissipation mechanisms have to be included for a realistic description at long times. Nevertheless, at intermediate times the physics will still be dominated by the meta-stable states found below. It is argued that one possible internal mechanism for the suppression of the instability may be the inclusion of quadratic corrections of the initial fermionic dispersion relation. But this renders the problem nonintegrable and the exact solvability is spoiled, see Sec. 2.2. Possible dissipation mechanisms depend strongly on the particular experimental realization of the system. For an implementation in a solid state context such as gold chains on surfaces [18] the coupling of the system to phonons of the underlying bulk structure will constitute an important mechanism to dissipate energy. When realized in optical lattices where phonons are absent an important mechanism will be the emission of photons.

The instability shows different manifestations in different quantities. In the fermionic particle density perturbations are exponentially amplified yielding a superlattice with a periodicity set by the driving frequency Ω , the interaction strength, and the finite range of the interaction. The fermionic momentum distribution develops steps that can be associated with processes where fermions scatter off each other by absorbing quanta of the driving frequency. This is another example where for periodically driven systems the dominant processes are not only the energy conserving ones but rather those where the energy is conserved up to a multiple of the driving frequency, see also the discussion about photon-assisted tunneling in Sec. 5.2. The external periodic driving force provides an energy reservoir in quantized units of the driving frequency Ω that particles can use to overcome energy barriers as in case of photon-assisted tunneling, see Sec. 5.2, or that allows fermions to enlarge their available phase space at higher energies where more free states are accessible for scattering, see below.

Another consequence of the parametric instability is the breakdown of the adiabatic limit even in case of a vanishing driving frequency $\Omega \rightarrow 0$. The number of periods that the system can adiabatically follow the ground state is independent of the driving frequency and only depends on the interaction strength. Thus, irrespective of how slowly the system is driven the regime of adiabaticity is limited.

5.3.1 Nonequilibrium time evolution

For the dynamics of all the quantities considered such as energy density, fermionic density, and the momentum distribution it is sufficient to solve the Heisenberg equations of motion for the bosonic operators

$$\frac{d}{dt} b_{q\eta}(t) = -i\omega_q(t)b_{q\eta}(t) + iq \frac{U_q(t)}{2\pi} b_{q\bar{\eta}}^\dagger \quad (5.14)$$

with $\bar{\eta}$ the conjugate species of η , i.e., $\bar{L} = R$ and vice versa. These differential equations for operators can be transformed into differential equations for complex functions $\chi_{q\eta}(t)$ and $\lambda_{q\eta}(t)$ defined by

$$b_{q\eta}(t) = \chi_{q\eta}(t)b_{q\eta} + \lambda_{q\eta}(t)b_{q\bar{\eta}}^\dagger. \quad (5.15)$$

when inserted into Eq. (5.14). The resulting systems of coupled differential equations can be cast into a more familiar form by regarding appropriate superpositions

$$\alpha_{q\eta} = \chi_{q\eta} - \lambda_{q\eta}^*, \quad \beta_{q\eta} = \chi_{q\eta} + \lambda_{q\eta}^*. \quad (5.16)$$

The function $\alpha_{q\eta}$ is the solution of a parametrically driven harmonic oscillator and obeys a Mathieu equation in properly scaled parameters

$$\frac{d^2\alpha_{q\eta}(\tau)}{d\tau^2} + \epsilon_q^2 [1 + 2\gamma_q \cos(2\tau)] \alpha_{q\eta}(\tau) = 0 \quad (5.17)$$

with the dimensionless time $\tau = \Omega t/2$, the natural frequency $\epsilon_q = 2v_F q \Omega^{-1} \sqrt{1 + V_q/(\pi v_F)}$ of the harmonic oscillator, and $\gamma_q = \nu V_q/(2\pi v_F + 2V_q)$ the coupling strength of the periodic perturbation. The initial conditions for the solution of the Mathieu equation are $\alpha_{q\eta}(t=0) = 1$ and $\alpha'_{q\eta}(t=0) = -iv_F q$. The remaining function $\beta_{q\eta} = i(qv_F)^{-1} d\alpha_{q\eta}(t)/dt$ is just proportional to the time derivative of $\alpha_{q\eta}$.

Concluding, the time evolution in the periodically driven Luttinger liquid is equivalent to a set of parametrically driven harmonic oscillators. The Mathieu equation in Eq. (5.17) in general exhibits no analytic solution in terms of elementary functions, for special cases, however, such as parametric resonance, approximate analytical solutions are available, see below. For the general case the differential equations are solved numerically using a standard 4-th order Runge-Kutta algorithm.

The driven harmonic oscillator in Eq. (5.17) shows an instability with exponentially growing amplitudes $\alpha_{q\eta}$ in the case of parametric resonance which occurs for that particular plasmonic mode q for which $\epsilon_q = 1$ or equivalently $\Omega/2 = v_F q \sqrt{1 + V_q/(\pi v_F)}$ [102].

In the following it is important to distinguish two different cases of fast and slow driving. The energy scale Ω^* associated with the crossover between the two limits is set by

$$\Omega^* = v_F q_c. \quad (5.18)$$

For slow driving $\Omega \ll \Omega^*$ the resonant bosonic mode q^* for which parametric occurs is determined by

$$\frac{q^*}{q_c} \xrightarrow{\Omega \ll \Omega^*} \frac{1}{\sqrt{1 + 2\alpha}} \frac{\Omega}{2\Omega^*} \quad (5.19)$$

to leading order in Ω/Ω^* . The rate Γ of the associated exponential growth in time can be determined using standard methods [102]

$$\Gamma \stackrel{\Omega \ll \Omega^*}{=} \frac{1}{4} \frac{\alpha\nu}{1+2\alpha} \Omega. \quad (5.20)$$

The time scale t^* for the onset of the instability is then determined by the rate Γ via

$$t^* = \Gamma^{-1}. \quad (5.21)$$

In the opposite case $\Omega \gg \Omega^*$ of fast driving the resonant mode

$$\frac{q^*}{q_c} \stackrel{\Omega \gg \Omega^*}{\longrightarrow} \frac{\Omega}{2\Omega^*} \quad (5.22)$$

is independent of the interaction potential up to corrections suppressed by the cutoff q_c . The associated rate of the exponential growth is then given by

$$\Gamma \stackrel{\Omega \gg \Omega^*}{=} \frac{1}{4} \Omega \nu V_{q^*}. \quad (5.23)$$

Its precise behavior for $\Omega/\Omega^* \gg 1$ or equivalently $q^*/q_c \gg 1$ depends on the details of the large momentum behavior of the interaction potential. If $V_q \sim \exp[-Cq]$ for some constant $C > 0$ the rate $\Gamma \sim \exp[-D\Omega/\Omega^*]$ with $D = Cq_c/2$ is suppressed exponentially. Analogously, algebraically decaying potentials $V_q \sim (q/q_c)^{-\mu}$ yield a power law dependence $\Gamma \sim (\Omega/\Omega^*)^{1-\mu}$.

Remarkably, as Γ is linear in Ω for slow driving, see Eq. (5.20), the adiabatic approximation breaks down after a fixed number of periods $N_{\text{per}} \sim \Omega/\Gamma = 4(1+2\alpha)/(\alpha\nu)$ set by the interaction strength α and the coupling to the periodic perturbation ν irrespective of Ω . By reducing the driving frequency one cannot increase the number of periods for the validity of the adiabatic approximation.

5.3.2 Internal energy density

Typically, the periodically driven quantum many-body systems considered so far in the literature ignore the possible influence of dissipation mechanisms onto the dynamics, with the exceptions of Refs. [174, 9, 3]. This is an important issue because the energy in the system will increase during the considered nonequilibrium protocol. For bounded Hamiltonians, fermionic or spin systems on a lattice, for example, the internal energy will necessarily saturate, for unbounded Hamiltonians this need not be the case. Due to the parametric instability the internal energy of the Luttinger liquid diverges as will be shown below. Even though the internal energy for bounded Hamiltonians will always stay finite, the question whether the unavoidable presence of dissipation mechanisms may at some point in time have a considerable influence onto the dynamics is still largely unanswered. The existence of the instability naturally sets the time scale t^* , see Eq. (5.21), beyond which

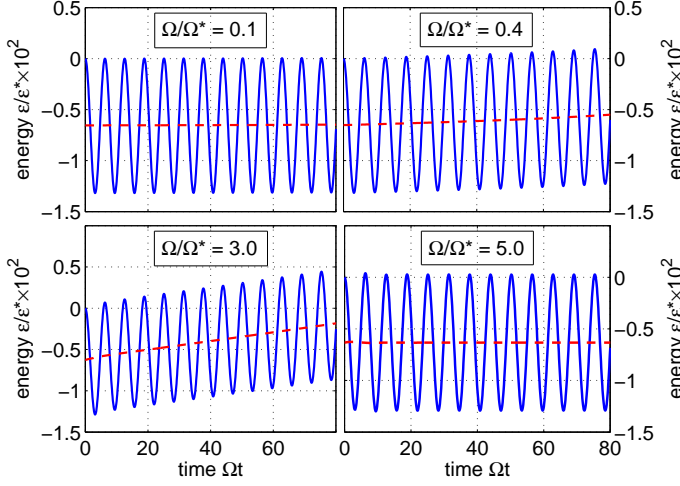


Figure 5.2: Time evolution of the internal energy density $\mathcal{E}(t)$ (blue lines) and its time average $\bar{\mathcal{E}}(t)$ (red dashed lines) for different driving frequencies Ω in units $\mathcal{E}^* = q_c \Omega^*$. For these numerical simulations an analytic interaction potential $V_q/(2\pi v_F) = \alpha \exp(-(q/q_c)^2)$ has been chosen with $\alpha = 1/2$ and $\nu = 1/5$.

additional internal properties such as the curvature of the fermionic dispersion relation or external dissipation mechanisms have to be included for a realistic description.

The internal energy density $\mathcal{E}(t)$ of the periodically driven Luttinger liquid system at time t is given by

$$\mathcal{E}(t) = \int_0^\infty \frac{dq}{2\pi} \left[2\omega_q(t) K_q^1(t) - q \frac{U_q(t)}{2\pi} K_q^2(t) \right] + \frac{\Delta(t)}{L} \quad (5.24)$$

where

$$\begin{aligned} K_q^1(t) &= \sinh^2(\theta_q) + |\lambda_{qL}(t)|^2 \cosh(2\theta_q) + \\ &\quad + \text{Re}[\chi_{qL}(t)\lambda_{qL}^*(t)] \sinh(2\theta_q), \\ K_q^2(t) &= \sinh(2\theta_q) \text{Re}[\lambda_{qL}^2 + \chi_{qL}^2] + \\ &\quad + 2 \cosh(2\theta_q) \text{Re}[\lambda_{qL}\chi_{qL}], \end{aligned} \quad (5.25)$$

and $\omega_q(t)$ given by Eq. (5.13). The Bogoliubov angles θ_q corresponding to the initial state are determined by the formula $\tanh(2\theta_q) = V_q(1+\nu)/(2\pi v_F + V_q(1+\nu))$. Note that the Luttinger liquid Hamiltonian in Eq. (5.6) appears typically as the low-energy theory derived from more complicated many-body systems. Within such a mapping additional time-dependent contributions to $\Delta(t)$ in Eq. (5.12) can be generated in the periodically driven case. Those contributions depend on the details of the model and have to be worked out for each particular case. In the present work we are interested in the generic low-energy properties that are all contained in the Luttinger liquid description of the model

Hamiltonian in Eq. (5.6). Thereby we ignore additional contributions to the energy density that are generated by the mapping onto this low-energy theory.

In Fig. 5.2 plots for $\mathcal{E}(t)$ are shown for different driving frequencies. Periodically driven systems without instabilities develop stationary states at long times where expectation values time-averaged over one period become time-independent [151]. Besides the internal energy density also its time average has been included

$$\bar{\mathcal{E}}(t) = \frac{\Omega}{2\pi} \int_t^{t+2\pi/\Omega} dt' \mathcal{E}(t') \quad (5.26)$$

in Fig. 5.2 for the identification of such stationary states.

In case of fast driving $\Omega \gg \Omega_*$ the rate Γ of the parametric resonance is strongly suppressed due to the finite cutoff scale q_c of the interaction potential, see Eq. (5.23). After the initial transient dynamics following the start of the periodic driving the system settles to a stationary state with a constant time-averaged energy density. As Γ is small but still finite the system will nevertheless develop the instability for times $t > t^*$. Consequently this intermediate state is only meta-stable.

In the limit $\Omega \rightarrow \infty$ the dynamics becomes effectively equivalent to one of a time-averaged Hamiltonian if there exists a mechanism that prevents the absorption of high-energy photons [71]. In the present model system this mechanism is provided due to the finite range q_c of the interaction. Physically speaking, the system is not able to follow the fast external perturbation and only perceives its average contribution. As the initial state is not an eigenstate of the time-averaged Hamiltonian for times $t > 0$ the dynamics becomes equivalent to that of an interaction quench. Indeed, the time-averaged energy density $\bar{\mathcal{E}}(t)$ follows precisely the behavior of the interaction quench scenario.

When the driving frequency is lowered below the crossover scale Ω_* the rate of the instability Γ grows rapidly. As a consequence, the transient dynamics is directly followed by a linearly increasing contribution due to the influence of the instability. For $\Omega \lesssim \Omega_*$ the instability is so strong that it hinders the buildup of a meta-stable state completely. For even lower frequencies, however, the rate $\Gamma \sim \Omega$ decreases again opening up the window for the meta-stable state for times t up to $t \sim \Omega^{-1}$ as can be clearly observed in Fig. 5.2.

5.3.3 Fermionic density

The internal energy density of the system mirrors the instability by showing a divergence at times $t > t^*$. The question, however, which internal perturbations can prevent the buildup of the instability has not been touched up to now. Regarding the time evolution of the fermionic density it is argued that it may be sufficient to include the curvature of the fermionic dispersion relation.

In the following the dynamics of an initially localized fermionic density wave packet is analyzed in presence of the periodic driving. The time evolution of a local perturbation in the fermionic density is solely determined by the solution $\alpha_{q\eta}(t)$ of the Mathieu equation,

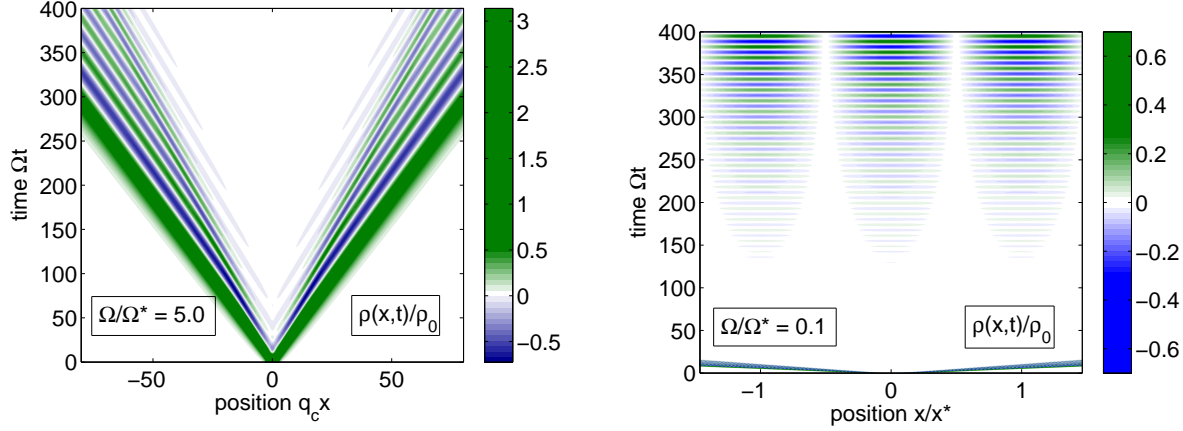


Figure 5.3: Time evolution a localized perturbation in the fermionic density $\rho(x, t)$ for the cases of fast (upper plot) and slow (lower plot) driving. Again, an analytic interaction potential $V_q/(2\pi v_F) = \alpha \exp(-(q/q_c)^2)$ has been chosen with $\alpha = 1/5$ and $\nu = 1/2$ for these numerical simulations. The initial density profile is a Gaussian.

see Eq. (5.17),

$$\rho(x, t) = 2 \int_0^\infty \frac{dq}{2\pi} \cos(qx) \rho_q^0 \operatorname{Re}[\alpha_{qL}(t)] \quad (5.27)$$

with $\rho_q^0 = \int dq e^{-iqx} \rho^0(x)$ characterising the initial density profile $\rho^0(x) = \rho(x, t = 0)$. In Fig. 5.3 the fermionic density is shown for the fast and slow driving regimes where a Gaussian wave packet has been chosen as initial condition for illustration.

For fast driving $\Omega \gg \Omega_*$ one observes that the initial local perturbation first splits into right- and left-moving contributions. In course of time, however, away from the main peak satellites appear within a light cone whose maximal extent one can estimate by the maximal bosonic phase velocity $v_{max} = v_F \sqrt{1 + 2\alpha(1 + \nu)}$ of the instantaneous equilibrium Hamiltonians. This picture is suitable for times $t < t^*$ before the onset of instability.

In the opposite case $\Omega \ll \Omega_*$ a completely different picture emerges. After a fixed number of periods $N_{per} \sim \Omega/\Gamma = 4(1 + 2\alpha)/(\alpha\nu)$ to leading order in Ω/Ω^* the dynamics is dominated by the parametric resonance leading to an exponential growth of the initial perturbation for $x \ll v_{max}t$

$$\rho(x, t) \xrightarrow{t \gg t^*} q_c A \cos(q^* x) \cos\left(\frac{\Omega t}{2} + \pi/4\right) e^{\Gamma t} \quad (5.28)$$

with A a constant nonuniversal prefactor. A superlattice forms with a period

$$x^* = 2\pi/q^* \quad (5.29)$$

set by the resonant mode, see Eqs. (5.19,5.22), whose amplitude is growing exponentially at a rate Γ . Note that this does not lead to a violation of particle number conservation as it might seem from the plot in Fig. 5.4. For each density hump there also exists a valley

of depletion of fermionic charge carriers. Moreover, the superlattice extends only over a distance $d \sim v_{max}t$ within the light cone set by the maximal sound velocity. Integrating over the whole real-space shows that the particle number is still conserved as one can directly check via Eq. (5.27).

The aim of the following is to argue that including the curvature of the fermionic dispersion relation will cut off the exponential growth of the superlattice for sufficiently large densities. In the limit of slow driving one can approximately neglect the influence of the finite range of the interaction and set $V_q \approx V_0$. For a q -independent interaction the influence of a nonlinear fermionic dispersion relation can be accounted for approximately [148, 76]. The time-independent version of the Hamiltonian in Eq. (5.6) including the quadratic curvature contribution can be mapped to a free Fermi gas [148, 76]. For a free Fermi gas the buildup of large densities is prevented due to the nonlinear dispersion eventually leading to the production of shock waves [15].

5.3.4 Momentum distribution

In equilibrium the momentum distribution for the fermionic particles exemplifies the different influence of repulsive interactions in one dimension compared to higher dimensions where Fermi liquid theory holds. In Luttinger liquids the momentum distribution shows no jump at the Fermi energy even at zero temperature reminiscent of the absence of a finite quasiparticle weight.

The momentum distribution function $f_k(t)$ for the left-moving fermions

$$f_k(t) = \langle \psi_0 | c_{kL}^\dagger(t) c_{kL}(t) | \psi_0 \rangle, \quad (5.30)$$

with $|\psi_0\rangle$ the initial state, is connected to an equal-time correlation function $f(x, t)$ in real-space via Fourier transformation

$$f_k(t) = \int \frac{dx}{2\pi} e^{-ikx} f(x, t), \quad (5.31)$$

$$f(x, t) = \langle \psi_0 | \psi_L^\dagger(x, t) \psi_L(0, t) | \psi_0 \rangle \quad (5.32)$$

that can be calculated analytically using the bosonization technique [34]

$$f(x, t) = \frac{1}{a + ix} e^{-F(x, t)}. \quad (5.33)$$

with a^{-1} an ultraviolet cut-off. The rate function $F(x, t) = F_{eq}(x) + F_p(x, t)$ can be split into an equilibrium part F_{eq} associated with the initial state and a nonequilibrium contribution $F_p(x, t)$ due to the periodic driving.

$$F_{eq}(x) = 4 \int_0^\infty \frac{dq}{q} \sin^2 \left(\frac{qx}{2} \right) \sinh^2(\theta_q), \quad (5.34)$$

$$\begin{aligned} F_p(x, t) &= 4 \int_0^\infty \frac{dq}{q} \sin^2 \left(\frac{qx}{2} \right) \\ &\times [| \lambda_{qL} |^2 \cosh(2\theta_q) + \text{Re}(\chi_{qL} \lambda_{qL}^*) \sinh(2\theta_q)] \end{aligned} \quad (5.35)$$

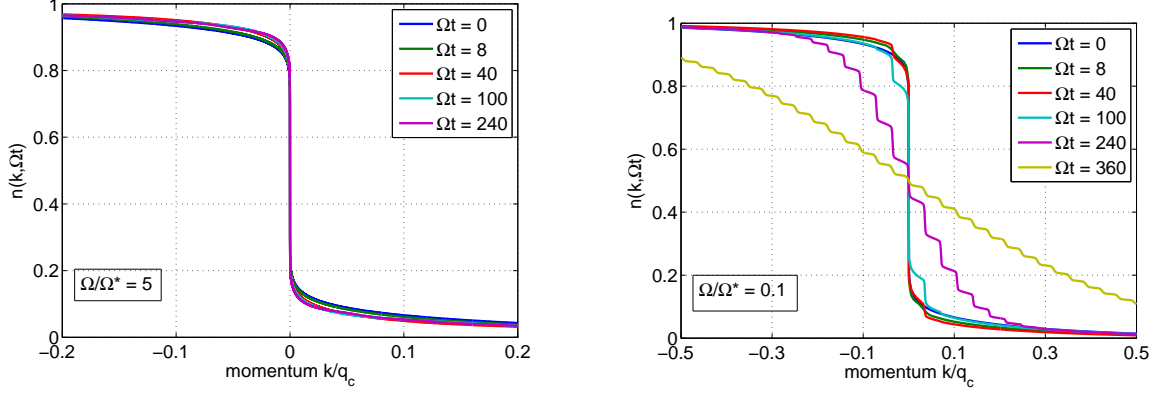


Figure 5.4: Time evolution of the momentum distribution $f_k(t)$ for fast (left plot) and slow (right plot) driving. The parameters of the numerical simulation are chosen as for the previous plots.

Here, θ_q denotes the Bogoliubov angles of the diagonalizing transformation for the initial equilibrium Hamiltonian obeying the equation $\tanh(2\theta_q) = V_q(1 + \nu)/(2\pi v_F + V_q(1 + \nu))$. In Fig. 5.4 numerical results for the momentum distribution for fast and slow driving are shown.

For $\Omega \gg \Omega^*$ the behavior under time evolution is consistent with the picture observed for the internal energy density in Sec. 5.3.2. Following the initial transient dynamics the momentum distribution becomes meta-stable on intermediate times $t < t^*$. The momentum distribution is self-averaging in the sense that it is time-independent in contrast to the energy density where only the time average becomes constant. In the limit $\Omega \rightarrow \infty$ we recover the interaction quench limit of an effectively time-averaged Hamiltonian as for the internal energy density, see Sec. 5.3.2. In the vicinity of the Fermi level the momentum distribution shows a nonanalytic behavior for large times

$$n_k(t \rightarrow \infty) - \frac{1}{2} \xrightarrow{\Omega \rightarrow \infty} \text{sgn}(k)|k/q_c|^\gamma \quad (5.36)$$

with $\text{sgn}(k)$ the sign function. The exponent γ is in precise agreement with an interaction quench scenario [29, 141].

For slow driving $\Omega \ll \Omega^*$, however, the picture differs considerably compared to the internal energy density. Immediately after the start of the periodic driving the momentum distribution shows the presence of the parametric instability even for times $t \ll t^*$ by a redistribution of momenta near the Fermi point $k = 0$. The momentum distribution smears out in the vicinity of the Fermi surface indicating that scattering between the fermionic particles becomes very effective at low momenta. The periodic perturbation provides sufficient energy for scattering processes similar to a finite temperature in equilibrium even though the excitations for both scenarios are fundamentally different. Physically speaking, due to the periodic driving in a scattering process the energy difference $\delta\varepsilon$ of the participating fermions is only conserved up to multiples of the driving frequency $\delta\varepsilon \rightarrow \delta\varepsilon + n\Omega$

corresponding to the absorption ($n > 0$) or emission ($n < 0$) of n photons of energy Ω . For larger times, this mechanism of absorption of photons becomes more pronounced as one can see in Fig. 5.4. The momentum distribution develops steps each of which can be associated with fermions that have been scattered from a state $v_F k$ to $v_F k + n\Omega$. Note that this step structure is remarkably similar to a simplified picture where in spirit of the work by Tien and Gordon [170] for noninteracting systems the periodic driving generates a weighted superposition of equilibrium momentum distributions shifted by an energy $n\Omega$. It is, however, not possible to establish such a superposition principle precisely in the present interacting system. Due to the parametric instability the fermions are redistributed completely for times $t \rightarrow \infty$ leading to a momentum distribution $f_k(t \rightarrow \infty) = 1/2$ of infinite temperature.

5.3.5 Conclusions

In this section the dynamics of a Luttinger liquid with a periodically time-dependent repulsive interaction potential has been studied. Under the periodic driving the system develops an instability due to a parametric resonance. The associated time scale t^* , see Eqs. (5.20,5.23), sets the limit beyond which dissipation mechanisms or internal perturbations have to be included into an appropriate and realistic description of the dynamics. On intermediate time scales before the onset of instability, it is possible to identify metastable states for fast and slow driving with constant time-averaged internal energies. The parametric instability generates an exponential growth of perturbations in the fermionic density leading to the buildup of a superlattice with period x^* , confirm Eq. (5.29). The fermionic momentum distribution develops a step structure that can be associated with fermionic scattering processes under the absorption or emission of photons of quanta of the driving frequency Ω .

Chapter 6

Conclusion and outlook

Within this work nonequilibrium phenomena in quantum many-particle systems have been investigated from different perspectives with the focus on two different generic nonequilibrium processes - on the one hand sudden perturbations also called quantum quenches and on the other hand periodic driving.

The nonequilibrium properties of systems undergoing quantum quenches have been investigated from three different points of view, namely dynamics, thermodynamics, and dynamical phase transitions. In Ch. 2 the real-time dynamics of strongly correlated many-body systems has been analyzed for local quenches only acting on a nonextensive part of the system. These include the local spin dynamics in consequence of a quench in the exchange interaction of the Kondo model in Sec. 2.1, the sudden switch on of a mobile impurity in a chiral Luttinger liquid in Sec. 2.2 thereby identifying a new scattering channel, and the local energy dynamics in the anisotropic Heisenberg chain in Sec. 2.3.

In Ch. 3 the properties of nonequilibrium systems has been studied from a thermodynamic perspective. The work performed on a system constitutes one of the central objects in the thermodynamic description of nonequilibrium processes. Remarkably, quantum work is not an observable but rather a random variable with an associated probability distribution function termed work distribution. Work distributions obey fundamental nonequilibrium work fluctuation theorems such as the Jarzynski equality or the Crooks relation that can be viewed as nonequilibrium analogues to the fluctuation-dissipation theorems in the linear response regime. Remarkably, quantum work distribution functions have not been determined in experiments yet mainly because this needs a series of two energy measurements where at least the first one has to be nondestructive.

An important contribution of this thesis is the observation that there is a deep relation between work distributions for quenches in quantum impurity models and optical spectra of the x-ray edge type as shown in Sec. 3.3. This allows for a detailed and controlled experimental access to quantum work distributions. In the remainder of Ch. 3 the experimental implementation of x-ray edge spectra in quantum dots is discussed that could then be used in future experiments for the verification and analysis of nonequilibrium work fluctuation theorems and related questions.

The central aspect of the present work is the introduction of a dynamical phase tran-

sition for closed quantum many-body systems in Ch. 4. This definition is based on the observation that quantum systems can exhibit nonanalyticities in real-time evolution at critical times analogously to nonanalyticities of thermodynamic potentials in equilibrium phase transitions at critical points. The existence of the nonanalyticities is based on an extension of the concept of Fisher or Lee-Yang zeros to nonequilibrium quantities. These ideas have been applied in Sec. 4.2 to quenches in the transverse magnetic field in the one-dimensional Ising model. For the nonequilibrium dynamics the underlying equilibrium quantum critical point turns out to play a crucial role. Only for quenches across the equilibrium critical point real-time nonanalyticities appear. The relevance of the dynamical phase transitions onto the dynamics of the equilibrium order parameter is determined numerically.

In the context of the introduced dynamical phase transition it is of particular importance in the future to address a number of immediate questions. The dynamical phase transition has been demonstrated for a special model, its general relevance can only be tested by analyzing other systems as well. Central to the notion of a phase transition is the concept of universality. Whether and in which way this concept can be carried over to the dynamical phase transition remains to be investigated in the future. In close relationship to universality is the question of how robust the dynamical phase transition is to perturbations in particular those that preserve the symmetries of the model but break its integrability.

The last part of this thesis is concerned with periodically driven quantum many-body systems. In Sec. 5.1 a periodically driven Kondo model is investigated with periodically switched exchange interactions where it is shown that for particular cases the steady state in the fast driving limit cannot be described by an effective equilibrium Hamiltonian due to the inapplicability of the Trotter formula. The ac transport through a quantum dot beyond the linear response regime has been studied in Sec. 5.2 for a special choice of the periodic protocol. In Sec. 5.3 the influence of a periodically modulated interaction strength on the dynamics of interacting electrons in one dimensions has been investigated within the Luttinger liquid paradigm. Irrespective of the details this system develops a parametric instability leading to a breakdown of the adiabatic limit even for slow driving in the sense that the number of periods that the system can adiabatically follow becomes independent of the driving frequency.

Bibliography

- [1] R. Aguado, R. Lopez, G. Platero and C. Tejedor, *Physica B* **256 - 258** (1998), 165.
- [2] A. Altand, V. Gurarie, T. Kriecherbauer and A. Polkovnikov, *Phys. Rev. A* **79** (2009), 042703.
- [3] A. Amaricci, C. Weber, M. Capone and G. Kotliar, *arXiv* (2011).
- [4] F. Anders and A. Schiller, *Phys. Rev. Lett.* **95** (2005), 196801.
- [5] F. Anders and A. Schiller, *Phys. Rev. B* **74** (2006), 245113.
- [6] F.B. Anders and A. Schiller, *Phys. Rev. Lett.* **95** (2005), 196801.
- [7] P.W. Anderson, *J. Phys. C: Solid State Phys.* **3** (1970), 2436.
- [8] N. Andrei, *Phys. Rev. Lett.* **45** (1980), 379.
- [9] C. Aron, G. Kotliar and C. Weber, *Phys. Rev. Lett.* **108** (2012), 086401.
- [10] C. Ates, B. Olmos, J.P. Garrahan and I. Lesanovsky, *arXiv* (2011), 1112.4273v2.
- [11] P. Barmettler, M. Punk, V. Gritsev, E. Demler and E. Altman, *Phys. Rev. Lett.* **102** (2009), 130603.
- [12] T. Barthel and U. Schollwöck, *Phys. Rev. Lett.* **100** (2008), 100601.
- [13] J. Berges, S. Borsanyi and C. Wetterich, *Phys. Rev. Lett.* **93** (2004), 142002.
- [14] M.V. Berry, *Proc. R. Soc. Lond. A* **392** (1984), 45.
- [15] E. Bettelheim, A.G. Abanov and P.B. Wiegmann, *Phys. Rev. Lett.* **97** (2006), 246402.
- [16] G. Biroli, C. Kollath and A.M. Läuchli, *Phys. Rev. Lett.* **105** (2010), 250401.
- [17] I. Bloch, J. Dalibart and W. Zwerger, *Rev. Mod. Phys.* **80** (2008), 885.
- [18] C. Blumenstein, J. Schäfer, S. Mietke, S. Meyer, A. Dollinger, M. Lochner, X.Y. Cui, L. Patthey, R. Matzdorf and R. Claessen, *Nature Phys.* **7** (2011), 776.

- [19] G.N. Bochkov and Y.E. Kuzovlev, *Physica A* **106** (1981), 443.
- [20] B. Braunecker, *Phys. Rev. B* **73** (2006), 075122.
- [21] P. Calabrese and J. Cardy, *Phys. Rev. Lett.* **96** (2006), 136801.
- [22] P. Calabrese, F.H.L. Essler and M. Fagotti, *Phys. Rev. Lett.* **106** (2011), 227203.
- [23] P. Calabrese, F.H.L. Essler and M. Fagotti, *arXiv* (2012), 1204.3911v1.
- [24] H.B. Callen and T.A. Welton, *Phys. Rev.* **83** (1951), 34.
- [25] M. Campisi, P. Hänggi and P. Talkner, *Rev. Mod. Phys.* **83** (2011), 771.
- [26] M. Campisi, P. Talkner and P. Hänggi, *Phys. Rev. Lett.* **102** (2009), 210401.
- [27] M. Campisi, P. Talkner and P. Hänggi, *Philos. Transact. A Math. Phys. Eng. Sci.* **369** (2011), 291.
- [28] J.S. Caux and J. Mossel, *J. Stat. Mech.* (2011), P02023.
- [29] M.A. Cazalilla, *Phys. Rev. Lett.* **97** (2006), 156403.
- [30] D. Collin, F. Ritort, C. Jarzynski, S.B. Smith, I. Tinoco, Jr and C. Bustamante, *Nature* **437** (2005), 231.
- [31] M. Cramer, C.M. Dawson, J. Eisert and T.J. Osborne, *Phys. Rev. Lett.* **100** (2008), 030602.
- [32] G. Crooks, *Phys. Rev. E* **60** (1999), 2721.
- [33] N. d'Ambrumenil and B.A. Muzykantskii, *Phys. Rev. B* **71** (2005), 045326.
- [34] J. von Delft and H. Schoeller, *Ann. Phys. (Leipzig)* **7** (1998), 225.
- [35] J.M. Deutsch, *Phys. Rev. A* **43** (1991), 2046.
- [36] F. Douarche, S. Ciliberto and A. Petrosyan, *J. Stat. Mech.* (2005), P09011.
- [37] D.H. Dunlap and V.M. Kenkre, *Phys. Rev. B* **34** (1986), 3625.
- [38] A. Eckhardt, C. Weiss and M. Holthaus, *Phys. Rev. Lett.* **95** (2005), 26004.
- [39] M. Eckstein and M. Kollar, *Phys. Rev. Lett.* **100** (2008), 120404.
- [40] M. Eckstein, M. Kollar and P. Werner, *Phys. Rev. Lett.* **103** (2009), 056403.
- [41] M. Eckstein, T. Oka and P. Werner, *Phys. Rev. Lett.* **105** (2010), 146404.
- [42] M. Eckstein and P. Werner, *Phys. Rev. B* **82** (2010), 115115.

- [43] V. Eisler and I. Peschel, *Ann. Phys. (Berlin)* **17** (2008), 410.
- [44] J.M. Elzerman, S. De Franceschi, D. Goldhaber-Gordon, W.G. van der Wiel and L. Kouwenhoven, *J. Low Temp. Phys.* **118** (2000), 375.
- [45] A. Faribault, P. Calabrese and J.S. Caux, *J. Stat. Mech.* (2009), P03018.
- [46] M.E. Fisher: *The nature of critical points*, Band VIIC von *Lectures in Theoretical Physics*. Gordon and Breach, New York, 1968.
- [47] V.V. Flambaum and F.M. Izrailev, *Phys. Rev. E* **64** (2001), 036220.
- [48] T. Frankel: *The Geometry of Physics*. Cambridge University Press, 2004.
- [49] J.K. Freericks, *Phys. Rev. B* **77** (2008), 075109.
- [50] J.K. Freericks, V. Turkowski and V. Zlatic, *Phys. Rev. Lett.* **97** (2006), 266408.
- [51] A. Gambassi and A. Silva, *arXiv* (2011), 1106.2671v1.
- [52] D.M. Gangardt and M. Pustilnik, *Phys. Rev. A* **77** (2008), 041604(R).
- [53] N. Garnier and S. Ciliberto, *Phys. Rev. E* **71** (2005), 060101.
- [54] J.P. Garrahan, A.D. Armour and I. Lesanovsky, *Phys. Rev. E* **84** (2011), 021115.
- [55] J.P. Garrahan, R.L. Jack, V. Lecomte, E. Pitard, K. van Duijvendijk and F. van Wijland, *Phys. Rev. Lett.* **98** (2007), 195702.
- [56] J.P. Garrahan, R.L. Lack, V. Lecomte, E. Pitard, K. van Duijvendijk and F. van Wijland, *J. Phys. A: Math. Theor.* **42** (2009), 075007.
- [57] J.P. Garrahan and I. Lesanovsky, *Phys. Rev. Lett.* **104** (2010), 160601.
- [58] T. Giamarchi: *Quantum Physics in One Dimension*. Oxford University Press, 2004.
- [59] D. Goldhaber-Gordon, H. Shtrikman, D. Mahalu, D. Abusch-Magder, U. Meirav and M.A. Kastner, *Nature* **391** (1998), 156.
- [60] Y. Goldin and Y. Avishai, *Phys. Rev. Lett.* **81** (1998), 5394.
- [61] Y. Goldin and Y. Avishai, *Phys. Rev. B* **61** (2000), 16750.
- [62] D.C. Graf, G. Weick and E. Mariani, *Eur. Phys. Lett.* **89** (2010), 40005.
- [63] M. Greiner, O. Mandel, T.W. Hänsch and I. Bloch, *Nature* **419** (2002), 51.
- [64] V. Gritsev and A. Polkovnikov, *PNAS* **109** (2012), 6457.

- [65] A. Hackl, D. Roosen, S. Kehrein and W. Hofstetter, *Phys. Rev. Lett.* **102** (2009), 196601.
- [66] M.Z. Hasan and C.L. Kane, *Rev. Mod. Phys.* **82** (2010), 3045.
- [67] L.O. Hedges, R.L. Jack, J.P. Garrahan and D. Chandler, *Science* **323** (2009), 1309.
- [68] R.W. Helmes, M. Sindel, L. Borda and J. von Delft, *Phys. Rev. B* **72** (2005), 125301.
- [69] M.H. Hettler and H. Schoeller, *Phys. Rev. Lett.* **74** (1995), 4907.
- [70] A. Hewson: *The Kondo Problem to Heavy Fermions*. Cambridge University Press, Cambridge, 1993.
- [71] M. Heyl and S. Kehrein, *Phys. Rev. B* **81** (2010), 144301.
- [72] J.J. Hopfield, *Comments Solid State Phys.* **2** (1969), 40.
- [73] G. Huber, F. Schmidt-Kaler, S. Deffner and E. Lutz, *Phys. Rev. Lett.* **10** (2008), 070403.
- [74] F. Igloi and H. Rieger, *Phys. Rev. Lett.* **85** (2000), 3233.
- [75] F. Igloi and H. Rieger, *Phys. Rev. Lett.* **106** (2011), 035701.
- [76] A. Imambekov and L. Glazman, *Science* **323** (2009), 228.
- [77] A. Imambekov, T.L. Schmidt and L.I. Glazman, *arXiv* (2011), 1110.1374v1.
- [78] R.A. Jalabert and H.M. Pastawski, *Phys. Rev. Lett.* **86** (2001), 2490.
- [79] W. Janke and R. Kenna, *J. Stat. Phys.* **102** (2001), 1211.
- [80] C. Jarzynski, *Phys. Rev. Lett.* **78** (1997), 2690.
- [81] Y. Ji, Y. Chung, D. Sprinzak, M. Heiblum, D. Mahalu and H. Shtrikman, *Nature* **422** (2003), 415.
- [82] A.V. Joura, J.K. Freericks and T. Pruschke, *Phys. Rev. Lett.* **101** (2008), 196401.
- [83] I. Junier, A. Mossa, M. Manossa and F. Ritort, *Phys. Rev. Lett.* **102** (2009), 070602.
- [84] Y. Kagan and L.A. Manakova, *Phys. Rev. A* **80** (2009), 023625.
- [85] A. Kamenev and A. Levchenko, *Adv. Phys.* **58** (2009), 197.
- [86] A. Kaminski, Y.V. Nazarov and L. Glazman, *Phys. Rev. B* **62** (2000), 8154.
- [87] Y.V. Kaminski, A .and Nazarov and L. Glazman, *Phys. Rev. Lett.* **83** (1999), 384.

- [88] C.L. Kane and E.J. Mele, *Phys. Rev. Lett.* **95** (2005), 146802.
- [89] Z.P. Karkuszewski, C. Jarzynski and W.H. Zurek, *Phys. Rev. Lett.* **89** (2002), 170405.
- [90] C. Karrasch, T. Enss and V. Meden, *Phys. Rev. B* **73** (2006), 235337.
- [91] S. Kehrein: *The Flow Equation Approach to Many-Particle Systems*. Springer, Berlin, 2006.
- [92] M. Khodas, M. Pustilnik, A. Kamenev and L.I. Glazman, *Phys. Rev. B* **76** (2007), 155402.
- [93] T. Kinoshita, T. Wenger and D.S. Weiss, *Nature* **440** (2006), 900.
- [94] T. Kita, K. Ohtaka and Y. Tanabe, *J. Phys. Soc. Jpn.* **56** (1987), 4609.
- [95] M. Kollar, F.A. Wolf and M. Eckstein, *Phys. Rev. B* **84** (2011), 054304.
- [96] C. Kollath, A.M. Läuchli and E. Altman, *Phys. Rev. Lett.* **98** (2007), 180601.
- [97] J. Kondo, *Prog. Theor. Phys.* **32** (1964), 37.
- [98] A. Kotani and Y. Toyozawa, *J. Phys. Soc. Jpn.* **35** (1973), 1073.
- [99] A. Kotani and Y. Toyozawa, *J. Phys. Soc. Jpn.* **35** (1973), 1082.
- [100] H.R. Krishna-murty, J.W. Wilkins and K.G. Wilson, *Phys. Rev. B* **21** (1980), 1003.
- [101] H.R. Krishna-murty, J.W. Wilkins and K.G. Wilson, *Phys. Rev. B* **21** (1980), 1044.
- [102] L.D. Landau and E. Lifshitz: *Mechanics*. Elsevier, 2008.
- [103] S. Langer, F. Heidrich-Meisner, J. Gemmer, I.P. McCulloch and U. Schollwöck, *Phys. Rev. B* **79** (2009), 214409.
- [104] C. Latta, F. Haupt, M. Hanl, A. Weichselbaum, M. Claassen, W. Wuester, P. Fallahi, S. Faelt, L. Glazman, J. von Delft, H.E. Türeci and A. Imamoglu, *Nature* **474** (2011), 627.
- [105] A. LeClair, G. Mussardo, H. Saleur and S. Skorik, *Nuclear Physics B* **453** (1995), 581.
- [106] T.D. Lee and C.N. Yang, *Phys. Rev.* **87** (1952), 410.
- [107] A.J. Leggett, S. Chakravarty, A.T. Dorsey, M.P.A. Fisher, A. Garg and W. Zwerger, *Rev. Mod. Phys.* **59** (1987), 1.
- [108] F. Lesage and H. Saleur, *Phys. Rev. Lett.* **80** (1998), 4370.
- [109] E. Lieb, T. Schultz and D. Mattis, *Annals of Physics* **16** (1961), 407.

- [110] J. Liphardt, S. Dumont, S.B. Smith, I. Tinoco, Jr and C. Bustamante, *Science* **296** (2002), 1832.
- [111] D. Lobaskin and S. Kehrein, *Phys. Rev. B* **71** (2005), 193303.
- [112] D. Lobaskin and S. Kehrein, *J. Stat. Phys.* **123** (2006), 301.
- [113] R. Lopez, R. Aguado, G. Platero and C. Tejedor, *Phys. Rev. Lett.* **81** (1998), 4688.
- [114] R. Lopez, R. Aguado, G. Platero and C. Tejedor, *Phys. E* **6** (2000), 379.
- [115] G.D. Mahan, *Phys. Rev.* **163** (1967), 612.
- [116] S.R. Manmana, S. Wessel, R.M. Noack and A. Muramatsu, *Phys. Rev. Lett.* **98** (2007), 210405.
- [117] L. Mathey, K.L. Günter, J. Dalibard and A. Polkovnikov, *arXiv* (2011), 1112.1204v1.
- [118] B.M. McCoy, E. Barouch and D.B. Abraham, *Phys. Rev. A* **4** (1971), 2331.
- [119] P. Mehta and N. Andrei, *Phys. Rev. Lett.* **96** (2006), 216802.
- [120] M. Möckel and S. Kehrein, *Phys. Rev. Lett.* **100** (2008), 175702.
- [121] J.E. Moore and L. Balents, *Phys. Rev. B* **75** (2007), 121306.
- [122] L. Muehlbacher and E. Rabani, *Phys. Rev. Lett.* **100** (2008), 176403.
- [123] S. Mukamel, *Phys. Rev. Lett.* **90** (2003), 170604.
- [124] T.K. Ng, *Phys. Rev. Lett.* **76** (1996), 487.
- [125] P. Nordlander, M. Pustilnik, Y. Meir, N.S. Wingreen and D.C. Langreth, *Phys. Rev. Lett.* **83** (1999), 808.
- [126] P. Nordlander, N.S. Wingreen, Y. Meir and D.C. Langreth, *Phys. Rev. B* **61** (2000), 2146.
- [127] P. Nozieres, *J. Low Temp. Phys.* **17** (1974), 31.
- [128] P. Nozieres and C.T. De Dominicis, *Phys. Rev.* **178** (1969), 1097.
- [129] K. Ohtaka and Y. Tanabe, *Rev. Mod. Phys.* **62** (1990), 929.
- [130] R.G. Pereira, S.R. White and I. Affleck, *Phys. Rev. B* **79** (2009), 165113.
- [131] A. Peres, *Phys. Rev. A* **30** (1984), 1610.
- [132] P. Pfeuty, *Annals of Physics* **57** (1970), 79.

- [133] S. Pielawa, *Phys. Rev. A* **83** (2011), 013628.
- [134] D. Poletti and C. Kollath, *Phys. Rev. A* **84** (2011), 013615.
- [135] A. Polkovnikov, *Annals of Phys.* **325** (2010), 1790.
- [136] A. Polkovnikov, *Ann. Phys. (NY)* **326** (2011), 486.
- [137] A. Polkovnikov, K. Sengupta, A. Silva and M. Vengalattore, *Rev. Mod. Phys.* **83** (2011), 863.
- [138] F. Pollmann, S. Mukerjee, A.G. Green and J.E. Moore, *Phys. Rev. E* **81** (2010), 020101(R).
- [139] M. Pustilnik, M. Khodas, A. Kamenev and L.I. Glazman, *Phys. Rev. Lett* **96** (2006), 196405.
- [140] Z. Ratiani and A. Mitra, *Phys. Rev. B* **81** (2010), 125110.
- [141] J. Rentrop, D. Schuricht and V. Meden, *arXiv* (2012), 1203.0932v1.
- [142] R. Resta, *J. Phys. C: Condens. Matter* **12** (2000), R107.
- [143] M. Rigol, *Phys. Rev. Lett.* **103** (2009), 100403.
- [144] M. Rigol, V. Dunjko and M. Olshanii, *Nature* **452** (2008), 854.
- [145] M. Rigol, V. Dunjko, V. Yurovsky and M. Olshanii, *Phys. Rev. Lett.* **98** (2007), 050405.
- [146] D. Rossini, A. Silva, G. Mussardo and G.E. Santoro, *Phys. Rev. Lett.* **102** (2009), 127204.
- [147] D. Rossini, S. Suzuki, A. Silva, G. Mussardo and G.E. Santoro, *Phys. Rev. B* **82** (2010), 144302.
- [148] A.V. Rozhkov, *The European Physical Journal B* **47** (2005), 193.
- [149] S. Sachdev: *Quantum phase transitions*. Cambridge University Press, 1999.
- [150] M. Salmhofer and C. Honerkamp, *Prog. Theor. Phys.* **105** (2001), 1.
- [151] H. Sambe, *Phys. Rev. A* **7** (1973), 2203.
- [152] A. Schiller and S. Hershfield, *Phys. Rev. Lett.* **77** (1996), 1821.
- [153] M. Schiro and M. Fabrizio, *Phys. Rev. Lett.* **105** (2010), 076401.
- [154] H. Schoeller, *Eur. Phys. J. Special Topics* **168** (2009), 179.

- [155] U. Schollwoeck, *Rev. Mod. Phys.* **77** (2005), 259.
- [156] K. Schönhammer and V. Meden, *Phys. Rev. B* **47** (1993), 16205.
- [157] K.D. Schotte and U. Schotte, *Phys. Rev.* **182** (1969), 479.
- [158] S. Schuler, T. Speck, C. Tietz, J. Wrachtrup and U. Seifert, *Phys. Rev. Lett.* **94** (2005), 180602.
- [159] B. Sciolla and G. Biroli, *Phys. Rev. Lett.* **105** (2010), 220401.
- [160] K. Sengupta, S. Powell and S. Sachdev, *Phys. Rev. A* **69** (2004), 053616.
- [161] R. Sensarma, D. Pekker, E. Altman, E. Demler, N. Strohmaier, D. Greif, R. Jördens, L. Tarruell, H. Moritz and T. Esslinger, *Phys. Rev. B* **82** (2010), 224302.
- [162] A. Silva, *Phys. Rev. Lett.* **101** (2008), 120603.
- [163] B. Simon, *Phys. Rev. Lett.* **51** (1983), 2167.
- [164] M. Srednicki, *Phys. Rev. E* **50** (1994), 888.
- [165] T. Stoferle, H. Moritz, C. Schori, M. Koehl and T. Esslinger, *Phys. Rev. Lett.* **92** (2004), 130403.
- [166] P. Talkner and P. Hänggi, *J. Phys. A: Math. Theor.* **40** (2007), F569.
- [167] P. Talkner, E. Lutz and P. Hänggi, *Phys. Rev. E* **75** (2007), 050102.
- [168] H. Tasaki, *arXiv* (2000), condmat/0009244v2.
- [169] D.J. Thouless, M. Kohmoto, M.P. Nightingale and M. den Nijs, *Phys. Rev. Lett.* **49** (1982), 405.
- [170] P.K. Tien and J.P. Gordon, *Phys. Rev.* **129** (1963), 647.
- [171] H. Touchette, *Phys. Rep.* **478** (2009), 1.
- [172] G. Toulouse, *C. R. Acad. Sc. Paris B* **286** (1969).
- [173] N. Tsuji, T. Oka and H. Aoki, *Phys. Rev. B* **78** (2008), 235124.
- [174] N. Tsuji, T. Oka and H. Aoki, *Phys. Rev. Lett.* **103** (2009), 047403.
- [175] N. Tsuji, T. Oka, P. Werner and H. Aoki, *Phys. Rev. Lett.* **106** (2011), 236401.
- [176] H.E. Türeci, M. Hanl, M. Claasen, A. Weichselbaum, T. Hecht, B. Braunecker, A. Govorov, L.I. Glazman, A. Imamoglu and J. von Delft, *Phys. Rev. Lett.* **106** (2011), 107402.

- [177] V. Turkowski and J.K. Freericks, *Phys. Rev. B* **71** (2005), 085104.
- [178] T. Volz, N. Syassen, D.M. Bauer, E. Hansis, S. Dürr and G. Rempe, *Nature Phys.* **2** (2006).
- [179] G.M. Wang, E.M. Sevick, E. Mittag, D.J. Searles and D.J. Evans, *Phys. Rev. Lett.* **89** (2002), 050601.
- [180] P. Werner, T. Oka and A.J. Millis, *Phys. Rev. B* **79** (2009), 035320.
- [181] G.C. Wick, *Phys. Rev.* **80** (1950), 268.
- [182] P.B. Wiegmann, *J. Phys. C: Solid State Phys.* **14** (1981), 1463.
- [183] W.G. van der Wiel, S. De Franceschi, T. Fujisawa, J.M. Elzerman, S. Tarucha and L.P. Kouwenhoven, *Science* **289** (2000), 2105.
- [184] K.G. Wilson, *Rev. Mod. Phys.* **47** (1975), 773.
- [185] G. Yuval and P.W. Anderson, *Phys. Rev. B* **1** (1970), 1522.
- [186] G. Zarand and J. von Delft, *Phys. Rev. B* **61** (2000), 6918.

List of Publications

Parts of this thesis were published in the following articles:

1. **Nonequilibrium steady state in a periodically driven Kondo model**
M. Heyl and S. Kehrein, *Phys. Rev. B* **81**, 144301 (2010).
2. **Interaction quench dynamics in the Kondo model in presence of a local magnetic field**
M. Heyl and S. Kehrein, *J. Phys. C: Condens. Matt.* **22**, 345604 (2010).
3. **Electron-plasmon scattering in 1D chiral systems with nonlinear dispersion**
M. Heyl, S. Kehrein, F. Marquardt, and C. Neuenhahn, *Phys. Rev. B* **82**, 033409 (2010).
4. **Exact results for nonlinear ac-transport through a resonant level model**
P. Wang, M. Heyl, and S. Kehrein, *J. Phys. C: Condens. Matt.* **22**, 275604 (2010).
5. **Real-time energy dynamics in spin-1/2 Heisenberg chains**
S. Langer, M. Heyl, I. McCullloch, and F. Heidrich-Meisner, *Phys. Rev. B* **84**, 205115 (2011).
6. **X-ray edge singularity in optical spectra of quantum dots**
M. Heyl and S. Kehrein, *Phys. Rev. B* **85**, 155413 (2012).
7. **Crooks Relation in Optical Spectra: Universality in Work Distributions for Weak Local Quenches**
M. Heyl and S. Kehrein, *Phys. Rev. Lett.* **108**, 190601 (2012).

Acknowledgements

First of all I would like to thank my PhD advisor Prof. Stefan Kehrein. His valuable way of letting me freely explore the world of physics laid the foundations for deeply enjoying the years as a PhD and diploma student under his supervision. His willing ear for new ideas and at the same time his intuition as well as his way of questioning those have influenced my physical way of thinking substantially. I am very grateful for his interest to also touch elementary and fundamental questions.

This work benefited a lot from the insights, the knowledge, and ideas from those people that I have been working together with on different projects: Clemens Neuenhahn, Prof. Florian Marquardt, Pei Wang, Fabian Heidrich-Meisner, Stephan Langer, Marin Bukov, and Prof. Anatoli Polkovnikov. In particular, I enjoyed the innumerable discussions with Clemens Neuenhahn at different occasions that sharpened substantially my ability and my demand for physical pictures even for complex physical problems. Additionally I would like to thank Florian Marquardt for all the insights and his intuition that inspired my physical view on problems.

I would like to thank all group members members that have been part of the chair in recent years, in particular all the office colleagues Max Ludwig, Clemens Neuenhahn, Peter Fritsch, Florian Bauer, Jan Heyder, Georg Heinrich, Alexander Buchner, Arne Alex, and Pei Wang. Especially, I thank Max Treiber for all the breaks outside breathing fresh air and Michael Möckel for his warm and deep thoughts about physics and way beyond. Moreover, I would like to thank Oleg Yevtushenko for a lot of discussions and for sharing his knowledge over so many different things as well as Prof. Jan von Delft for the productive environment that he has established at his chair.

I acknowledge financial support during my PhD studies from the DFG via the Sonderforschungsbereiche SFB 631 and SFB TR 12 as well as the German Excellence Initiative through the Nanosystems Initiative Munich (NIM).

In the end I would like to thank all those people in my life beyond my physics work that form the basic foundation for all the effort that has been invested in this thesis. I really hope they know about their invaluable importance!

Curriculum vitae

Name: Markus Philip Ludwig Heyl

Date of birth: 21.10.1981

Place of birth: Starnberg

Academic education

Since 05/2009

Ludwig-Maximilians-University Munich

PhD student under the supervision of Prof. S. Kehrein

Nonequilibrium phenomena in many-body quantum systems

04/2007 - 04/2009

Ludwig-Maximilians-University Munich

Studies of physics and mathematics

Diploma 04/2009

Diploma thesis under the supervision of Prof. S. Kehrein

Periodic time dependent Kondo model

10/2002 - 03/2007

University of Augsburg

Studies of physics and mathematics